

Performance Analysis of Fractional Derivative in Image Processing Applications

A thesis submitted

in fulfillment of the requirement for the award of degree

of

Doctor of Philosophy

Submitted by

Kanwarpreet Kaur

Registration Number: 901606016

Under the Supervision of

Dr. Kulbir Singh
Professor, ECED

Dr. Neeru Jindal
Assistant Professor, ECED



**DEPARTMENT OF ELECTRONICS AND COMMUNICATION
ENGINEERING
THAPAR INSTITUTE OF ENGINEERING AND TECHNOLOGY,
PATIALA-147004**

FEBRUARY 2021

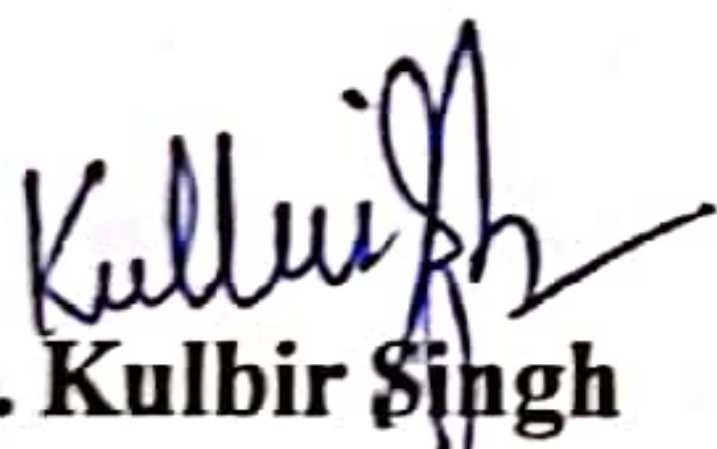
CERTIFICATE

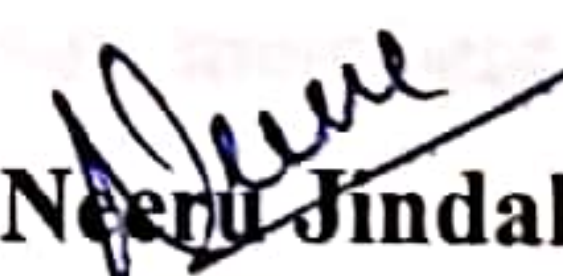
I hereby certify that the work which is being presented in the thesis entitled, "**Performance Analysis of Fractional Derivative in Image Processing Applications**", for the award of degree of **Doctor of Philosophy** in Electronics and Communication Engineering Department (ECED), Thapar Institute of Engineering and Technology, Patiala, is an authentic record of my own work carried out under the supervision and guidance of Dr. Kulbir Singh, Professor, ECED, and Dr. Neeru Jindal, Assistant Professor, ECED, Thapar Institute of Engineering and Technology, Patiala.

The results presented in this thesis have not been submitted in part or in full to any other University or Institute for the award of any degree or diploma.


Kanwarpreet Kaur

This is to certify that the above statement made by the candidate is correct to the best of my knowledge and belief.


Dr. Kulbir Singh
Professor, ECED
TIET, Patiala, India


Dr. Neeru Jindal
Assistant Professor, ECED
TIET, Patiala, India

ACKNOWLEDGEMENTS

First and foremost, I bow down to the Almighty for always showering His blessings on me. I am indebted to Him for his benevolence that held me in the moments of despair and inspired me to move forward by enlightening my thoughts with His wisdom. It is solely His grace that guided me from the very inception to the completion of this research work.

I would like to express my sincere, humble and immense gratitude to my supervisors **Dr. Kulbir Singh**, Professor, and **Dr. Neeru Jindal**, Assistant Professor, Department of Electronics and Communication Engineering, Thapar Institute of Engineering and Technology, Patiala for their support and motivation throughout this research work. The completion of the research work carried out in this thesis is attributed to extensive guidance from my supervisors. A special thanks to Dr. Kulbir Singh for convincing me to go down this road and Dr. Neeru Jindal for never letting me go off track with her intriguing ideas. Their foresight and vision worked as a silver lining for me in the dark clouds. Their enthusiastic supervision, untiring efforts, constructive criticism, and beneficial remarks during inspiring discussions helped a lot in the accomplishment of this thesis.

I am highly grateful to **Dr. Alpana Agarwal**, Head of Electronics and Communication Engineering Department, Thapar Institute of Engineering and Technology, Patiala for her continuous support and encouragement in my research work. I would like to thank **Dr. Anil Kumar Verma**, Professor, Department of Computer Science and Engineering, Thapar Institute of Engineering and Technology, Patiala for his guidance and cooperation. Moreover, I would also like to express sincere gratitude to my doctoral committee members **Dr. Hem Dutt Joshi**, Associate Professor, **Dr. Vinay Kumar**, Associate Professor in Electronics and Communication Engineering Department, Thapar Institute of Engineering and Technology, Patiala, and **Dr. Mandeep Singh**, Professor in Electrical and Instrumentation Engineering Department, Thapar Institute of Engineering and Technology, Patiala for their valuable suggestions during my entire research.

I am also immensely thankful to my fellow researchers, Dr. Gurinder Singh, Dr. Gittaly, Amit Kumar, Hari Shankar, Navneet Kaur, Gurvinder Singh, and Tanvi at Thapar Institute of Engineering and Technology, Patiala for helping me throughout my research. I would never forget the support of my friends Dr. Sandeep Kaur, Dr. Avneet Kaur, Dr. Ramandeep Kaur, Nitika, Harleen Kaur, Paramvir Kaur, and Deepa during my stay at the hostel.

I am also grateful to the researchers who share their ideas and experiences on ResearchGate, Academia.edu, etc. The acknowledgment would be incomplete if I do not express my gratitude to the non-teaching staff of the department for their help during the course of this study.

Last but not the least, I would like to thank my family and friends for their love, affection, encouragement, and support. I also owe the completion of this work to my dearest parents Dr. Gurvinderjit Singh and Mrs. Daljeet Kaur who supported me in all pursuits of life and always motivated me to move ahead by learning from past experiences with a positive attitude towards life. I am also thankful to my maternal aunt Ms. Swarnjit Kaur and grandmother Mrs. Gurdial Kaur for their blessings. Lastly, I would like to acknowledge the love of my younger sister Dr. Manavdeep Kaur who is the stress-buster of my life.

Kanwarpreet Kaur

ABSTRACT

The primary objective of the reported work is to thoroughly explore the aspects of Fractional Order Derivatives (FODs) in the prospective applications of image processing. The majority of integer-order based algorithms in the prevailing literature are not able to accurately model the systems owing to the problem of loss of information details, noise sensitivity, and deterioration in the smooth regions of an image. Moreover, in the case of color images, additional issues such as loss of correlation and information details exist when the color images are converted into grayscale images before processing or individual color channels are processed. Several techniques based on optimization, learning, and fractional exist in literature to deal with these issues but the fractional based methods are more efficient in terms of computational cost for smaller datasets. Despite being efficient, FODs such as Riemann-Liouville (RL) and Grünwald-Letnikov (GL) possess the demerit in terms of phase shifting that can cause image blurred distortion. In order to resolve these issues, Riesz FOD (RFOD) is considered in this work which possesses the inherent property of zero phase shifting. However, instead of utilizing the RFOD solely on the basis of theoretical concepts and findings, its mathematical and experimental analysis is conducted in spatial, FrFT, and quaternion domains. The imperative objective of the presented work is to incorporate the concept of RFOD in Fractional Fourier Transform (FrFT) and quaternion domain for utilizing the benefit of the fractional parameter in achieving design flexibility. To validate the proficiency of the proposed concept, the applications of edge detection and image enhancement are considered as they can further assist in the high-level image processing applications.

The robustness of RFOD in signal and image processing applications is confirmed judiciously by evaluating it in spatial, FrFT, and quaternion domain orderly. In the spatial domain, RFOD is incorporated in the Unsharp Masking (UM) for image enhancement. Upon subjecting to evaluation based on several standard images of various datasets as well as Fundus images, RFOD yielded better image visual quality as compared to RL, GL, and other image enhancement techniques. Thus, the promising results obtained by RFOD in the spatial domain for the image enhancement further stimulated to explore RFOD in the frequency domain. Hence, mathematical analysis of RFOD is carried out in the FrFT domain, thus, deriving a novel closed-form analytical expression for RFOD in the FrFT domain which is further utilized for the filtering application of signal processing. The efficacy of the low pass Finite Impulse Response (FIR) differentiator designed on the basis of RFOD in the FrFT

domain is validated by considering a design example of signal corrupted with high-frequency chirp noise. The simulation results exhibit that RFOD outperforms the RL and Caputo FODs in the FrFT domain in terms of minimum Root Mean Square Error (RMSE) of 0.115136 for the fractional order ranging from 0.2-0.6. Moreover, the proposed concept of RFOD in FrFT domain is extended for the two-dimensional applications of image sharpening and Homomorphic Filtering (HF) for the improvement in image visual quality. The substantial performance of RFOD in the FrFT domain further encouraged to utilize this exceptional combination for applications of image processing. Henceforth, RFOD is used to obtain the masks by employing various interpolation methods for the applications of image enhancement and edge detection. Consequently, a unified approach based on RFOD in the FrFT domain is developed for edge detection and enhancement of grayscale images which provided superior results than the existing FOD based approaches for edge detection and image enhancement. The concept of edge detection is further extended to color images. A quaternion based RFOD edge detection approach is developed that processes all the channels of a color image simultaneously to avoid the problem of loss of information details and correlation among color channels. Extensive experimentation is conducted on the standard datasets to demonstrate its effectiveness in comparison to the existing techniques. The proposed technique is further utilized for enhancing the color images. Another important point that is considered in both these approaches is that selection of mask size is done on the basis of both visual comparison and performance metrics. To further evaluate the adequacy of the proposed approaches, uncontrolled conditions are taken into consideration. Although some of the existing approaches are tested against the uncontrolled features of noise and illumination, the JPEG compression artifacts are not considered in the existing edge detection techniques. Therefore, the robustness of the developed approaches is validated by subjecting them to not only noise and variation in illumination but also JPEG compression.

Thus, a unique concept of integration of RFOD with FrFT as well as quaternion domain is devised in the presented work to provide effective and reliable techniques for the applications of signal and image processing. The future work can be dedicated to extend the present work for the applications of computer vision and pattern recognition.

Keywords: Fractional Fourier Transform; Fractional Order Calculus; Image Edge Detection; Image Enhancement; Riesz Fractional Order Derivative

LIST OF PUBLICATIONS

Published Journal Publications:

- [P.1] K. Kaur, N. Jindal, and K. Singh, "Improved homomorphic filtering using fractional derivatives for enhancement of low contrast and non-uniformly illuminated images," *Multimed. Tools Appl.*, vol. 78, no. 19, pp. 27891-27914, Oct. 2019, doi: 10.1007/s11042-019-7621-5. **(SCIE-Indexed, Impact factor: 2.757)**
- [P.2] K. Kaur, N. Jindal, and K. Singh, "Riesz fractional order derivative in Fractional Fourier Transform domain: An insight," *Digit. Signal Process. A Rev. J.*, vol. 93, pp. 58-69, Oct. 2019, doi: 10.1016/j.dsp.2019.07.007. **(SCI/SCIE-Indexed, Impact factor: 3.381)**
- [P.3] K. Kaur, N. Jindal, and K. Singh, "Fractional Derivative based Unsharp Masking Approach for Enhancement of Digital Images," *Multimed. Tools Appl.*, vol. 80, pp. 3645-3679, Jan. 2021, doi: 10.1007/s11042-020-09795-5. **(SCIE-Indexed, Impact factor: 2.757)**
- [P.4] K. Kaur, N. Jindal, and K. Singh, "Fractional Fourier Transform based Riesz fractional derivative approach for edge detection and its application in image enhancement," *Signal Process.*, vol. 180, Mar. 2021, Art. no. 107852, doi: 10.1016/j.sigpro.2020.107852. **(SCIE-Indexed, Impact factor: 4.662)**

Communicated Journal Publications:

- [C.1] K. Kaur, N. Jindal, and K. Singh, "QRFODD: Quaternion Riesz Fractional Order Directional Derivative for color image edge detection," *IEEE Transactions on Image Processing*.

LIST OF ACRONYMS AND ABBREVIATIONS

AG	Average Gradient
AHE	Adaptive Histogram Equalization
BPDFHE	Brightness Preserving Dynamic Fuzzy Histogram Equalization
BPDHE	Brightness Preserving Dynamic Histogram Equalization
BSDS	Berkeley Segmentation Dataset and Benchmarks
BUM	Blurriness-Guided Unsharp Masking
CC	Correlation Coefficient
CEEF	Contrast Enhancement using Exposure Fusion
CFrFT	Chirp Fractional Fourier Transform
CHF	Confluent Hypergeometric Function
CLAHE	Contrast Limited Adaptive Histogram Equalization
CRONE	Contour Robuste d'Ordre Non Entier (French)
CUM	Conventional Unsharp Masking
DCS	Detect Correct Similarity
DCT	Discrete Cosine Transform
DFT	Discrete Fourier Transform
DFrFT	Discrete Fractional Fourier Transform
DHT	Discrete Hartley Transform
DR	Diabetic Retinopathy
DST	Discrete Sine Transform
ECG	Electrocardiogram
eCRONE	extended Contour Robuste d'Ordre Non Entier (French)
EI	Edge Intensity
EME	Measure of Enhancement
EPI	Edge Preservation Index
ET	Edge Tracking
FFT	Fast Fourier Transform
FIR	Finite Impulse Response
FOC	Fractional Order Calculus
FOD	Fractional Order Derivative
FODs	Fractional Order Derivatives
FOM	Figure of Merit

FrCT	Fractional Cosine Transform
FrFT	Fractional Fourier Transform
FrFTD	Fractional Fourier Transform Domain
FrST	Fractional Sine Transform
FrWT	Fractional Wavelet Transform
FT	Fourier Transform
GL	Grünwald-Letnikov
GLCM	Gray Level Co-occurrence Matrix
GLIS	Grünwald-Letnikov and Information Sets
GT	Ground Truth
HE	Histogram Equalization
HF	Homomorphic Filtering
HMFD	Homomorphic filtering based on Fractional Derivative
HPF	High Pass Filter
HRF	High Resolution Fundus
IE	Information Entropy
IFrFT	Inverse Fractional Fourier Transform
IFT	Inverse Fourier Transform
JPEG	Joint Photographic Experts Group
KCHF	Kummer Confluent Hypergeometric Function
LED	Learning-based Edge Detection
LoG	Laplacian of Gaussian
LT	Laplace Transform
MAE	Mean Absolute Error
MHE	Median-Mean based Sub-Image-Clipped Histogram Equalization
Mod GL	Modified Grünwald-Letnikov
MSE	Mean Square Error
NIFD	Newton Interpolation based Fractional Differentiation
PCF	Parabolic Cylinder Function
Pr	Precision
PSNR	Peak Signal to Noise Ratio
PSO	Particle Swarm Optimization
QFD	Quaternion Fractional Differential
QRFODD	Quaternion Riesz Fractional Order Directional Derivative

QV	Quadratic Volterra
QWM	Quadratic Weighted Median
Re	Recall
RFOD	Riesz Fractional Order Derivative
RL	Riemann-Liouville
RLFD	Riemann-Liouville Fractional Derivative
RMSE	Root Mean Square Error
ROI	Region of Interest
RUM	Riesz based Unsharp Masking
SSIM	Structural Similarity Index Measure
UIQI	Universal Image Quality Index
UM	Unsharp Masking
UMHE	Unsharp Masking in combination with Histogram Equalization
UMKG	Unsharp Masking filter Kernel and Gain using PSO

GLOSSARY OF SYMBOLS

a	Fractional parameter of FrFT
\mathcal{G}	Order of fractional derivative
ϕ	FrFT rotation angle
$*$	Convolution operation
ω	Frequency
$\psi(\cdot)$	Noise
A	Amplification factor
α_1, α_2	Scaling factors
$\Gamma(\cdot)$	Gamma function
$\delta(t)$	Dirac's delta function
$\Omega(\cdot)$	Angle of gradient
$(a)_k$	Pochhammer symbol
$\cos(\cdot)$	Cosine function
$\cot(\cdot)$	Cotangent function
$\csc(\cdot)$	Cosecant function
$D^n(\cdot)$	Integer order derivative
$D^{\mathcal{G}}(\cdot)$	FOD
$D_{\nu}(\cdot)$	PCF
$\mathcal{D}_F^{\phi}(\cdot)$	DFrFT operator
$\exp(\cdot), e^{(\cdot)}$	Exponential function
${}_1F_1(a; b; z)$	CHF of the first kind
${}_2F_1(a, b; c; z)$	Gauss hypergeometric function
$F^{\phi}(\cdot)$	FrFT operator
$F^{-\phi}(\cdot)$	IFrFT operator
Gr	Gradient function
h	Sampling period

$H(\cdot)$	Filter
$h^{\phi}(n)$	Fractional order impulse response filter
$H^{\phi}(u_{\phi})$	Fractional order impulse response filter in FrFT domain
$\text{Im}(\cdot)$	Imaginary part
$K(t, u)$	Kernel of a specified transform
$k_{\phi}(t, u_{\phi})$	Kernel of FrFT
$\kappa(t)$	Riesz kernel
$\log(\cdot)$	Logarithm function
$\ln(\cdot)$	Natural logarithm
$\text{mag}(\cdot)$	Magnitude
$FM(\cdot), M(\cdot)$	Mask
$N(\cdot)$	Norm
q	Quaternion function
R^+	Real numbers
$\text{Re}(\cdot)$	Real part
$\sin(\cdot)$	Sine function
$\tan^{-1}(\cdot)$	Inverse Tangent function
t_0, t_1, t_2	Nodes/ Data points
$T^{\phi}(m, n)$	Kernel of DFrFT
$z(\cdot)$	Input signal
$Z_E(\cdot)$	Edge detected image
$Z_{FD}(\cdot)$	FOD mask for specified fractional order
$Z_G(\cdot)$	Gradient image
$Z_{GL}(\cdot)$	GLFOD mask for specified fractional order
$Z_L(\cdot)$	Laplacian mask
$Z_R(\cdot)$	RFOD mask for specified fractional order

$Z_{RL}(\cdot)$	RLFOD mask for specified fractional order
$Z_{R_p}(\cdot)$	RFOD mask for specified fractional order in p direction
$\check{z}(\cdot), Z(\cdot)$	Output signal
$Z^\phi(n)$	Discrete output signal in FrFT domain

LIST OF FIGURES

Figure No.	Figure Label	Page No.
1.1	Edge Profile of (a) binary image (b) grayscale image [52]	06
1.2	Roberts Mask	07
1.3	Prewitt Mask	07
1.4	Sobel Mask	08
1.5	Laplacian Mask	08
1.6	Image Enhancement Techniques [12]	11
1.7	CUM Technique [81]	13
1.8	Generalized HF Technique [12]	14
1.9	Framework of thesis	15
1.10	Hierarchy of contributions of presented work	16
2.1	Time-frequency plane [151]	31
2.2	Flow chart of work done	48
3.1	Framework of the proposed FOD based UM approach	51
3.2	Edge information obtained by various masks for Lena image (256×256)	55
3.3	Edge information obtained by various masks for Barbara image (512×512)	56
3.4	Lena image (256×256) enhanced by using various masks in UM	57
3.5	Barbara image (512×512) enhanced by using various masks in UM	58
3.6	Enhanced Lena image (256×256) and its zoomed portion obtained by various techniques	60
3.7	Enhanced test images along with its zoomed portion	63
3.8	Simulated results for test images with variation in illumination conditions	73
3.9	Average performance parameters for test images of various datasets	81
3.10	Simulation results for Fundus images	84
4.1	Coefficient sequence $g_k^g(k)$ for different fractional orders (g)	93
4.2	Proposed algorithm for FrFT based Riesz fractional order differentiator	95

Figure No.	Figure Label	Page No.
4.3	(a), (b) Input signal corrupted with noise $z(n)+\psi(n)$; Results of fractional order differentiating filter: (c), (d) time-domain filtered output signal $\hat{z}(n)$; (e), (f) Fourier domain filtered output signal $\hat{z}(n)$; (g), (h) FrFTD filtered output signal $\hat{z}(n)$; (i), (j) FrFTD filtered signal $\hat{z}(n)$ with respect to original signal	96
4.4	Surface plot for RMSE obtained by varying FrFT parameter (a) and the order of RFOD (ρ)	97
4.5	RMSE based comparison of the proposed RFOD with other FODs	99
4.6	Enhanced Lena image (256×256) along with its zoomed portion for various fractional orders	102
4.7	Enhanced Vase_Color image (321×481) along with its zoomed portion for various fractional orders	104
4.8	Simulation results for the proposed approach along with the zoomed portion	106
4.9	Simulation results of test images with variation in illumination conditions using the proposed approach	108
4.10	FOD based improved HF approach	111
4.11	Kids image (400×318) enhanced by various image enhancement techniques	112
4.12	Test images enhanced by various enhancement techniques	114
4.13	Test images with variation in illumination conditions enhanced by various image enhancement techniques	118
4.14	Average assessment parameters for test images enhanced by various techniques	123
5.1	FOD masks of $n \times n$ size in eight directions	130
5.2	Framework of proposed FrFT based RFOD approach	132
5.3	Gradient images for various mask sizes for Lena image (256×256)	134
5.4	Images for different mask sizes	135
5.5	Comparative analysis of proposed approach with classical edge detection operators in FrFTD for Butterfly image (256×256)	137
5.6	FOM based surface plot for Lena image (256×256)	138

Figure No.	Figure Label	Page No.
5.7	Edges detected by various approaches for Lena image (256×256)	139
5.8	Simulation results for various edge detection techniques	140
5.9	Simulation results of Lena image (256×256) for image enhancement techniques	142
5.10	Images enhanced by various techniques along with the zoomed portions	143
5.11	Edge maps of Lena image (256×256) corrupted with Gaussian noise	153
5.12	Edge maps of Lena image (256×256) corrupted with Poisson noise for various techniques	154
5.13	Edge maps obtained by various techniques for test images with variation in illumination conditions	155
5.14	Enhancement results for test images with variation in illumination conditions	157
5.15	Edges detected by various techniques for JPEG compressed images of Lena (256×256) with different quality factors	160
5.16	Comparative analysis for edge detection methods with respect to quality factors	161
5.17	Simulation results for JPEG compressed images of Lena (256×256) with different quality factors	162
5.18	Comparative analysis of image enhancement techniques based on various performance metrics with variation in quality factors	163
6.1	Quaternion based RFOD masks in eight directions	168
6.2	Proposed framework based on QRFODD	168
6.3	Test images used for simulation	170
6.4	Effect of variation in mask size on edge detection for House image (481×321)	171
6.5	Edge maps yielded by various approaches for the Car image (481×321)	173
6.6	Edge maps yielded for various approaches	174
6.7	Edge maps obtained by various techniques for Car images (481×321) corrupted by Salt and Pepper noise having noise density of 0.02 and 0.04	178

Figure No.	Figure Label	Page No.
6.8	Effect on performance metrics with respect to variation in noise density	179
6.9	Edge maps obtained by various techniques for Car images (481×321) corrupted by the Gaussian noise having zero mean and variance of 0.02 and 0.04	180
6.10	Effect on performance metrics with respect to variation in variance of Gaussian noise	181
6.11	Simulation results obtained by various edge detection approaches	182
6.12	Edge maps yielded by various approaches for JPEG compressed Car images (481×321) with quality factor of 50, 80, and 95	184
6.13	Comparison of performance metrics with respect to quality factors	185
6.14	Edge map obtained for Fundus images	186
6.15	Simulation results obtained for image enhancement of Building image (481×321)	188
6.16	Simulation results for image enhancement of various color images	189

LIST OF TABLES

Table No.	Table Title	Page No.
2.1	Review of FODs in signal processing	22
2.2	Data for interpolation	39
3.1	Performance metrics for various FOD and Laplacian masks in UM	59
3.2	IE and AG for the test images enhanced by various techniques	67
3.3	SSIM for the test images enhanced by various techniques	68
3.4	EME and CC for the test images enhanced by various techniques	69
3.5	GLCM based contrast and correlation measure for the test images enhanced by various techniques with rotation offset	71
3.6	GLCM based energy and homogeneity measure for the test images enhanced by various techniques with rotation offset	72
3.7	IE and AG for the test images with variation in illumination conditions	76
3.8	SSIM and EME for the test images with variation in illumination conditions	77
3.9	CC for the test images with variation in illumination conditions	78
3.10	GLCM based contrast and correlation for the test images with variation in illumination conditions	79
3.11	GLCM based energy and homogeneity for the test images with variation in illumination conditions	80
3.12	Average processing time (in secs) of various image enhancement approaches	83
3.13	Performance metrics for the Fundus images	86
3.14	GLCM parameters for the Fundus images	87
4.1	RMSE and MAE for filtering in various domains for varying fractional order (ρ)	98
4.2	RMSE of FODs in the FrFTD for varying order of fractional derivative (ρ)	99
4.3	Average computational time	100
4.4	Performance metrics for test images of various sizes	107

Table No.	Table Title	Page No.
4.5	Image assessment parameters for test images with varying illumination conditions	110
4.6	Average PSNR (dB) for the test images	115
4.7	MSE for the test images	115
4.8	IE for the test images	116
4.9	SSIM for the test images	116
4.10	UIQI for the test images	117
4.11	PSNR (dB) of test images with variation in illumination conditions	120
4.12	MSE of test images with variation in illumination conditions	120
4.13	IE of test images with variation in illumination conditions	121
4.14	SSIM of test images with variation in illumination conditions	121
4.15	UIQI of test images with variation in illumination conditions	122
5.1	Effect of variation in mask sizes on edge detection parameters	136
5.2	Parameters of Butterfly image for various edge detection masks in FrFTD	137
5.3	Effect of variation in fractional order (g) on FOM	145
5.4	FOM for the test images subjected to various edge detection techniques	145
5.5	EPI for the test images subjected to various edge detection techniques	146
5.6	IE of the test images enhanced by various image enhancement techniques	147
5.7	AG of the test images enhanced by various image enhancement techniques	147
5.8	EME of the test images enhanced by various image enhancement techniques	148
5.9	EI of the test images enhanced by various image enhancement techniques	149
5.10	Mean of the test images enhanced by various image enhancement techniques	149
5.11	Number of Corners for the test images enhanced by various image enhancement techniques	150

Table No.	Table Title	Page No.
5.12	GLCM based contrast measure for various images with rotation offsets	150
5.13	GLCM based correlation measure for various images with rotation offsets	151
5.14	GLCM based energy measure for various images with rotation offsets	151
5.15	GLCM based homogeneity measure for various images with rotation offsets	152
5.16	Performance metrics for the Lena image corrupted with Poisson noise	154
5.17	FOM and EPI obtained from various edge detection approaches for test images with variation in illumination conditions	156
5.18	Performance metrics for image enhancement techniques for test images with variation in illumination conditions	158
5.19	GLCM parameters obtained by various image enhancement techniques for test images with variation in illumination conditions	159
5.20	Computational cost of various approaches	165
6.1	Variation of performance metrics based on mask size	172
6.2	Variation of FOM with respect to the fractional order (g)	175
6.3	Performance metrics of the proposed approach as compared to classical edge detection approaches	176
6.4	Performance metrics of various edge detection approaches for BSDS500	176
6.5	Performance metrics of various edge detection approaches for BSDS300	176
6.6	FOM of the proposed approach as compared to classical edge detection techniques	183
6.7	Computational time of various techniques (in seconds)	185
6.8	Performance metrics of the proposed approach as compared to classical edge detection approaches	187
6.9	Image assessment parameters for test images	190

TABLE OF CONTENTS

<i>Certificate</i>	ii
<i>Acknowledgments</i>	iii
<i>Abstract</i>	v
<i>List of Publications</i>	vii
<i>List of Acronyms and Abbreviations</i>	viii
<i>Glossary of Symbols</i>	xi
<i>List of Figures</i>	xiv
<i>List of Tables</i>	xviii
<i>Table of Contents</i>	xxi
CHAPTER 1 INTRODUCTION	01-17
1.1 General	01
1.2 Concept of Fractionalization	02
1.2.1 Historical Perspective of FOC	02
1.2.2 Historical Perspective of FrFT	03
1.3 Framework of FODs in various domains for Image Processing	05
1.4 Image Processing Applications	05
1.4.1 Image Edge Detection	06
1.4.1.1 Color Image Edge Detection	09
1.4.2 Image Enhancement	10
1.4.2.1 Histogram Equalization and its variants	12
1.4.2.2 Linear Filtering	12
1.4.2.3 Unsharp Masking	12
1.4.2.4 Homomorphic Filtering	13
1.5 Focus and Contributions of Research Work	15
1.6 Organization of Thesis	17
CHAPTER 2 LITERATURE SURVEY	18-49
2.1 Context of FODs in Signal and Image Processing	18
2.2 Preliminaries of FODs	19
2.2.1 Riemann-Liouville Definition	19
2.2.2 Grünwald-Letnikov Definition	20
2.2.3 Caputo Definition	20
2.2.4 Riesz Definition	20
2.3 Concept of FODs in various domains for applications of Signal Processing	21
2.4 Applications of FODs in Image Processing	25
2.4.1 Image Edge Detection	25
2.4.2 Image Enhancement	27
2.4.3 Uncontrolled Features	29
2.4.3.1 Noise	29
2.4.3.2 Illumination Conditions	30
2.4.3.3 JPEG Compression Artifacts	30
2.5 Preliminaries of FrFT	31

2.5.1 Definition of FrFT	32
2.5.2 Basic Properties of FrFT	33
2.6 Preliminaries of Quaternions	35
2.7 Mathematical Concepts related to FOC in Signal and Image Processing	35
2.7.1 Gamma Function	36
2.7.2 Kummer Confluent Hypergeometric Function (KCHF)	36
2.7.3 Parabolic Cylinder Function (PCF)	37
2.7.4 Interpolation Methods	39
2.8 Performance Metrics	40
2.9 Motivation	45
2.10 Research Gaps	46
2.11 Research Objectives	47
2.12 Research Methodology	47
CHAPTER 3 FRACTIONAL ORDER DERIVATIVE BASED UNSHARP MASKING	50-88
3.1 Improved UM based on FOD Approach	50
3.2 Performance Analysis of FOD based UM Approach	54
3.2.1 Effect of Various Masks in UM	54
3.3 Simulation Results for Test Images of Standard Datasets	59
3.3.1 Qualitative Performance Analysis	59
3.3.2 Quantitative Performance Analysis	66
3.4 Simulation Results for Images with Variation in Illumination Conditions	70
3.4.1 Qualitative Performance Analysis	70
3.4.2 Quantitative Performance Analysis	75
3.5 Comparative Analysis	81
3.6 Computational Cost	83
3.7 Application of Proposed Approach in Fundus Images	84
3.8 Summary	88
CHAPTER 4 RIESZ FRACTIONAL ORDER DERIVATIVE IN FRFT DOMAIN	89-124
4.1 Mathematical Expression for RFOD in FrFTD	89
4.2 Computation of Proposed Approach in Discrete Domain	92
4.3 Fractional Fourier Domain Based Riesz Fractional Order Differentiator	94
4.4 Design Example	95
4.5 Computational Cost	100
4.6 Applications of the Proposed Approach	100
4.6.1 Image Sharpening	101
4.6.1.1 Simulation Results for Test Images of Standard Datasets	101
4.6.1.2 Simulation Results for Test Images with Variation in Illumination Conditions	108
4.6.2 Homomorphic Filtering	111
4.6.2.1 Simulation Results for Test Images of Standard Datasets	112
4.6.2.2 Simulation Results for Test Images with Variation in Illumination Conditions	117

4.6.2.3 Comparative Analysis	122
4.7 Summary	124
CHAPTER 5 RFOD BASED APPROACH FOR EDGE DETECTION AND IMAGE ENHANCEMENT IN FRFT DOMAIN	125-166
5.1 RFOD based Approach in FrFTD	125
5.1.1 RFOD Mask	125
5.1.2 Framework of Proposed Approach	131
5.2 Performance Analysis of FrFT based RFOD Approach	133
5.2.1 Selection of Mask Size	133
5.2.2 Comparative Analysis with Classical Edge Detectors in FrFTD	136
5.2.3 Qualitative Performance Analysis	138
5.2.3.1 Edge Detection	139
5.2.3.2 Image Enhancement	141
5.2.4 Quantitative Performance Analysis	144
5.2.4.1 Edge Detection	144
5.2.4.2 Image Enhancement	146
5.3 Performance Analysis on the basis of Uncontrolled Features	152
5.3.1 Noise immunity	152
5.3.1.1 Gaussian Noise	153
5.3.1.2 Poisson Noise	153
5.3.2 Illumination Conditions	154
5.3.2.1 Edge Detection	154
5.3.2.2 Image Enhancement	156
5.3.3 JPEG Compression Artifacts	159
5.3.3.1. Edge Detection	159
5.3.3.2 Image Enhancement	162
5.4 Computational Cost	165
5.5 Summary	166
CHAPTER 6 QUATERNION BASED RFOD FOR COLOR IMAGE EDGE DETECTION AND IMAGE ENHANCEMENT	167-190
6.1 Quaternion Riesz Fractional Order Directional Derivative (QRFODD) Mask	167
6.2 Proposed Approach for Edge Detection in Color Images	168
6.3 Performance Analysis of Proposed Approach for Edge Detection in Color Images	170
6.3.1 Selection of Mask Size	170
6.3.2 Qualitative Performance Analysis	172
6.3.3 Quantitative Performance Analysis	175
6.4 Performance Analysis on the basis of Uncontrolled Features	177
6.4.1 Noise Immunity	177
6.4.1.1 Salt and Pepper Noise	177
6.4.1.2 Gaussian Noise	179
6.4.2 Illumination Conditions	181
6.4.3 JPEG Compression Artifacts	183
6.5 Computational Cost	185

6.6 Real Application of Edge Detection in Fundus Images	186
6.7 Application of Proposed Approach for Image Enhancement	187
6.8 Summary	190
CHAPTER 7 CONCLUSIONS AND FUTURE SCOPE	191-194
7.1 Conclusions	191
7.2 Main Highlights of the Research Work	193
7.3 Future Scope	193
REFERENCES	195-211
APPENDIX-I	212-216
VITA	217-217

INTRODUCTION

This chapter is oriented to provide a brief outline of the fundamental concepts that are the foundation to arouse the interest for diving into the depths of the research work conducted in this thesis. It deals with the historical perspectives and terms related to the fractional operators, fractional transforms, and their prospective applications in the current scenario.

1.1 General

Over the past decades, most of the systems in signal and image processing are modeled on the basis of mathematical tools. There exist numerous integer operator based methods to devise solutions for the problems of signal and image processing. However, they are not able to accurately model the real-world challenges. Therefore, fractional operator based systems can be used as the fundamental mathematical tools for providing solutions to such models. In the last few decades, fractional operators are widely employed in various fields of science and engineering because they provide an extra degree of freedom to optimize their performance [1], [2]. The concept of fractions existed earlier in the fuzzy logic that provided superior outcomes as compared to the crisp ones, but in the previous decades, the concept of fractionalization has revolutionized even the calculus and transforms in various fields ranging from control systems to signal and image processing [2]–[7]. Most of the applications either considered the fractional transforms or fractional calculus but Kilbas *et al.* [8], Singh *et al.* [9], and Kumar *et al.* [10], [11] further came up with an exceptional idea of integrating Fractional Order Calculus (FOC) and Fractional Fourier Transform (FrFT) to boost the performance by utilizing two fractional parameters. Based on the aforementioned concepts, the research work carried out in this thesis aims to explore the benefits of the fractional domain for improving the performance of various techniques in image processing. Although there are several areas of research in the fractional domain, image processing is selected due to the substantial increase in its applicability in the disciplines of science and engineering [12]. Image processing further encompasses several applications that are beneficial in numerous forms such as enhancement [13], [14], edge detection [15], [16], denoising [17], [18], security [19], segmentation [20], etc., however, the applications of image edge detection and image enhancement are immensely employed in practical scenarios. Moreover, the

principal motivations behind image processing are to improve the visual image quality for human perception and processing of the image for transmission, storage, and data extraction for machine perception [21]. Therefore, edge detection and image enhancement are considered that accomplishes the task of both human and machine perception. Hence, the concept of a fractional domain is analyzed by considering the applications of edge detection and image enhancement.

1.2 Concept of Fractionalization

The notion of fractions revolutionized the field of signal processing with the introduction of fractional concepts in calculus and transforms as it provided remarkable improvement in the performance of the systems modeled by fractional based approaches. To commence with this work, the origin of FOC and FrFT is briefly described in the ensuing sections.

1.2.1 Historical Perspective of FOC

Conventionally, the concept of derivatives was associated with the integers; the derivative of a function is obtained a whole number of times. However, Leibniz's inquisitiveness to investigate the derivative of real (non-integer) order paved the way to the concept of FOC in 1695. It basically evolved following the discourse between Leibniz and Bernoulli regarding the non-integer order of differentiation. Besides, a similar query is received by Leibniz from L' Hôpital: "*What if n is 1/2 ?*" Leibniz replied: "*It will lead to a paradox, a paradox from which one day useful consequences will be drawn, because there are no useless paradoxes.*" In 1730, Euler recommended the generalization of a rule and obtained the derivatives of order 1/2 for the power function. However, FOC was systematically studied only in the nineteenth century. Despite the fact that Laplace presented an integral formulation in 1812, the term "derivative of arbitrary order" only came into light in Lacroix's works in 1819. He utilized the gamma function for obtaining the Fractional Order Derivative (FOD) of the power function. Moreover, Fourier generalized the differentiation of an arbitrary function in 1822 as [1], [22]:

$$\frac{d^g z(t)}{dt^g} = \frac{1}{2\pi} \int_{-\infty}^{\infty} z(\tau) d\tau \int_{-\infty}^{\infty} u^g \cos(ut - u\tau + (g\pi/2)) du \quad (1.2.1)$$

where 'g' can be positive or negative. Nevertheless, in the mid-nineteenth century, Liouville laid the foundation of FOC followed by Grünwald, Letnikov, Riemann, and Holmgren. FOC is the generalization of conventional Newtonian calculus [3], [4]. The integer-order derivative

is obtained from $D^n z(x) = d^n z(x) / dx^n$ whereas, the non-integer/FOD is determined from $D^g z(x)$, where 'g' symbolizes a real number. If $g > 0$, $D^g z(x)$ is considered as a fractional derivative whereas, if $g < 0$ then $D^g z(x)$ is considered to be a fractional integral [23].

In order to recapitulate, FOC deals with both fractional derivatives and integrals. Since last three centuries, several mathematicians and researchers such as Y. Sonnin, N. H. Abel, H. Laurent, A. Krug, J. Hadamard, O. Heaviside, A. Marchaud, N. Nekrasov, K. Nishimoto, S. C. D. Roy, R. P. Agarwal, B. Ross, K. S. Miller, K. B. Oldham, J. Spainer, G. H. Hardy, J. E. Littlewood, H. M. Srivastava, A. Oustaloup, I. Podlubny, L. Debnath, T. Hartley, C. Lorenzo, S. G. Samko, M. D. Ortigueira, R. K. Saxena, R. K. Bera, S. S. Ray, M. Riesz, W. Feller, M. Caputo, M. Fabrizio, A. Atangana, D. Baleanu and many more have contributed in the development of FOC [4], [24], [25]. Numerous definitions of fractional differintegrals such as Riemann-Liouville (RL), Grünwald-Letnikov (GL), Caputo, Riesz, etc. [4], [24], [25] exist to define the concept of FOC with each having its own merits and demerits. However, they are proficient to model systems that are non-linear in nature. Hence, the FODs are intended to play an instrumental role in the applications of several fields of science and engineering mainly physics, mechanics, control systems, signal and image processing [4], [26], [27].

Previously, most of the research in the engineering field is done in fractional order control systems, but recently emphasis is laid out on the applications of FOC in the field of signal and image processing to enhance its performance by exploiting the extra degree of freedom given by fractional parameter.

1.2.2 Historical Perspective of FrFT

Transforms perform the task of mapping signal to frequency domain from the time or space domain. The signal transform of a continuous input signal $z(t)$ is modeled by:

$$Z(u) = \int z(t) K(t, u) dt \quad (1.2.2)$$

where $Z(u)$ is the output signal in the transform domain and $K(t, u)$ denotes the kernel of a specified transform [28]. Numerous transforms such as Laplace Transform (LT), Fourier Transform (FT), z-transform, and many more are reported in the literature based on different kernels that are applicable in various fields. However, these transforms have certain shortcomings for different categories of signals, for instance, FT is extensively employed in signal and image processing applications but it is not suitable for the processing of non-

stationary signals because it failed to provide the time-frequency characteristics of the signal [29]. Then, to overcome this issue, time-frequency based transforms are used, for instance, window-based transforms. These include short-time FT and modified Wigner distributions such as smoothed-Wigner distribution and pseudo-Wigner distribution. Nevertheless, these transforms also have inherent shortcomings of undesirable effects on the signals. Moreover, the inevitable suppression of the information present in the signal by windows reduced the time and frequency resolution. However, on the basis of the uncertainty principle, it is apparently difficult to provide a solution to the problem related to window-based time-frequency transforms [30]. In another category of time-frequency based transforms, the time-varying signal characteristics are described by the kernels. One such transform is FrFT whose kernel has a parameter ϕ that rotates the time-frequency distribution in the time-frequency plane. It is a generalization of FT that can be aptly used for dealing with time-frequency characteristics of non-stationary signals [5]. The history of fractional order in FT is dated back to 1929 but it was only in 1980 that Victor Namias [31] introduced the concept of FrFT in the field of quantum mechanics. Moreover, several researchers such as N. Wiener, H. Weyl, E. U. Condon, H. Kober, A. P. Guinand, A. L. Patterson, V. Bargman, D. Bruijn, R. S. Khare, and some others proposed the similar work earlier but under a different name. So, Namias was apparently oblivious about this work [32]. Furthermore, McBride and Kerr refined the work done by Namias in 1987 [33]. Mustard also carried out similar research in 1987 by considering Condon and Bargman as his base but without citing Namias's work. Moreover, the surge of research work carried out in the field of FrFT in the last three decades also led to the fractionalization of other transforms namely Fractional Sine Transform (FrST), Fractional Cosine Transform (FrCT), Fractional Wavelet Transform (FrWT), etc. However, a lot of work is carried out on the properties of the FrFT such as linearity, translation, scaling, conjugation, modulation, differentiation, integration, convolution, uncertainty principle, etc. [7], [34]–[40]. The discrete form of FrFT known as Discrete Fractional Fourier Transform (DFrFT) is also suggested by various researchers [32], [41]–[45]. Furthermore, FrFT found its application in the various fields of quantum mechanics, optics, signal, and image processing [5], [7], [29], [31], [46].

Besides, the research work done by combining the Fractional Order Derivatives (FODs) and fractional transforms in signal and image processing [9]–[11] provides the benefit of varying two fractional parameters, that is, the fractional derivative of order ' \mathcal{G} ' and the FrFT rotation angle ' ϕ '. The substantial research carried out in the domain of fractional operators has

proved its efficacy over integer-order operators. Therefore, it aroused the interest to conduct further analysis in the field of image processing.

1.3 Framework of FODs in various domains for Image Processing

Image processing is one of the rapidly progressing fields in the current scenario owing to the increase in demand for processing of data in its visual form especially its applications in realistic scenarios such as biomedical images for the diagnosis in healthcare, radar images for target detection, and satellite images for remote sensing in surveillance and geographical sciences, etc. [13], [47], [48]. In order to process this realistic data efficiently, fractional order algorithms are developed by the research fraternity. However, the research in the field of FODs in image processing applications increased significantly in the last two decades [2]. The generalized framework for image processing applications using FODs in various domains (spatial, frequency, FrFT, and quaternion) is described in the following steps:

- Initially, the FOD definition is considered for the application of image processing.
- Secondly, mathematical analysis of considered FOD is carried out for the construction of the mask.
- Finally, the input image is processed by the FOD based mask to obtain the output image in the considered domain.

Hence, the above-mentioned steps can be utilized for the approaches based on FOD in various domains for the area of image processing. Such approaches are beneficial because the fractional order provides an extra degree of freedom that aids in optimizing its performance [2]. Therefore, FODs are employed in the presented work to take the advantage of an extra parameter ' ρ '. Furthermore, the concept of unification of FOD and FrFT provides an additional benefit of two degrees of freedom which is considered in the present work.

1.4 Image Processing Applications

Owing to the extensive use of visual information in various fields, image processing is one of the hot topics of research. Although all the sub-fields of image processing are indispensable, image edge detection and image enhancement are paramount as they satisfy the motivations behind image processing and are applicable for pattern recognition and computer vision applications [2], [49]–[51]. Therefore, the elementary concepts of the considered applications of image edge detection and image enhancement are provided in the subsequent sub-sections.

1.4.1 Image Edge Detection

Edge is defined as the abrupt change that occurs either due to the change in shapes of physical objects or their innate characteristics. The edges play an instrumental role in the image analysis and interpretation for applications of biological vision and computer image analysis [52]. Image edge is defined as the boundary that separates the image regions with sharp variations in the characteristics of an image such as intensity, color, texture, etc. Therefore, edge detection is a mathematical operation that is utilized for the identification of discontinuities in an image [53]. It is the procedure to determine the pixels that can be considered edge pixels. The output of the edge detection approach is an edge map which is an image describing the edge classification for each pixel and perhaps the other edge features such as edge magnitude and edge orientation [52]. Figure 1.1 (a) depicts an ideal edge map in which transition occurs from black to white over a single pixel and Figure 1.1 (b) illustrates the edge map in case of images with the transition in intensity over a large number of pixels that results in a ramp-like profile.

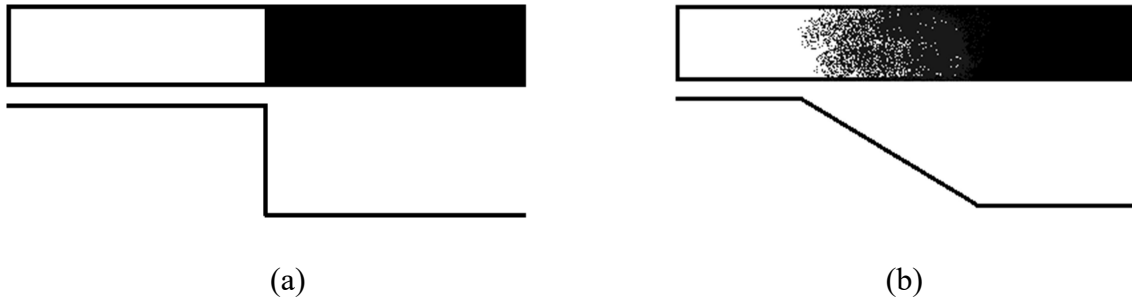


Figure 1.1: Edge Profile of (a) binary image (b) grayscale image [52]

There are numerous techniques for the detection of edges based on derivatives [54]–[58], estimation and learning [59]–[61], statistical [62], multiscale [63], [64], diffusion [65], and anchor detection methods [66], [67]. However, the majority of the prevailing edge detection approaches employ either first-order or second-order derivatives. The first-order derivatives are also referred to as gradients. The gradient of a two-dimensional function $z(i, j)$ refers to the maximum rate of change of z at the coordinates (i, j) in the direction ∇z which is provided as [21]:

$$\nabla z = \begin{bmatrix} Gr_i \\ Gr_j \end{bmatrix} = \begin{bmatrix} \partial z / \partial i \\ \partial z / \partial j \end{bmatrix} \quad (1.4.1)$$

The magnitude of the gradient commonly known as edge strength is computed as:

$$\nabla z = \text{mag}(\nabla f) = \sqrt{Gr_i^2 + Gr_j^2} = \sqrt{(\partial z/\partial i)^2 + (\partial z/\partial j)^2} \quad (1.4.2)$$

The angle of gradient $\Omega(i, j)$ also known as edge direction refers to the direction in which the maximum rate of change occurs defined as:

$$\Omega(i, j) = \tan^{-1} \left[\frac{Gr_j}{Gr_i} \right] \quad (1.4.3)$$

The edge direction is orthogonal to the gradient vector's direction at that point. The gradient computed using the first-order derivative masks/operators are defined as [21]:

- Roberts Mask: The Roberts mask of size 2×2 is used to approximate the difference between the adjacent pixels. The Roberts edge detector mask is illustrated in Figure 1.2.

-1	0
0	1

(a)

-1	0
0	1

(b)

Figure 1.2: Roberts Mask

These masks of size 2×2 are simple for implementation; however, they are less beneficial in comparison to the masks of size 3×3 because they are symmetric about their center points.

- Prewitt Mask: The Prewitt mask of size 3×3 approximates the difference in a better way in comparison to the Roberts mask is depicted in Figure 1.3.

-1	-1	-1
0	0	0
1	1	1

(a)

-1	0	1
-1	0	1
-1	0	1

(b)

Figure 1.3: Prewitt Mask

The mask size of 3×3 considers the data on both sides of the center point, thus carrying more information about the direction of the edge. Its implementation is the simplest one but it produces slightly noisier results.

- Sobel Mask: It is the mask of size 3×3 whose computation is slightly more in comparison to the Prewitt mask illustrated in Figure 1.4.

-1	0	1
-2	0	2
-1	0	1

(a)

-1	-2	-1
0	0	0
1	2	1

(b)

Figure 1.4: Sobel Mask

The center pixel in each row or column is weighted by a factor of two providing better noise suppression.

Furthermore, the second-order derivative based edge detector is obtained by considering the Laplacian mask of size 3×3 . It is generally the isotropic filter that is presented in the two forms as shown in Figure 1.5.

0	1	0
1	-4	1
0	1	0

(a)

1	1	1
1	-8	1
1	1	1

(b)

Figure 1.5: Laplacian Mask

The Laplacian mask in Figure 1.5(a) obtains isotropic results for the increment of 90° while Figure 1.5 (b) attains the isotropic results for the increment of 45° . Nevertheless, it is seldom utilized for the purpose of edge detection in its original form as it produces double edges while being inept to detect the direction of edges. However, the Laplacian mask proves to be beneficial when used in combination with the other edge detection approaches. To exemplify, the Laplacian mask is used in combination with the Gaussian function, generally referred to as Laplacian of Gaussian (LoG) for the detection of edges that involves three steps. The filtering of an input image is done with a $n \times n$ Gaussian filter for noise reduction before applying the Laplacian mask. Then, edges are detected by finding the zero crossings between the double edges [21]. However, these first-order and second-order derivatives possess certain demerits as first-order derivatives provided thicker edges that perhaps cause the information loss while the second-order derivatives are sensitive to noise.

Nevertheless, a multi-stage edge detection approach is developed by J. F. Canny in 1986. It is believed to provide better performance in terms of localized edge response, less error rate, and a single edge point response. Canny edge detection involves the following steps [21]:

- To suppress the noise, the image smoothing is done utilizing the Gaussian filter.
- The edge strength and edge direction are calculated for each point of the image.
- Then non-maximal suppression is applied that generally involved the tracking along the top of ridges that are determined by the edges in the gradient image. Here, the non-ridge pixels are set to be zero to produce a thin line while the ridge pixels are thresholded on the basis of hysteresis thresholding that depends on two thresholds Th_1 and Th_2 , such that $Th_1 < Th_2$. The ridge pixels that possess values higher than Th_2 are strong edge pixels while the ones with value in between Th_1 and Th_2 are weak edge pixels.
- Eventually, edge linking is done by including the weak edge pixels which are 8-connected to the strong edge pixels.

Despite being able to provide a wide range of edges, the Canny edge detector can detect spurious edges which arises the need for an edge detection approach that can detect the continuous edges without being sensitive to noise or loss of information. This issue can be resolved by employing FOD based techniques for yielding edge maps as they provide sharper edges and a better edge detection rate.

1.4.1.1 Color Image Edge Detection

Color image processing plays an indispensable role because most of the images encountered in day-to-day life are color images. Color is a dominant descriptor that not only contains more information but also aids in the identification and extraction of an object from an image [21]. Therefore, color image edge detection is a paramount area of research. It is further classified into three approaches:

- The first approach includes the detection of edges by gradients after the conversion of a color image into grayscale. It involves the loss of edge information while converting from color to a grayscale image. Moreover, approximately 90% of the edges in the color image are similar to the grayscale images [68]. Thus, it can be deduced that the remaining 10% of edges are different from those of grayscale images. Hence, these edges cannot be detected from the grayscale images.
- The second approach involves applying the gradient operator to individual channels (red, green, and blue) of the color image. Afterward, the outputs are combined to attain

the edges in a color image. However, this approach leads to the loss of correlation that exists between the color channels, thus, resulting in color artifacts. Furthermore, the process of combining the information of different color channels is also ambiguous [21], [69].

- The third approach is based on the processing of all color channels simultaneously, that is, the vector and quaternion approach. Hence, it can preserve the correlation that exists between the color channels.

The majority of color edge detection approaches in the literature are based on the conversion of color images into grayscale images or other color models and then working on either a single channel or all channels separately [15], [67], [70]–[74]. However, color gradient vector and quaternions are used for color image based edge detection in [66], [68], [75], [76]. These techniques motivated to further explore the concept of color image edge detection by utilizing FOD in the quaternion domain.

1.4.2 Image Enhancement

Nowadays, image enhancement techniques are substantially utilized in most image processing applications particularly when the image quality is of utmost importance for interpretation by humans. It basically involves the sharpening of the image features such as edges, contrast, and texture or removal of noise for improving the image quality [12], [21], [77]. Such techniques only aim to improve the dynamic range of the selected features for their easier detection. The image enhancement approaches are broadly classified into four categories [12], [21] as illustrated in Figure 1.6.

- Point-based techniques: It generally involves the operations in which enhancement at any location is dependent only on the gray level at that particular location. They are also referred to as zero memory operations. Contrast stretching, window slicing, noise clipping, and histogram modeling are the commonly used point processing techniques that aim to enhance the contrast of an image. Histogram modeling generally involves Histogram Equalization (HE) and its variants for contrast enhancement.
- Spatial techniques: Spatial techniques perform the transformation of pixels in an image by considering its neighborhood. It usually involves the task of convolving the image with a filter or mask. Basically, the filter or mask is an array of a pre-defined size that affects the nature of the operation to be performed. It mainly performs the task of smoothing, removal of noise, filtering, zooming, and image sharpening based on Unsharp Masking (UM).

- Transform techniques: In transform-based techniques, the images are converted into the frequency domain by employing the transforms such as FT, Discrete Cosine Transform (DCT), etc. Afterward, the processing is done in the frequency domain. Eventually, an image is converted back to the spatial domain. It performs the task of linear and root filtering for the enhancement of images. Similarly, Homomorphic Filtering (HF) increases the dynamic range of dark images.
- Pseudo coloring: It involves the process in which colors are assigned to gray values based on certain criteria. It mainly distinguishes the method of assigning colors to monochrome images from the methods related to the true color images.

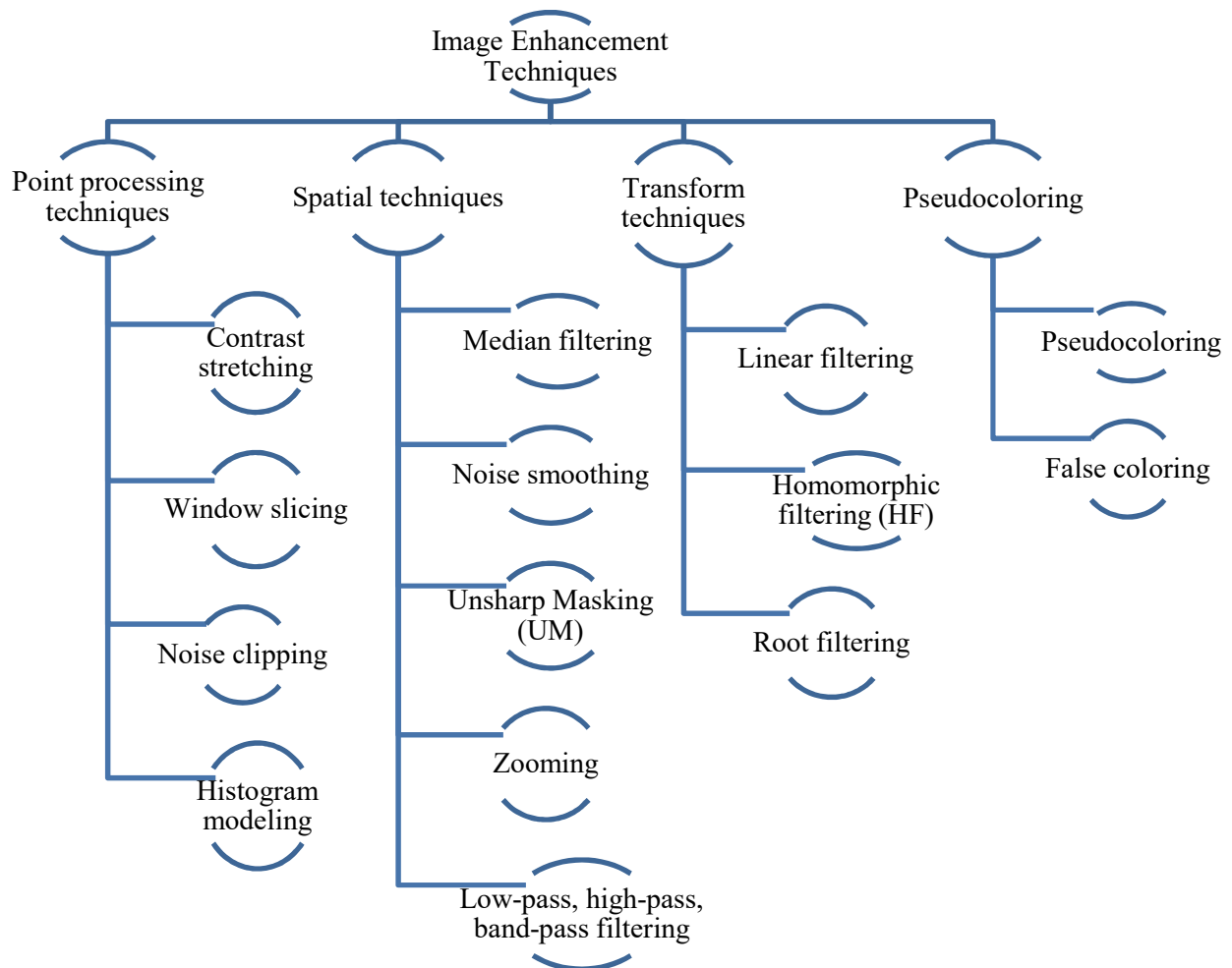


Figure 1.6: Image Enhancement Techniques [12]

The process of image enhancement comprises the manipulation of an image in accordance with the requirement of an application so that the obtained image is better than the original image. Generally, the image enhancement approaches are selected based on the nature of the application. The subsequent sub-sections describe the image enhancement techniques that are used in the presented work.

1.4.2.1 Histogram Equalization and its variants

HE is one of the rudimentary non-linear techniques of enhancing the low contrast images based on the histogram. In this technique, the input image is mapped into the output image in such a manner that the intensity levels are uniformly distributed over the entire image, thus, increasing its dynamic range [12], [52]. However, the changes in this technique are made over the entire image which is not capable of preserving the brightness of an image. Moreover, sometimes it is required to improve only the contrast of some region of an image. Such enhancement is done by considering the variants of HE such as Adaptive Histogram Equalization (AHE), Median-Mean based Sub-Image-Clipped Histogram Equalization (MHE), Contrast Limited Adaptive Histogram Equalization (CLAHE), Brightness Preserving Dynamic Histogram Equalization (BPDHE), Brightness Preserving Dynamic Fuzzy Histogram Equalization (BPDFHE), etc. [21], [78]–[80]. BPDFHE is the fuzzy-based modified version of BPDHE that depends on a fuzzy histogram for performing the smoothing before partitioning the image into sub-histograms. It is beneficial in terms of improved capability to preserve the brightness and contrast of the images along with reduced computation time [79]. MHE enhanced the images while controlling the over enhancement. Despite being capable of preserving the brightness and entropy of the image, it is solely beneficial for images with substantial peaks in their histograms [80]. Therefore, such techniques can only be used for specific applications.

1.4.2.2 Linear Filtering

In linear filtering, a predefined operation is performed on the image $z(i, j)$ by considering a filter mask. Initially, a center point is selected and then, an operation is performed on the pixels present in the predefined neighborhood and computing the result at that particular point. The aforementioned steps are repeated for all the points in the image defined as [21]:

$$Z = \sum_{s=-b}^b \sum_{t=-a}^a M(s, t) z(i + s, j + t) \quad (1.4.4)$$

where i and j are varied in such a manner that every pixel in M visits each pixel in z . Moreover, it can be employed in both spatial and frequency domains.

1.4.2.3 Unsharp Masking

In CUM, High Pass Filter (HPF) is employed to perform the image filtering. The filtered image is scaled before its addition to the original image in order to achieve the enhanced

image as depicted in Figure 1.7. The value of the scaling factor (α) lies in the range 0.2–0.7 [78], [81].

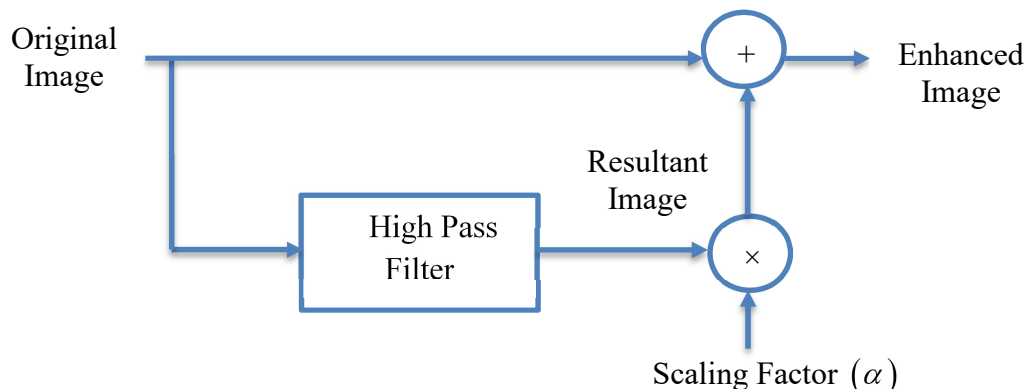


Figure 1.7: CUM Technique [81]

However, its secondary stage may also be referred to as high boost filtering if a constant β , such that $\beta > 1$ is multiplied by the original image instead of the high pass filtered image [21], [78]. In [81], the Gauss-Newton method is utilized for updating the coefficients in the directional filter based UM approach to enhance the medium contrast details. Owing to some transient effects, it also resulted in noise. Further, in [82] the edge enhancement is obtained by applying the Quadratic Weighted Median (QWM) filter that performs better as compared to the Quadratic Volterra (QV) schemes. However, it is primarily focused to enhance the bright areas of an image. In another approach, Particle Swarm Optimization (PSO) is incorporated in the UM approach for image enhancement [83]. However, over-enhancement occurs in certain cases. Besides, filter parameters and the number of iterations involved in this approach also increased its complexity. Kansal *et al.* [84] utilized HE in combination with UM (UMHE) and Joseph *et al.* [85] used the Gaussian-based UM technique for image sharpening. These approaches enhanced the contrast of an image, but the information details of an image are not preserved by the Gaussian filter. Thus, it is required to retain the information details while enhancing an image. In [86], the pixel-wise enhancement is utilized to process the detail and base layer separately referred to as Blurriness-guided UM (BUM) approach thus preventing the over-enhancement artifacts.

1.4.2.4 Homomorphic Filtering

HF is a model based on illumination and reflectance. Illumination measures the source illumination that is incident on the viewed scene which is represented by $I(i, j)$. Reflectance measures the illumination reflected by the objects in that scene which is represented by $R(i, j)$. The intensity of an image $z(i, j)$ at the point (i, j) is defined by [21]:

$$z(i, j) = I(i, j)R(i, j) \quad (1.4.5)$$

such that, $0 < I(i, j) < \infty$ and $0 < R(i, j) < 1$. Reflectance is bounded by 0 and 1 that is inferred as total absorption and total reflectance, respectively. Here, reflectance is dependent on the characteristics of the image objects while the nature of illumination relies on its source. Initially, an input image is mapped into the additive domain from the multiplicative domain by taking its logarithm. Then, the transformation of the obtained image is done into the frequency domain before performing its filtering in the frequency domain to attenuate the low frequencies while amplifying the high frequencies. Finally, the exponential of the inverse transformed image is taken to obtain the enhanced image [21] as shown in Figure 1.8.

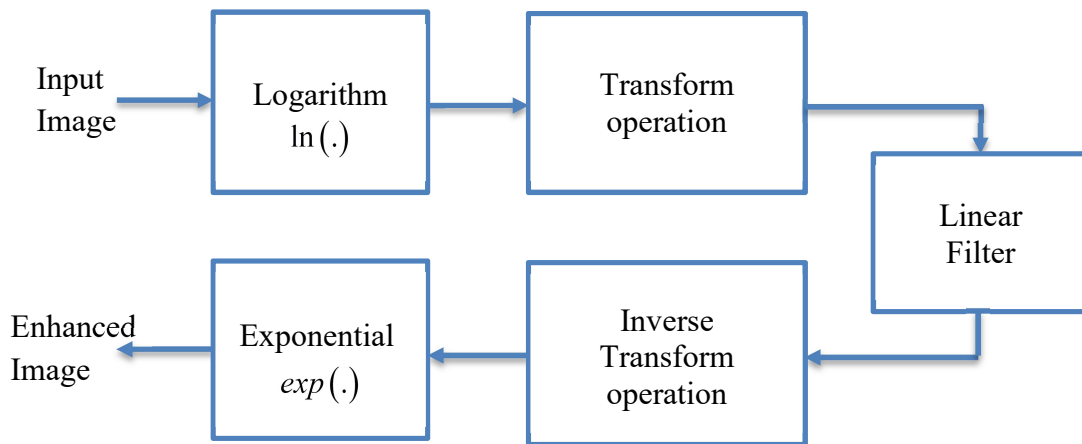


Figure 1.8: Generalized HF Technique [12]

A modified form of the basic ideal HPFs in the frequency domain is used in this technique by considering the two parameters γ_L and γ_H in the ideal HPF equation which increases the contribution of high frequencies while decreasing the contribution of low frequencies such that $\gamma_L < 1$ while $\gamma_H > 1$ as [21]:

$$H(u, v) = (\gamma_H - \gamma_L) * (HPF) + \gamma_L \quad (1.4.6)$$

This approach increases the contrast and sharpens the edges of an image [21]. In [87], the integrated image fusion and DCT based HF approach is utilized for enhancing the weakly illuminated images. In [88], DCT based matrix HF technique is presented to enhance the grayscale and color images. The HF technique is generally used for the enhancement of dark images.

To recapitulate, most of these enhancement techniques utilized integer order differentiation that enhances the high-frequency features of an image but deteriorates its performance in the

smooth regions of an image. This issue can be resolved by utilizing the fractional order differential operators that possess the inherent characteristics of preserving the high-frequency contour features in addition to the low-frequency textural details of the smooth area. Moreover, the fractional differential based techniques in spatial and FrFT domain are used to improve the contrast of an image while achieving the enhanced edges and textural details with either none or seldom introduction of noise [2]. Thus, the benefit of FODs can be utilized in various domains for the enhancement of images.

1.5 Focus and Contributions of Research Work

The utilization of the additional fractional parameter of FOD for the applications of image processing is the central idea behind this research work. The framework of this thesis is presented in the pictorial form in Figure 1.9 which elucidates the work proposed in this thesis along with the different conditions against which it is evaluated.

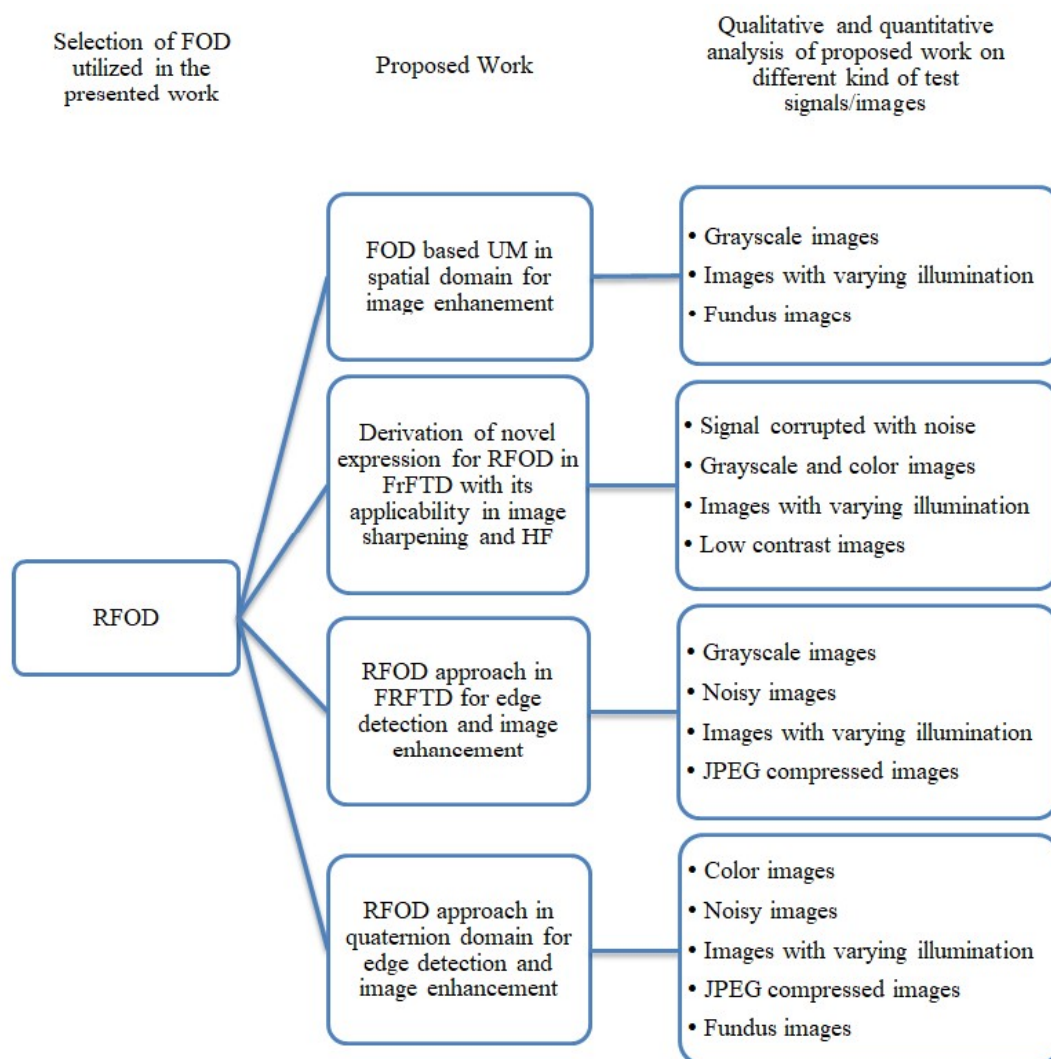


Figure 1.9: Framework of thesis

The major contributions of the presented work based on Riesz FOD (RFOD) in various domains are depicted hierarchically in Figure 1.10.

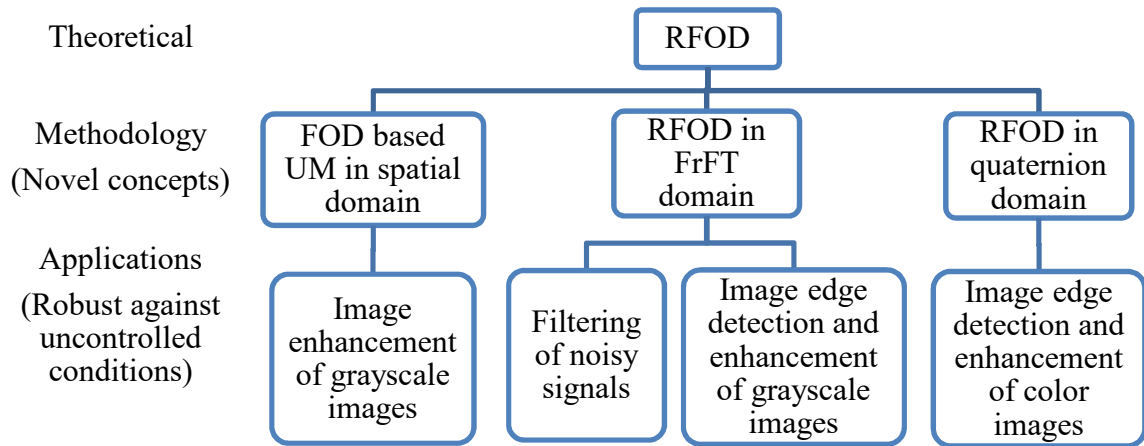


Figure 1.10: Hierarchy of contributions of presented work

In the presented work, RFOD is utilized to provide efficient and reliable solutions for the problems that exist in the field of signal and image processing. The contribution in the methodology involves the novel concepts of integration of Riesz FOD (RFOD) with UM in the spatial domain, RFOD with FrFT domain (FrFTD), and RFOD with quaternion domain which utilizes the benefits provided by the two fractional parameters, that is, order of fractional derivative (ϱ) and FrFT parameter (a). These integrated concepts are applied to different applications of signal and image processing. Firstly, FOD based UM technique is developed for image enhancement that provided better results for RFOD based UM as compared to other FODs. Secondly, a novel closed-form analytical expression is derived for RFOD in FrFTD. The applicability of this exceptional combination of RFOD with FrFT is confirmed by considering one-dimensional and two-dimensional applications. Thirdly, the mathematical framework is proposed to obtain RFOD mask coefficients for the applications of image processing. Subsequently, this mask is utilized to develop the FrFT based RFOD and quaternion based RFOD approaches for edge detection in grayscale images and color images respectively. The gradient images thus obtained are utilized for the enhancement of grayscale as well as color images. The robustness of the proposed edge detection approaches is also established by taking into consideration the uncontrolled features particularly noise, varying illumination conditions, and Joint Photographic Experts Group (JPEG) compression artifacts.

1.6 Organization of Thesis

The flow of the work carried out in this thesis is summarized in the following manner:

Chapter 2 includes the in-depth study of fractional calculus, fractional transforms, and their applications in image processing. It also comprises the preliminaries of the mathematical functions required for the proposed work. Further, the performance metrics used to evaluate the FODs in signal and image processing applications are scrutinized. The research gaps, objectives, and research methodology are also discussed in this chapter.

Chapter 3 deals with the FOD based UM approach for image enhancement. The proposed technique utilized the FOD based masks in combination with the Laplacian mask in the Conventional UM (CUM). The effect of various FOD based masks is considered in the proposed approach for the enhancement of images. Furthermore, the efficacy of the FOD based UM approach is confirmed on the basis of comparative analysis with image enhancement techniques.

Chapter 4 presents an analytical expression in the closed-form for RFOD in the FrFTD. Moreover, its counterpart is obtained in the discrete domain which is further used to validate the effectiveness of FrFT based Riesz fractional order differentiator by considering the design example. Furthermore, the proposed design is extended for the two-dimensional applications of image processing.

Chapter 5 focuses on the RFOD technique in the FrFTD for the applications of edge detection as well as image enhancement of grayscale images. Initially, the mathematical framework is obtained for the RFOD mask which is further utilized to detect edges. The edges thus detected are used for the image enhancement. The performance of this presented technique is also validated by taking into account various uncontrolled features. Moreover, the potential of the proposed approach is established against state-of-the-art existing approaches.

Chapter 6 describes the quaternion based RFOD technique for detecting the edges in color images of the Berkeley Segmentation Dataset and Benchmarks (BSDS). The performance of the presented scheme is further validated by taking into account the uncontrolled features. Furthermore, the proposed technique is compared with the classical edge detectors. Also, the enhancement of color images is achieved by utilizing the detected edges. Moreover, the performance of the proposed technique is also confirmed for realistic scenarios.

Chapter 7 eventually provides the conclusion as well as the future scope of the research work carried out in this thesis.

LITERATURE SURVEY

This chapter is dedicated to study and analyze the fundamental concepts of the literature involving FOC, transforms, special mathematical functions, and their applications in signal and image processing. It provides comprehensive information about the terms, functions, and methods that are utilized in the presented research work. Furthermore, various performance metrics that are used to evaluate the FOD based techniques are also discussed. Besides, this chapter covers the motivation, research gaps, objectives, and research methodology.

2.1 Context of FODs in Signal and Image Processing

Despite being in existence from the previous three hundred centuries, FOC is considered to be an abstract mathematical concept until the research fraternity rediscovered its applicability in the discipline of science and engineering a few decades ago [3], [4]. Moreover, it is a well-known fact that various concepts such as optimization techniques, learning-based methods, fractional order systems, or their combinations are utilized to improve the performance of a model. However, the learning-based methods are more successful when very large data is under consideration [89]. Moreover, the optimization techniques and learning-based methods are of high complexity as their output is dependent on prior experience which further increases the computational cost [14], [49], [59], [90], [91]. Meanwhile, the fractional methods are more efficient. Furthermore, the notion of unification of FODs and FrFT in [8]–[11] motivated to analyze the performance of FODs in the time-frequency domain. Hence, the presented work is based only on the fractional domain either considering the FODs exclusively or in combination with the FrFT. It is well-known fact that the flexibility provided by the fractional parameters has opened up new horizons to comprehend and analyze the natural phenomenon [4]. In order to comprehend the concept of fractionalization in calculus and transforms, the fundamental concepts of FOC and FrFT are described in this chapter.

Several applications require the attention of the research fraternity, but the excessive usage of images stimulates to work in the field of image processing. Hence, the frequently used applications of edge detection and image enhancement are considered for analysis in this work that can be further employed in high-level image applications of computer vision. The analysis of FODs in the field of image processing especially by Kumar *et al.* [11], Nandal *et*

al. [92], Gao *et al.* [68], [93], Pu *et al.* [94], Tseng and Lee [95], Chen *et al.* [2], Garg and Singh [96] inspired to conduct the performance analysis of FODs in the image processing applications. Furthermore, the detailed analysis elucidates the concept of fractional operators in signal and image processing applications.

2.2 Preliminaries of FODs

The origin of FOC dates back to the foundation of classical Newtonian calculus. However, systematic research began in the early 19th century. Earlier the mathematicians such as Euler, Fourier, and Lagrange discussed the derivatives of arbitrary order without considering any particular application. Most of the work is carried out by mathematicians who mainly contributed to the theoretical concepts of FODs. However, in the last few decades, the applicability of FODs is explored in science and engineering such as diffusion theory, rheology [30], fluid flow, electrical networks [26], control systems, signal and image processing [2], [4], etc. Hence, remarkable contributions are made to both theories as well as the applications of FODs in the 20th century [27]. FODs are generally the differintegrals whose fractional order is positive. They have an advantage over the integer-order models due to the additional fractional parameter. Several definitions of differintegrals exist in the literature but RL, GL, Caputo, Caputo-Fabrizio, and Riesz [4], [25], [97] are frequently encountered in the prevailing literature. They are widely applied in the applications of signal and image processing owing to their capability of preserving the low-frequency contour features in smooth regions while maintaining the high-frequency features in addition to enhancement of medium-frequency details. However, the definitions of FODs that are used in the work carried out in this thesis are elaborated in the subsequent sub-sections.

2.2.1 Riemann-Liouville Definition

The RLFOD for a function $z(t)$ is defined by [4], [98]:

$$D^{\mathcal{G}}z(t) = \frac{1}{\Gamma(m-\mathcal{G})} \left(\frac{d}{dt}\right)^m \int_a^t (t-\tau)^{m-\mathcal{G}-1} z(\tau) d\tau \quad (2.2.1)$$

where, t and a are upper and lower integration limits. Here, $\mathcal{G} \in R^+$ (real numbers) for $m-1 < \mathcal{G} < m$, where m is the order of operation. The convolution is interpreted at all the instances from $\tau=0$ to $\tau=t$. It is considered as a forward derivative. With RLFOD, an arbitrary function does not have to be continuous at the origin or differentiable. Moreover, the RLFOD of a constant is not zero. It possesses certain drawbacks when trying to simulate real-world processes with fractional differential equations [4], [30].

2.2.2 Grünwald-Letnikov Definition

The definition of GL differintegral for a function $z(t)$ is defined by [4]:

$$D^{\varrho} z(t) = \lim_{h \rightarrow 0} \frac{1}{\Gamma(-\varrho) h^{\varrho}} \sum_{k=0}^{((t-a)/h)} \frac{\Gamma(k-\varrho)}{\Gamma(k+1)} z(t-kh) \quad (2.2.2)$$

where h is the sampling period and k varies from 0 to $((t-a)/h)$ and $((t-a)/h)$ is an integer. Here, if fractional order (ϱ) is positive then the above definition corresponds to be a fractional derivative otherwise it corresponds to be a fractional integral. It is the generalization of the integer-order derivative. The GLFOD is preferred in most of the applications such as control systems, signal and image processing, etc., due to its discrete nature and flexibility [4].

2.2.3 Caputo Definition

The Caputo FOD for a function $z(t)$ is obtained as [4], [98]:

$$D^{\varrho} z(t) = \frac{1}{\Gamma(m-\varrho)} \int_a^t z^{(m)}(\tau) (t-\tau)^{m-\varrho-1} z(\tau) d\tau \quad (2.2.3)$$

It is dependent on the initial conditions and boundary conditions that are sometimes required to formulate the problem, however, it needs to be a well-posed problem. Besides, its derivative for a constant is also zero. It is more suitable for solving engineering problems than RLFOD as it has better relation with LT. Moreover, the differentiation in Caputo is inside the integral, thus, alleviating the effects of noise as well as numerical differentiation [1], [30].

2.2.4 Riesz Definition

The two-sided Riesz kernel $\kappa(t)$ is defined by [1], [99], [100]:

$$\kappa(t) = \frac{|t|^{-\varrho-1}}{2\Gamma(-\varrho) \cos\left(\frac{\varrho\pi}{2}\right)} \quad \varrho > -1 \quad (2.2.4)$$

When $\varrho=1$, (2.2.4) reduces to $\kappa(t) = -|t|^{-2}/\pi$. The Riesz fractional operator $D^{\varrho} z(t)$ on the real axis for an order $\varrho > -1$ is given by [1], [99], [100]:

$$D^{\varrho} z(t) = \kappa(t) * z(t) = \frac{1}{2\Gamma(-\varrho) \cos\left(\frac{\varrho\pi}{2}\right)} \int_{-\infty}^{\infty} |t-\tau|^{-\varrho-1} z(\tau) d\tau \quad (2.2.5)$$

where $*$ denotes the convolution operation. It is referred to as RFOD or hypersingular integral for $\mathcal{G} > 0$ and Riesz potential for the fractional order $-1 < \mathcal{G} < 0$. The presented work considered one of the two types of RFOD defined in [1], [22] as its discrete counterpart. By approximating Type-I RFOD with step h in accordance with the second-order fractional centered difference model given by [99]:

$$D^{\mathcal{G}}z(t) = \lim_{h \rightarrow 0} \frac{\Gamma(\mathcal{G}+1)}{h^{\mathcal{G}}} \sum_{k=-\infty}^{\infty} \frac{(-1)^k}{\Gamma((\mathcal{G}/2)-k+1)\Gamma((\mathcal{G}/2)+k+1)} z(t-kh) \quad (2.2.6)$$

where k ranges from $-\infty$ to ∞ . RFOD is independent of any initial conditions in addition to being a two-sided FOD that can reflect past as well as future memory effects. Besides, it possesses zero phase shifting property whereas RL, GL, and Caputo provide a phase shift upon considering an ideal frequency response. Thus, RFOD is suitable for certain applications of signal and image processing such as edge detection, image sharpening, filtering, etc. as it prevents blurriness distortion which further preserves the features [1], [95]. The aforementioned FODs are used in the proposed work for the time or spatial, frequency, FrFT, and quaternion domain.

2.3 Concept of FODs in various domains for applications of Signal Processing

After studying the foundational concepts of FODs, its applicability is considered for the one-dimensional applications in various domains in this section. The analysis of FODs is carried out in time, frequency, or fractional transform domain in the last few decades by utilizing the transforms whereas previously the majority of research in the field of FOC is done by mathematicians, to exemplify, the applications of fractional derivatives are considered in summation of series and definite integrals in [101]. However, it is only during the last decade of the twentieth century that significant contributions are made by scientists and engineers in the field of control systems, electromagnetics, signal processing, etc. [1], [3], [102]. Besides, the remarkable contribution is made by the researchers in the last decade by utilizing the exceptional notion of FODs in FrFTD [8]–[11]. Furthermore, they are implemented in the practical applications of signal processing. A brief summary of the prevailing literature in the fractional order differentiators is provided in Table 2.1.

Table 2.1: Review of FODs in signal processing

Reference No.	Signal/FOD	Domain/ Transform	Design Example/ Application	Description
[103]	Generalization of Cauchy integral formula	FT	Yes	Fractional order differentiator is designed using the least-squares method which is utilized for the generation of the random fractal process from Gaussian white noise.
[104]	Power function	Time	Yes	Finite Impulse Response (FIR) fractional order differentiator's impulse response is obtained by solving the linear equations.
[105]	RL	Time	Yes	Discrete-time FIR fractional order differentiator is developed based on the expansion of the Newton series. The fractional derivative of the signal is yielded from the additive combination of time-varying weighted responses obtained from the N cascaded first-order differentiators.
[106]	Power signal	Frequency	Yes	FIR fractional order differentiator is designed by selecting the FIR filter with impulse response whose frequency response is approximately the same as the frequency response of the desired fractional differentiator.
[107]	GL	Z-transform	Yes	Radial basis function interpolation is utilized to derive the non-integer delay sample estimation that is further utilized for designing a fractional order differentiator in combination with GL.
[108]	RL	Time	Yes	RL definition is utilized to generalize the integer-order Savitzky-Golay differentiator to fractional order. Its analysis is also carried out in the frequency domain.
[10]	RL and GL	FrFT	Yes	Closed-form analytical expression is derived for RL and GL FODs in the FrFTD in terms of Confluent Hypergeometric Function (CHF).
[9]	Caputo	FrFT	Yes	An analytical expression in closed-form is obtained for Caputo FOD in FT and FrFTD in terms of CHF function.

Reference No.	FOD	Domain/ Transform	Design Example/ Application	Description
[109]	GL	DCT-II	Yes	GLFOD in combination with DCT interpolation is utilized for designing a closed-form fractional order differentiator.
[110]	GL	DCT-III	Yes	The filter response of FIR fractional order differentiator designed on the basis of GL and DCT-III is modified by considering the windows.
[95]	Riesz	Frequency	Yes	Riesz fractional order differentiator is developed by considering the fractional differencing, Tustin approach, and DCT. The developed differentiator is further improved by employing a fractional sample delay filter. It is further extended to the two-dimensional application of image sharpening.
[111]	GL	Frequency	Yes	Closed-form matrix fractional order differentiator is designed using various transforms such as DFT, DCT, Discrete Sine Transform (DST), and Discrete Hartley Transform (DHT).
[112]	GL	DST and DCT	Yes	Matrix fractional order differentiator is designed using DST, DCT as well as optimization techniques. It is extended to the two-dimensional image enhancement application.
[113]	Riesz	DST	Yes	RFOD is developed based on the response of FOD in the DST domain.
[114]	GL	Frequency	Yes	FIR fractional order differentiator yields the fractional derivative for input transformed into power function using Taylor series expansion. The least-squares approach is employed for obtaining the filter coefficients.
[115]	GL	DCT-III and DCT-IV	Yes	DCT interpolation is used for designing FIR fractional order differentiator whose coefficients are modified to improve its frequency response.

Reference No.	FOD	Domain/ Transform	Design Example/ Application	Description
[91]	GL	Frequency	Yes	PSO based FIR fractional order differentiator is designed.
[116]	Caputo-Fabrizio	Time	Yes	The closed-formula derived for Caputo–Fabrizio based fractional derivative of the Gaussian function is used in signal processing applications.
[117]	RL and GL	Time	Yes	The fractional derivative of a signal is computed by performing the Cauchy finite convolution of the GL and signal. The comparative analysis is performed with RLFOD that obtained analogous results but the execution time is less.
[118]	Riesz	Frequency	Yes	Riesz fractional order differentiator developed on the basis of difference method is utilized for detection of R-peak in Electrocardiogram (ECG) signal.
[119]	Riesz	Frequency	Yes	Manta-ray foraging optimization in combination with the zero-phase Riesz fractional order differentiator is developed for detecting the R-peak in ECG.
[120]	Riesz	Frequency	Yes	Riesz FIR fractional order differentiator is developed by optimizing the design parameters using optimization techniques.

Therefore, it can be summarized that most of the fractional order differentiators are modeled on the basis of RL and GL FODs either in the time or frequency domain. Still, there is a lot of scope in the mathematical analysis of FODs. Some of these approaches also used optimization techniques but these approaches result in more complexity, therefore, alternative procedures are considered that are more robust and efficient [90]. However, Kumar *et al.* [10] and Singh *et al.* [9] analyzed the RL, GL, and Caputo FODs in FrFTD. These FODs possess certain demerits, for instance, RL and Caputo FOD depend on the initial conditions that perhaps cause accuracy issues, and the ideal frequency response of RL, GL, and Caputo obtained from their FT is $(j\omega)^q$ which causes the issue of phase shifting that result in phase distortion [1], [94], [95]. Nevertheless, RFOD is independent of any such initial conditions.

Furthermore, the FT based frequency response for RFOD is $(\omega)^g$, thus avoiding the issue of phase shifting that exists in RL, GL, and Caputo FOD [1], [95]. It is noted that the mathematical analysis of RFOD in the time-frequency domain is not carried out in the existing literature. Hence, the analysis of RFOD in FrFTD is an open research problem. Moreover, the concept of FODs is further extended to the two-dimensional applications of image processing. Hence, the next section deals with the intended applications of FODs in image processing.

2.4 Applications of FODs in Image Processing

This section categorically outlines the FOD based techniques that are available in the literature for the deemed realm of applications. Further, it also provides an insight into the challenges that affect the performance of these applications.

2.4.1 Image Edge Detection

Owing to the benefits of FODs in preserving the image details, they are generally utilized in the applications of edge detection.

Mathieu *et al.* [121] designed the Contour Robuste d'Ordre Non Entier (CRONE) edge detector based on the generalization of derivative to fractional order. Although it improved the detection of thin edges and noise sensitivity against the Prewitt edge detector yet it needs improvement as the detection accuracy and noise immunity are compromised. In order to resolve this issue, Yang *et al.* [122] proposed an edge operator by utilizing the concepts of fractional order integration and differentiation named as YE&YANG operator that provided superior results to CRONE and Canny operator.

Gao *et al.* [93] developed the Newton Interpolation based Fractional Differentiation (NIFD) masks from the GL definition for edge detection in grayscale images. The gradient images thus obtained are non-maximally suppressed to obtain the edge map in the spatial domain. The robustness of NIFD approach is further confirmed in the noisy environment that provides effective results than Sobel and Canny edge detectors in its visual form.

Telke and Beitelschmidt [123] utilized the GL in CRONE operator for edge detection that is more immune to noise than [121]. It is employed for practical applications in railway track images. However, it involved the use of two fractional orders that increased its computational complexity.

Amoako-Yirenkyi *et al.* [124] utilized the RL Fractional Derivative (RLFD) in the spatial domain for edge detection in a variety of images such as synthetic and medical images. The uncontrolled features such as noise and motion that occur while procuring the images are considered. Moreover, it sometimes detected the redundant edges as detected by the Canny edge detector. Further, the aforementioned approach utilized the Gaussian filter for smoothing purposes. However, in [125], the technique in [124] is analyzed using various smoothing techniques.

Kumar *et al.* [11] presented the GL based edge detection technique in the FrFTD that provided better performance for the noisy images than the traditional edge detectors in the FrFTD by taking into consideration the concept of two fractional parameters. Further, Nandal *et al.* [92] presented a FOC mask based on RL for edge detection that provided superior results to the existing fractional order based edge detectors. Despite providing more features than most of the existing techniques, it sometimes leads to the loss of edge information. Further, GLFOD whose fractional order is optimized based on the correlation coefficient is used for edge detection in [126]. However, in order to avoid the issue of phase distortion by RL and GL FODs, RFOD integrated with classical edge detectors in the spatial domain is developed for edge detection in medical images in [127]. Despite being able to provide better features, it is not competent in a noisy environment.

Aboutabit [128] presented a modified Caputo-Fabrizio method utilized for edge detection on the natural images in both noisy and noiseless environments that provided superior results in both scenarios. In [116], closed-form expression is derived for Gaussian function on the basis of Caputo-Fabrizio FOD which is further extended for the two-dimensional application of edge detection. Similarly, Caputo-Fabrizio based Gaussian FOD is utilized for detecting the edges that provided satisfactory results even in a noisy environment [65]. Another FOD definition of Atangana and Baleanu in the Caputo sense is considered for the detection of edges. It not only obtained accurate results but also enhanced the edge information which is better than conventional FOD masks [129].

The color image edge detection is achieved in [72] by transforming the image into grayscale images. It utilized the concept of integration of GL and Information Sets (GLIS) whose performance is compared with the traditional edge detectors. However, it is not able to provide coherent edges. Gao *et al.* [68] presented GL based edge detection approach for the color images by using the concept of quaternions. This concept is further extended for the directional derivatives in [75]. The superior results are attained by even detecting the edges

that are somewhat defined by texture as compared to traditional edge detectors in both approaches, thus, being consistent with the human visual system.

It is worth noting that the majority of existing FOD based edge detection approaches are implemented in the spatial domain. Thus, there is considerable scope of research in the transform domain methods for edge detection, especially in the time-frequency plane. Furthermore, in the prevailing literature, only noise is considered as an uncontrolled feature for edge detection. In some cases, noise pixels tend to appear as edge pixels, thus, detecting the false edges in case of edge detection techniques. However, the effect of illumination conditions and JPEG compression artifacts are not taken into consideration in edge detection.

2.4.2 Image Enhancement

FODs are employed extensively in the image enhancement techniques to preserve the smooth regions while enhancing the images that are otherwise deteriorated in the integer-order methods.

Pu [130] demonstrated the capability of the GL approach for the enhancement of texture-rich images against the integer-order based methods. The aforementioned approach is further extended by considering the directional derivative masks for enhancing the texture enriched images [131]. The practical implementation is also provided for the latter approach.

Gan and Yang [132] developed an isotropic gradient mask based on the RLFOD for texture enhancement. The developed mask is also dependent on the intensity factor that controls the lightness of an image. The visual comparison confirmed that the developed approach avoided the distortion that exists in the case of Laplacian operator and smoothing of edges by conventional GL filter. Garg and Singh [96] utilized this concept for the GLFOD and confirmed its proficiency over the RL technique in the form of both visual comparison and performance parameters.

Pu *et al.* [94] presented six fractional derivative masks based on RL and GL FODs by obtaining the mask coefficients from different methods. However, the optimum results are obtained by the fractional GL based mask whose coefficients are obtained by using the 3-point Lagrange interpolation method. Its capability is confirmed against the integer-based masks in both visual and quantitative form.

Chen *et al.* [133] also developed an isotropic RL based fractional mask obtained by utilizing the fractional masks in the eight directions for the enhancement of low contrast images. It provides better enhancement than the existing fractional and traditional approaches.

Tseng and Cheng [134] developed GLFOD and Mach band effect based filter in the DCT domain for sharpening the color images. In this approach, the filter is applied individually on each of the RGB (Red, Green, Blue) channels and after processing, all the color channels are combined to obtain the sharpened image that may result in the loss of correlation that exists among color channels.

Jalab and Ibrahim [135] generalized the Savitzky-Golay filter in the Srivastava-Owa sense for the texture enhancement of images based on fractional parameters. It provided prominent edges and enhanced texture which is evident from the Gray Level Co-occurrence Matrix (GLCM) parameters.

Yu *et al.* [136] presented a second-order RFOD based approach for non-linearly enhancing the texture and edges of an image while maintaining the details in smooth regions for the noisy environment. Its comparative analysis with the integer-order and GLFOD based approaches show better results for RFOD in the spatial domain in both visual form and performance parameters. Tseng and Lee [137] also demonstrated the effective visual results for RFOD mask in integration with DHT and Mach band effect in the form of sharpened images.

Gao *et al.* [138] presented the directional derivative masks in the eight directions based on Taylor's formula. The coefficients are varying in the eight directions, thus, enhancing the texture differently in different directions. Moreover, its efficacy is confirmed against the traditional fractional derivative and integer-order methods.

Yu *et al.* [139] utilized the variable second-order RFOD mask obtained from 3-point Lagrange interpolation for enhancing the texture in medical images. The superiority of this approach is confirmed against the existing fractional order enhancement techniques. In [140], matrix Riesz based UM (RUM) is designed in the DST domain for sharpening the images. Furthermore, RFOD is also utilized in [49] for enhancing the license plates even in the varying illumination and weather conditions, night images, etc., The enhanced images are further utilized for text detection and recognition in the license plates that provided significant improvement as compared to the existing techniques.

In [141], GLFOD is modified based on the autocorrelation among the pixels in the neighborhood for the texture enhancement of images. Its improvement is verified from the GLCM parameters. Moreover, the efficacy is also confirmed for realistic scenarios considering medical and remote sensing images. Guan *et al.* [142] proposed GLFOD based

directional derivative masks in eight directions that are constructed based on the structural pixels and surrounding information for medical image enhancement. The superiority of the presented approach is validated in the form of both visual and quantitative analysis by considering four different kinds of medical images.

Luo *et al.* [143] compared the enhancement achieved by the integer-order and FOD masks for Landsat images. The GLFOD mask used for enhancing the images is obtained by summing the masks obtained in the eight directions. The aforementioned mask is applied on the I (Intensity) channel of HSI (Hue, Saturation, Intensity) color space. The enhanced images are then converted back to the RGB color channel. It demonstrated the superiority of fractional operators to integer-order operators. Singh *et al.* [144] developed the RL mask in association with piecewise gamma correction for enhancing the satellite images. An optimization technique is used for finding the optimal parameters to enhance the poorly illuminated and dark images. Despite providing better results, it increased the computational cost of the approach.

It is noted that noise and illumination conditions are considered for image enhancement in the prevailing literature. However, the effect of JPEG compression artifacts is not considered in this application. Hence, there is a need to consider the effect of these uncontrolled features in image enhancement applications. Furthermore, it is noteworthy that the majority of existing FOD based approaches are either utilized for edge detection or image enhancement. Hence, it is required to design a new technique dealing with both image processing applications.

2.4.3 Uncontrolled Features

Images get corrupted with uncontrolled features either due to environmental conditions or the quality of sensing components during image acquisition and transmission [124]. These features negatively impact the output of edge detection and image enhancement approaches in the form of missing and discontinuous edges, loss of image details, thus, reducing their image visual quality. Some of these uncontrolled features that often occur while acquiring the images such as noise, illumination conditions, and JPEG compression artifacts are taken into consideration in the presented work.

2.4.3.1 Noise

Images usually get corrupted with noises such as Salt and Pepper, Gaussian, and Poisson noise due to several reasons. Salt and Pepper noise refers to white and black pixels that may be few but they are extremely noisy. It may be perhaps due to the transient variations in the

image or transmission of the image over a noisy link. Its concentration can be varied in terms of noise density [21]. However, the Gaussian noise commonly occurs while acquiring an image owing to sensor noise or electronic circuit noise arising due to high temperature or low illumination. The concentration of mean and variance are varied in the simulations to consider its effect [21], [52]. Another kind of non-additive noise that occurs while capturing the images in low-intensity illuminations is the Poisson noise. It strongly depends on the image pixel intensity [52], [145]. Occasionally, the edge detection techniques considered noise pixels as edge pixels thus posing a challenge for them. Hence, noisy images can be examined for confirming the ability of the edge detection techniques.

2.4.3.2 Illumination Conditions

This is one of the uncontrolled features that may occur due to the change in weather conditions such as fog, haze, rainfall, lighting conditions from sunshine to darkness, positioning of a camera, etc. The variation of these illumination conditions may also result in low contrast and dark images. Hence, it may result in missing edges in the case of shadow or dark regions of an image [146]. Further, it may also affect the enhancement of such images. Hence, the ability of edge detection and image enhancement algorithm is confirmed by taking into consideration the images with variation in illumination conditions.

2.4.3.3 JPEG Compression Artifacts

Owing to the upsurge in data in its visual form, the data is transmitted in its compressed form. However, the compression leads to degradation in the quality of an image particularly near block boundaries which perhaps affects the edge detection and image enhancement methods in the form of blocking artifacts or loss in image details [147]. In the case of edge detection technique, the loss in information content may lead to discontinuous edges. Hence, the proficiency of the approach can be validated by considering the effect of compression on its performance by considering the quality factors. In the proposed work, the variation in quality factor is done from 50 to 95 because quality factor below 50 leads to image degradation whereas there is a slight improvement in the quality factor above 95 with a significant increase in the image size [148].

Thus, it is outlined by thoroughly examining the edge detection and image enhancement techniques that integer-order derivatives are commonly used that may cause the loss of information details as well as degrade the performance of the enhancement techniques in a particular region of an image. Moreover, the uncontrolled features further degrade the

performance of these techniques. Hence, FOC based techniques particularly FODs can be utilized to resolve the issues related to integer-order derivative based techniques.

2.5 Preliminaries of FrFT

The notion of the fractionalization of the Fourier operator actually originated in 1929 in the work done by Wiener [149]. A lot of work is carried out in a similar context but under a different name. It is widely acknowledged only after Namias employed the concept of FrFT in the field of quantum mechanics in the 1980s [31]. However, it required refinement in mathematics which is done by McBride and Kerr in 1987 to improve operational calculus to further describe the concept of FrFT [33].

FrFT is an indispensable tool in the field of signal and image processing as it provides more flexibility in implementation as compared to the time or space domain as well as frequency domain due to an additional degree of freedom. Its applicability in the case of time-varying signals provides an edge over the time and frequency domain. FrFT performs the task of transforming the given function into an intermediate domain between time and frequency by rotating the function in the time-frequency plane with rotation angle ϕ . The FrFT rotation angle ϕ is subsequently dependent on the fractional parameter ' a ', such that, $\phi = a\pi/2$, where ' a ' is varied from 0 to 2 [150]. Figure 2.1 illustrates the Fractional Fourier domain in the time-frequency plane.

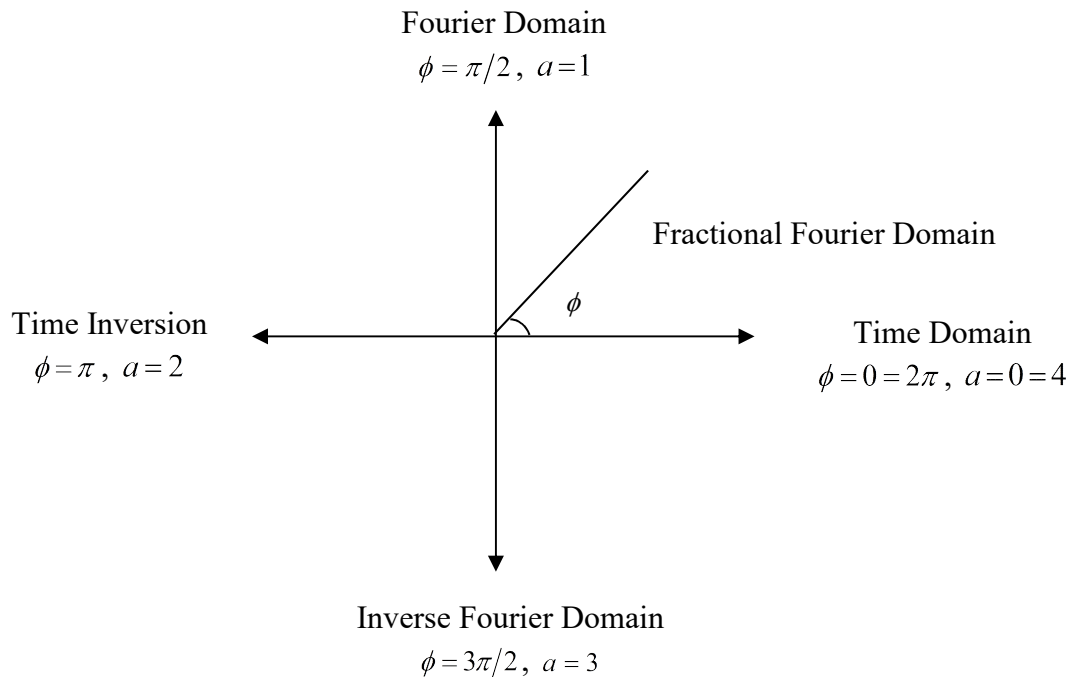


Figure 2.1: Time-frequency plane [151]

The FrFT kernel corresponds to the identity operation when $a=0$ ($\phi=0=2\pi$) and reflection operator when $a=2$ ($\phi=\pi$). However, the FrFT kernel corresponds to the classical FT when $a=1$ ($\phi=\pi/2$) and Inverse FT (IFT) when $a=3$ ($\phi=3\pi/2$). Thus, the FrFT parameter 'a' in the rotation angle ' ϕ ' provides an extra degree of freedom which can be selected on the basis of nature of the application [151].

2.5.1 Definition of FrFT

The a^{th} order FrFT of function $z(t)$ is [32]:

$$F^\phi(z(t)) = Z(u_\phi) = \int_{-\infty}^{\infty} z(t) k_\phi(t, u_\phi) dt \quad (2.5.1)$$

such that $F^\phi(\cdot)$ refers to the FrFT operator, the FrFT parameter $0 < |a| < 2, \phi = a\pi/2$ such that $a \in R^+$, and $k_\phi(t, u_\phi)$ refers to the FrFT kernel function provided by:

$$k_\phi(t, u_\phi) = \begin{cases} \sqrt{\frac{1 - j \cot(\phi)}{2\pi}} \exp\left(j \left(\frac{t^2 + u_\phi^2}{2}\right) \cot(\phi) - ju_\phi t \csc(\phi)\right) & \text{if } \phi \neq n\pi \\ \delta(t - u_\phi) & \text{if } \phi = 2n\pi \\ \delta(t + u_\phi) & \text{if } \phi + \pi = 2n\pi \end{cases} \quad (2.5.2)$$

and $\csc(\cdot)$ is the cosecant function while $\delta(t)$ denotes the Dirac's delta function. Here, F^ϕ is considered to be the FrFT operator provided it satisfies the following properties:

- linearity
- FT condition, that is $F^1 = F$
- additivity, $F^\phi F^\theta = F^{\phi+\theta}$

It can be noticed that the FrFT parameter 'a' in the rotation angle ' ϕ ' can be freely changed as if it is the power of the FT operator. Furthermore, it can be noted that FrFT is obtained by considering the following sequence of operations [150]:

Step 1: Product with a chirp in the reference domain;

Step 2: Obtain its FT;

Step 3: Product with a chirp in transform domain;

Step 4: Product with the amplitude factor.

The description of the concept of FrFT provided beforehand is also referred to as Chirp FrFT (CFrFT). Moreover, the inverse FrFT (IFrFT) is obtained with the rotation angle of $-\phi$, that is, ϕ is replaced with $-\phi$ in (2.5.1) and (2.5.2). Despite being extensive utilization in the applications of quantum mechanics, optics, signal and image processing, etc. [7], [151]–[153], it is quite difficult to utilize the continuous version of FrFT due to its computational cost. Hence, there is a requirement for the definition of FrFT in the discrete domain. In the last few decades, various researchers provided definitions of a discrete version of FrFT [7], [41]–[43], [154]. The basic instinct behind establishing the DFrFT is that it should possess similar relation with FrFT as Discrete Fourier Transform (DFT) has with FT. The ideal DFrFT is the generalization of the DFT that satisfies the basic properties of continuous FrFT [5]. Pei *et al.* [42] provided the merits and demerits of prevailing DFrFT algorithms. Further, a closed-form expression is derived for DFrFT by sampling the continuous FrFT which performed in an almost similar manner to the continuous FrFT defined as [42]:

$$Z^\phi(n) = \sum_{m=-N}^N T^\phi(m, n) z(m) \quad (2.5.3)$$

Here, the kernel $T^\phi(m, n)$ is defined as:

$$T_\phi(m, n) = \sqrt{\frac{\text{sgn}(\sin(\phi))(\sin(\phi) - \cos(\phi))}{2P+1}} \exp\left(\frac{j}{2} \cot(\phi) m^2 \Delta u_\phi^2\right) \exp\left(\frac{j}{2} \cot(\phi) n^2 \Delta t^2\right) \exp\left(-j \frac{\text{sgn}(\sin(\phi)) 2\pi nm}{2P+1}\right) \quad (2.5.4)$$

Although (2.5.4) lacks some characteristics, it exhibits the significant properties of continuous FrFT such as unitarity, reversibility, and flexibility. However, due to its low computational complexity, it is used in combination with RFOD in the proposed work such that FrFT parameter is chosen on the basis of preliminary experimentation before the selection of fractional parameter of FOD. The synergy of the fractional aspects of FrFT and FOD provides a wider horizon by exploiting the advantage of two extra degrees of freedom to ameliorate the performance of an algorithm.

2.5.2 Basic Properties of FrFT

This section provides the basic properties of FrFT as well as the properties that are used in the current research work. The FrFT operator should possess the following properties [5]:

- It must be linear, such that, $F^\phi [b_1 z(t) + b_2 z(t)] = b_1 F^\phi [z(t)] + b_2 F^\phi [z(t)]$, where b_1 and b_2 are constants.
- It must obey the inverse property, that is, $(F^\phi)^{-1} = F^{-\phi}$.
- It must be additive, such that, $F^\phi F^\theta = F^{\phi+\theta}$.
- It must satisfy the periodicity property, that is, $F^\phi (z(t)) = F^{\phi+2N\pi} (z(t))$, where N is an integer.
- It must verify the FT condition, that is, $F^{\pi/2} = FT$.

Moreover, the other properties of FT are also extended to the FrFTD, such as time-shifting, modulation, time-scaling, differentiation, integration, etc. [150]. However, the properties of the FrFT operator that are considered while carrying out the analysis of the current research work are described below:

- Time-shifting: The time-shifting property of function $z(t)$ in the FrFTD is defined as [150]:

$$F^\phi (z(t-\tau)) = F^\phi (u_\phi - \tau \cos(\phi)) \exp\left(j\left(\frac{\tau^2}{2}\right) \sin(\phi) \cos(\phi) - ju_\phi \tau \sin(\phi)\right) \quad (2.5.5)$$

- Differentiation: The differentiation property $z(t)$ in the FrFTD is defined as [150]:

$$F^\phi (z'(t)) = F^{\phi'} (u_\phi) \cos(\phi) + ju_\phi F^\phi (u_\phi) \sin(\phi) \quad (2.5.6)$$

such that $F^{\phi'} (u_\phi) = dF^\phi (u_\phi) / du_\phi$.

- Convolution: Several researchers attempted to provide the convolution theorem in the FrFTD but the expressions do not generalize to the conventional FT. Hence, Zayed proposed a convolution structure that even preserved the convolution theorem for FT. It is defined as follows [37]:

$$F^\phi (z_1(t) * z_2(t)) = \exp\left(-\frac{j}{2} u_\phi^2 \cot(\phi)\right) z_1(u_\phi) z_2(u_\phi) \quad (2.5.7)$$

The convolution theorem is further modified by Singh and Saxena [34] defined as:

$$F^\phi (z_1(t) * z_2(t)) = \sqrt{\frac{2\pi}{1-j \cot(\phi)}} \exp\left(-\frac{j}{2} u_\phi^2 \cot(\phi)\right) z_1(u_\phi) z_2(u_\phi) \quad (2.5.8)$$

Both (2.5.7) and (2.5.8) generalize to the convolution theorem of FT. Moreover, some other researchers also contributed to obtaining the convolution theorem in the FrFTD by attempting to reduce its complexity [39], [155].

2.6 Preliminaries of Quaternions

In 1843, William Rowan Hamilton came up with the mathematical concept of quaternions which is the extension of complex numbers to four dimensions. A quaternion q is represented by [68]:

$$q = a + b\hat{i} + c\hat{j} + d\hat{k} \quad (2.6.1)$$

where a, b, c and d are the real numbers. Here, a is the scalar component while $b\hat{i} + c\hat{j} + d\hat{k}$ are the imaginary components of the quaternion q . The multiplication of the imaginary components $\hat{i}, \hat{j}, \hat{k}$ is given as [68], [69]:

$$jk = -kj = i, ki = -ik = j, ij = -ji = k, i^2 = j^2 = k^2 = -1 \quad (2.6.2)$$

Further, by considering two quaternions q_1 and q_2 , their basic properties are defined as follows [68]:

- Addition and Subtraction: $q_1 \pm q_2 = (a_1 \pm a_2) + \hat{i}(b_1 \pm b_2) + \hat{j}(c_1 \pm c_2) + \hat{k}(d_1 \pm d_2)$
- Multiplication: $q_1 \cdot q_2 = (a_1a_2 - b_1b_2 - c_1c_2 - d_1d_2) + \hat{i}(c_1d_2 - c_2d_1 + a_1b_2 + a_2b_1) + \hat{j}(b_2d_1 - b_1d_2 + a_1c_2 + a_2c_1) + \hat{k}(b_1c_2 - b_2c_1 + a_1d_2 + a_2d_1)$
- Conjugate: $\bar{q} = a - b\hat{i} - c\hat{j} - d\hat{k}$ such that $\bar{\bar{q}} = q$ and $\overline{q_1q_2} = \bar{q}_2 \bar{q}_1$
- Norm: $N(q) = q\bar{q} = \bar{q}q = a^2 + b^2 + c^2 + d^2$ such that $N(q) = N(\bar{q})$ and $N(q_1q_2) = N(q_1)N(q_2)$

It is worth noting that the addition and subtraction of quaternions are commutative and associative. However, the multiplication of two quaternions is not commutative as it is not essential that the product of $q_1 \cdot q_2$ and $q_2 \cdot q_1$ are equal. However, quaternions are generally employed in the field of bioinformatics, signal and image processing, navigation systems, etc. [69]. In the presented work, quaternions are utilized for color image processing as the three color channels can be simultaneously processed using the quaternion based approach. The subsequent section deals with the several mathematical concepts that are encountered during the course of this research work.

2.7 Mathematical Concepts related to FOC in Signal and Image Processing

The mathematical concepts are extensively used in the field of science and engineering to provide the best solutions for the problems in these domains. There exists a variety of

mathematical functions but the functions that are extensively used in the research work are discussed.

2.7.1 Gamma Function

Gamma function is a transcendental function that generalized the factorial function $z!$, where, z can be a non-integer. Euler defined the Gamma function as [156]:

$$\Gamma(z) = \lim_{n \rightarrow \infty} \frac{n! n^z}{z(z+1) \cdots (z+n)} \quad (2.7.1)$$

such that $z \neq 0, -1, -2, \dots, -\infty$. Its integral form is defined as [4]:

$$\Gamma(z) = \int_0^{\infty} e^{-t} t^{z-1} dt \quad (2.7.2)$$

It converges in the right half of a complex plane $\text{Re}(z) > 0$ where z is real. The properties of gamma function that are commonly used are given as [4]:

- Euler's functional equation: $\Gamma(z+1) = z!$; $z\Gamma(z) = \Gamma(z+1)$ if z is an integer, such that $\Gamma(1) = 0! = 1$ and $\Gamma(1/2) = \sqrt{\pi}$.
- Reflection formula: $\Gamma(z)\Gamma(1-z) = \frac{\pi}{\sin(\pi z)}$
- Duplication formula: $\Gamma(2z) = 2^{(2z-1)} \pi^{(-1/2)} \Gamma(z)\Gamma\left(z + \frac{1}{2}\right)$

These basic properties are widely employed in the FOC based applications of signal and image processing.

2.7.2 Kummer Confluent Hypergeometric Function (KCHF)

The hypergeometric functions are the special mathematical functions that are used in the field of quantum physics, mathematics, optics, electromagnetics, signal processing, etc. [30]. Initially, the Gauss hypergeometric function ${}_2F_1(a, b; c; z)$ is obtained by [156], [157]:

$${}_2F_1(a, b; c; z) = \sum_{k=0}^{\infty} \left[\frac{(a)_k (b)_k}{(c)_k} \right] \left(\frac{z^k}{k!} \right) \quad (2.7.3)$$

such that $(a)_k = a(a+1)(a+2) \cdots (a+k-1)$ refers to the Pochhammer symbol (rising factorial) and $(a)_0 = 1$. The series in (2.7.3) converges if c is a positive integer on the unit circle $|z|=1$ and the entire $|z| < 1$ if $\text{Re}[c-b-a] > 0$. The CHF of the first kind ${}_1F_1(a; b; z)$ is obtained from the degenerate form of (2.7.3) given as:

$${}_1F_1(a; b; z) = \sum_{k=0}^{\infty} \left[\frac{(a)_k}{(b)_k} \right] \left(\frac{z^k}{k!} \right) \quad (2.7.4)$$

The series in (2.7.4) is usually not defined for $b=0, -1, -2, \dots$ and the series will truncate if a is a negative integer. It is perceived on the basis of ratio test that this series converges for entire (finite) values of z . It provides the solution for Kummer confluent hypergeometric equation defined in the complex plane for $z \in (-\infty, \infty)$ having an irregular singularity at $z=\infty$ and regular singularity at $z=0$ defined as [156], [157]:

$$z \frac{d^2x}{dz^2} - (z-b) \frac{dx}{dz} - ax = 0 \quad (2.7.5)$$

The commonly used functions such as Hermite, Bessel, Coulomb wave, Parabolic Cylinder, etc. are the special cases of CHF.

2.7.3 Parabolic Cylinder Function (PCF)

PCF is a class of functions referred to as Weber functions. It is the solution of Weber differential equation given by [158], [159]:

$$\frac{d^2y}{dz^2} + \left(\nu + \frac{1}{2} - \frac{1}{4}z^2 \right) y(z) = 0 \quad (2.7.6)$$

The solution to (2.7.6) in the form of CHF is defined as [158], [159]:

$$D_\nu(z) = \frac{2^{\nu/2} \exp(-z^2/4) (-jz)^{1/4} (jz)^{1/4}}{\sqrt{z}} \left[{}_1F_1 \left(\frac{-\nu}{2}; \frac{1}{2}; \frac{z^2}{2} \right) \right] \quad (2.7.7)$$

that is equivalent to (2.7.8) in the right half-plane:

$$D_\nu(z) = 2^{\nu/2} \exp\left(\frac{-z^2}{4}\right) \left[{}_1F_1 \left(\frac{-\nu}{2}; \frac{1}{2}; \frac{z^2}{2} \right) \right] \quad (2.7.8)$$

where ${}_1F_1\left(\frac{-\nu}{2}; \frac{1}{2}; \frac{1}{2}z^2\right)$ is CHF of the first kind. However, there is a need to fix the branch cut of multivalued expressions $(jz)^{1/4}$ and $(-jz)^{1/4}$ in (2.7.7). Hence, the expression $(z)^{1/4}$ is considered to understand the concept of fixing the branch cuts. In case of $(z)^{1/4}$, 0 and ∞ are the branch points. Its polar form is represented as $(re^{j\theta})^{1/4}$, where $\theta = \theta_p + 2n\pi$, such that $-\pi \leq \theta_p < \pi$,

$$w = z^{1/4} = r^{1/4} e^{j\theta_p/4} e^{j\pi n/2} \quad (2.7.9)$$

where n is an integer and $(r)^{1/4} > 0$.

$$\text{When } n=0; \text{ for } \theta_p=\pi, w=r^{1/4}e^{j\pi/4} \text{ and } \theta_p=-\pi, w=r^{1/4}e^{-j\pi/4} \quad (2.7.10)$$

Hence, the negative real half axis is taken as a branch cut for $n=0$ and θ_p is confined to $-\pi \leq \theta_p < \pi$ as the function is discontinuous for the multivalued expressions. Thus, the idea of Riemann sheets is introduced to deal with this problem [160]. There exists exclusively a single value of a multi-valued function in this particular Riemann sheet. Upon the completion of this cycle from $-\pi$ to π , the point is shifted to the subsequent sheet in the surface at $\theta_p = \pi$. The point is shifted to the next sheet in the surface by repeating the cycle in this sheet. Moreover, the process continues until it reaches the original value. To exemplify, there exist four Riemann sheets for $(z)^{1/4}$ to solve the problem of multivalued functions as follows:

$$\text{When } n=1; \text{ for } \theta_p=\pi, w=r^{1/4}e^{j3\pi/4} \text{ and } \theta_p=-\pi, w=r^{1/4}e^{j\pi/4} \quad (2.7.11)$$

$$\text{When } n=2; \text{ for } \theta_p=\pi, w=r^{1/4}e^{j5\pi/4} \text{ and } \theta_p=-\pi, w=r^{1/4}e^{j3\pi/4} \quad (2.7.12)$$

$$\text{When } n=3; \text{ for } \theta_p=\pi, w=r^{1/4}e^{j7\pi/4}=r^{1/4}e^{-j\pi/4} \text{ and } \theta_p=-\pi, w=r^{1/4}e^{j5\pi/4} \quad (2.7.13)$$

A similar procedure is followed for $(-z)^{1/4}$ whose branch cut is the positive real half axis. In the case of m^{th} roots of z where m is a positive integer and $z \neq 0$. Then, its branch is provided as [160]:

$$F_m(z) = \sqrt[m]{r} \exp\left(j\left(\frac{\theta_p + 2n\pi}{m}\right)\right) \quad (2.7.14)$$

such that $-\pi \leq \theta_p < \pi$ and $n = 0, 1, 2, \dots, m-1$. Therefore, m Riemann sheets exist for $(z)^{1/m}$.

In (2.7.7), $(-jz)^{1/4}$ and $(jz)^{1/4}$ are the multivalued expressions. In accordance with symmetry $f(iz) = -f(z)$, the branch cuts of $(jz)^{1/4}$ and $(-jz)^{1/4}$ can be obtained by a rotation of $\pi/2$. Hence, the branch cuts for $(jz)^{1/4}$ and $(-jz)^{1/4}$ are upper and lower imaginary axis respectively. The expression $(-jz)^{1/4}(jz)^{1/4} = (z)^{1/2}$ is simplified to \sqrt{z} in the denominator in the right half-plane ($\text{Re}[z] > 0$) [159]. It can be further utilized in various applications of mathematics as well as physics.

2.7.4 Interpolation Methods

Interpolation is a significant tool for estimating the functions that are either difficult to compute or their values exist only at the distinct points also referred to as nodes. In addition to this, it can be further used for the development of numerical integration methods that further assist in providing the approximate solutions of differential and integral equations [161]. Table 2.2 shows the data that can be used in some of the interpolation methods that exist in the literature.

Table 2.2: Data for interpolation

t	t_0	t_1	t_2
$z(t)$	$z(t_0)$	$z(t_1)$	$z(t_2)$

The above data is provided for the nodes t_0, t_1, t_2 that are either uniformly or non-uniformly spaced. Several interpolation methods exist in the literature, but the 3-point interpolation methods that are used in the present work are discussed in this section.

- Lagrange Interpolation: Initially, the interpolation formula is presented by Waring in 1779. However, it is published later in 1795 by Lagrange after being rediscovered by Euler in 1783 [162]. The Lagrange interpolation can be defined as [163]:

$$z(t) = \frac{(t-t_2)(t-t_1)}{(t_0-t_2)(t_0-t_1)} z(t_0) + \frac{(t-t_2)(t-t_0)}{(t_1-t_2)(t_1-t_0)} z(t_1) + \frac{(t-t_1)(t-t_0)}{(t_2-t_1)(t_2-t_0)} z(t_2) \quad (2.7.15)$$

- Newton Divided Difference Interpolation: This method of interpolation is given by [156]:

$$z(t) = z(t_0) + (t-t_0)z[t_0, t_1] + (t-t_0)(t-t_1)z[t_0, t_1, t_2] \quad (2.7.16)$$

such that, $z[t_0, t_1] = \frac{z(t_0) - z(t_1)}{t_0 - t_1}$ and

$$z[t_0, t_1, t_2] = \frac{z[t_1, t_2] - z[t_0, t_1]}{t_2 - t_0} = \frac{1}{t_2 - t_0} \left(\frac{z(t_2) - z(t_1)}{t_2 - t_1} - \frac{z(t_1) - z(t_0)}{t_1 - t_0} \right)$$

- Aitken Interpolation: The Aitken interpolation can be defined by [156]:

$$z(t) = z(t | t_0, t_1, t_2) = \frac{1}{(t_2 - t_1)} \begin{vmatrix} z(t | t_0, t_1) & t_1 - t \\ z(t | t_0, t_2) & t_2 - t \end{vmatrix} \quad (2.7.17)$$

where, $z(t | t_0, t_1) = \frac{1}{(t_1 - t_0)} \begin{vmatrix} z(t_0) & t_0 - t \\ z(t_1) & t_1 - t \end{vmatrix}$ and $z(t | t_0, t_2) = \frac{1}{(t_2 - t_0)} \begin{vmatrix} z(t_0) & t_0 - t \\ z(t_2) & t_2 - t \end{vmatrix}$.

Lagrange interpolation is convenient to use in case of fewer data points. However, for a large number of data points, the computation becomes cumbersome. Besides, the Newton and Aitken interpolation provides the benefit as the recalculation of the basis polynomial is not required in the case of addition of any nodes [161]. Hence, Aitken and Newton interpolation methods are more efficient in comparison to the Lagrange interpolation.

2.8 Performance Metrics

It is inferred from the existing literature that the performance of each approach is evaluated both qualitatively and quantitatively. The qualitative analysis involves the comparison in the visual form while the quantitative analysis includes comparison in the form of performance metrics. It is found that most of the image processing applications only performed qualitative analysis. However, the robustness of any technique is validated from the performance analysis of the technique quantitatively. Therefore, the performance metrics that are used to confirm the effectiveness of the presented work in the area of signal and image processing are defined below:

- Signal processing: The parameters used to evaluate the algorithm devised for filtering include Root Mean Square Error (RMSE) and Mean Absolute Error (MAE). RMSE measures the difference between the predicted and actual values of the model. It is computed by the square root of the mean squared error defined by [164]:

$$RMSE = \sqrt{\frac{\sum_{i=1}^n (Z_{actual,i} - Z_{predicted,i})^2}{n}} \quad (2.8.1)$$

where $Z_{predicted,i}$ and $Z_{actual,i}$ denotes the predicted and actual value at a time i . It is suitable for calculating the model's accuracy solely when the estimated errors of various models are compared for specific variable and not among the variables as it is scale-dependent. Moreover, it is mostly used for normally distributed data and is sensitive to outliers. Therefore, another parameter MAE is used for the evaluation purpose. It is computed as the average of the absolute errors obtained by [164]:

$$MAE = \frac{\sum_{i=1}^n |Z_{actual,i} - Z_{predicted,i}|}{n} \quad (2.8.2)$$

such that $Z_{predicted,i}$ and $Z_{actual,i}$ denotes the predicted and actual value at a time i . MAE is less sensitive to outliers as it provides equal weight to all values while RMSE

provides less weight to errors having small absolute values and more weight to large absolute values.

- Image edge detection: It is observed that various performance metrics exist for the evaluation of edge detection techniques, but there are no universally accepted metrics for their evaluation [74]. Hence, the performance metrics such as Figure of Merit (FOM), F-Score, and Edge Preservation Index (EPI) are considered for the evaluation of grayscale and color image edge detection that are widely used in the existing literature [53], [66], [67], [72], [74], [92], [165]. FOM is mainly utilized for the evaluation of edge detection algorithms by comparing the edge map obtained by the proposed scheme with the approximately ideal edge map [53]. Generally, it is computed from the ground truths [72], but in case of the absence of the Ground Truth (GT) images, the ideal edge map is approximated by the traditional edge detectors. The approximately ideal edge map is attained by considering a pixel to be an edge pixel if it is detected by the majority of the traditional edge detectors [74]. Furthermore, detailed edge maps with clean and continuous edges can be estimated to be ideal ones provided they should not detect the redundant edges. Moreover, the FOD based edge detection techniques can detect even weak edges. FOM is defined as [53]:

$$FOM = \frac{1}{\max(M, m)} \sum_{i=1}^m \frac{1}{1 + \tau(D_i)^2} \quad (2.8.3)$$

Here, 'm' and 'M' represents the index of the edges detected by the presented method and the ideal edge map whereas D_i provides the distance between the ideal edge point and i^{th} detected edge. Here, $\tau = 1/9$ is considered to be a scaling factor [53]. If the value of FOM is close to unity, it indicates better localization [92]. Nevertheless, EPI is utilized for determining the edge preservation that is computed by [165]:

$$EPI = \frac{\Upsilon(\Delta Z - \overline{\Delta Z}, \Delta \hat{Z} - \overline{\Delta \hat{Z}})}{\sqrt{\Upsilon(\Delta Z - \overline{\Delta Z}, \Delta Z - \overline{\Delta Z}) \Upsilon(\Delta \hat{Z} - \overline{\Delta \hat{Z}}, \Delta \hat{Z} - \overline{\Delta \hat{Z}})}} \quad (2.8.4)$$

where, $\Upsilon(Z_1, Z_2) = \sum_{i,j \in ROI} Z_1(i, j) Z_2(i, j)$. Here, $\overline{\Delta \hat{Z}}$ and $\overline{\Delta Z}$ depict the mean of Region of Interest (ROI) obtained after applying the Laplacian mask of size 3×3 to the transformed and reference image respectively. $\Delta \hat{Z}(i, j)$ and $\Delta Z(i, j)$ are attained by high pass filtering of ROI regarding $\hat{Z}(i, j)$ (a transformed version of $Z(i, j)$) and $Z(i, j)$ with a Laplacian mask. The EPI ought to be close to one. Another parameter that is

generally used for color image edge detection is F-Score. It is calculated as the harmonic mean of Precision (Pr) and Recall (Re). Mathematically, it is defined as [66], [166]:

$$F - Score = \frac{2(Pr \times Re)}{Pr + Re} \quad (2.8.5)$$

where, $Pr = \frac{Z \cap GT}{Z}$ and $Re = \frac{Z \cap GT}{GT}$. Here, Z represents the edges detected by the proposed approach and GT contains the edge information in the images. It is used to compute the accuracy of the edges.

- Image enhancement: The metrics used for the evaluation of the image enhancement approaches are also specific to the kind of application. Several performance metrics that are used to confirm the efficacy of image enhancement approaches include Information Entropy (IE), Average Gradient (AG), Edge Intensity (EI), Measure of Enhancement (EME), Number of corners, Mean, Mean Square Error (MSE), Peak Signal to Noise Ratio (PSNR), Structural Similarity Index Measure (SSIM), Correlation Coefficient (CC), Universal Image Quality Index (UIQI), and GLCM parameters. IE is utilized for computing the extent of information present in an enhanced image. Based on Shannon's information, the entropy of an image is defined as [96]:

$$E = -\sum_{i=0}^{255} P_i \log_2 P_i \quad (2.8.6)$$

where P_i represents the probability of i image gray levels in an image. The increased entropy indicates the preservation of information details. In a similar manner, AG shows an improvement in the image visual quality. It also indicates an improvement in the contrast of minute image details [94]. It is defined as [96]:

$$AG = \frac{1}{(Q-1)(P-1)} \sum_{i=1}^{Q-1} \sum_{j=1}^{P-1} \sqrt{\frac{\left(\frac{\partial Z(i,j)}{\partial i}\right)^2 + \left(\frac{\partial Z(i,j)}{\partial j}\right)^2}{2}} \quad (2.8.7)$$

where $Z(i,j)$ is the pixel value of an image at the spatial coordinates (i,j) . The contrast and optimization parameters based enhancement measure, EME is computed by classifying an image $Z(i,j)$ into b_1 and b_2 blocks of $W_{b,c}(i,j)$ obtained by [167]:

$$EME = \frac{1}{b_1 b_2} \sum_{c=1}^{b_1} \sum_{b=1}^{b_2} \left[20 \ln \left(\frac{Z_{\max;b,c}}{Z_{\min;b,c}} \right) \right] \quad (2.8.8)$$

where $Z_{\min;b,c}$ and $Z_{\max;b,c}$ are minimum and maximum of the image inside the block $W_{b,c}(i,j)$, respectively. In order to evaluate the technique that is oriented to perform the edge enhancement, performance parameter EI computes the intensity of edges of an image obtained by [168]:

$$EI = \sum_i^m \sum_j^n \left[g_x^2(i,j) + g_y^2(i,j) \right] \quad (2.8.9)$$

Here, $g_x(i,j)$ and $g_y(i,j)$ are computed as:

$$g_x(i,j) = [Z(i+1,j+1) + Z(i+1,j-1) + 2Z(i+1,j)] - [Z(i-1,j+1) + Z(i-1,j-1) + 2Z(i-1,j)]$$

$$g_y(i,j) = [Z(i+1,j+1) + Z(i-1,j+1) + 2Z(i,j+1)] - [Z(i+1,j-1) + Z(i-1,j-1) + 2Z(i,j-1)]$$

where 'm' and 'n' denotes the rows and columns of an image whereas $Z(i,j)$ provides the image intensity at a location (i,j) . Furthermore, the number of corners can be determined because the enhancement of edges also enhanced the corners [92] as they are the junctions of edges. Another parameter, mean [92] is computed to determine the average gray levels of the complete image. Further, the enhancement of the images with low contrast is evaluated using PSNR which is computed on the basis of the ratio of the square of maximum intensity of an image to the MSE on a logarithmic scale. PSNR is computed by [169]:

$$PSNR = 10 \log_{10} \left(\frac{Max_I^2}{MSE} \right) \quad (2.8.10)$$

Here, Max_I refers to the maximum intensity of the pixel while MSE is given as [169]:

$$MSE = \frac{1}{k \times l} \sum_{i=0}^{k-1} \sum_{j=0}^{l-1} [Z(i,j) - z(i,j)]^2 \quad (2.8.11)$$

where Z and z represents the enhanced and reference images of size $k \times l$. The high PSNR indicates the superior quality of an image besides noise suppression. Also, SSIM is used to indicate the structural similarity that exists between the enhanced and reference images defined as [170]:

$$SSIM(z, Z) = \frac{(2\mu_z\mu_Z + K_1)(2\rho_{zZ} + K_2)}{(\mu_z^2 + \mu_Z^2 + K_1)(\rho_z^2 + \rho_Z^2 + K_2)} \quad (2.8.12)$$

where μ_z and μ_Z denote the mean intensities, ρ_z and ρ_Z symbolize the contrast whereas K_1 and K_2 denote the constants. The image enhancement leads to the change in the image's structure, thus resulting in the reduction in the value of SSIM. Similarly, UIQI also indicates the amount of similarity and dissimilarity. It is computed by taking into account the three components while SSIM considered only one component. UIQI is computed by performing the comparison of two images on the basis of three components, that is, contrast $C(z,Z)$, luminance $L(z,Z)$, and structure $S(z,Z)$ as [171]:

$$UIQI = C(z,Z)L(z,Z)S(z,Z) = \frac{4\mu_z\mu_Z\mu_{zZ}}{(\mu_z^2 + \mu_Z^2)(\sigma_z^2 + \sigma_Z^2)} \quad (2.8.13)$$

Here, $C(z,Z) = \frac{2\sigma_z\sigma_Z}{(\sigma_z^2 + \sigma_Z^2)}$, $L(z,Z) = \frac{2\mu_z\mu_Z}{(\mu_z^2 + \mu_Z^2)}$, and $S(z,Z) = \frac{2\sigma_{zZ}}{(\sigma_z + \sigma_Z)}$, such that,

σ_z and σ_Z depict the standard deviation of reference and enhanced images, σ_{zZ} representing the covariance of both images whereas μ_z and μ_Z denote the mean intensities of reference and enhanced images. Moreover, CC can be used to determine the relation among two images in a precise form as [172], [173]:

$$CC = \frac{\sum_{i=1}^{Di} (x_i - \bar{x})(y_i - \bar{y})}{\sqrt{\sum_{i=1}^{Di} (x_i - \bar{x})^2 \sum_{i=1}^{Di} (y_i - \bar{y})^2}} \quad (2.8.14)$$

where x_i and y_i are the adjacent pixel values while Di is the sum of adjacent pixel pairs along each direction. GLCM parameters can also be utilized for evaluating the image enhancement techniques. GLCM is a matrix arrangement that provides several combinations of pixel values which shows the relationship among two spatially related pixels with regards to the distance between different directions [174]. It is usually formed by varying the distance among the pixels in a pair at the rotation offsets such as 0° , 45° , 90° , and 135° . The GLCM parameters such as contrast, correlation, energy, and homogeneity show texture enhancement. The contrast provides the intensity between the image pixel and its neighbor. If the pixel values are similar, it shows low contrast. Correlation indicates the relation between a pixel and its neighbor pixels. Energy depicts the uniformity in an image whereas homogeneity provides the closeness in the

spatial distribution of gray levels over the entire image. The decrease in correlation, homogeneity, and energy depicts more enhancement [141].

Hence, the aforementioned performance metrics are utilized for the assessment of presented work depending on the nature of the application.

2.9 Motivation

The comprehensive study of the available literature elucidates the fact that FODs are extensively used in the numerous applications of science and engineering. However, the detailed analysis of prevalent literature that employed FODs in various domains (spatial, FrFT, quaternion) particularly in signal and image processing is carried out in the presented work. Although optimization techniques and learning-based methods can be utilized for improving performance, they are computationally more expensive and usually preferred for large datasets [14], [49], [59], [90], [145]. Hence, the reported work is based on fractional-based methods. Moreover, the insightful concept of FrFT in combination with FODs explored in few research works [8]–[11] encouraged to consider this interesting notion. Nevertheless, the motivation behind the presented work of FODs in various domains for the signal and image processing applications is provided by Kumar *et al.* [10], [11], Singh *et al.* [9], Gao *et al.* [68], [75], [93], Tseng and Lee [95]. Most of these techniques are based on the RL, GL, and Caputo FODs that possess certain demerits of initial conditions and phase shifting due to the ideal frequency response of $(j\omega)^g$. These issues can be resolved by the RFOD as it is independent of initial conditions and provides the frequency response of $(\omega)^g$, thus, avoiding the issue of phase shifting [1], [95]. Hence, it motivated to carry out this research work by utilizing the RFOD in various domains.

Therefore, Kumar *et al.* [10] and Singh *et al.* [9] analyzing the RL and Caputo FOD in FrFTD and Tseng and Lee [95] exploring the RFOD in FT domain inspired to further analyze the RFOD in the FrFTD. Further, the study of Kumar *et al.* [11] employing GL in FrFTD, Gao *et al.* utilizing the GLFOD based on NIFD in [93] and quaternion based GLFOD in [68] and [75], Nandal *et al.* [92] employing the concept of FOC manifested the necessity to explore the several aspects of image processing that still needs improvement. For instance, the aforementioned techniques are generally used for edge detection, but Nandal *et al.* [92] also enhanced the contrast of edges along with detection. Hence, it inspired to develop RFOD based technique that successfully performs the task of edge detection as well as the enhancement of image features. Moreover, the unification of RFOD and FrFT does not exist

in the literature, hence, its applications can be discovered in image processing. In the case of color images, Gao *et al.* [68], [75], and Kothapalli *et al.* [72] further aroused the interest to perform analysis of RFOD based approach in the quaternion domain for edge detection to preserve information details as well as the correlation among color channels. Hence, a technique based on RFOD in the quaternion domain can be developed for color edge detection. In a similar manner, Amoako-Yirekyi *et al.* [124], [125] employing the RLFD further motivated to consider the effect of uncontrolled features in the proposed approach. Hence, it aroused interest to evaluate the performance of the technique against uncontrolled features such as varying illumination conditions, JPEG compression artifacts, and noise.

Hence, the intriguing notion of integrating RFOD with FrFT and quaternion domain is utilized to propose the techniques for signal and image processing applications. Thus, the inherent benefits of the above concepts improve their performance which is verified in both qualitative and quantitative manner. Moreover, the proposed approaches are also better than the learning-based methods which are computationally more complex and beneficial only in the case of very large datasets.

2.10 Research Gaps

Based on the thorough study of the rich literature, the following research gaps are explored:

- There is a scope of research in the analysis of FODs in the time or spatial, frequency, FrFT, and quaternion domain. The mathematical analysis can be carried out for the FODs in FrFTD.
- Some of the FODs used in image processing applications also result in the phase distortion. So, there is a scope to improvise the FOD based approaches to avoid the phase distortion.
- The problem of loss of information due to thick edges by first-order derivatives and sensitivity to noise by second-order derivatives is resolved by using FODs. However, in the presence of high-level noise, some of these operators tend to mistakenly detect fake edges. So, there is scope of improvement in the existing techniques.
- Even though noise is commonly considered by most of the existing approaches but JPEG compression artifacts and varying illumination conditions are not taken into consideration previously in the edge detection approaches.
- The fractional differentiation masks are used to avoid the deterioration in the performance of integer order differentiations for the enhancement of smooth regions in an image. Most

of these techniques ignored the uncontrolled features such as noise, compression artifacts, illumination effects, etc. So, there is scope to consider the effect of these uncontrolled features while enhancing the images.

- Most of the work reported in edge detection and image enhancement is in spatial domain. There is limited research done in the transform-based methods for these applications of image processing.
- A few techniques exist that utilized the concept of integrating FOD and FrFT but their applications in image processing are not commonly available in the literature. Therefore, FOD definitions can be considered in the FrFTD for image processing applications.
- The most of available literature focuses on edge detection and image enhancement in isolation. So, a new algorithm can be explored by combining both edge detection and image enhancement.

2.11 Research Objectives

On the basis of initial studies, comprehensive literature survey, and research gaps, the following objectives are proposed:

1. To study the fractional order derivative and their utilization in the fractional domains.
2. To propose the fractional order derivative for the edge detection of grayscale images.
3. To propose the fractional order derivative for the edge detection in color images.
4. To confirm the capability of the proposed schemes for the image enhancement.

2.12 Research Methodology

The key factor to accomplish the above research objectives is to conduct a thorough survey of the prevailing literature to garner the knowledge that assists in comprehending the fundamental concepts of the deemed area of study. The flowchart of the work carried out in this thesis is presented in Figure 2.2. Initially, the comprehensive study of the pre-requisite mathematical functions, fractional concepts in calculus, and transforms are studied especially in the area of signal and image processing. This in-depth analysis of the available literature in the field of FOD further aids to find the prospective solutions for the open research problems. The reported work emphasizes on analyzing the performance of FODs in various domains such as time or spatial, FT, FrFT, and quaternion domain for signal and image processing applications. Initially, the performance of FODs is explored in UM technique that provided superior results for RFOD. Hence, the mathematical analysis of RFOD is carried out in FrFTD whose efficacy is confirmed in the form of signal and image processing applications.

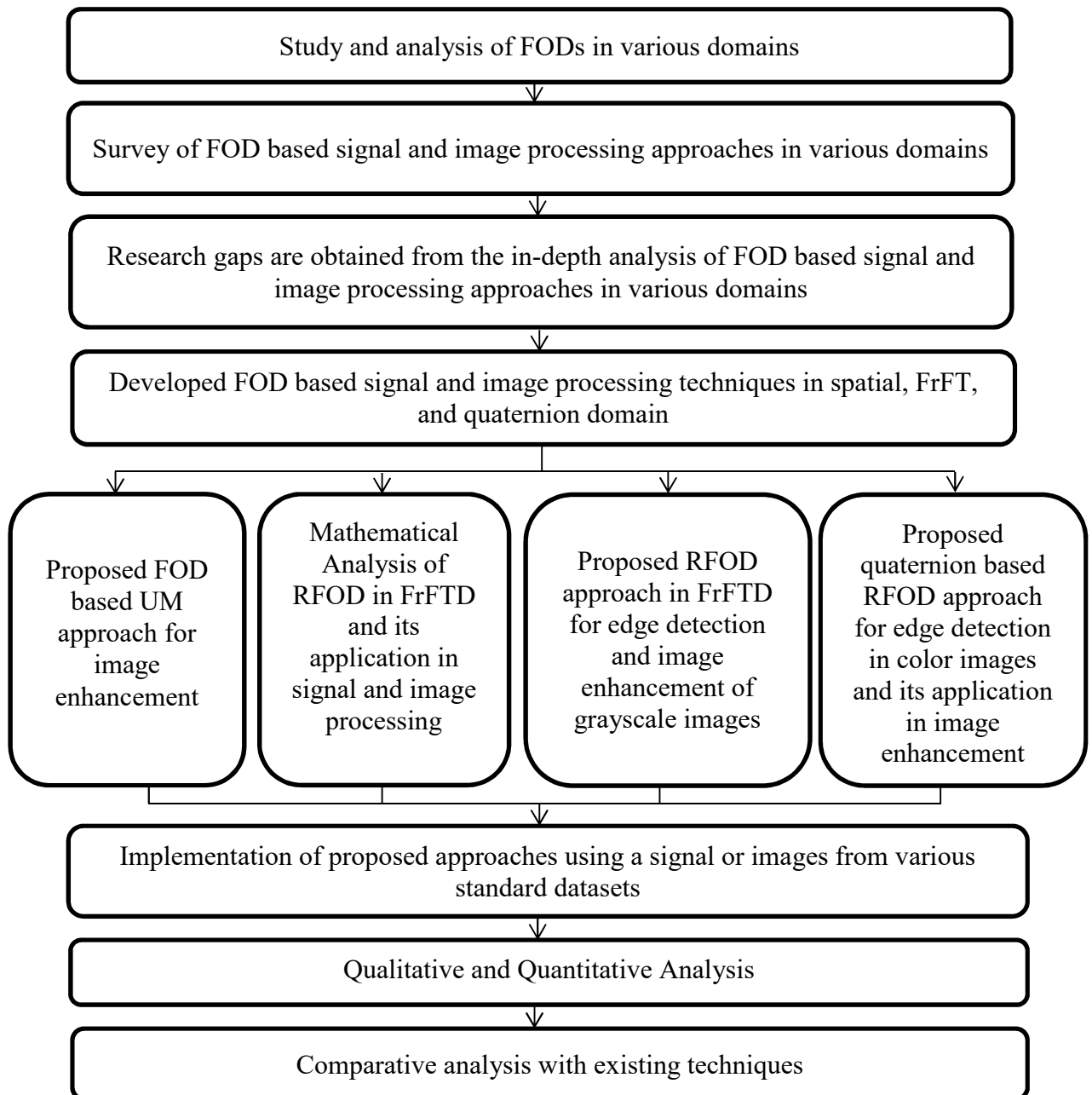


Figure 2.2: Flow chart of work done

Then, a mathematical framework is obtained for RFOD to conduct the experimentation. Consequently, the RFOD mask is constructed that is further used for potential applications in image processing. Further, the RFOD based edge detection methods are developed for grayscale and color images in FrFT and quaternion domain respectively. Subsequently, the proposed edge detection techniques are further extended to achieve image enhancement. The effectiveness of the aforementioned techniques is evaluated both qualitatively and quantitatively by considering the standard images from various datasets. The selection of the images used for the simulation is done on the basis of the nature of the application from different datasets such as USC-SIPI [175], LIVE [176], MATLAB in-built images, Classic 5,

BSD68, Set12 [177], RESIDE [178], Normalized Broadtz [179], BSDS300, BSDS500 [180], [181], TP-RDMM [182], VIP Illumination Saliency [183], and High Resolution Fundus (HRF) [184] shown in Appendix-I. Moreover, the performance metrics such as FOM, EPI, F-Score, IE, EME, AG, PSNR, EI, Number of Corners, CC, GLCM parameters, etc. are used for the quantitative analysis. The comparative analysis of the developed approaches is further performed against the classical edge detectors such as Prewitt, Sobel, Canny, etc., and other existing techniques for edge detection and image enhancement. The simulation of the proposed FOD based work is conducted on the platforms of Wolfram Mathematica and MATLAB (versions R2016a and R2017a) on a system having a configuration of Intel® CPU 2.7 GHz processor with 16 GB RAM and 8 GB RAM respectively.

FRACTIONAL ORDER DERIVATIVE BASED UNSHARP MASKING

The comprehensive study of the literature related to fractional calculus creates the necessity to further explore the applicability of FODs in the domain of image processing. In this chapter, the RL, GL, and Riesz FODs are incorporated in the UM approach for image enhancement. Besides sharpening of edges, the presented technique also preserved the low-frequency and medium-frequency details of an image. The extensive simulations conducted on several standard images demonstrated that the proposed approach yields better image visual quality than the existing ones. The potential of the proposed FOD based UM is further validated by confirming its performance against the uncontrolled feature of illumination conditions. Furthermore, its applicability in practical applications is determined from the Fundus images.

3.1 Improved UM based on FOD Approach

Image enhancement methods perform the task of smoothing the image irregularities with a slight change in the information. Additionally, its dynamic range is improved by sharpening the image features such as edges, texture, and contrast for easier detection [78]. Despite being capable of enhancing the images, the current UM approaches cannot preserve the image information. Therefore, the FODs are utilized in the CUM to preserve the information details while enhancing the image. FOD based UM approach is intended to achieve edge enhancement besides the improvement in image contrast and texture. Figure 3.1 shows the framework of the proposed FOD based UM approach. It utilizes both the Laplacian mask and FODs in the UM technique for detecting the gray level discontinuities (edges) present in the image that are considered in the existing techniques. Firstly, the convolution of an input image $z(i, j)$ is performed with the Laplacian masks (M_L) [21] given as:

$$\nabla^2 z = z(i+1, j-1) + z(i+1, j) + z(i+1, j+1) + z(i, j+1) + z(i, j-1) + z(i-1, j+1) + z(i-1, j) + z(i-1, j-1) - 8z(i, j) \tag{3.1.1}$$

$$\nabla^2 z = -z(i+1, j+1) - z(i+1, j) - z(i+1, j-1) - z(i, j+1) - z(i, j-1) - z(i-1, j+1) - z(i-1, j) - z(i-1, j-1) + 8z(i, j) \tag{3.1.2}$$

The outcome of this chapter is published as: K. Kaur, N. Jindal, and K. Singh, "Fractional Derivative based Unsharp Masking Approach for Enhancement of Digital Images," *Multimed. Tools Appl.*, vol. 80, no. 3, pp. 3645-3679, 2021.

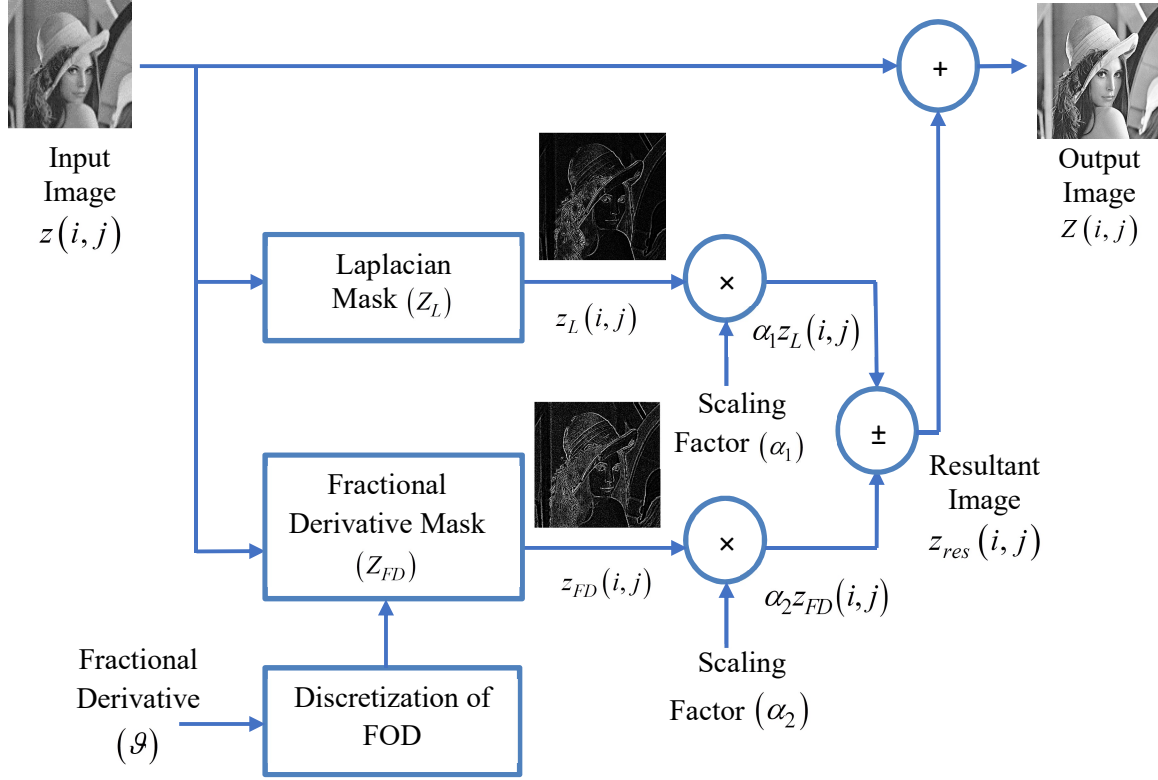


Figure 3.1: Framework of the proposed FOD based UM approach

In the same way, the convolution of an input image $z(i, j)$ is performed with the FOD mask (FM_{FD}) obtained from discretized mask coefficients from RL [94], [132], GL [94], and Riesz [49] FODs. By partitioning the interval 'a' to 't' in RL definition into n equal portions, the RL mask coefficients are obtained, such that n is very large given as [94], [132]:

$$\begin{aligned} \frac{\partial^g}{\partial i^g} z(i, j) \cong & \frac{z(i, j)}{\Gamma(2-g)} + \frac{1}{\Gamma(2-g)} \sum_{k=1}^{n-1} ((k+1)^{1-g} - 2(k)^{1-g} + (k-1)^{1-g}) z(i-k, j) \\ & + \frac{z(i-n, j)}{\Gamma(2-g)} ((n-1)^{1-g} - (n)^{1-g} + (1-g)n^{1-g}) \end{aligned} \quad (3.1.3)$$

$$\begin{aligned} \frac{\partial^g}{\partial j^g} z(i, j) \cong & \frac{z(i, j)}{\Gamma(2-g)} + \frac{1}{\Gamma(2-g)} \sum_{k=1}^{n-1} ((k+1)^{1-g} - 2(k)^{1-g} + (k-1)^{1-g}) z(i, j-k) \\ & + \frac{z(i, j-n)}{\Gamma(2-g)} ((n-1)^{1-g} - (n)^{1-g} + (1-g)n^{1-g}) \end{aligned} \quad (3.1.4)$$

when $k \rightarrow n = 2m - 1$, n is generally an odd number and the mask size is $(2m + 1) \times (2m + 1)$.

Likewise, GL mask coefficients are provided by [94]:

$$\begin{aligned}
\frac{\partial^{\mathcal{G}}}{\partial i^{\mathcal{G}}} z(i, j) &\cong \left(\frac{\mathcal{G}}{4} + \frac{\mathcal{G}^2}{8} \right) z(i+1, j) + \left(1 - \frac{\mathcal{G}^2}{2} - \frac{\mathcal{G}^3}{8} \right) z(i, j) + \frac{z(i-k, j)}{\Gamma(-\mathcal{G})} \sum_{k=1}^{n-2} \left[\frac{\Gamma(k+1-\mathcal{G})}{\Gamma(k+2)} \left(\frac{\mathcal{G}}{4} + \frac{\mathcal{G}^2}{8} \right) + \right. \\
&\quad \left. \frac{\Gamma(k-\mathcal{G})}{\Gamma(k+1)} \left(1 - \frac{\mathcal{G}^2}{4} \right) + \frac{\Gamma(k-1-\mathcal{G})}{\Gamma(k)} \left(-\frac{\mathcal{G}}{4} + \frac{\mathcal{G}^2}{8} \right) \right] \\
&\quad + \frac{z(i-n+1, j)}{\Gamma(-\mathcal{G})} \left[\frac{\Gamma(n-1-\mathcal{G})}{\Gamma(n)} \left(1 - \frac{\mathcal{G}^2}{4} \right) + \frac{\Gamma(n-2-\mathcal{G})}{\Gamma(k)} \left(-\frac{\mathcal{G}}{4} + \frac{\mathcal{G}^2}{8} \right) \right] + \\
&\quad \frac{\Gamma(n-\mathcal{G}-1)}{\Gamma(n)\Gamma(-\mathcal{G})} \left(-\frac{\mathcal{G}}{4} + \frac{\mathcal{G}^2}{8} \right) z(i-n, j)
\end{aligned} \tag{3.1.5}$$

$$\begin{aligned}
\frac{\partial^{\mathcal{G}}}{\partial j^{\mathcal{G}}} z(i, j) &\cong \left(\frac{\mathcal{G}}{4} + \frac{\mathcal{G}^2}{8} \right) z(i, j+1) + \left(1 - \frac{\mathcal{G}^2}{2} - \frac{\mathcal{G}^3}{8} \right) z(i, j) + \frac{z(i, j-k)}{\Gamma(-\mathcal{G})} \sum_{k=1}^{n-2} \left[\frac{\Gamma(k+1-\mathcal{G})}{\Gamma(k+2)} \left(\frac{\mathcal{G}}{4} + \frac{\mathcal{G}^2}{8} \right) + \right. \\
&\quad \left. \frac{\Gamma(k-\mathcal{G})}{\Gamma(k+1)} \left(1 - \frac{\mathcal{G}^2}{4} \right) + \frac{\Gamma(k-1-\mathcal{G})}{\Gamma(k)} \left(-\frac{\mathcal{G}}{4} + \frac{\mathcal{G}^2}{8} \right) \right] \\
&\quad + \frac{z(i, j-n+1)}{\Gamma(-\mathcal{G})} \left[\frac{\Gamma(n-1-\mathcal{G})}{\Gamma(n)} \left(1 - \frac{\mathcal{G}^2}{4} \right) + \frac{\Gamma(n-2-\mathcal{G})}{\Gamma(k)} \left(-\frac{\mathcal{G}}{4} + \frac{\mathcal{G}^2}{8} \right) \right] + \\
&\quad \frac{\Gamma(n-\mathcal{G}-1)}{\Gamma(n)\Gamma(-\mathcal{G})} \left(-\frac{\mathcal{G}}{4} + \frac{\mathcal{G}^2}{8} \right) z(i, j-n)
\end{aligned} \tag{3.1.6}$$

The proposed work considered the RFOD for $0 < \mathcal{G} < 1$. The Riesz mask coefficients are attained correspondingly as in the case of RL and GL fractional coefficients given as:

$$\begin{aligned}
\frac{\partial^{\mathcal{G}}}{\partial i^{\mathcal{G}}} z(i, j) &\cong \frac{2\Gamma(1+\mathcal{G})}{\left(\Gamma((\mathcal{G}/2)+1)\right)^2} \left(\frac{\mathcal{G}}{4} + \frac{\mathcal{G}^2}{8} \right) z(i+1, j) + \left(\frac{2\Gamma(1+\mathcal{G})}{\left(\Gamma((\mathcal{G}/2)+1)\right)^2} \left(1 - \frac{\mathcal{G}^2}{4} \right) - \right. \\
&\quad \left. \frac{2\Gamma(1+\mathcal{G})}{\Gamma(\mathcal{G}/2)\Gamma((\mathcal{G}/2)+2)} \left(\frac{\mathcal{G}}{4} + \frac{\mathcal{G}^2}{8} \right) \right) \\
&\quad z(i, j) + \dots + \left(\frac{(-1)^{n-1} 2\Gamma(1+\mathcal{G})}{\Gamma((\mathcal{G}/2)-n+2)\Gamma((\mathcal{G}/2)+n)} \left(-\frac{\mathcal{G}}{4} + \frac{\mathcal{G}^2}{8} \right) + \right. \\
&\quad \left. \frac{(-1)^n 2\Gamma(1+\mathcal{G})}{\Gamma((\mathcal{G}/2)-n+1)\Gamma((\mathcal{G}/2)+n+1)} \left(1 - \frac{\mathcal{G}^2}{4} \right) - \right. \\
&\quad \left. \frac{(-1)^{n+1} 2\Gamma(1+\mathcal{G})}{\Gamma((\mathcal{G}/2)+n+2)\Gamma((\mathcal{G}/2)-n)} \left(\frac{\mathcal{G}}{4} + \frac{\mathcal{G}^2}{8} \right) \right) z(i-n, j)
\end{aligned} \tag{3.1.7}$$

$$\begin{aligned}
\frac{\partial^g}{\partial j^g} z(i, j) &\cong \frac{2\Gamma(1+g)}{(\Gamma((g/2)+1))^2} \left(\frac{g}{4} + \frac{g^2}{8} \right) z(i, j+1) + \left(\frac{2\Gamma(1+g)}{(\Gamma((g/2)+1))^2} \left(1 - \frac{g^2}{4} \right) - \right. \\
&\quad \left. \frac{2\Gamma(1+g)}{\Gamma(g/2)\Gamma((g/2)+2)} \left(\frac{g}{4} + \frac{g^2}{8} \right) \right) \\
z(i, j) &+ \dots + \left(\frac{(-1)^{n-1} 2\Gamma(1+g)}{\Gamma((g/2)-n+2)\Gamma((g/2)+n)} \left(-\frac{g}{4} + \frac{g^2}{8} \right) + \right. \\
&\quad \frac{(-1)^n 2\Gamma(1+g)}{\Gamma((g/2)-n+1)\Gamma((g/2)+n+1)} \left(1 - \frac{g^2}{4} \right) - \\
&\quad \left. \frac{(-1)^{n+1} 2\Gamma(1+g)}{\Gamma((g/2)+n+2)\Gamma((g/2)-n)} \left(\frac{g}{4} + \frac{g^2}{8} \right) \right) z(i, j-n)
\end{aligned} \tag{3.1.8}$$

The isotropic mask invariant to the increment in the rotation of 45° [21] is used in the proposed technique. The scaling of resultant images $z_L(i, j)$ and $z_{FD}(i, j)$ attained after performing the convolution with FOD and Laplacian masks is done by the scaling factors of α_1 and α_2 , respectively. The range of these scaling factors is 0.2-0.7 [78]. The Laplacian mask deemphasizes the gradually varying regions of an image while emphasizing the image edges, so, the scaling factor α_1 is considered to be less than α_2 in the simulation work. Therefore, the scaled images are either subtracted or added on the basis of center coefficient of the Laplacian mask defined in (3.1.1) and (3.1.2). The scaled image will be subtracted if its center coefficient is negative as in (3.1.1), otherwise it will be added [21]. After scaling, the obtained resultant image is provided by:

$$z_{res}(i, j) = \alpha_1 z_L(i, j) \pm \alpha_2 z_{FD}(i, j) \tag{3.1.9}$$

The enhanced image $Z(i, j)$ is obtained by adding the resultant image $z_{res}(i, j)$ to the input image as:

$$Z(i, j) = z_{res}(i, j) + z(i, j) \tag{3.1.10}$$

Thus, the sharpened images are obtained with the proposed approach by combining the Laplacian and FOD masks. The pseudo-code of the proposed FOD based UM algorithm is as follows:

Pseudo-code of the proposed technique

Inputs: $z, \vartheta, \alpha_1, \alpha_2$; **Output:** Z z : Test Image; ϑ : Fractional order of derivative; α_1, α_2 : Scaling factors $FM_{RL}(\)$: RLFOD mask $FM_{GL}(\)$: GLFOD mask $FM_R(\)$: Riesz FOD mask $Z_L(\)$: Laplacian mask**start** $Z_{RL} = FM_{RL}(\vartheta), Z_{GL} = FM_{GL}(\vartheta), Z_R = FM_R(\vartheta)$; $z_{RL} = Z_{RL}(z)$ or $z_{GL} = Z_{GL}(z)$ or $z_R = Z_R(z)$; $z_L = Z_L(z)$; $z_{res} = \alpha_2 z_{RL} \pm \alpha_1 z_L$ or $z_{res} = \alpha_2 z_{GL} \pm \alpha_1 z_L$ or $z_{res} = \alpha_2 z_R \pm \alpha_1 z_L$; $Z = z + z_{res}$;**end**

3.2 Performance Analysis of FOD based UM Approach

The proficiency of the proposed FOD based UM approach is confirmed both qualitatively and quantitatively by taking into account the standard grayscale images of Lena, Surface, Moon, Baboon, Barbara, Pirate, Vase, Bridge, Lighthouse, Truck, Airplane, Bark, and Wall from USC-SIPI [175], LIVE [176], BSD68, Set12 [177] datasets. Moreover, the proposed approach is compared against the existing image enhancement approaches, such as CUM [21], Unsharp Masking Filter Kernel and Gain using PSO (UMKG) [83], MHE [80], Contrast Enhancement using Exposure Fusion (CEEF) [185], UMHE [84], Riesz based enhancement (Riesz) [49], RUM [140], and Modified GL (Mod GL) [141]. Initially, the effect of various masks in the proposed approach is examined in the following sub-section.

3.2.1 Effect of Various Masks in UM

The proposed approach utilized various masks in the UM approach. Therefore, the Lena and Barbara images are taken into consideration for investigating the effect of each mask in the UM approach. Figure 3.2 and Figure 3.3 demonstrate the edge information extracted for Lena and Barbara images by the RL, GL, Riesz, and Laplacian masks.



Laplacian



RL



GL

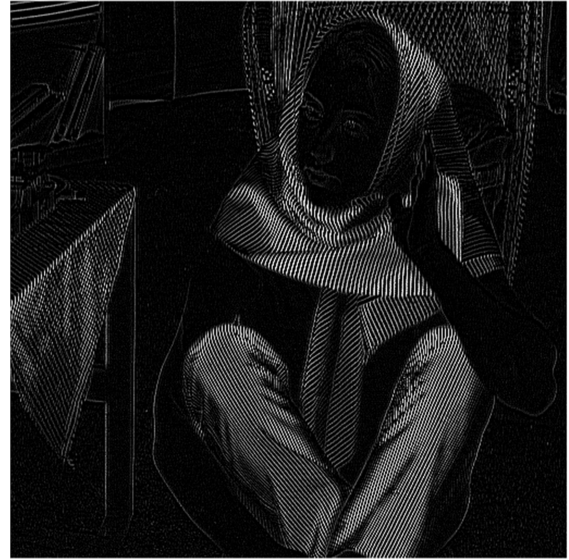


Riesz

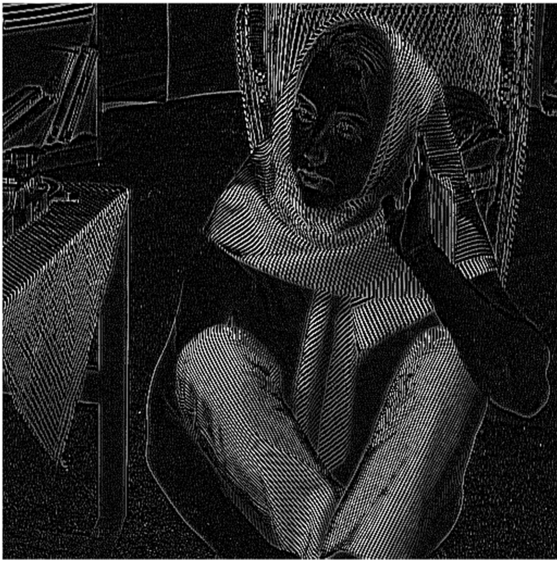
Figure 3.2: Edge information obtained by various masks for Lena image (256×256)



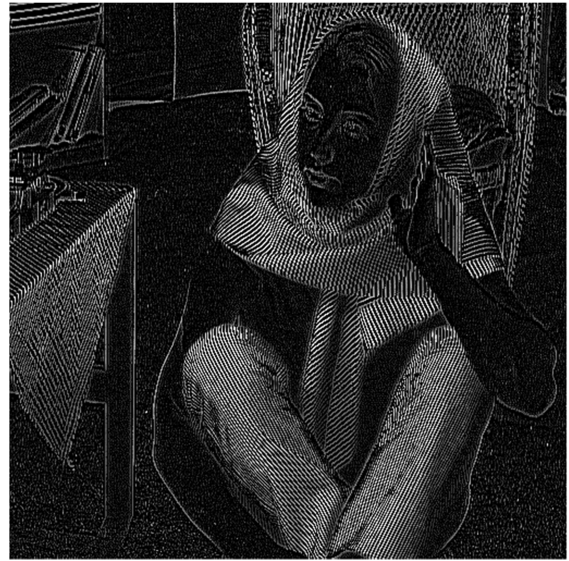
Laplacian



RL



GL



Riesz

Figure 3.3: Edge information obtained by various masks for Barbara image (512×512)

It is perceived that GL and Riesz FOD extracted more information for both Lena and Barbara images. The edge information thus obtained is further used for image enhancement. Additionally, the contribution of the considered masks in the UM technique is assessed both qualitatively and quantitatively. The visual effect of the Laplacian mask with scaling factor of

α_1 and fractional derivative masks with the scaling factor of α_2 in the image enhancement is shown in Figure 3.4 and Figure 3.5.



Laplacian



RL



GL



Riesz

Figure 3.4: Lena image (256×256) enhanced by using various masks in UM



Laplacian



RL



GL



Riesz

Figure 3.5: Barbara image (512×512) enhanced by using various masks in UM

It is perceived that the edges, contrast, and texture are enhanced by the FOD masks besides the sharpening of fine details by the Laplacian mask. However, GL and Riesz FOD masks provided more enhancement than other masks. Table 3.1 provided the quantitative analysis based on various assessment metrics.

Table 3.1: Performance metrics for various FOD and Laplacian masks in UM

Images	Lena				Barbara			
Mask/ Metrics	Laplacian	RL	GL	Riesz	Laplacian	RL	GL	Riesz
IE	7.6068	7.6383	7.6678	7.6678	7.5979	7.7197	7.7525	7.7556
AG	10.2281	9.1449	12.1188	12.1190	12.8985	12.3259	15.9843	16.3559
SSIM	0.9236	0.9627	0.8566	0.8566	0.9172	0.9324	0.8132	0.7946
EME	11.6497	8.2607	11.7118	11.7120	12.2666	9.7718	12.2506	12.4987
CC	0.9864	0.9994	0.9904	0.9904	0.9718	0.9967	0.9714	0.9706
Contrast	1.0240	0.8360	1.2921	1.2922	1.8299	1.5873	2.3775	2.4431
Corr- elation	0.8086	0.8714	0.8065	0.8065	0.6486	0.7681	0.6473	0.6412
Energy	0.0836	0.0797	0.0638	0.0638	0.0659	0.0620	0.0476	0.0460
Homo- geneity	0.7915	0.8168	0.7609	0.7609	0.7435	0.7687	0.7092	0.7015

Bold indicates the optimum values

It is evident that the performance parameters are almost similar for both GL and Riesz FOD masks for the Lena image, but the RFOD mask obtained better quantitative results for the Barbara image.

3.3 Simulation Results for Test Images of Standard Datasets

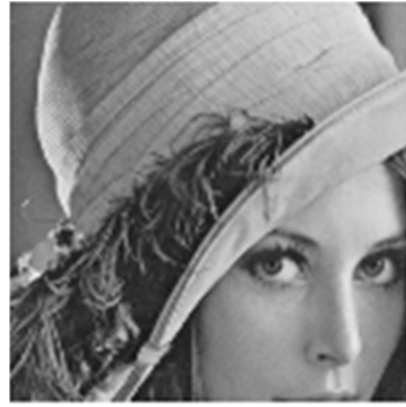
Both qualitative and quantitative analysis is conducted on the test images from standard datasets for confirming the capability of the presented FOD based UM technique. After carrying out the intensive simulations, the scaling factors α_1 and α_2 are considered to be 0.2 and 0.21-0.35 respectively in the proposed approach. However, the fractional orders are varied from 0 to 1 for implementing the proposed approach. It is perceived that superior performance is obtained by RL, GL, and Riesz FOD for the fractional orders in the range 0.4-0.5, 0.72-0.96, and 0.53-0.95 respectively.

3.3.1 Qualitative Performance Analysis

The qualitative comparative analysis between the proposed and existing approaches is done on the basis of enhanced images. The adequacy of the proposed FOD based UM approach is validated by the scaled version of the Lena image of size 256×256 which provides a better interpretation of the results as compared to existing techniques along with its zoomed portion as shown in Figure 3.6.



CUM [21]



CUM [21] (Zoomed)



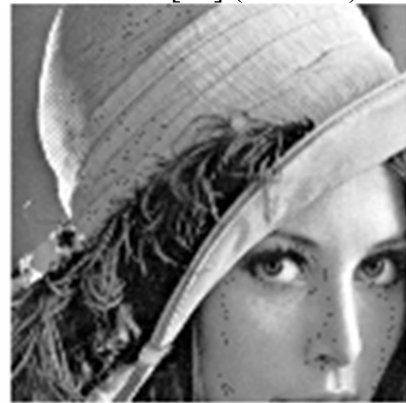
UMKG [83]



UMKG [83] (Zoomed)



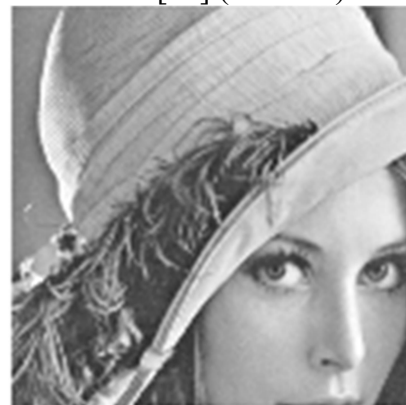
MHE [80]



MHE [80] (Zoomed)



CEEF [185]



CEEF [185] (Zoomed)

Figure 3.6: Enhanced Lena image (256×256) and its zoomed portion obtained by various techniques (contd.)



UMHE [84]



UMHE [84] (Zoomed)



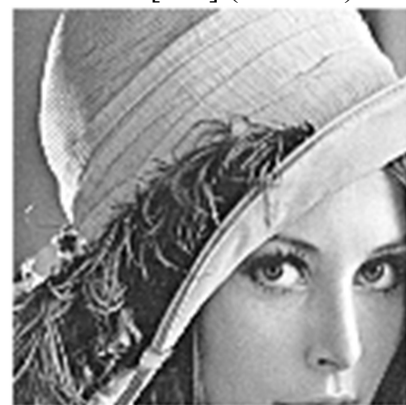
RUM [140]



RUM [140] (Zoomed)



Riesz [49]



Riesz [49] (Zoomed)



Mod GL [141]



Mod GL [141] (Zoomed)

Figure 3.6: Enhanced Lena image (256×256) and its zoomed portion obtained by various techniques (contd.)



RL ($\mathcal{G} = 0.43$)



RL ($\mathcal{G} = 0.43$) (Zoomed)



GL ($\mathcal{G} = 0.83$)



GL ($\mathcal{G} = 0.83$) (Zoomed)



Riesz ($\mathcal{G} = 0.71$)



Riesz ($\mathcal{G} = 0.71$) (Zoomed)

Figure 3.6: Enhanced Lena image (256×256) and its zoomed portion obtained by various techniques

It can be figured out from the enhanced images of Lena and its zoomed portion that a better texture and contrast is provided by the proposed approach in addition to the sharp edges because it utilized the merits of FODs and the Laplacian mask as described in Section 2.2. Moreover, the simulation results for some of the other test images along with their zoomed portion are also demonstrated in Figure 3.7.

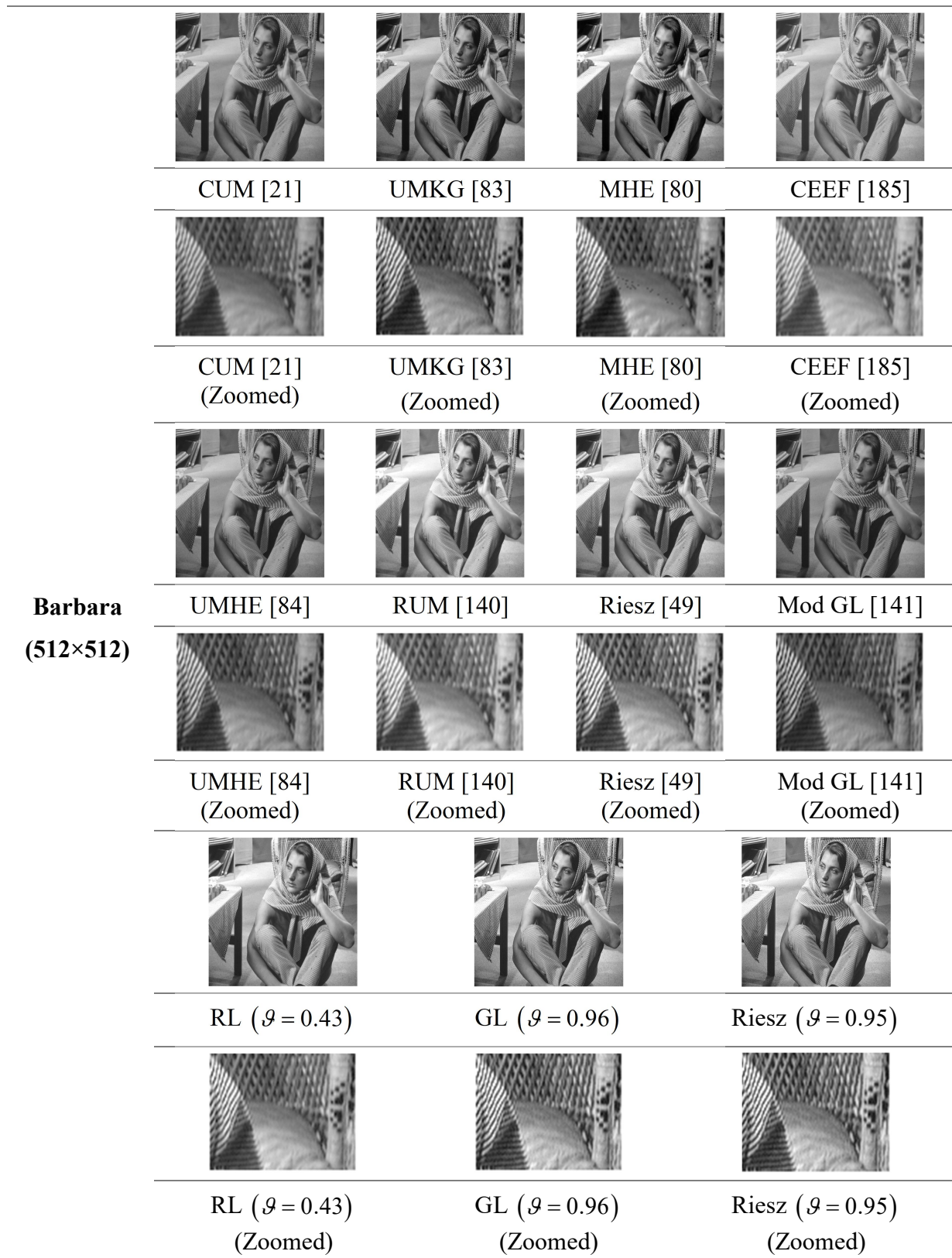


Figure 3.7: Enhanced test images along with its zoomed portion (contd.)

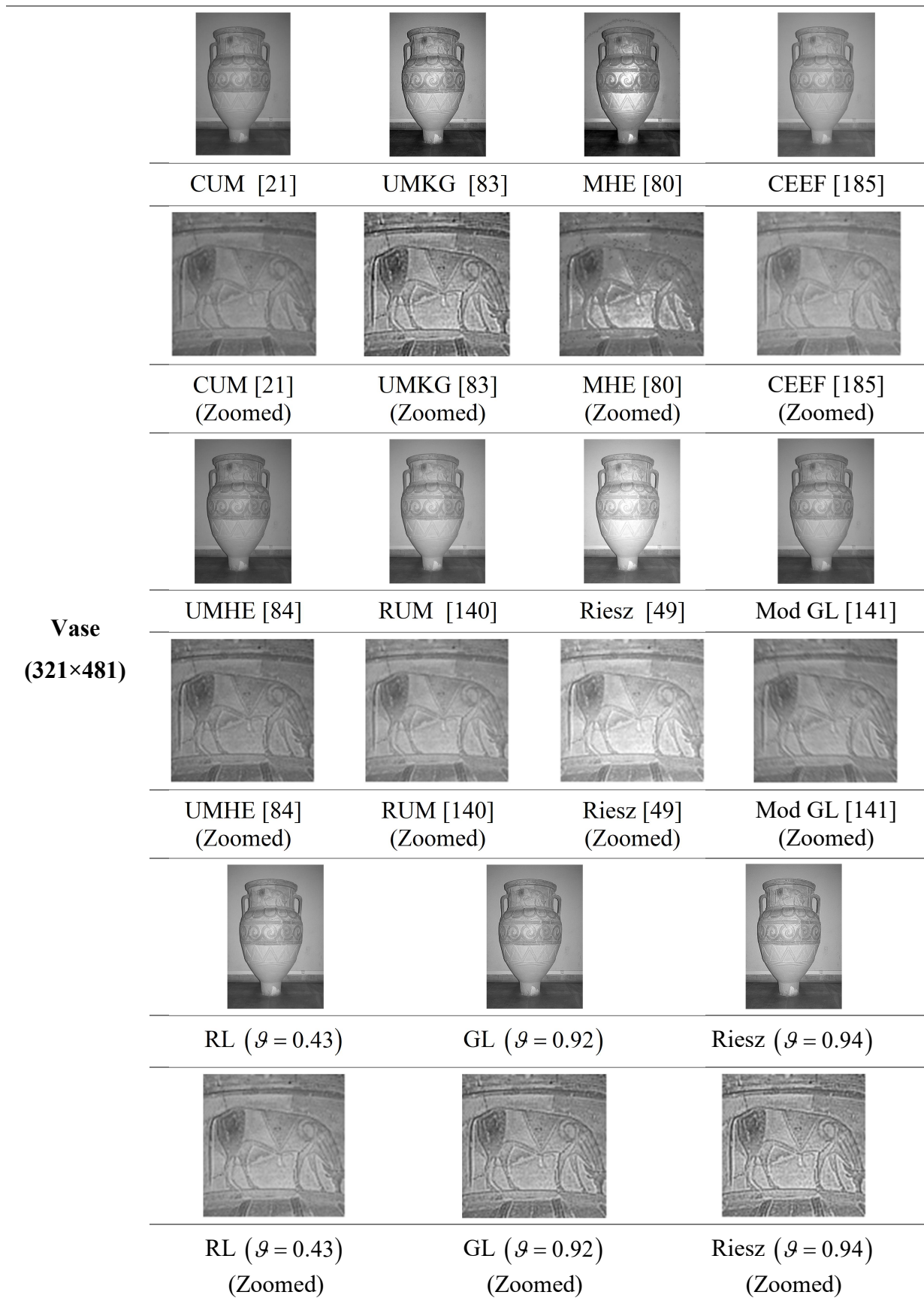


Figure 3.7: Enhanced test images along with its zoomed portion (contd.)



Figure 3.7: Enhanced test images along with its zoomed portion

The proposed approach enhanced the features of an image, thus, improving the minute details present in the image. Moreover, the improvement in the visual quality of an image by the presented technique against the existing ones is evident from the zoomed portion of the images. The zoomed portion in the case of a chair in Barbara and animal in Vase demonstrated the improvement in contrast and sharpened edges. Moreover, the texture of the sleeve in the Pirate image is also improved along with the improvement in contrast of the image. Therefore, it is worth noting that the benefits of FODs in UM can be exploited to retain the low-frequency components while enhancing the medium and high-frequency components (Section 2.2). It also provided the superiority of RFOD over the RL and GL FODs in the form of image visual quality. Furthermore, the visual comparison of the presented FOD based UM technique against the other enhancement approaches confirmed that RFOD can be efficiently used in UM to enhance the images.

3.3.2 Quantitative Performance Analysis

Besides the qualitative analysis, the proposed approach is also assessed quantitatively by taking into consideration various performance metrics. Some of the prevailing studies only performed the visual comparison of the image enhancement methods, but the presented technique is evaluated by various assessment parameters that are utilized by few existing techniques. Hence, the proposed FOD based UM approach is subjected to evaluation on the basis of performance parameters such as IE, AG, SSIM, CC, EME, and GLCM based contrast, correlation, energy, and homogeneity parameters. The widely used parameters of IE and AG are considered for confirming the capability of the proposed FOD based UM approach to preserve its details along with the enhancement of image details as compared to state-of-the-art existing image enhancement schemes. Table 3.2 shows IE and AG of the standard images of different sizes that are enhanced by the various image enhancement approaches.

Table 3.2: IE and AG for the test images enhanced by various techniques

Metrics	Images	Lena	Surface	Moon	Baboon	Barbara	Pirate	Bridge	Lighthouse	Vase	Truck	Airplane	Bark	Wall	
IE	Original Image	7.4429	6.8554	6.7093	7.3579	7.4664	7.2367	7.7056	7.4486	6.7188	6.0274	4.0045	7.3250	6.7990	
	CUM [21]	7.6019	7.0484	6.8392	7.6305	7.6286	7.4177	7.7936	7.6528	6.8113	6.6873	5.5424	7.5101	7.0348	
	UMKG [83]	7.7340	7.0427	7.1469	7.7350	7.7476	7.5952	7.7782	7.6413	7.1480	6.8817	5.5282	7.5659	7.1160	
	MHE [80]	7.3971	6.7430	6.6048	7.2891	7.4191	7.1981	5.7025	7.3676	6.6714	5.9905	3.9918	7.2642	6.7255	
	CEEF [185]	7.4504	6.9157	6.6759	7.3474	7.4778	7.2887	7.6385	7.4763	6.6949	6.5411	5.1954	7.3311	6.7187	
	UMHE [84]	7.4492	6.9213	6.7148	7.3689	7.4696	7.2407	7.7064	7.4751	6.7660	6.1638	4.1203	7.4137	6.9260	
	RUM [140]	7.6627	7.2030	7.0614	7.6793	7.7226	7.5193	7.6992	7.6017	7.0198	6.9945	5.5734	7.6060	7.1011	
	Riesz [49]	7.7402	7.3009	7.1775	7.7636	7.7606	7.5982	7.8044	7.6554	7.0367	7.0559	5.5953	7.6032	7.1915	
	Mod GL [141]	7.5705	6.8579	7.0195	7.4420	7.6494	7.3303	7.5192	7.5545	6.9139	6.6018	5.5219	7.3852	6.9093	
	Proposed Mask	RL	7.7124	7.1918	7.1172	7.7583	7.7743	7.5886	7.7444	7.4552	7.0547	6.7594	5.6157	7.6261	7.1363
		GL	7.7430	7.3899	7.3447	7.8314	7.8121	7.6770	7.8048	7.6805	7.1423	7.1443	6.0204	7.6267	7.2846
		Riesz	7.7430	7.4055	7.3796	7.8337	7.8143	7.6838	7.8054	7.6831	7.1563	7.1701	6.0482	7.6268	7.2974
	AG	Original Image	7.1832	9.8775	5.6510	12.9654	8.4663	6.1580	10.5495	9.3854	2.9082	5.0927	2.3261	15.1307	9.6338
		CUM [21]	10.1148	13.9778	8.5587	19.8053	12.8607	8.6520	15.3283	13.7442	4.3479	7.2589	3.5418	20.1894	13.8782
UMKG [83]		9.7550	13.5236	14.1615	21.2802	12.9902	8.4069	13.7734	12.5901	5.7275	8.7137	4.4196	22.3644	15.6894	
MHE [80]		9.7029	15.6769	9.9463	17.9893	11.0631	8.8596	11.3089	11.9738	5.6955	9.9063	5.5000	19.5522	14.3319	
CEEF [185]		7.7851	10.7423	6.0477	13.9961	9.1745	6.7007	11.6497	10.2298	3.1572	5.7193	2.3878	15.9436	10.0062	
UMHE [84]		8.2435	11.2205	7.3756	16.8518	10.9919	7.4775	13.1917	11.7389	3.6689	6.8054	3.2327	18.0087	12.0076	
RUM [140]		9.2005	12.9771	9.6091	17.4212	11.1771	7.9639	13.1646	11.5873	3.9129	7.6722	3.3993	20.5395	13.7864	
Riesz [49]		11.4619	16.1438	10.0408	22.5941	14.5820	9.8343	16.9300	14.9444	5.0799	8.8718	4.0282	22.6908	15.8666	
Mod GL [141]		8.6481	10.6957	6.8945	15.4728	10.8475	7.2562	12.5553	11.3056	3.9051	6.1215	3.2989	17.5507	11.5641	
Proposed Mask		RL	10.3526	14.3920	9.5849	20.3441	13.4656	9.1319	15.1605	13.3052	4.5374	7.4417	3.9212	21.8454	14.6374
		GL	13.4054	19.5904	16.2569	26.4310	17.9710	13.0988	18.3029	17.3601	5.7050	12.1634	6.4669	22.8274	20.2767
		Riesz	13.4056	20.0435	17.2708	26.8313	18.3447	13.5690	18.7373	17.7846	5.7365	12.7377	6.8296	22.8298	20.8273

Bold indicates the maximum values

It is ascertained that RFOD based UM approach achieved high IE and AG as compared to the existing approaches as it can preserve the image information details without causing any blurriness distortion (Section 2.2.4). In the case of Lena and Bark images, the assessment metrics are nearly equivalent for both GL and Riesz FODs, but for the most of considered images, RFOD provided better enhancement. However, the SSIM parameter is also considered in Table 3.3 to perform the comparison of various techniques with respect to the corresponding original image.

Table 3.3: SSIM for the test images enhanced by various techniques

Images	CUM [21]	UMKG [83]	MHE [80]	CEEF [185]	UMHE [84]	RUM [140]	Riesz [49]	Mod GL [141]	Proposed Mask		
									RL	GL	Riesz
Lena	0.9522	0.9464	0.9016	0.9653	0.9889	0.9658	0.9040	0.9198	0.9337	0.8164	0.8164
Surface	0.9477	0.9536	0.8550	0.9730	0.9897	0.9266	0.8353	0.9300	0.9238	0.7830	0.7687
Moon	0.9287	0.6749	0.7852	0.9772	0.9656	0.9332	0.8105	0.8827	0.8575	0.5996	0.5680
Baboon	0.9218	0.8797	0.8923	0.9729	0.9646	0.9409	0.8572	0.8845	0.8964	0.7447	0.7315
Barbara	0.9454	0.9328	0.9061	0.9649	0.9757	0.9431	0.8923	0.9204	0.9131	0.7722	0.7541
Pirate	0.9553	0.8487	0.8434	0.9586	0.9819	0.9606	0.9046	0.9197	0.9236	0.7708	0.7499
Bridge	0.9357	0.9597	0.9437	0.9571	0.9723	0.9695	0.8909	0.8981	0.9153	0.8396	0.8275
Light-house	0.9372	0.9524	0.9225	0.9499	0.9737	0.9752	0.8947	0.9031	0.9212	0.7935	0.7777
Vase	0.9658	0.8177	0.8164	0.9660	0.9863	0.9613	0.9231	0.8930	0.9395	0.8330	0.8154
Truck	0.9510	0.8730	0.7811	0.9552	0.9797	0.8920	0.8379	0.9236	0.9254	0.7156	0.6902
Airplane	0.9698	0.8985	0.7183	0.9918	0.9862	0.9661	0.9393	0.9340	0.9235	0.7477	0.7181
Bark	0.9442	0.9133	0.9266	0.9811	0.9793	0.9405	0.9077	0.9188	0.9181	0.9013	0.9012
Wall	0.9255	0.8711	0.8733	0.9834	0.9659	0.9267	0.8600	0.8899	0.8900	0.7192	0.7034

Bold indicates the minimum values

As compared to existing approaches, the proposed approach possessed minimum SSIM because the enhancement by FODs results in the modification of the image structure after the enhancement than the original image. Hence, the SSIM is less in the proposed approach because it is the measure of similarity between the two images. Moreover, the image enhancement obtained by various techniques is also computed based on EME and CC in Table 3.4 that indicates the measure of enhancement and correlation with respect to the corresponding original image.

Table 3.4: EME and CC for the test images enhanced by various techniques

Metrics	Images	Lena	Surface	Moon	Baboon	Barbara	Pirate	Bridge	Light-house	Vase	Truck	Airplane	Bark	Wall	
EME	Original Image	7.5988	10.3999	5.6932	12.2243	8.1969	6.4943	12.1201	9.6102	2.3419	6.6122	1.6193	13.6070	6.9450	
	CUM [21]	11.7998	13.6099	8.4424	19.8341	13.1465	9.5625	17.1966	14.6467	3.7508	9.9246	2.5960	19.6062	11.2758	
	UMKG [83]	15.0852	15.0332	15.5824	20.8231	15.1627	17.0639	17.5844	14.3140	4.3283	10.4002	3.8532	20.3739	14.2894	
	MHE [80]	15.1044	13.6749	11.4027	20.4840	13.6365	14.8360	13.3870	16.1355	4.3267	12.6531	4.3201	19.8707	14.1761	
	CEEF [185]	6.3135	8.8243	4.9540	10.1591	7.0782	5.5084	10.2776	8.0082	2.0341	5.0606	1.5653	11.4004	6.3368	
	UMHE [84]	9.0491	11.4365	7.4565	16.5744	11.2084	8.1253	15.9569	12.6556	3.1166	7.8054	2.4025	17.1136	9.9690	
	RUM [140]	8.5352	10.2131	5.9942	13.1132	8.6970	7.0631	13.9294	11.0921	2.6029	6.6151	2.2921	16.5749	10.2075	
	Riesz [49]	11.8629	11.5805	7.0382	19.2651	12.7210	11.1024	18.4133	16.3762	3.7957	9.5920	3.4561	19.7857	13.8666	
	Mod GL [141]	8.1587	11.0271	7.6288	16.7104	11.3461	8.9307	16.2904	13.5217	3.6673	8.1539	2.6254	16.8317	10.2836	
	Proposed Mask	RL	12.6626	12.1952	9.6925	18.1780	11.9893	12.4099	15.9541	13.0294	3.2317	7.6330	2.5117	19.4110	10.6477
		GL	15.4038	16.0958	14.7492	22.1086	15.4760	16.7491	18.9212	16.7967	4.3291	12.4151	4.2976	19.3108	14.3951
		Riesz	15.4040	16.3562	15.5915	22.2685	15.7269	17.0796	19.1939	17.0478	4.3305	12.8309	4.4810	20.4127	14.5965
	CC	CUM [21]	0.9905	0.9828	0.9860	0.9756	0.9823	0.9934	0.9882	0.9874	0.9936	0.9897	0.9910	0.9859	0.9823
		UMKG [83]	0.9983	0.9832	0.9598	0.9736	0.9906	0.9995	0.9931	0.9929	0.9795	0.9942	0.9865	0.9823	0.9810
MHE [80]		0.9923	0.9754	0.9643	0.9886	0.9915	0.9900	0.9837	0.9839	0.9764	0.9536	0.9584	0.9886	0.9801	
CEEF [185]		0.9968	0.9975	0.9963	0.9945	0.9964	0.9965	0.9929	0.9932	0.9970	0.9936	0.9947	0.9972	0.9937	
UMHE [84]		0.9961	0.9933	0.9941	0.9892	0.9920	0.9967	0.9944	0.9947	0.9978	0.9956	0.9956	0.9947	0.9921	
RUM [140]		0.9992	0.9957	0.9972	0.9989	0.9990	0.9996	0.9977	0.9982	0.9997	0.9995	0.9972	0.9963	0.9940	
Riesz [49]		0.9904	0.9824	0.9869	0.9733	0.9853	0.9948	0.9794	0.9768	0.9930	0.9969	0.9802	0.9814	0.9794	
Mod GL [141]		0.9876	0.9685	0.9776	0.9617	0.9749	0.9901	0.9816	0.9806	0.9866	0.9802	0.9818	0.9839	0.9695	
Proposed Mask		RL	0.9960	0.9904	0.9901	0.9882	0.9907	0.9972	0.9912	0.9920	0.9972	0.9973	0.9958	0.9941	0.9900
		GL	0.9840	0.9567	0.9414	0.9571	0.9671	0.9815	0.9788	0.9740	0.9788	0.9596	0.9620	0.9813	0.9598
		Riesz	0.9840	0.9529	0.9296	0.9542	0.9649	0.9791	0.9767	0.9717	0.9756	0.9532	0.9581	0.9812	0.9546

Bold indicates the optimum values

It is ascertained that maximum EME and minimum CC are achieved by the proposed FOD based UM approach as compared to the existing ones because the FODs provide better enhancement in terms of features of the image. The enhancement of contrast, texture, and edges by the proposed approach resulted in maximum EME. Therefore, images enhanced by the FODs are not similar to the original image. Hence, the CC value is minimum for the proposed approach based on RFOD as compared to the existing ones. Furthermore, the competency of image enhancement is established from the GLCM parameters such as contrast, correlation, energy, and homogeneity. The experimentation is done by considering the rotation offsets of 0° , 45° , 90° , and 135° , but here, the results of only that rotation offset are reported which provided maximum enhancement. Hence, the GLCM parameters namely contrast, correlation, energy, and homogeneity are depicted in Table 3.5 and Table 3.6 for the rotation offsets that provided better performance. It is discerned that RFOD usually provided more contrast and minimum energy, correlation, and homogeneity at rotation offset of 45° and 135° , thus, providing superior performance than the existing techniques. This is because of the improvement in contrast and textural details at different rotation offsets. Hence, it is also confirmed from the quantitative analysis that the proposed RFOD approach in UM technique provided superior results than existing techniques.

3.4 Simulation Results for Images with Variation in Illumination Conditions

The test images c1, c2, c3, c4, statue1, statue2, statue3, statue4, and statue5 with variation in the illumination conditions for the same scene obtained from VIP Illumination Saliency Dataset [183] are considered for validating the robustness of the proposed approach. Its performance analysis is conducted in both qualitative and quantitative manner in the subsequent sections.

3.4.1 Qualitative Performance Analysis

This section is oriented to visually analyze the proposed FOD based UM approach by comparing them with the existing techniques on the basis of test images with variation in the illumination conditions. Figure 3.8 illustrates the simulation results of the various enhancement approaches for some of the test images with variation in illumination conditions.

Table 3.5: GLCM based contrast and correlation measure for the test images enhanced by various techniques with rotation offset

Metrics	Images	Lena		Surface		Moon		Baboon		Barbara		Pirate		Bridge		Light-house		Vase		Truck		Airplane		Bark		Wall		
		135°	45°	45°	45°	45°	45°	45°	45°	45°	45°	45°	45°	45°	45°	45°	45°	45°	45°	45°	45°	45°	45°	45°	45°	45°	45°	45°
	Rotation Offset	135°	45°	45°	45°	45°	45°	45°	45°	45°	45°	45°	45°	45°	45°	45°	45°	45°	45°	45°	45°	45°	45°	45°	45°	45°	45°	45°
	Original Image	0.5413	0.6845	0.3276	1.1407	0.8133	0.3644	0.7406	0.8853	0.1781	0.2842	0.1638	1.1531	0.6500														
	CUM [21]	1.0631	1.2671	0.6079	2.6729	1.9496	0.6775	1.5118	1.7575	0.3242	0.4752	0.2870	2.1548	1.2629														
	UMKG [83]	0.9781	1.2422	1.5098	3.0223	1.9144	0.5951	1.2581	1.5074	0.4250	0.7761	0.5294	2.4548	1.5703														
	MHE [80]	0.8991	1.5981	0.7901	1.9661	1.2692	0.6365	0.8121	1.1274	0.4311	0.7093	0.3170	1.7160	1.3023														
	CEEF [185]	0.6287	0.7858	0.3597	1.3038	0.9243	0.4255	0.8680	0.9277	0.1980	0.3327	0.1813	1.2858	0.7178														
Contrast	UMHE [84]	0.7181	0.9777	0.4825	1.9616	1.4403	0.5160	1.1561	1.3450	0.2513	0.3913	0.2237	1.6689	0.9743														
	RUM [140]	0.8369	1.0401	0.4836	1.9773	1.2961	0.5583	1.1169	1.2531	0.2553	0.4806	0.2694	2.2591	1.1832														
	Riesz [49]	1.2992	1.5343	0.7312	3.4066	2.2760	0.8202	1.8943	2.1027	0.4290	0.6243	0.4035	2.5574	1.6384														
	Mod GL [141]	0.8588	0.7689	0.4409	1.5810	1.4815	0.5906	1.3027	1.4053	0.3135	0.4117	0.2173	1.8398	1.0676														
	RL	1.0645	1.2984	0.7122	2.7650	1.9769	0.7111	1.2829	1.5714	0.3308	0.4804	0.3901	2.3326	1.3846														
	GL	1.5949	2.1943	1.7362	4.3480	3.1243	1.3031	2.1507	2.3572	0.4318	1.1120	0.6311	2.5617	2.5226														
	Riesz	1.5950	2.2652	1.9138	4.4344	3.1970	1.3689	2.2404	2.4248	0.4329	1.2003	0.6598	2.5624	2.6377														
	Rotation Offset	135°	45°	45°	45°	45°	45°	45°	45°	45°	45°	45°	45°	45°	45°	45°	45°	45°	45°	45°	45°	45°	45°	45°	45°	45°	45°	45°
	Original Image	0.8823	0.6172	0.7984	0.6853	0.8155	0.9177	0.8738	0.8476	0.9192	0.8274	0.8433	0.7422	0.6956														
	CUM [21]	0.7954	0.4660	0.6782	0.4745	0.6337	0.8583	0.7764	0.7358	0.8602	0.7425	0.7436	0.6237	0.5557														
	UMKG [83]	0.8532	0.4334	0.4872	0.4926	0.7079	0.9113	0.8060	0.7664	0.8546	0.7798	0.6986	0.6144	0.5474														
	MHE [80]	0.8758	0.6211	0.8015	0.6988	0.8215	0.9212	0.8709	0.8432	0.9104	0.8169	0.8564	0.7398	0.7145														
	CEEF [185]	0.8582	0.6006	0.7834	0.6339	0.7983	0.8961	0.8401	0.8118	0.9004	0.8090	0.8109	0.7680	0.6702														
	UMHE [84]	0.8495	0.5258	0.7264	0.5518	0.7055	0.8871	0.8189	0.7848	0.8886	0.7764	0.7896	0.6712	0.6057														
	RUM [140]	0.8687	0.6311	0.8144	0.6559	0.8128	0.9163	0.8402	0.8151	0.9134	0.8396	0.8039	0.6705	0.6287														
	Riesz [49]	0.8064	0.5620	0.7737	0.4766	0.6795	0.8810	0.7363	0.6927	0.8543	0.8192	0.6851	0.6150	0.5453														
	Mod GL [141]	0.8191	0.5736	0.7335	0.5135	0.7507	0.8587	0.7748	0.7542	0.8934	0.7693	0.7734	0.6576	0.5457														
	RL	0.8442	0.5445	0.7471	0.5706	0.7218	0.8998	0.8121	0.7919	0.8888	0.7985	0.8109	0.6790	0.6115														
	GL	0.7785	0.3941	0.5174	0.4314	0.6065	0.8274	0.7432	0.7004	0.8549	0.6463	0.6953	0.6175	0.4838														
	Riesz	0.7785	0.3850	0.4862	0.4237	0.5997	0.8197	0.7340	0.6921	0.8528	0.6259	0.6833	0.6174	0.4687														

Bold indicates the optimum values

Table 3.6: GLCM based energy and homogeneity measure for the test images enhanced by various techniques with rotation offset

Metrics	Images	Lena		Surface Moon		Baboon		Barbara		Pirate		Bridge		Light-house		Vase		Truck		Airplane		Bark		Wall					
		135°	45°	45°	135°	135°	45°	45°	135°	135°	45°	45°	135°	135°	45°	45°	135°	135°	45°	45°	135°	135°	45°	45°	135°	135°			
Energy	Rotation Offset	135°	45°	45°	135°	135°	45°	45°	135°	135°	45°	45°	135°	135°	45°	45°	135°	135°	45°	45°	135°	135°	45°	45°	135°	135°			
	Original Image	0.1089	0.1637	0.2230	0.0737	0.0885	0.1199	0.0663	0.0894	0.2171	0.2075	0.6188	0.0734	0.1695	CUM [21]	0.0864	0.1166	0.1603	0.0467	0.0676	0.0994	0.0455	0.0668	0.1847	0.1629	0.5981	0.0542	0.1144	
	UMKG [83]	0.0759	0.1201	0.0889	0.0403	0.0575	0.0914	0.0505	0.0708	0.1588	0.1323	0.4035	0.0526	0.0898	MHE [80]	0.0874	0.1321	0.1336	0.0486	0.0706	0.0832	0.0615	0.0649	0.1503	0.1383	0.4452	0.0521	0.1191	
	CEEF [185]	0.1076	0.1418	0.2156	0.0748	0.0838	0.1161	0.0623	0.0884	0.2263	0.1989	0.6199	0.0768	0.1745	UMHE [84]	0.1004	0.1369	0.1819	0.0556	0.0751	0.1090	0.0528	0.0752	0.1983	0.1765	0.6144	0.0612	0.1348	
	RUM [140]	0.0827	0.1019	0.1403	0.0466	0.0632	0.0851	0.0507	0.0720	0.1756	0.1536	0.6468	0.0530	0.1058	Riesz [49]	0.0724	0.0744	0.1013	0.0382	0.0576	0.0754	0.0403	0.0632	0.1651	0.1308	0.6951	0.0521	0.0880	
	Mod GL [141]	0.0918	0.1532	0.1801	0.0620	0.0639	0.1053	0.0507	0.0751	0.1684	0.2173	0.7056	0.0590	0.1138	RL	0.0749	0.0958	0.1144	0.0407	0.0592	0.0783	0.0446	0.0722	0.1631	0.1515	0.4110	0.0555	0.1020	
	Proposed Mask	GL	0.0591	0.0624	0.0625	0.0289	0.0434	0.0604	0.0370	0.0535	0.1474	0.0950	0.3330	0.0517	0.0683	Riesz	0.0591	0.0599	0.0575	0.0283	0.0419	0.0587	0.0361	0.0517	0.1461	0.0898	0.3251	0.0517	0.0658
	Rotation Offset	135°	45°	45°	135°	135°	45°	45°	135°	135°	45°	45°	135°	135°	45°	45°	135°	135°	45°	45°	135°	135°	45°	45°	135°	135°			
	Original Image	0.8520	0.7871	0.8602	0.7303	0.8115	0.8716	0.7731	0.7953	0.9218	0.8721	0.9478	0.6932	0.7845	CUM [21]	0.7991	0.7205	0.7896	0.6409	0.7494	0.8239	0.6971	0.7284	0.8963	0.8167	0.9264	0.6232	0.7005	
	UMKG [83]	0.8039	0.7245	0.6621	0.6241	0.7516	0.8356	0.7178	0.7414	0.8916	0.7438	0.8912	0.6166	0.6746	MHE [80]	0.8070	0.7200	0.7823	0.6728	0.7842	0.8299	0.7594	0.7580	0.8731	0.7795	0.9108	0.6458	0.7211	
CEEF [185]	0.8399	0.7696	0.8510	0.7200	0.8035	0.8543	0.7556	0.7860	0.9157	0.8559	0.9419	0.6838	0.7751	UMHE [84]	0.8319	0.7509	0.8166	0.6734	0.7727	0.8458	0.7268	0.7538	0.9009	0.8368	0.9363	0.6513	0.7338		
RUM [140]	0.8203	0.7364	0.8180	0.6730	0.7819	0.8390	0.7316	0.7525	0.9053	0.8183	0.9248	0.6168	0.7106	Riesz [49]	0.7848	0.6889	0.7609	0.6155	0.7431	0.8059	0.6734	0.7064	0.8651	0.7306	0.9150	0.6247	0.6713		
Mod GL [141]	0.8647	0.7780	0.8173	0.6900	0.7644	0.8230	0.6985	0.7397	0.8996	0.8446	0.9403	0.6218	0.6961	RL	0.7997	0.7127	0.7722	0.6385	0.7565	0.8188	0.7038	0.7563	0.8869	0.8203	0.8986	0.6256	0.7015		
Proposed Mask	GL	0.7425	0.6305	0.6393	0.5623	0.6889	0.7473	0.6572	0.6880	0.8671	0.7139	0.8416	0.6094	0.6094	Riesz	0.7425	0.6235	0.6218	0.5566	0.6811	0.7389	0.6506	0.6804	0.8659	0.7017	0.8333	0.6161	0.6007	

Bold indicates the minimum values

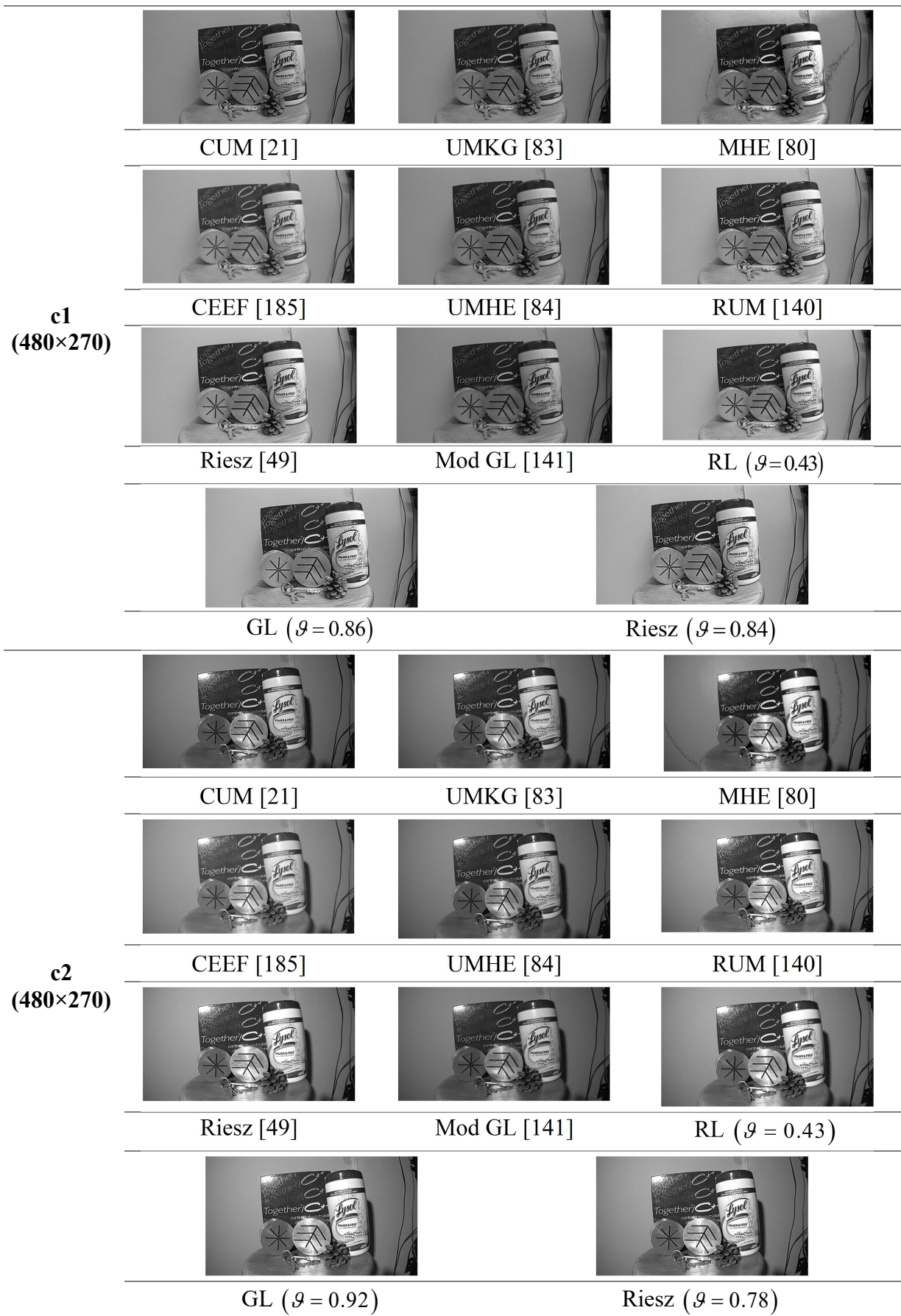


Figure 3.8: Simulated results for test images with variation in illumination conditions (contd.)

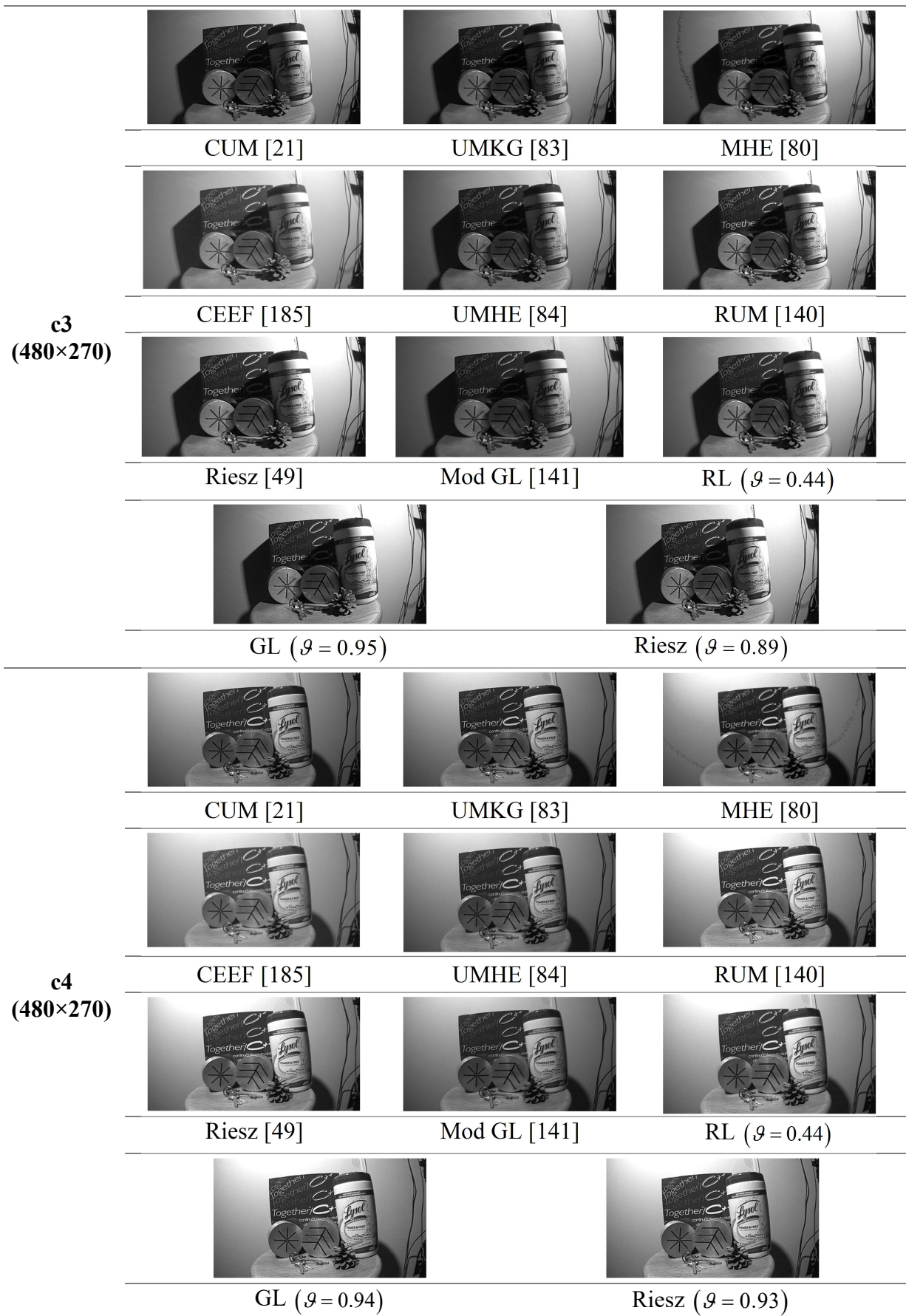


Figure 3.8: Simulated results for test images with variation in illumination conditions

Images enhanced by the presented approach provided improved features in terms of contrast and edges as the FODs in combination with the Laplacian mask are able to enhance the edges and contrast of the images as described in Section 2.2. The images enhanced by MHE [80] are distorted while the CEEF [185] approach provides better contrast only in the case of images with darker regions as seen from Figure 3.8. The proposed approach enhanced the images with bad illumination but some of the existing techniques provided better enhancement as they tend to improve the contrast in such images. For instance, in the case of c3 image, the non-uniform lighting conditions affected the images enhanced by the various techniques. The proposed FOD based UM technique is not able to preserve the other end of the electrical wire case on the wall in c3 image. Therefore, it is required to preserve the image details that are non-uniformly illuminated during enhancement. Nevertheless, upon comparing the proposed approach to most of the existing image enhancement techniques, the former provided more clarity.

3.4.2 Quantitative Performance Analysis

After performing the qualitative analysis of images with variation in illumination conditions, the proposed FOD based approach is also assessed quantitatively from some assessment parameters as utilized for confirming the adequacy of the proposed FOD based UM approach with respect to existing methods in Section 3.3.2. In a similar manner, IE and AG are computed in Table 3.7 to comprehend the capability of the proposed FOD based UM technique for images with variation in illumination conditions in terms of the information content in enhanced image and clarity of an image after enhancement. Moreover, Table 3.8 shows SSIM and EME that measures the degree of similarity with the original image and amount of enhancement attained by the various image enhancement approaches respectively for images with variation in illumination conditions for the same scene obtained from the VIP Illumination Saliency Dataset [183].

Table 3.7: IE and AG for the test images with variation in illumination conditions

Metrics	Images	c1	c2	c3	c4	Statue1	Statue2	Statue3	Statue4	Statue5	
IE	Original Image	6.8656	7.2828	7.6681	7.6124	5.8162	3.1571	3.5082	6.4032	6.0852	
	CUM [21]	6.9567	7.3646	7.7117	7.6730	5.9727	3.2604	3.6021	6.5399	6.2073	
	UMKG [83]	6.9295	7.3500	7.7065	7.6933	6.4304	3.4829	4.3358	7.0501	6.4221	
	MHE [80]	6.7968	7.2077	7.6049	7.5408	5.7574	2.3821	3.4963	6.3534	6.0225	
	CEEF [185]	6.8872	7.3133	7.7150	7.6077	5.9435	4.5093	4.1593	6.5832	6.2708	
	UMHE [84]	6.8944	7.3005	7.6833	7.6307	5.8816	3.1942	3.5386	6.4629	6.1312	
	RUM [140]	7.2159	7.5184	7.6554	7.6942	6.0548	3.3845	3.6588	6.6255	6.3053	
	Riesz [49]	7.2214	7.5275	7.6623	7.6958	6.3519	3.6394	3.8472	6.8583	6.4500	
	Mod GL [141]	6.8585	7.2630	7.6374	7.5969	5.9865	3.2011	3.7613	6.5584	6.2706	
	Proposed Mask	RL	7.2482	7.5395	7.7239	7.7188	6.2176	3.5449	3.8172	6.8207	6.3791
		GL	7.3315	7.5823	7.7446	7.7582	6.4570	3.7049	4.0187	7.0531	6.6292
		Riesz	7.3394	7.5855	7.7475	7.7610	6.4722	3.7248	4.0214	7.0533	6.6327
	AG	Original Image	4.8922	5.3054	4.3333	4.5952	1.6986	0.7439	0.4910	1.4625	1.1803
		CUM [21]	6.9662	7.4790	5.9146	6.3044	2.3059	0.9851	0.6485	1.9042	1.5332
UMKG [83]		5.9452	6.6486	4.9712	6.3687	3.5525	1.3043	1.9359	3.1576	1.8609	
MHE [80]		6.9149	7.0140	4.9764	5.5882	3.7144	1.2684	2.5492	3.0120	2.3210	
CEEF [185]		5.6086	5.9707	5.2074	5.2710	1.9402	2.7633	0.5459	1.5963	1.2784	
UMHE [84]		5.9574	6.4251	5.0897	5.4238	1.9876	0.8517	0.5610	1.6691	1.3453	
RUM [140]		7.9777	8.3608	6.7608	7.3240	2.1682	0.9653	0.6217	1.8775	1.4705	
Riesz [49]		8.0361	8.3850	6.6241	7.1430	2.8733	1.2261	0.8022	2.3208	1.7724	
Mod GL [141]		5.5198	5.6407	5.0197	5.3994	2.0797	0.8450	0.6269	1.7540	1.4171	
Proposed Mask		RL	7.6023	7.7205	5.9956	6.5958	2.5995	1.1594	0.8032	2.2256	1.6923
		GL	10.2221	9.7472	7.6539	8.7000	3.9158	1.6358	1.3181	3.3128	2.5593
		Riesz	10.5028	9.8397	7.8478	8.9233	4.1052	1.6987	1.3429	3.4829	2.6040

Bold indicates the maximum values

Table 3-8: SSIM and EME for the test images with variation in illumination conditions

Metrics	Images	c1	c2	c3	c4	Statue1	Statue2	Statue3	Statue4	Statue5
SSIM	CUM [21]	0.9703	0.9705	0.9748	0.9732	0.9855	0.9948	0.9955	0.9893	0.9913
	UMKG [83]	0.9890	0.9844	0.9830	0.9640	0.8959	0.9777	0.8768	0.8653	0.9726
	MHE [80]	0.9055	0.9381	0.9599	0.9467	0.7249	0.9217	0.8010	0.8550	0.8554
	CEEF [185]	0.9600	0.9464	0.8928	0.9470	0.9585	0.1821	0.9672	0.9605	0.9583
	UMHE [84]	0.9888	0.9888	0.9912	0.9905	0.9949	0.9983	0.9985	0.9964	0.9971
	RUM [140]	0.9223	0.9230	0.9222	0.9198	0.9792	0.9891	0.9864	0.9746	0.9663
	Riesz [49]	0.9245	0.9249	0.9291	0.9281	0.9033	0.9527	0.9463	0.9331	0.9216
	Mod GL [141]	0.9316	0.9292	0.9342	0.9293	0.9728	0.9917	0.9889	0.9770	0.9823
	RL	0.9335	0.9478	0.9569	0.9480	0.9479	0.9628	0.9457	0.9467	0.9479
	GL	0.8400	0.8763	0.8955	0.8670	0.8763	0.9289	0.9053	0.8791	0.8930
Proposed Mask	Riesz	0.8264	0.8651	0.8856	0.8549	0.8647	0.9225	0.9032	0.8668	0.8898
EME	Original Image	5.2500	5.3946	6.7071	5.5139	2.3513	8.1896	0.4874	1.7264	1.5170
	CUM [21]	7.1696	7.7754	9.9952	8.2238	3.4529	8.4911	0.6792	2.4268	2.0935
	UMKG [83]	9.0606	9.2444	10.4768	9.4898	5.1552	12.3055	2.6180	5.0436	2.8835
	MHE [80]	9.4122	8.6193	9.2369	7.4810	5.2666	8.5678	2.5298	5.1203	4.0251
	CEEF [185]	5.4020	4.9861	5.3447	4.4659	1.8818	4.6696	0.4084	1.3976	1.2193
	UMHE [84]	8.2744	7.9521	8.8185	7.0041	2.9338	7.9181	0.5856	2.0748	1.7955
	RUM [140]	6.7490	6.3195	7.0841	5.6553	2.6037	10.2455	0.5433	1.8343	1.5577
	Riesz [49]	6.4548	6.5376	7.4965	5.8816	2.8908	9.9433	0.6188	2.1279	1.7377
	Mod GL [141]	5.1858	5.2425	6.6055	5.4043	3.5095	10.2878	0.7566	2.5700	2.1783
	Proposed Mask	RL	7.4952	7.8284	9.5123	7.3737	3.1115	9.3336	0.6168	3.1907
GL	9.5228	9.6635	11.7741	9.4088	5.1271	14.5363	1.1119	5.1170	2.9153	
Riesz	9.7008	9.8397	12.0103	9.5803	5.3089	14.9533	1.1363	5.1274	2.9639	

Bold indicates the maximum values

It is ascertained that excluding the dark and foggy images, the proposed approach performed better than the existing approaches. SSIM is minimum for MHE [80] and CEEF [185] in some images as these approaches either drastically change the enhanced images owing to distortion or increase the contrast of an image. Besides, it is noticed that the statue images enhanced by MHE [80] are mostly distorted, but the CEEF [185] approach enhanced the image contrast. Table 3.9 illustrates CC for test images with variation in illumination conditions for the same scene that indicate the correlation with respect to the original images.

Table 3.9: CC for the test images with variation in illumination conditions

Images	CUM [21]	UMKG [83]	MHE [80]	CEEF [185]	UMHE [84]	RUM [140]	Riesz [49]	Mod GL [141]	Proposed Mask		
									RL	GL	Riesz
c1	0.9893	0.9968	0.9865	0.9963	0.9961	0.9989	0.9928	0.9889	0.9956	0.9793	0.9772
c2	0.9887	0.9941	0.9909	0.9933	0.9956	0.9958	0.9898	0.9868	0.9930	0.9810	0.9796
c3	0.9963	0.9994	0.9975	0.9899	0.9979	0.9966	0.9943	0.9957	0.9967	0.9888	0.9886
c4	0.9948	0.9948	0.9962	0.9937	0.9973	0.9978	0.9946	0.9937	0.9975	0.9927	0.9879
Statue1	0.9978	0.9960	0.9403	0.9973	0.9993	0.9998	0.9994	0.9966	0.9991	0.9772	0.9737
Statue2	0.9919	0.9764	0.9924	0.9334	0.9972	0.9989	0.9951	0.9903	0.9958	0.9861	0.9798
Statue3	0.9974	0.9943	0.9385	0.9971	0.9992	0.9996	0.9988	0.9938	0.9987	0.9898	0.9891
Statue4	0.9987	0.9969	0.9623	0.9984	0.9996	0.9999	0.9995	0.9977	0.9994	0.9945	0.9935
Statue5	0.9989	0.9970	0.9596	0.9972	0.9997	0.9919	0.9795	0.9982	0.9878	0.9829	0.9826

Bold indicates the minimum values

CC is minimum in some images because the enhanced images are entirely different from the original images due to distortion by MHE [80] and improvement in contrast by CEEF [185] as in the case of the SSIM parameter. Moreover, the ability of the proposed FOD based UM technique to enhance the images with variation in illumination conditions for the same scene is also confirmed by considering the GLCM based contrast, correlation, energy, and homogeneity parameters as shown in Table 3.10 and Table 3.11 for the rotation offsets that provided maximum enhancement.

Table 3.10: GLCM based contrast and correlation for the test images with variation in illumination conditions

Metrics	Images	c1	c2	c3	c4	Statue1	Statue2	Statue3	Statue4	Statue5
	Rotation Offset	135°	135°	135°	135°	45°	135°	135°	45°	45°
	Original Image	0.4514	0.4850	0.3140	0.3519	0.0846	0.0234	0.0301	0.0926	0.0647
	CUM [21]	0.8585	0.9638	0.5818	0.6674	0.1486	0.0372	0.0470	0.1384	0.0980
	UMKG [83]	0.6628	0.7996	0.4160	0.6983	0.3026	0.0567	0.1500	0.2657	0.1431
	MHE [80]	0.7588	0.7866	0.3713	0.4637	0.2296	0.0267	0.1570	0.2092	0.1576
	CEEF [185]	0.5800	0.6057	0.4106	0.4307	0.1008	0.1628	0.0171	0.0929	0.0737
	UMHE [84]	0.6713	0.7418	0.4499	0.5036	0.1159	0.0314	0.0360	0.1156	0.0819
	RUM [140]	1.1055	1.1308	0.7370	0.8513	0.1393	0.0334	0.0278	0.1125	0.0926
	Riesz [49]	1.1086	1.1787	0.7289	0.8390	0.2231	0.0501	0.0322	0.1797	0.1197
	Mod GL [141]	0.5038	0.5479	0.4309	0.4978	0.1515	0.0285	0.0446	0.1173	0.0987
Proposed Mask	RL	0.9673	1.0210	0.5917	0.7068	0.2067	0.0442	0.0326	0.1516	0.1090
	GL	1.5883	1.4387	0.8957	1.1175	0.4200	0.0774	0.0764	0.3065	0.2324
	Riesz	1.6408	1.4739	0.9250	1.1479	0.4451	0.0820	0.0794	0.3302	0.2379
	Rotation Offset	135°	135°	135°	135°	45°	135°	135°	45°	45°
	Original Image	0.8701	0.8632	0.9558	0.9344	0.9679	0.8320	0.9419	0.9720	0.9794
	CUM [21]	0.7789	0.7601	0.9213	0.8827	0.9449	0.7636	0.9132	0.9584	0.9690
	UMKG [83]	0.8229	0.7914	0.9433	0.8800	0.9424	0.7072	0.8807	0.9535	0.9536
	MHE [80]	0.8569	0.8503	0.9570	0.9346	0.9609	0.8142	0.9451	0.9668	0.9726
	CEEF [185]	0.8484	0.8349	0.9382	0.9131	0.9591	0.8716	0.9537	0.9655	0.9734
	UMHE [84]	0.8175	0.8039	0.9378	0.9086	0.9564	0.7882	0.9317	0.9651	0.9740
	RUM [140]	0.7989	0.7911	0.9271	0.8933	0.9659	0.8271	0.8988	0.9754	0.9767
	Riesz [49]	0.8048	0.7903	0.9283	0.8955	0.9593	0.8224	0.9145	0.9664	0.9725
	Mod GL [141]	0.7507	0.7369	0.9131	0.8609	0.9464	0.7639	0.8223	0.9605	0.9644
Proposed Mask	RL	0.8301	0.8087	0.9387	0.9101	0.9553	0.8220	0.9145	0.9705	0.9742
	GL	0.7408	0.7435	0.9094	0.8627	0.9114	0.7371	0.8232	0.9416	0.9462
	Riesz	0.7344	0.7366	0.9065	0.8591	0.9064	0.7285	0.8180	0.9373	0.9449

Bold indicates the optimum value

Table 3.11: GLCM based energy and homogeneity for the test images with variation in illumination conditions

Metrics	Images	c1	c2	c3	c4	Statue1	Statue2	Statue3	Statue4	Statue5
	Rotation Offset	135°	135°	135°	135°	45°	135°	135°	45°	45°
	Original Image	0.2108	0.1639	0.1097	0.1207	0.5028	0.9407	0.4940	0.2314	0.2919
	CUM [21]	0.1956	0.1475	0.1015	0.1075	0.4943	0.9377	0.4798	0.2228	0.2846
	UMKG [83]	0.1979	0.1544	0.1098	0.1038	0.2936	0.9313	0.4815	0.1654	0.2712
	MHE [80]	0.1472	0.1449	0.1043	0.1068	0.2894	0.9389	0.2150	0.1508	0.1947
	CEEF [185]	0.1956	0.1633	0.1013	0.1225	0.5035	0.4182	0.6241	0.2783	0.2790
	UMHE [84]	0.2025	0.1550	0.1050	0.1140	0.4986	0.9393	0.4895	0.2271	0.2880
	RUM [140]	0.1622	0.1163	0.0826	0.0865	0.4249	0.9337	0.7002	0.2064	0.2536
	Riesz [49]	0.1826	0.1160	0.0838	0.0875	0.4115	0.9247	0.6465	0.1906	0.2680
	Mod GL [141]	0.1548	0.1698	0.1095	0.1127	0.4461	0.9428	0.8418	0.2666	0.2891
	RL	0.1889	0.1204	0.0886	0.0910	0.2918	0.9286	0.6960	0.1850	0.2139
	GL	0.1487	0.1154	0.0799	0.0860	0.2703	0.9215	0.6818	0.1620	0.1935
	Riesz	0.1460	0.1132	0.0776	0.0855	0.2679	0.9202	0.6879	0.1507	0.1928
	Rotation Offset	135°	135°	135°	135°	45°	135°	135°	45°	45°
	Original Image	0.8982	0.9017	0.9104	0.9064	0.9651	0.9930	0.9850	0.9602	0.9728
	CUM [21]	0.8699	0.8726	0.8870	0.8794	0.9520	0.9911	0.9769	0.9477	0.9647
	UMKG [83]	0.8801	0.8820	0.9012	0.8744	0.9112	0.9883	0.9413	0.9050	0.9554
	MHE [80]	0.8727	0.8796	0.9034	0.8902	0.9151	0.9918	0.9319	0.9305	0.9495
	CEEF [185]	0.8812	0.8895	0.8971	0.8965	0.9606	0.9367	0.9915	0.9606	0.9690
	UMHE [84]	0.8821	0.8857	0.8977	0.8928	0.9580	0.9921	0.9821	0.9542	0.9684
	RUM [140]	0.8588	0.8535	0.8734	0.8654	0.9481	0.9913	0.9863	0.9578	0.9641
	Riesz [49]	0.8683	0.8570	0.8769	0.8681	0.9318	0.9886	0.9847	0.9389	0.9604
	Mod GL [141]	0.8669	0.8794	0.8858	0.8804	0.9426	0.9923	0.9781	0.9534	0.9608
	RL	0.8742	0.8629	0.8880	0.8783	0.9296	0.9897	0.9845	0.9497	0.9638
	GL	0.8344	0.8277	0.8574	0.8400	0.8919	0.9852	0.9697	0.9152	0.9346
	Riesz	0.8298	0.8229	0.8540	0.8396	0.8879	0.9846	0.9688	0.9042	0.9334

Bold indicates the minimum value

Ostensibly, excluding the dark and foggy images, the proposed approach provides better results for GLCM parameters than the existing approaches. However, on considering all performance metrics, the proposed approach seems to provide superior performance for the majority of images with variation in illumination conditions than the existing techniques.

3.5 Comparative Analysis

The average performance parameters are utilized for performing the comparative analysis of the proposed FOD based UM approach with respect to the original image, CUM [21], UMKG [83], MHE [80], CEEF [185], UMHE [84], RUM [140], Riesz [49], and Mod GL [141] for the considered test images of various datasets in Figure 3.9. RL (P), GL (P), and Riesz (P) signifies Proposed RL, GL, and Riesz in the below figures due to space constraints.

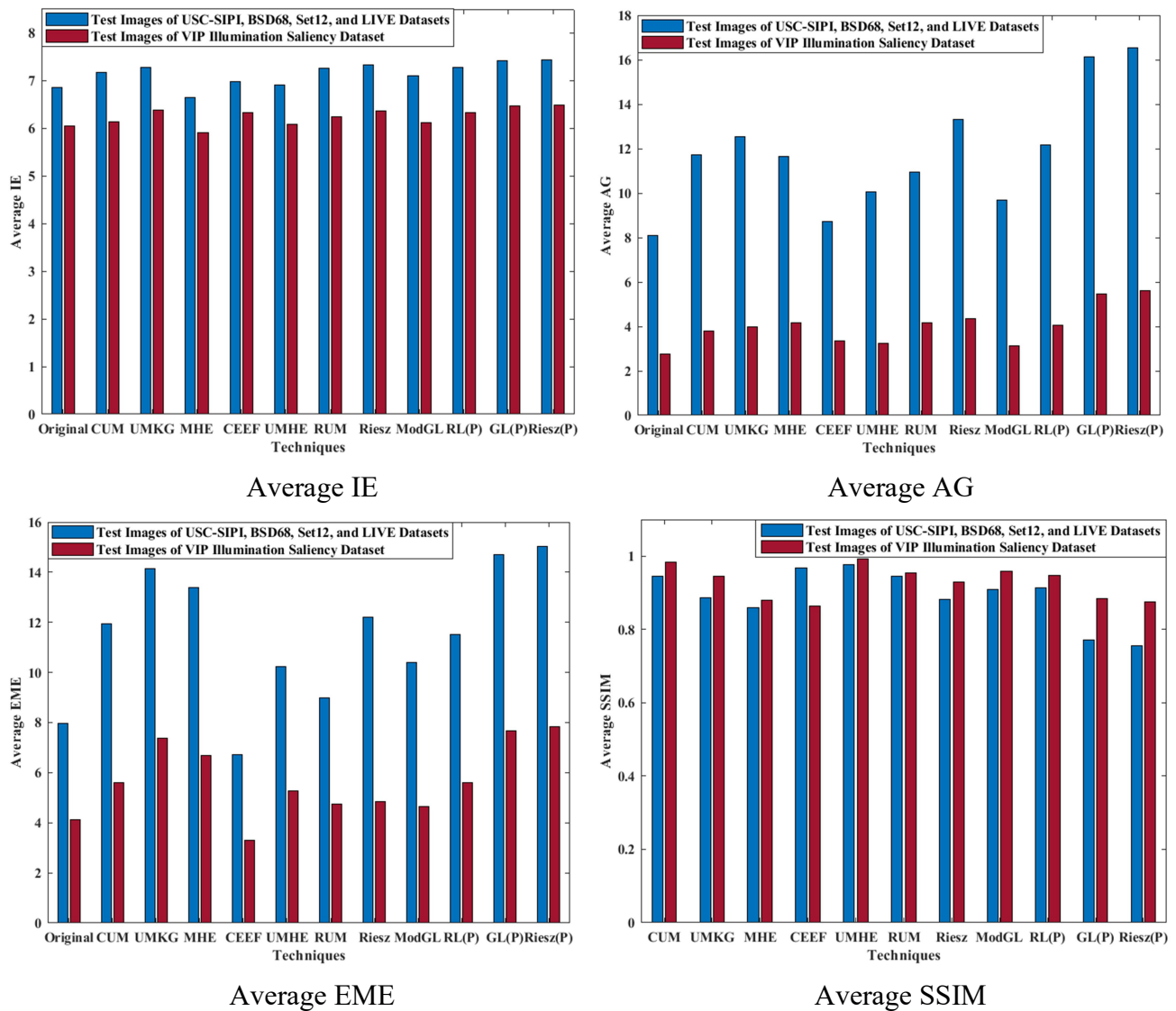
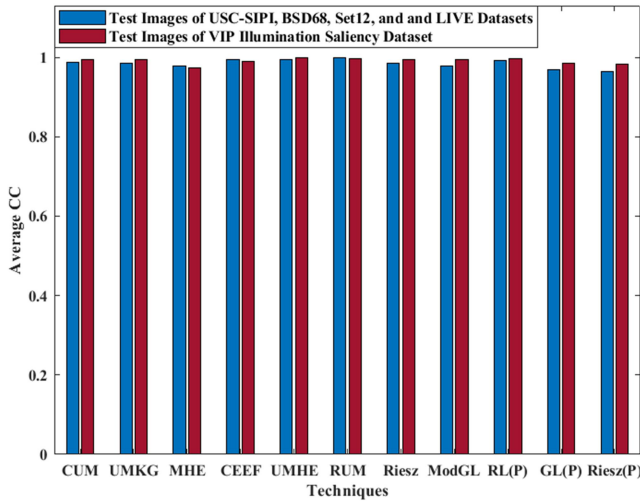
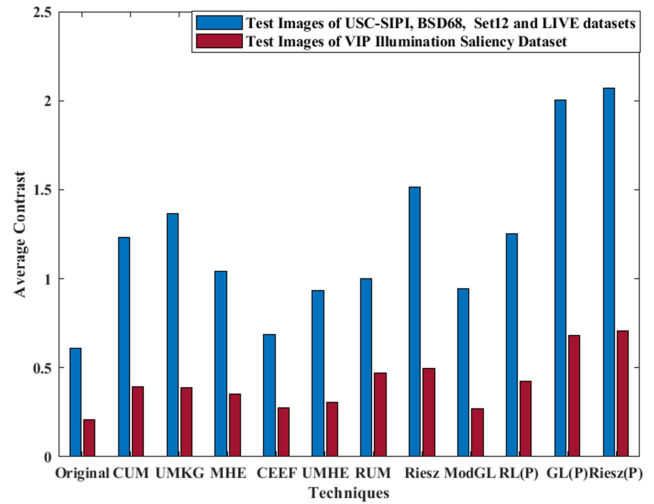


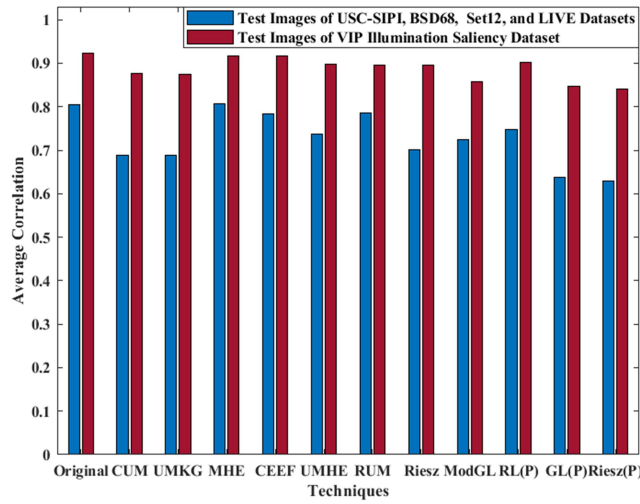
Figure 3.9: Average performance parameters for test images of various datasets (contd.)



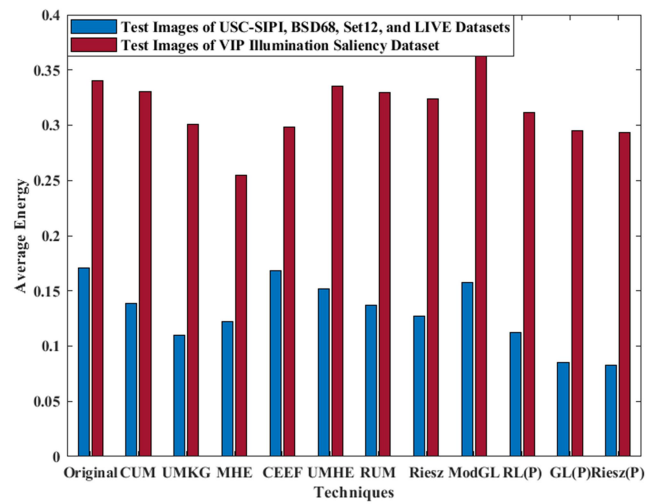
Average CC



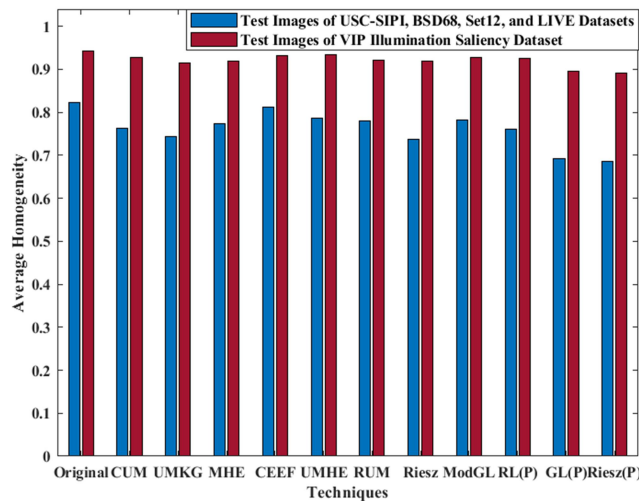
Average Contrast



Average Correlation



Average Energy



Average Homogeneity

Figure 3.9: Average performance parameters for test images of various datasets

Based on the average performance metrics, superior performance is achieved by the proposed FOD based UM approach against the existing techniques. It is exhibited that an improvement of at least 1.43 %, 24.20%, and 6.25% for average IE, AG, and EME respectively is achieved by the proposed RFOD based UM approach. Also, the minimum average improvement in GLCM based contrast is 36.59% as compared to existing techniques. Nevertheless, average SSIM and CC are low for MHE [80] and CEEF [185] for test images with variation in illumination conditions because images enhanced by MHE [80] are generally distorted while the images enhanced by CEEF [185] improved the image contrast. Moreover, the MHE [80] provided minimum energy for images with variation in illumination conditions that indicate less uniformity between the GLCM pixels. It is owing to the distorted foggy image obtained after enhancement that severely changed the uniformity among pixels. Conversely, RFOD based UM approach provided minimum average homogeneity and correlation, thus, indicating better performance than state-of-the-art enhancement approaches. Therefore, it is apparent that more enhancement is provided by the proposed RFOD mask in UM technique.

3.6 Computational Cost

The computational cost is important for evaluating the performance of the proposed FOD based UM technique. The computational complexity to add two images is $\Theta(MN)$ and to compute the FOD mask is $O(MN) + O(MN(\log(MN))^2)$ whereas computational complexity to perform the convolution is $O(MN \log(MN))$ [92]. Hence, the overall computational complexity is $2\Theta(MN) + O(MN) + O(MN(\log(MN))^2) + 2O(MN \log(MN))$. Additionally, Table 3.12 provides the average time elapsed for executing various techniques.

Table 3.12: Average processing time (in secs) of various image enhancement approaches

Techniques	CUM [21]	UMKG [83]	MHE [80]	CEEF [185]	UMHE [84]	RUM [140]	Riesz [49]	Mod GL [141]	Proposed
Processing Time	3.0672	38.9263	3.3461	3.3126	3.9271	5.4814	1.1649	4.9278	3.6798

It is apparent that excluding the Riesz [49] technique, the average processing time to execute the proposed FOD based UM technique is either slightly less or comparable to the existing image enhancement approaches. The average processing time is reliant on the complexity of the approach and image size.

3.7 Application of Proposed Approach in Fundus Images

Human eyes are generally examined using the Fundus images that assist in the detection of diseases such as Diabetic Retinopathy (DR), Glaucomatous, etc. that perhaps result in the loss of vision [73]. As these images are usually of low contrast, so, it is necessary to enhance such images. Therefore, the proposed approach is utilized to enhance the Fundus images of a DR patient and healthy individual acquired from the HRF database [184]. The simulation results of various approaches for Fundus images are illustrated in Figure 3.10.

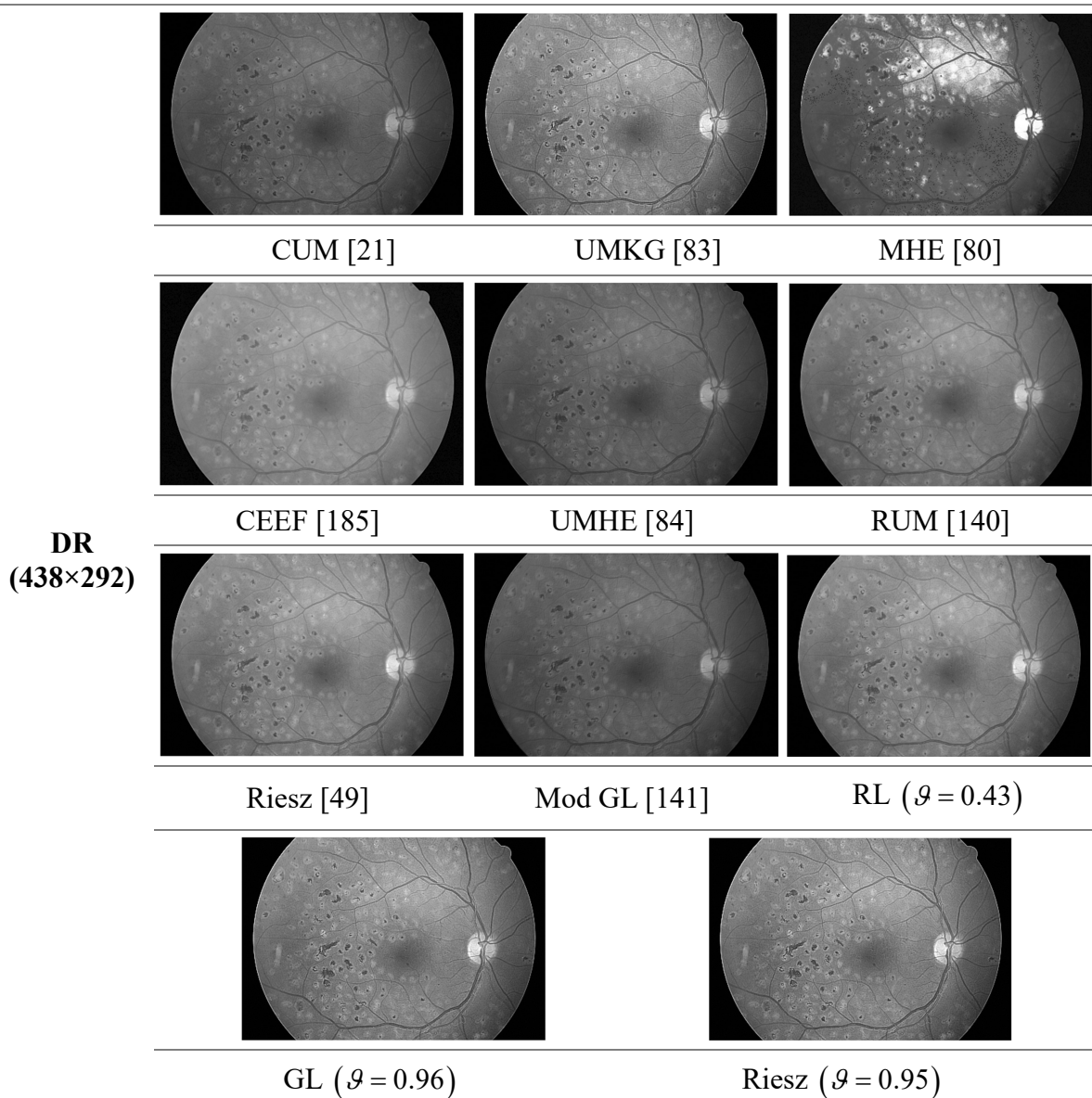


Figure 3.10: Simulation results for Fundus images (contd.)

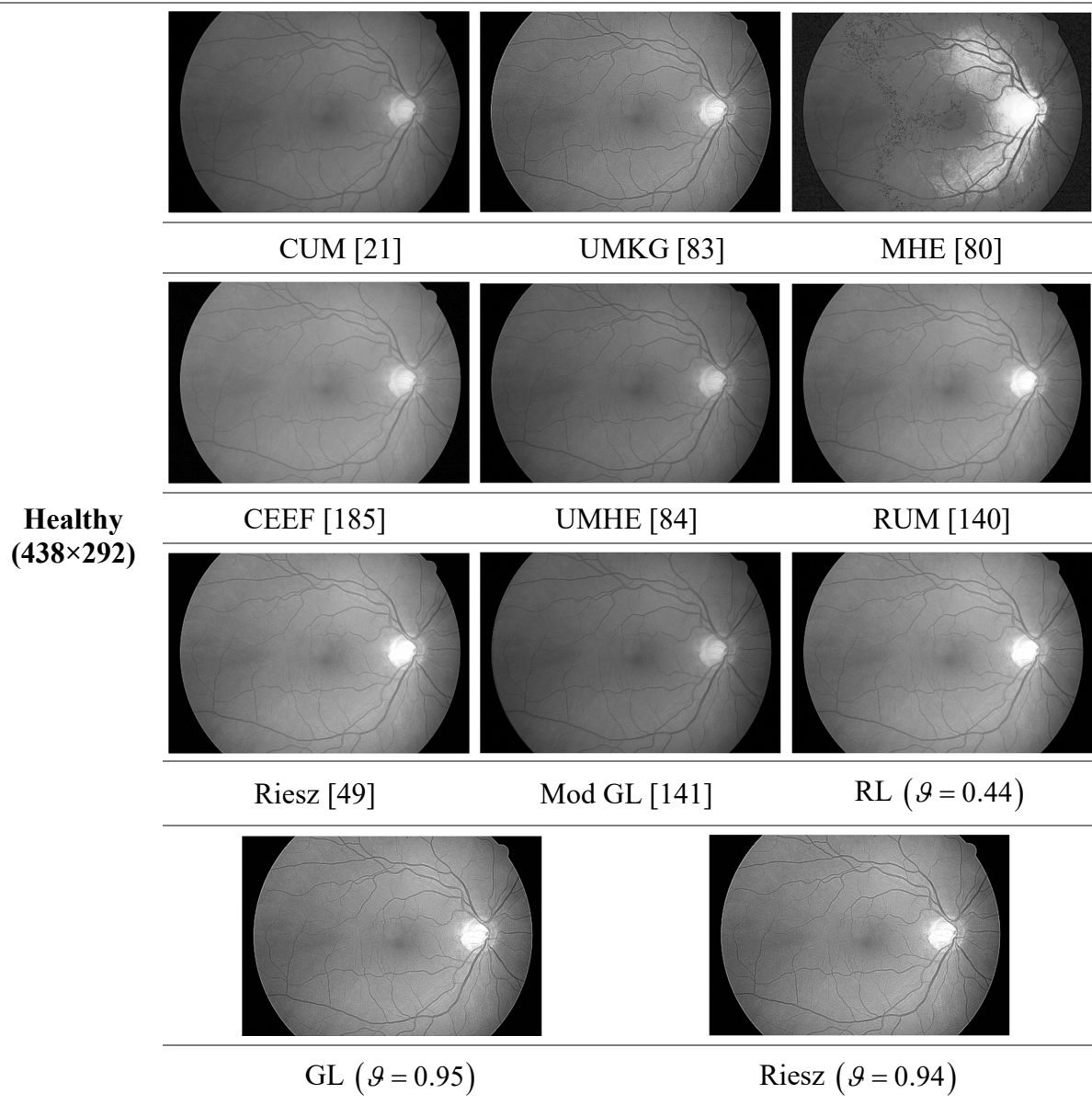


Figure 3.10: Simulation results for Fundus images

It is apparent that the proposed FOD based UM technique provides the contrast enhancement and sharpening of the image details, but the existing techniques either enhanced the contrast or sharpened the features of an image. Thus, the presented approach provided more enhancement than other image enhancement approaches. Moreover, it is visually apparent that MHE [80] results in image distortion. Table 3.13 and Table 3.14 show the quantitative analysis based on performance metrics of the Fundus images.

Table 3.13: Performance metrics for the Fundus images

Metrics/ Techniques	IE		AG		SSIM		EME		CC		
	DR	Healthy	DR	Healthy	DR	Healthy	DR	Healthy	DR	Healthy	
Original Image	5.9964	6.0858	2.2749	1.4615	-	-	1.9373	0.9567	-	-	
CUM [21]	6.0422	6.0926	3.2775	2.0004	0.9726	0.9873	2.9432	1.3478	0.9977	0.9994	
UMKG [83]	6.7793	6.4383	7.2209	4.5773	0.6739	0.8510	5.3082	3.1367	0.9847	0.9936	
MHE [80]	6.5410	5.9915	5.8340	5.2350	0.6461	0.6571	5.9299	5.1354	0.8787	0.8829	
CEEF [185]	6.0326	6.0701	3.0818	2.4930	0.8247	0.9081	1.4817	1.1129	0.9855	0.9904	
UMHE [84]	6.0173	6.0896	2.8302	2.5083	0.9888	0.9889	2.2455	1.6867	0.9992	0.9994	
RUM [140]	6.2890	6.3482	3.0649	2.6525	0.9564	0.9621	2.0578	1.5641	0.9999	0.9998	
Riesz [49]	6.5374	6.4957	3.9818	3.4866	0.8933	0.9063	2.7343	2.0413	0.9992	0.9990	
Mod GL [141]	6.0055	6.0879	2.7557	2.4900	0.9588	0.9600	2.7170	2.0277	0.9973	0.9982	
Proposed Mask	RL	6.4514	6.4685	4.0098	3.3986	0.8922	0.9120	2.6183	2.5401	0.9991	0.9992
	GL	6.7488	6.6176	7.5322	6.3514	0.6600	0.7015	5.5695	4.8824	0.9829	0.9891
	Riesz	6.7796	6.6708	8.0942	6.8398	0.6476	0.6672	5.9947	5.1634	0.9791	0.9866

Bold indicates the optimum value

Table 3.14: GLCM parameters for the Fundus images

Metrics	Contrast		Correlation		Energy		Homogeneity		
	DR	Healthy	DR	Healthy	DR	Healthy	DR	Healthy	
Rotation Offset	45°	45°	45°	45°	45°	45°	45°	45°	
Original Image	0.1175	0.0639	0.9429	0.9750	0.2662	0.3182	0.9458	0.9701	
CUM [21]	0.1933	0.1002	0.9084	0.9611	0.2317	0.2952	0.9167	0.9539	
UMKG [83]	0.6188	0.2936	0.8701	0.9215	0.1210	0.1826	0.8201	0.8905	
MHE [80]	0.3959	0.4251	0.9195	0.9001	0.1818	0.1674	0.8770	0.8622	
CEEF [185]	0.1567	0.1311	0.9643	0.9695	0.3082	0.3100	0.9426	0.9487	
UMHE [84]	0.1610	0.1411	0.9228	0.9455	0.2451	0.2706	0.9284	0.9359	
RUM [140]	0.1708	0.1485	0.9516	0.9656	0.2087	0.2137	0.9267	0.9360	
Riesz [49]	0.2480	0.2095	0.9419	0.9580	0.1753	0.1835	0.9019	0.9139	
Mod GL [141]	0.1505	0.1433	0.9239	0.9426	0.2527	0.2630	0.9296	0.9322	
Proposed Mask	RL	0.2503	0.2020	0.9411	0.9593	0.1733	0.1844	0.8995	0.9155
	GL	0.6268	0.4792	0.8617	0.9060	0.1194	0.1315	0.8149	0.8379
	Riesz	0.7006	0.5304	0.8476	0.8967	0.1128	0.1252	0.8015	0.8264

Bold indicates the optimum value

It is ascertained from the above performance metrics that more enhancement is provided by the proposed approach as compared to the existing approaches except for SSIM and CC. It is due to the fact that images enhanced by MHE [80] are subjected to image distortion. Nonetheless, the proposed approach analyzed on the basis of visual comparison and other performance metrics demonstrated its capability in enhancing the Fundus images.

3.8 Summary

In this chapter, FOD based UM approach is implemented to enhance the image visual quality in terms of the improved attributes of an image especially texture, contrast, and edges of the images. The test images from various datasets are considered to confirm the efficacy of FODs namely RL, GL, and Riesz in the UM approach. The proposed RFOD approach shows an improvement of 1.43-11.91% and 1.63-9.74% by considering the test images of standard datasets and VIP Illumination Saliency dataset respectively for average IE than the existing approaches. The GLCM based contrast shows the minimum improvement of 36.59% and 42.65% by considering the test images of standard datasets and VIP Illumination Saliency dataset respectively for the presented RFOD based UM approach. Moreover, the enhancement achieved by the proposed approach for Fundus images confirmed its applicability in the real-world scenario. Therefore, it is apparent that the RFOD based proposed UM approach outperformed the existing approaches. It further encouraged conducting the analysis of RFOD in the frequency domain. Hence, the next chapter deals with developing a novel expression for RFOD in the FrFTD.

RIESZ FRACTIONAL ORDER DERIVATIVE IN FRFT DOMAIN

The promising results obtained by RFOD in the spatial domain for the image enhancement application further create the necessity to explore it in the frequency domain. Therefore, this chapter provides the mathematical analysis of RFOD in FrFTD. The analytical expression is derived in closed-form in the terms of PCF and CHF. Moreover, the discrete counterpart is obtained by considering the DFrFT properties which is further used to design the low pass FIR differentiator. Afterward, a design example of signal with high-frequency chirp noise is considered that demonstrates the effectiveness of the proposed algorithm as compared to the existing approaches. Furthermore, the proposed algorithm is extended for the two-dimensional applications of image processing.

4.1 Mathematical Expression for RFOD in FrFTD

Initially, the novel analytical expression for the RFOD in the FrFTD is derived in the closed-form. The proposed work for a generalized fractional differintegral is confined to the two-sided RFOD definition of order ' \mathcal{G} ' defined in (2.2.5) and then taking its FrFT as:

$$F^\phi \left[D^\mathcal{G} z(t) \right] = F^\phi \left[\kappa(t) * z(t) \right] \tag{4.1.1}$$

where $F^\phi[\cdot]$ refers to the FrFT operation and ' ϕ ' denotes the FrFT rotation angle. Applying the convolution property of FrFT to (4.1.1) [34]:

$$F^\phi \left[D^\mathcal{G} z(t) \right] = \sqrt{\frac{2\pi}{1 - j \cot(\phi)}} \exp(-ju_\phi^2 \cot(\phi)) F^\phi \left[\frac{|t|^{-\mathcal{G}-1}}{2\Gamma(-\mathcal{G}) \cos\left(\frac{\mathcal{G}\pi}{2}\right)} \right] F^\phi [z(t)] \tag{4.1.2}$$

$$F^\phi \left[D^\mathcal{G} z(t) \right] = \frac{Z(u_\phi)}{2\Gamma(-\mathcal{G}) \cos\left(\frac{\mathcal{G}\pi}{2}\right)} \int_{-\infty}^{\infty} |t|^{-\mathcal{G}-1} \exp\left(\frac{jt^2}{2} \cot(\phi) - ju_\phi t \csc(\phi)\right) dt \tag{4.1.3}$$

such that $Z(u_\phi) = F^\phi [z(t)]$ symbolizes the FrFT of a signal $z(t)$.

The outcomes of this chapter are published as:

K. Kaur, N. Jindal, and K. Singh, "Riesz fractional order derivative in Fractional Fourier Transform domain: An insight," *Digit. Signal Process. A Rev. J.*, vol. 93, pp. 58-69, 2019.

K. Kaur, N. Jindal, and K. Singh, "Improved homomorphic filtering using fractional derivatives for enhancement of low contrast and non-uniformly illuminated images," *Multimed. Tools Appl.*, vol. 78, no. 19, pp. 27891-27914, 2019.

$$F^\phi \left[D^\vartheta z(t) \right] = \frac{Z(u_\phi)}{2\Gamma(-\vartheta) \cos\left(\frac{\vartheta\pi}{2}\right)} \left[\begin{array}{l} \int_{-\infty}^0 (-t)^{-\vartheta-1} \exp\left(\frac{jt^2}{2} \cot(\phi) - ju_\phi t \csc(\phi)\right) dt \\ + \int_0^{\infty} (t)^{-\vartheta-1} \exp\left(\frac{jt^2}{2} \cot(\phi) - ju_\phi t \csc(\phi)\right) dt \end{array} \right] \quad (4.1.4)$$

The integral in (4.1.4) is solved by considering the (4.1.5) that results in terms of PCF [158]:

$$\int_0^{\infty} x^{\nu-1} \exp(-\beta x^2 - \gamma x) dx = (2\beta)^{-(\nu/2)} \Gamma(\nu) \exp\left(\frac{\gamma^2}{8\beta}\right) D_{-\nu}\left(\frac{\gamma}{\sqrt{2\beta}}\right) \quad (4.1.5)$$

Considering the above integral expression and assuming, $\nu = -\vartheta$, $\beta = (-j/2)\cot(\phi)$ and $\gamma = -ju_\phi t \csc(\phi)$,

$$\begin{aligned} & \int_{-\infty}^0 (-t)^{-\vartheta-1} \exp\left(\frac{jt^2}{2} \cot(\phi) - ju_\phi t \csc(\phi)\right) dt \\ &= \exp\left(\frac{-j\vartheta\pi}{4}\right) (\cot(\phi))^{9/2} \Gamma(-\vartheta) \exp\left(\frac{-j}{2} u_\phi^2 \csc(2\phi)\right) D_\vartheta\left(-\sqrt{-2ju_\phi^2 \csc(2\phi)}\right) \end{aligned} \quad (4.1.6)$$

$$\begin{aligned} & \int_0^{\infty} (t)^{-\vartheta-1} \exp\left(\frac{jt^2}{2} \cot(\phi) - ju_\phi t \csc(\phi)\right) dt \\ &= \exp\left(\frac{-j\vartheta\pi}{4}\right) (\cot(\phi))^{9/2} \Gamma(-\vartheta) \exp\left(\frac{-j}{2} u_\phi^2 \csc(2\phi)\right) D_\vartheta\left(\sqrt{-2ju_\phi^2 \csc(2\phi)}\right) \end{aligned} \quad (4.1.7)$$

The resultant obtained after combining (4.1.6) and (4.1.7) in the terms of PCF,

$$\begin{aligned} & \int_{-\infty}^0 (-t)^{-\vartheta-1} \exp\left(\frac{jt^2}{2} \cot(\phi) - ju_\phi t \csc(\phi)\right) dt + \int_0^{\infty} (t)^{-\vartheta-1} \exp\left(\frac{jt^2}{2} \cot(\phi) - ju_\phi t \csc(\phi)\right) dt \\ &= \exp\left(\frac{-j\vartheta\pi}{4}\right) (\cot(\phi))^{9/2} \Gamma(-\vartheta) \exp\left(\frac{-j}{2} u_\phi^2 \csc(2\phi)\right) \left[\begin{array}{l} D_\vartheta\left(-\sqrt{-2ju_\phi^2 \csc(2\phi)}\right) + \\ D_\vartheta\left(\sqrt{-2ju_\phi^2 \csc(2\phi)}\right) \end{array} \right] \end{aligned} \quad (4.1.8)$$

The PCF in terms of CHF can be expressed as [158]:

$$D_\nu(z) = 2^{\nu/2} \sqrt{\pi} \exp\left(\frac{-z^2}{4}\right) \left[\frac{1}{\Gamma\left(\frac{1-\nu}{2}\right)} {}_1F_1\left(\frac{-\nu}{2}; \frac{1}{2}; \frac{z^2}{2}\right) - \frac{\sqrt{2}z}{\Gamma\left(\frac{-\nu}{2}\right)} {}_1F_1\left(\frac{1-\nu}{2}; \frac{3}{2}; \frac{z^2}{2}\right) \right] \quad (4.1.9)$$

Using (4.1.9) in (4.1.8), expression comes out to be,

$$\begin{aligned} & \int_{-\infty}^0 (-t)^{-\varrho-1} \exp\left(\frac{jt^2}{2} \cot(\phi) - ju_{\phi}t \csc(\phi)\right) dt + \int_0^{\infty} (t)^{-\varrho-1} \exp\left(\frac{jt^2}{2} \cot(\phi) - ju_{\phi}t \csc(\phi)\right) dt \\ &= 2^{\varrho/2+1} \sqrt{\pi} \exp\left(\frac{-j\varrho\pi}{4}\right) (\cot(\phi))^{\varrho/2} \frac{\Gamma(-\varrho)}{\Gamma\left(\frac{1-\varrho}{2}\right)} {}_1F_1\left(\frac{-\varrho}{2}; \frac{1}{2}; -ju_{\phi}^2 \csc(2\phi)\right) \end{aligned} \quad (4.1.10)$$

The expression obtained by utilizing Legendre's duplication formula [156],

$$\begin{aligned} & \int_{-\infty}^0 (-t)^{-\varrho-1} \exp\left(\frac{jt^2}{2} \cot(\phi) - ju_{\phi}t \csc(\phi)\right) dt + \int_0^{\infty} (t)^{-\varrho-1} \exp\left(\frac{jt^2}{2} \cot(\phi) - ju_{\phi}t \csc(\phi)\right) dt \\ &= 2^{-\varrho/2} \exp\left(\frac{-j\varrho\pi}{4}\right) (\cot(\phi))^{\varrho/2} \Gamma\left(\frac{-\varrho}{2}\right) {}_1F_1\left(\frac{-\varrho}{2}; \frac{1}{2}; -ju_{\phi}^2 \csc(2\phi)\right) \end{aligned} \quad (4.1.11)$$

Using (4.1.11) in (4.1.4),

$$F^{\varrho} [D^{\varrho} z(t)] = \frac{Z(u_{\phi})}{\Gamma(-\varrho) \cos\left(\frac{\varrho\pi}{2}\right)} 2^{-\varrho/2-1} \exp\left(\frac{-j\varrho\pi}{4}\right) (\cot(\phi))^{\varrho/2} \Gamma\left(\frac{-\varrho}{2}\right) {}_1F_1\left(\frac{-\varrho}{2}; \frac{1}{2}; -ju_{\phi}^2 \csc(2\phi)\right) \quad (4.1.12)$$

The expression in (4.1.12) provides the RFOD for $z(t)$ in the FrFTD. The RFOD expression in the FT domain is obtained by substituting $\phi = \pi/2$ in the (4.1.4),

$$F^{\pi/2} [D^{\varrho} z(t)] = \frac{Z(u_{\pi/2})}{2\Gamma(-\varrho) \cos\left(\frac{\varrho\pi}{2}\right)} \int_{-\infty}^{\infty} |t|^{-\varrho-1} \exp(-ju_{\pi/2}t) dt \quad (4.1.13)$$

$$F^{\pi/2} [D^{\varrho} z(t)] = \frac{Z(u_{\pi/2})}{2\Gamma(-\varrho) \cos\left(\frac{\varrho\pi}{2}\right)} \left[\int_{-\infty}^0 (-t)^{-\varrho-1} \exp(-ju_{\pi/2}t) dt + \int_0^{\infty} (t)^{-\varrho-1} \exp(-ju_{\pi/2}t) dt \right] \quad (4.1.14)$$

According to the integration formula [158],

$$\int_0^{\infty} x^{\nu-1} \exp(-\mu x) dx = \frac{1}{\mu^{\nu}} \Gamma(\nu) \quad (4.1.15)$$

Considering the formula in (4.1.15) and assuming $\nu = -\varrho$ and $\mu = ju_{\pi/2}$, (4.1.14) becomes,

$$F^{\pi/2} [D^g z(t)] = \Gamma(-g) \left[(ju_{\pi/2})^g + (-ju_{\pi/2})^g \right] = \Gamma(-g) \left[2|u_{\pi/2}|^g \cos\left(\frac{g\pi}{2}\right) \right] \quad (4.1.16)$$

After substituting (4.1.16) in (4.1.14), the expression becomes:

$$F^{\pi/2} [D^g z(t)] = |u_{\pi/2}|^g Z(u_{\pi/2}) \quad (4.1.17)$$

The FT of RFOD for $z(t)$ is obtained from (4.1.17). Thus, FrFT of Type-1 RFOD will be $|u_\phi|^g$ for $Z(u_\phi) = 1$ and $\phi = \pi/2$, that is, $z(t)$ must be an impulse function centered at $t = 0$.

4.2 Computation of Proposed Approach in Discrete Domain

The discrete counterpart of the expression derived in (4.1.12) is provided in this section. Several discrete versions exist for continuous FrFT but due to the low computational cost of DFrFT of Type-I [42], it is utilized in the presented work. Moreover, it is beneficial in terms of efficient computation because it comprises two chirp multiplications along with one Fast Fourier Transform (FFT), thus, involving a total of $[2N + (N/2)\log_2 N]$ multiplications, such that, $N = 2Q + 1$ is the length of the output. Its computational complexity is minimum as compared to various kinds of DFrFT that work like continuous FrFT. Hence, the DFrFT presented in [42] is utilized to obtain an expression for RFOD of a discrete signal. In discrete domain, the RFOD for a continuous-time signal is derived by uniformly sampling the input signal $z(t)$ and output signal $Z(u_\phi) = F^\phi [z(t)]$ with intervals Δt and Δu_ϕ provided by:

$$z(n) = z(n\Delta t) \text{ and } Z_\phi(m) = Z(m\Delta u_\phi) \quad (4.2.1)$$

such that, $m = -P, -P+1, \dots, P-1, P$ and $n = -Q, -Q+1, \dots, Q-1, Q$. Here, $(2Q+1, 2P+1)$ refer to the time and frequency domain points provided $P \geq Q$,

$$\Delta u_\phi \Delta t = 2\pi Z \sin(\phi) / (2P+1) \quad (4.2.2)$$

where $|Z|$ is an integer prime to $2P+1$, however, $Z = \text{sgn}(\sin(\phi)) = \pm 1$ and sgn refers to the signum function. The DFrFT kernel is provided as [42]:

$$T_\phi(m, n) = \sqrt{\frac{\text{sgn}(\sin(\phi))(\sin(\phi) - \cos(\phi))}{2P+1}} \exp\left(\frac{j}{2} \cot(\phi) m^2 \Delta u_\phi^2\right) \exp\left(\frac{j}{2} \cot(\phi) n^2 \Delta t^2\right) \exp\left(-j \frac{2\pi n m \text{sgn}(\sin(\phi))}{2P+1}\right) \quad (4.2.3)$$

The DFrFT obtained using the above kernel is given by [42]:

$$Z_\phi(m) = \sqrt{\frac{\text{sgn}(\sin(\phi))(\sin(\phi) - \cos(\phi))}{2P+1}} \exp\left(\frac{j}{2} \cot(\phi) m^2 \Delta u_\phi^2\right) \sum_{n=-Q}^Q \exp\left(-j \frac{\text{sgn}(\sin(\phi)) 2\pi n m}{2P+1}\right) \exp\left(\frac{j}{2} \cot(\phi) n^2 \Delta t^2\right) z(n) \quad (4.2.4)$$

where, $\phi \in 2V\pi + (0, \pi)$, V is an integer. The RFOD for the discrete signal $z(n)$ in the DFrFT domain is computed based on Riesz fractional definition [99] given by:

$$D^\vartheta z(t) = \lim_{\Delta t \rightarrow 0} \frac{2}{(\Delta t)^\vartheta} \sum_{k=0}^{\infty} g_k^\vartheta(k) z(t - k\Delta t) \quad (4.2.5)$$

such that the coefficient $g_k^\vartheta(k)$ is given as:

$$g_k^\vartheta(k) = (-1)^k \frac{\Gamma(\vartheta+1)}{\Gamma\left(\frac{\vartheta}{2} - k + 1\right) \Gamma\left(\frac{\vartheta}{2} + k + 1\right)} \quad (4.2.6)$$

Figure 4.1 depicts the output of the coefficient sequence $g_k^\vartheta(k)$ by varying the fractional order ' ϑ '.

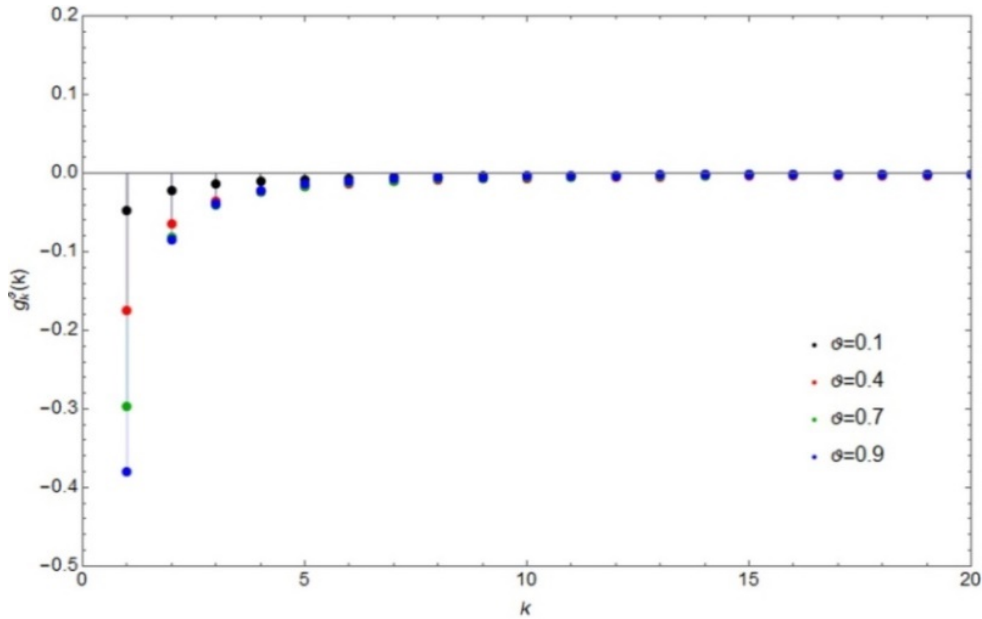


Figure 4.1: Coefficient sequence $g_k^\vartheta(k)$ for different fractional orders (ϑ)

It is perceived that for different fractional orders (ϑ), the sequence $g_k^\vartheta(k)$ decreases rapidly. The expression in (4.2.5) after truncating it to length L comes out to be:

$$D^\vartheta z(t) \approx \lim_{\Delta t \rightarrow 0} \frac{2}{(\Delta t)^\vartheta} \sum_{k=0}^L g_k^\vartheta(k) z(t - k\Delta t) \quad (4.2.7)$$

Then, removing the limit, (4.2.7) is approximated to:

$$D^g z(t) \approx \frac{2}{(\Delta t)^g} \sum_{k=0}^L g_k^g(k) z(t - k\Delta t) \quad (4.2.8)$$

The computation of $D^g z(t)$ at $t = n\Delta t$ is done by:

$$D^g z(t)_{|t=n\Delta t} = D^g z(n\Delta t) \approx \frac{2}{(\Delta t)^g} \sum_{k=0}^L g_k^g(k) z(n\Delta t - k\Delta t) \quad (4.2.9)$$

Then, the DFrFT of (4.2.9) is determined by:

$$\mathcal{D}_F^\phi [D^g z(n\Delta t)] \approx \mathcal{D}_F^\phi \left[\frac{2}{(\Delta t)^g} \sum_{k=0}^L g_k^g(k) z(n - k) \right] \approx \frac{2}{(\Delta t)^g} \sum_{k=0}^L g_k^g(k) \mathcal{D}_F^\phi [z(n - k)] \quad (4.2.10)$$

where \mathcal{D}_F^ϕ represents the DFrFT operator. Applying the shifting property [150], (4.2.10) becomes,

$$\mathcal{D}_F^\phi [D^g z(n)] = \frac{2}{(\Delta t)^g} \sum_{k=0}^L g_k^g(k) \exp \left[\begin{array}{l} \frac{j}{2} (k\Delta t)^2 \sin(\phi) \cos(\phi) - \\ j(m\Delta t_\phi)(k\Delta t) \sin(\phi) \end{array} \right] Z_\phi(m - k \cos(\phi)) \quad (4.2.11)$$

where $Z_\phi(m)$ is given by (4.2.4).

Hence, (4.2.11) presents the RFOD for a discrete-time signal $z(n)$ in the DFrFT domain with two fractional parameters, that is, FrFT rotation angle ' ϕ ' and fractional order of RFOD ' g '.

4.3 Fractional Fourier Domain Based Riesz Fractional Order Differentiator

The proposed FrFTD based Riesz fractional order differentiating filter is presented in Figure 4.2.

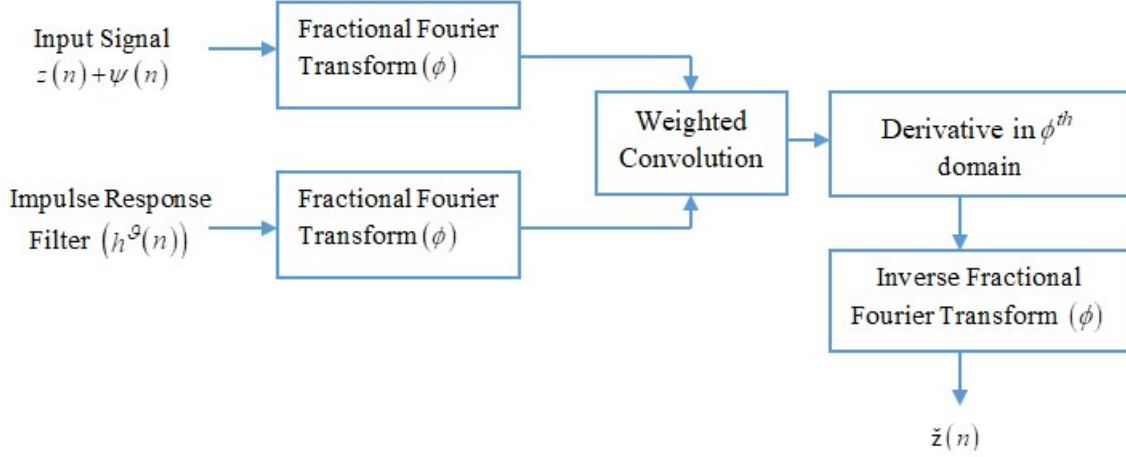


Figure 4.2: Proposed algorithm for FrFT based Riesz fractional order differentiator

Initially, the noisy input signal $z(n)+\psi(n)$ and fractional order impulse response filter $h^g(n)$ are transformed into ϕ^{th} domain of FrFT. It is worth noting that here the low pass filter is considered as an impulse response filter $h^g(n)$ that attenuates the frequencies higher than the cut-off frequency while passing the low frequencies. The weighted convolution [34] of ϕ^{th} domain based fractional impulse response filter $H^g(u_\phi)$ and transformed input signal is obtained before determining its derivative in the ϕ^{th} domain. Eventually, the IFrFT of the differentiated signal is taken with a rotation angle “ $-\phi$ ” to attain the output signal $\check{z}(n)$ in the time domain.

4.4 Design Example

The FrFT based RFOD of a signal is computed in the presented algorithm. The parameters such as truncation length, time, and fractional parameters that ought to be initialized before beginning the algorithm are selected by preliminary experimentation. The real and imaginary parts of the input signal $z(n)=0.667\exp(18jn\pi/32)+0.33\exp(-8jn\pi/32)$ corrupted with chirp noise $\psi(n)=0.1\exp(0.06j(n-1)^3)-7jn$ to be considered in this design example are illustrated in Figure 4.3(a) and Figure 4.3(b). The noise corrupted signal $z(n)+\psi(n)$ is then processed as depicted in Figure 4.2. The filtered signals obtained in the time domain ($\phi=0, \vartheta=0.43$), frequency domain ($\phi=\pi/2, \vartheta=0.43$), and the FrFTD ($\phi=0.45\pi, \vartheta=0.43$) are shown in Figure 4.3(c)-Figure 4.3(h) respectively.

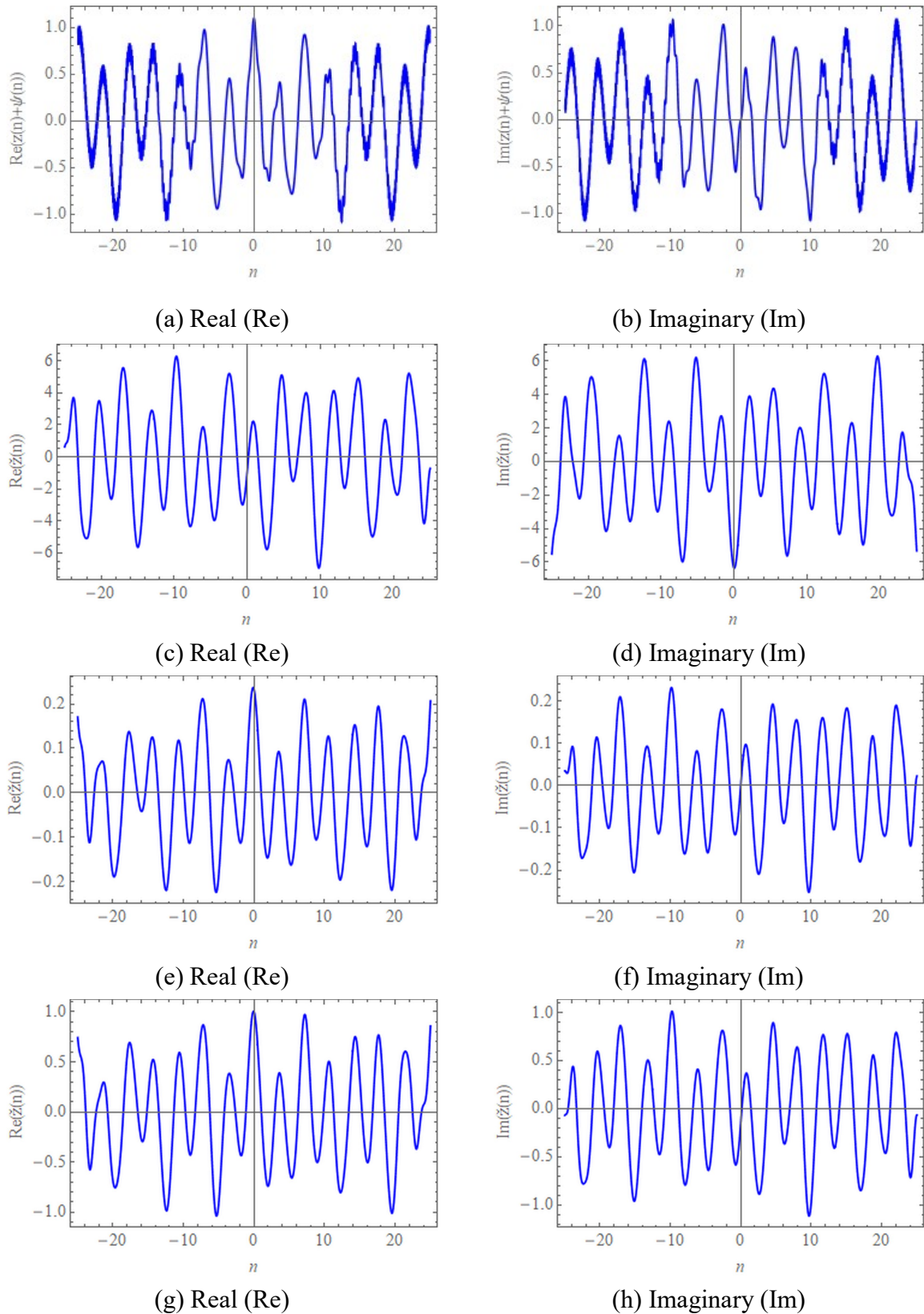
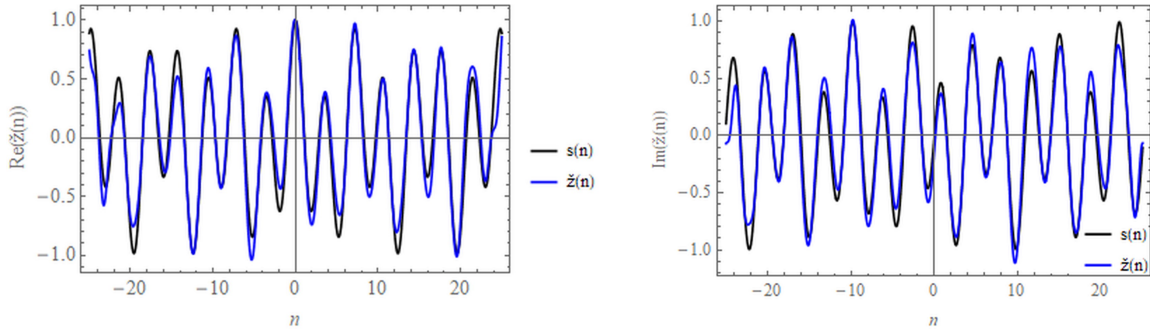


Figure 4.3: (a), (b) Input signal corrupted with noise $z(n)+\psi(n)$; Results of fractional order differentiating filter: (c), (d) time-domain filtered output signal $\check{z}(n)$; (e), (f) Fourier domain filtered output signal $\check{z}(n)$; (g), (h) FrFTD filtered output signal $\check{z}(n)$; (contd.)



(i) Real (Re)

(j) Imaginary (Im)

Figure 4.3: Results of fractional order differentiating filter: (i), (j) FrFTD filtered signal $\hat{z}(n)$ with respect to original signal

It is evident that FrFTD filtered signal is almost similar to the original signal but there exist few shifts in the filtered signal in reference to the original signal. Here, RMSE and MAE are computed between the filtered signals $\hat{z}(n)$ and original signal $z(n)$ for all three domains namely time, Fourier, and FrFT domain. The FrFT parameter (a) and the order of RFOD (ρ) are varied to obtain the filtered signal $\hat{z}(n)$ in the FrFTD. As RMSE depends on two fractional parameters, thus, the selection of optimal fractional parameters is done on the basis of a three-dimensional surface plot. However, it is not obtained for MAE as its trend is similar to RMSE. Figure 4.4 shows the surface plot for RMSE.

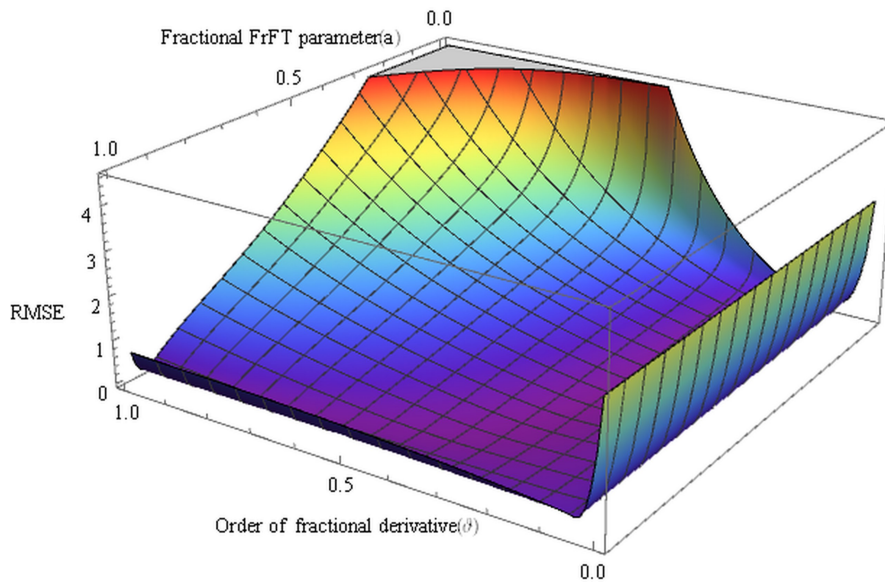


Figure 4.4: Surface plot for RMSE obtained by varying FrFT parameter (a) and the order of RFOD (ρ)

Thus, the fractional parameters that provide the optimal performance are obtained from the minimum RMSE. Only the positive fractional orders, that is, $\mathcal{G} \in (0,1)$ are considered in Figure 4.4 because the RMSE determined for the fractional order $\mathcal{G} \in (1,2)$ is more as compared to $\mathcal{G} \in (0,1)$ and for negative fractional orders it works as an integrator [95]. Moreover, for the time-domain filtered signal, RMSE is maximum because there is less similarity between the original and filtered signal. The Fourier domain filtered signal shows similarity to the original signal but it is quite less similar in comparison to the FrFTD filtered signal. Moreover, it is worth noting that the filtered signal in the FrFTD provides the least RMSE for the fractional orders $\mathcal{G}=0.43$ and $\phi=0.45\pi$ than the time-domain and Fourier domain filtered signal. Thus, the effect of noise is minimized by selecting the optimal parameters for the FrFT parameter (a) and fractional order of RFOD (\mathcal{G}). Table 4.1 shows the RMSE and MAE for filtering in time, Fourier, and FrFT domains.

Table 4.1: RMSE and MAE for filtering in various domains for varying fractional order (\mathcal{G})

Order of fractional derivative (\mathcal{G})	Time domain ($\phi = 0$)		Fourier domain ($\phi = \pi/2$)		FrFT domain ($\phi = 0.45\pi$)	
	RMSE	MAE	RMSE	MAE	RMSE	MAE
0	2.90371	2.47412	2.90125	2.47255	2.90155	2.47281
0.1	0.24375	0.23592	0.369596	0.350486	0.21846	0.199133
0.2	0.658737	0.60468	0.457328	0.432465	0.175728	0.155533
0.3	1.60164	1.48671	0.52503	0.497132	0.139704	0.118853
0.4	3.20366	2.97642	0.576369	0.546346	0.116481	0.097094
0.5	5.93074	5.50190	0.615521	0.583994	0.12629	0.100904
0.6	10.5857	9.79659	0.645535	0.612949	0.174276	0.144682
0.7	18.5526	17.1209	0.668645	0.635317	0.248227	0.210448
0.8	32.2221	29.6454	0.686505	0.652658	0.340363	0.296594
0.9	55.7296	51.1157	0.700351	0.666145	0.448345	0.402713
1	106.212	88.0077	0.711113	0.676660	0.572146	0.524231

Bold indicates the minimum value

Thus, the efficiency of the FrFTD based Riesz fractional order differentiator is validated from RMSE and MAE. In the case of time-domain, RMSE and MAE increase whereas it attains the lowest value and then rises again for Fourier and FrFT domain. RFOD in the FrFTD obtained the least value of 0.115136 for RMSE and 0.094223 for MAE at the fractional order $\mathcal{G}=0.43$. The minimum RMSE is obtained for FrFT based RFOD as compared to the RL [10] and Caputo [9] FODs as shown in Table 4.2.

Table 4.2: RMSE of FODs in the FrFTD for varying order of fractional derivative (ϑ)

Order of fractional derivative (ϑ)	RMSE		
	RL [10]	Caputo [9]	Riesz [Proposed]
0	0.251	0.188	2.90155
0.1	0.246	0.179	0.21846
0.2	0.243	0.177	0.175728
0.3	0.242	0.176	0.139704
0.4	0.241	0.1758	0.116481
0.5	0.2432	0.176	0.12629
0.6	0.244	0.1762	0.174276
0.7	0.246	0.1775	0.248227
0.8	0.2482	0.179	0.340363
0.9	0.252	0.18	0.448345
1	0.257	0.187	0.572146

Bold indicates the minimum value

It is ascertained that the optimal results are provided by RFOD for the fractional order (ϑ) ranging from 0.2 and 0.6. Figure 4.5 shows the comparison of RMSE for the RL [10], Caputo [9], and proposed RFOD.

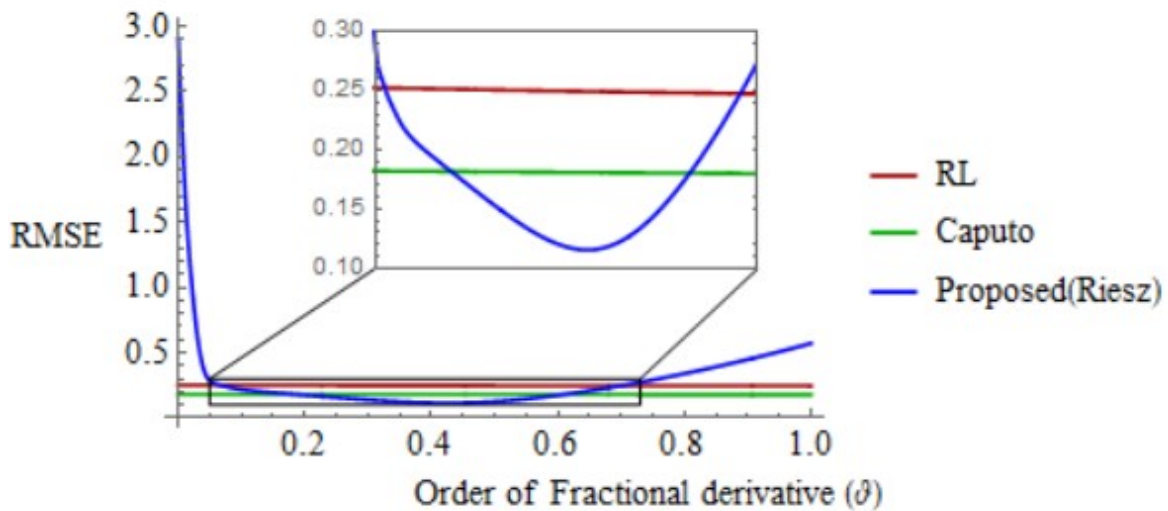


Figure 4.5: RMSE based comparison of the proposed RFOD with other FODs

It is perceived that RMSE for RFOD drops to the least value and then again increases with the increase in fractional order at the optimal FrFT rotation angle while it remains almost constant for RL and Caputo FODs.

4.5 Computational Cost

The computational cost is immensely important to confirm the effectiveness of an algorithm. The first stage out of three stages to measure the computational complexity of the presented scheme is to compute the FrFT provided by $2N + (N/2)\log_2 N$ [42]. The next stage computes the complexity of performing convolution in the FrFTD which also incorporates the multiplication with the chirp function provided by $N + O(N\log N)$. The last stage includes the computational complexity of FrFTD based differentiation given by $2N + 3O(N(\log N)^2)$ [92]. Therefore, the overall complexity is $5N + (N/2)\log_2 N + O(N\log N) + 3O(N(\log N)^2)$. The computational complexity is same for the proposed and existing approaches [9], [10]. Moreover, the average computational time is also computed for different approaches as depicted in Table 4.3.

Table 4.3: Average computational time

Approach	Time (seconds)
RL [10]	571
Caputo [9]	578
RFOD (Proposed)	567

It is perceived that the time elapsed to execute the proposed RFOD and existing approaches is almost comparable because all of them are dependent on two fractional parameters.

4.6 Applications of the Proposed Approach

This section is intended to describe the benefit of the FrFT based RFOD approach in two-dimensional image enhancement applications, that is, image sharpening and HF. Several image enhancement operations such as Gaussian filtering, median, mean, etc., exist but sometimes they cause extra smoothing that reduces the visual image quality [148]. Hence, RFOD in the FrFTD is utilized because RFOD deals with the problem of phase shifting as defined in Section 2.2.4 while the FrFT phase function preserved the edge information as well as textural details present in an image, thus, enhancing its visual quality [186]. Hence, the aforementioned approach is implemented on the variety of images obtained from the different datasets depending on the nature of application.

4.6.1 Image Sharpening

Image sharpening is used to enhance the fine details present in an image. Therefore, the proposed FrFT based RFOD approach is used for enhancing the features in an image. Its efficacy is confirmed both qualitatively and quantitatively. In the quantitative analysis, the image assessment parameters such as IE, AG, and EME are utilized for the purpose of evaluation.

4.6.1.1 Simulation Results for Test Images of Standard Datasets

The proposed approach is implemented on the grayscale images of Lena, Barbara, Pirate, and Vase, whereas the color images of Rabbit, Vase_Color, Car, and Building from standard datasets are considered for the purpose of sharpening [95], [177], [180], [181]. To conduct the experimentation, the fractional parameter ' \mathcal{G} ' is varied from 0 to 2 while the FrFT parameter ' ϕ ' is varied from 0 to $\pi/2$. However, it is observed from the intensive simulation work that better results are attained from $\phi=0.48\pi$ to $\phi=0.495\pi$ for the considered images. Moreover, these parameters are dependent on the nature of the image. It is noteworthy that for color images, the color channels are processed separately, and then results are combined to obtain the enhanced image. The scaled version of Lena and Vase_Color images enhanced with the proposed approach and their zoomed portions are shown in Figure 4.6 and Figure 4.7 for better interpretation. However, enhanced images of some other considered test images are also demonstrated in Figure 4.8 along with their zoomed portions. Moreover, the quantitative analysis of the proposed technique is also conducted in terms of performance parameters. Here, the simulation results are demonstrated for the fractional order ' \mathcal{G} ' of RFOD varying from 0.3 to 1.8 with a step size of 0.3 for an optimal FrFT rotation angle.



$\vartheta = 0.3$



$\vartheta = 0.3$ (Zoomed)



$\vartheta = 0.6$



$\vartheta = 0.6$ (Zoomed)



$\vartheta = 0.9$



$\vartheta = 0.9$ (Zoomed)

Figure 4.6: Enhanced Lena image (256×256) along with its zoomed portion for various fractional orders (contd.)



$g=1.2$



$g=1.2$ (Zoomed)



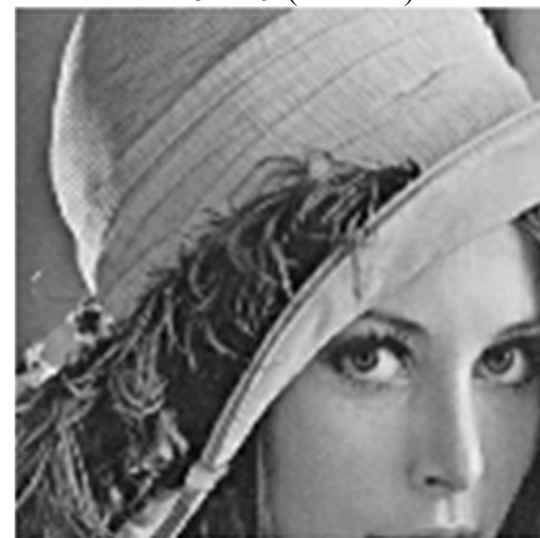
$g=1.5$



$g=1.5$ (Zoomed)



$g=1.8$



$g=1.8$ (Zoomed)

Figure 4.6: Enhanced Lena image (256×256) along with its zoomed portion for various fractional orders



$\vartheta = 0.3$



$\vartheta = 0.3$ (Zoomed)



$\vartheta = 0.6$



$\vartheta = 0.6$ (Zoomed)



$\vartheta = 0.9$



$\vartheta = 0.9$ (Zoomed)

Figure 4.7: Enhanced Vase_Color image (321×481) along with its zoomed portion for various fractional orders (contd.)



$g=1.2$



$g=1.2$ (Zoomed)



$g=1.5$



$g=1.5$ (Zoomed)



$g=1.8$



$g=1.8$ (Zoomed)

Figure 4.7: Enhanced Vase_Color image (321×481) along with its zoomed portion for various fractional orders

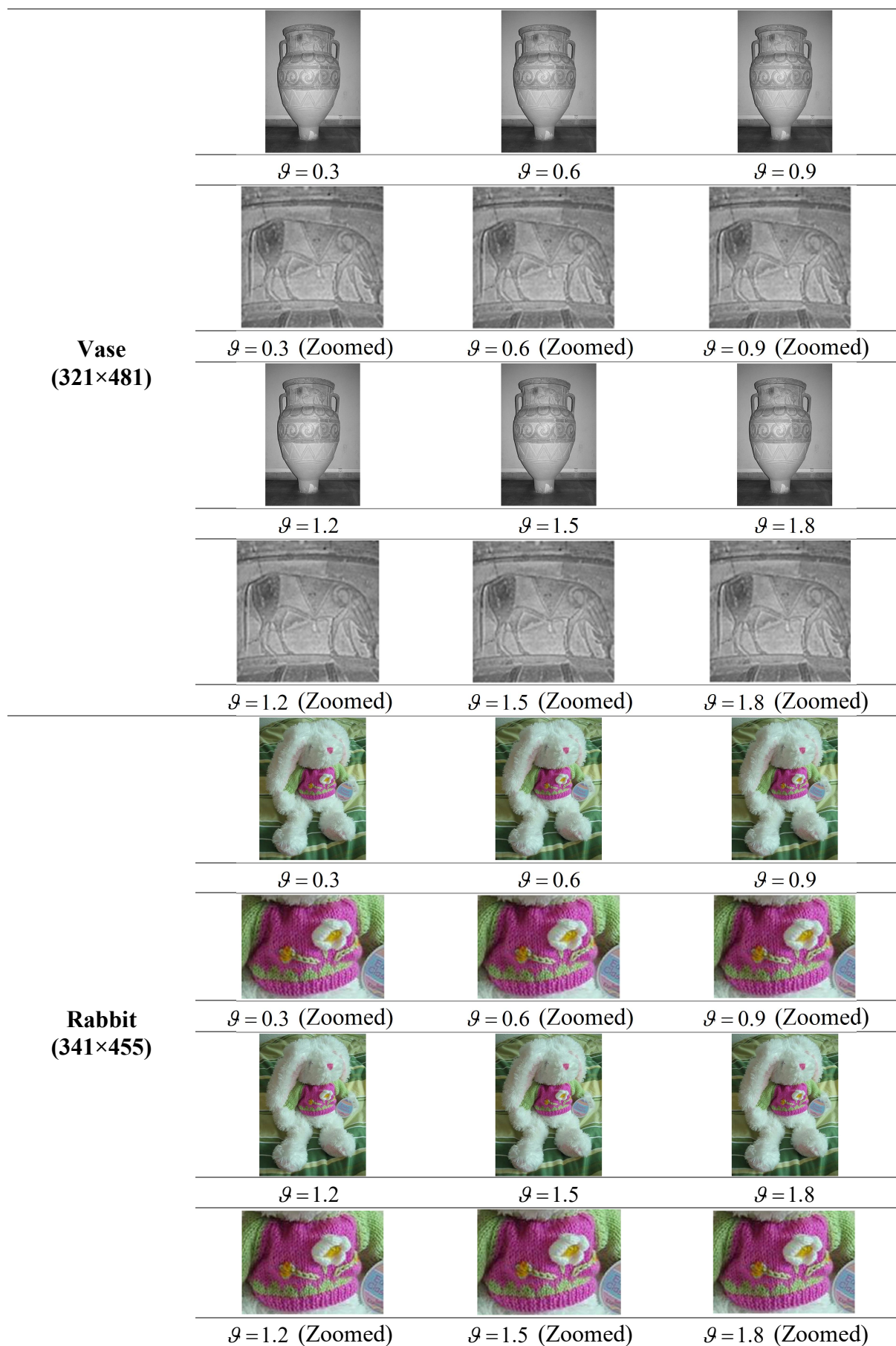


Figure 4.8: Simulation results for the proposed approach along with the zoomed portion

It is perceived that the FrFT based RFOD approach enhanced the details present in the image as apparent from the zoomed portion of the hat in the Lena image, an animal in the Vase image, and a sweater in the Rabbit image. However, there is only a slight improvement in the image features for some of the images. Hence, the quantitative analysis is done for evaluating the proposed technique in terms of IE, AG, and EME. Table 4.4 depicts the performance of the presented approach as compared to the original images.

Table 4.4: Performance metrics for test images of various sizes

Fractional parameter (α)/ Images	Metrics	Original	0.3	0.6	0.9	1.2	1.5	1.8
Lena	IE	7.4429	7.5325	7.5348	7.5354	7.5355	7.5354	7.5334
	AG	7.1958	8.4393	8.4783	8.4918	8.4958	8.4917	8.4609
	EME	5.7958	8.0181	8.1308	8.1396	8.1526	8.1396	8.0745
Barbara	IE	7.4664	7.5533	7.5526	7.5524	7.5523	7.5524	7.5527
	AG	8.4663	9.7643	9.7742	9.7772	9.7779	9.7772	9.7698
	EME	8.1969	9.7428	9.7763	9.7865	9.7894	9.7865	9.7619
Pirate	IE	7.2367	7.3888	7.3848	7.3823	7.3810	7.3824	7.3854
	AG	6.1580	7.3840	7.3717	7.3643	7.3610	7.3644	7.3748
	EME	6.4943	7.4281	7.4104	7.4079	7.4069	7.4085	7.4145
Vase	IE	6.7188	7.2393	7.2302	7.2273	7.2265	7.2273	7.2314
	AG	2.9082	5.0595	5.0662	5.0669	5.0676	5.0668	5.0628
	EME	2.3419	3.9142	3.9194	3.9202	3.9211	3.9202	3.9168
Rabbit	IE	7.5846	7.6851	7.6849	7.6851	7.6852	7.6852	7.6851
	AG	4.9488	5.6189	5.6288	5.6316	5.6325	5.6316	5.6243
	EME	3.2772	3.9486	3.9578	3.9609	3.9617	3.9609	3.9537
Vase_Color	IE	6.9043	7.4100	7.4091	7.4087	7.4086	7.4087	7.4094
	AG	2.9807	4.8984	4.9024	4.9033	4.9036	4.9033	4.9002
	EME	2.3797	3.5153	3.5174	3.5175	3.5176	3.5176	3.5158
Car	IE	7.4238	7.5300	7.5300	7.5301	7.5301	7.5301	7.5300
	AG	6.0858	6.7193	6.7196	6.7196	6.7197	6.7196	6.7194
	EME	7.4923	7.5778	7.5799	7.5805	7.5810	7.5805	7.5785
Building	IE	7.4636	7.4364	7.4371	7.4378	7.4378	7.4377	7.4377
	AG	7.4780	7.9487	7.9495	7.9498	7.9497	7.9495	7.9491
	EME	5.3761	5.3813	5.3834	5.3860	5.3858	5.3840	5.3827

Bold indicates the maximum value obtained by proposed technique

Hence, it is observed that the image assessment metrics show improvement as compared to the original images. Therefore, it is ascertained that more information and clarity is provided by the proposed approach for most of the images.

4.6.1.2 Simulation Results for Test Images with Variation in Illumination Conditions

The grayscale and color images namely c1, c2, c3, and c4 from VIP Illumination Saliency [183] are considered for confirming the potential of the FrFT based RFOD approach for variation in illumination conditions. The test images enhanced by the FrFT based RFOD technique are shown in Figure 4.9. It is observed that better results are obtained for $\phi = 0.49\pi$ and $\phi = 0.495\pi$ for the considered test images.

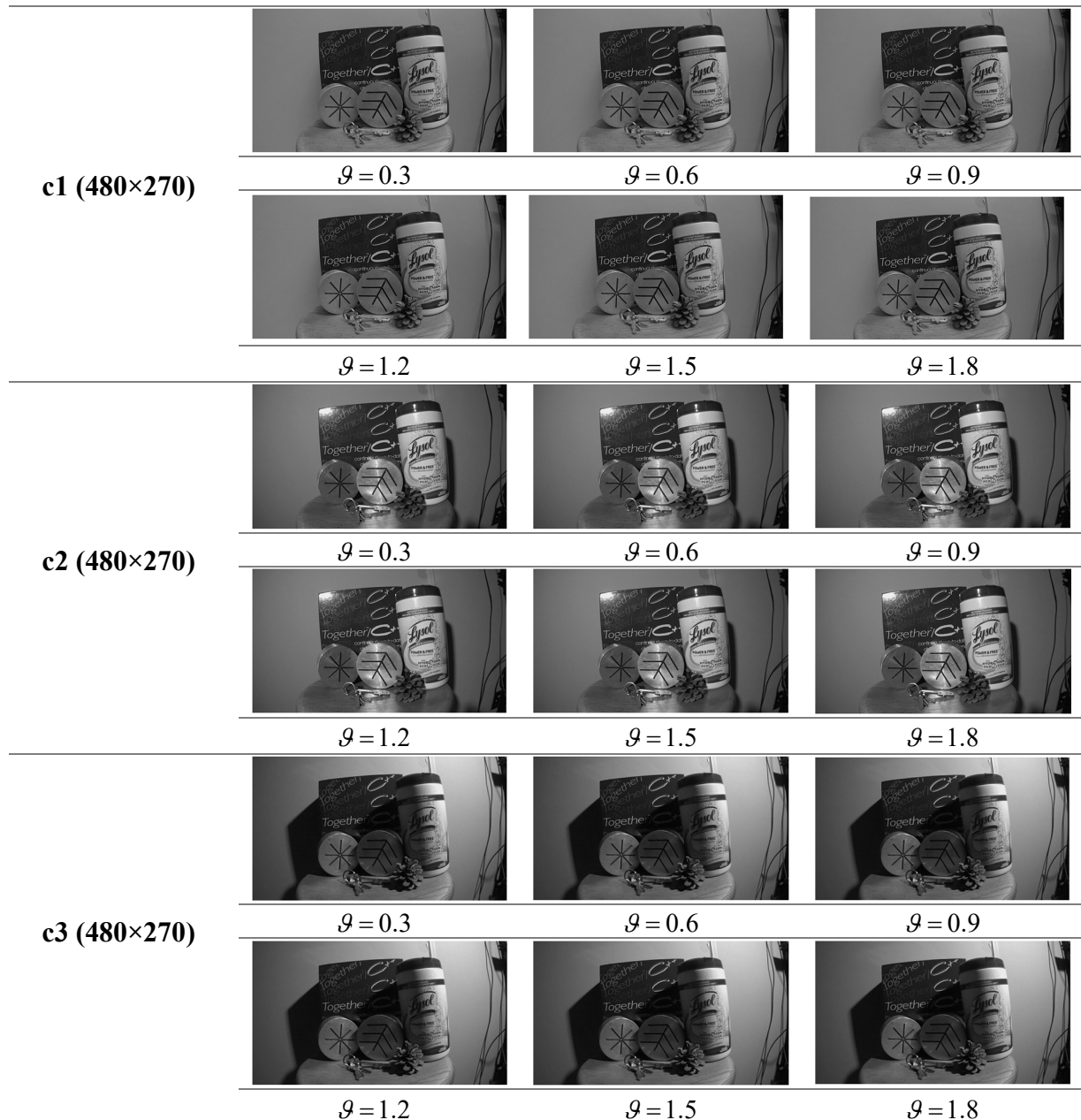


Figure 4.9: Simulation results of test images with variation in illumination conditions using the proposed approach (contd.)



Figure 4.9: Simulation results of test images with variation in illumination conditions using the proposed approach (contd.)

c4_color
(480×270)

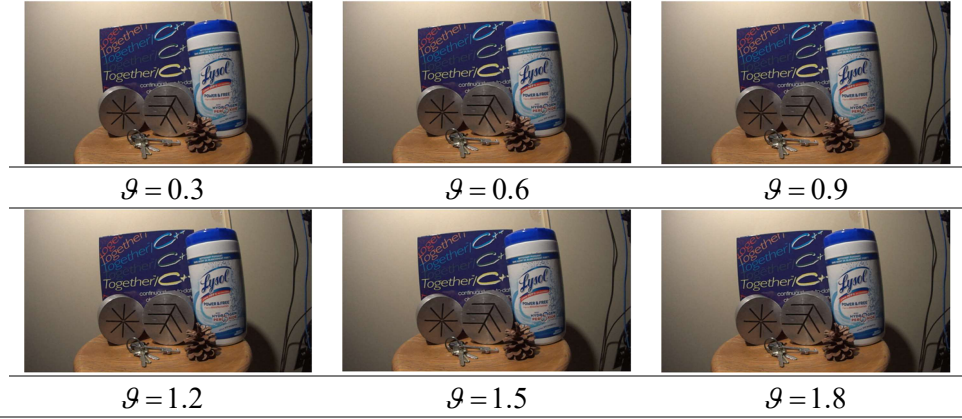


Figure 4.9: Simulation results of test images with variation in illumination conditions using the proposed approach

Despite the fact that images are enhanced with respect to the original images, there is only a slight variation with change in the fractional order. Moreover, it is evident from the image assessment parameters, that is, IE, AG, and EME provided in Table 4.5.

Table 4.5: Image assessment parameters for test images with varying illumination conditions

Fractional parameter (g) / Images	Metrics	Original	0.3	0.6	0.9	1.2	1.5	1.8
		c1	IE	6.8656	6.7496	6.7585	6.7581	6.7581
	AG	4.8922	4.9651	4.9588	4.9575	4.9572	4.9575	4.9613
	EME	5.2500	5.4039	5.4140	5.4102	5.4113	5.4102	5.4093
c2	IE	7.2828	7.2399	7.2457	7.2446	7.2426	7.2446	7.2438
	AG	5.3054	5.5577	5.5609	5.5620	5.5626	5.5620	5.5593
	EME	5.3946	5.1481	5.1693	5.1695	5.1703	5.1694	5.1656
c3	IE	7.6681	7.5716	7.5686	7.5675	7.5673	7.5675	7.5696
	AG	4.3333	4.9567	4.9547	4.9552	4.9554	4.9552	4.9551
	EME	6.7071	6.6344	6.6449	6.6509	6.6533	6.6509	6.6331
c4	IE	7.6124	7.5298	7.5257	7.5242	7.5238	7.5242	7.5254
	AG	4.5952	5.0633	5.0629	5.0628	5.0627	5.0629	5.0632
	EME	5.5139	5.3457	5.3632	5.3674	5.3691	5.3674	5.3571
c1_color	IE	7.1872	7.1062	7.1044	7.1041	7.1040	7.1041	7.1051
	AG	4.9858	5.0177	5.0184	5.0186	5.0188	5.0186	5.0183
	EME	5.6459	6.9525	6.9738	6.9763	6.9776	6.9763	6.9650
c2_color	IE	7.4493	7.3623	7.3615	7.3613	7.3612	7.3613	7.3619
	AG	5.4709	5.4811	5.4821	5.4818	5.4793	5.4818	5.4804
	EME	4.9883	5.9824	6.0082	6.0068	6.0059	6.0064	5.9926
c3_color	IE	7.7164	7.6502	7.6488	7.6485	7.6484	7.6485	7.6495
	AG	4.4065	4.4878	4.4878	4.4876	4.4875	4.4876	4.4879
	EME	5.3377	6.3996	6.3991	6.3986	6.3984	6.3987	6.3925
c4_color	IE	7.6716	7.6147	7.6135	7.6131	7.6130	7.6131	7.6141
	AG	4.6388	4.7386	4.7399	4.7402	4.7402	4.7402	4.7392
	EME	4.3959	5.1181	5.1332	5.1379	5.1401	5.1379	5.1265

Bold indicates the maximum value obtained by proposed technique

Furthermore, it is perceived that the test images with varying illumination show more clarity and enhancement, however, IE is slightly less in comparison to the original images. It may be due to the fact that image details are less preserved for the images with variation in illumination conditions. Moreover, it is worth noting that images lose information upon conversion from color images into grayscale images as the IE is less for the grayscale images even for the original images. Therefore, it becomes apparent that color images must be processed using the color models. Here, the color images are also processed by the individual processing of color channels and then combining them to obtain the enhanced color image. This also affects the correlation in the color channels that perhaps lead to the loss of information contained in the processed image. Thus, it is required to process the color channels simultaneously for preserving the details of the color image. Generally, it can be inferred that the images with non-uniform illumination conditions need to be enhanced by preserving the information details. Moreover, the FOD based UM is not able to effectively deal with the images with non-uniform lighting conditions as described in the preceding chapter. Hence, the application of the proposed algorithm in HF for the enhancement of grayscale images with varying contrast, varying illumination, and non-uniform lighting conditions is provided in the next section.

4.6.2 Homomorphic Filtering

In the presented FOD based HF technique, the original input image $z(i, j)$ is mapped into the additive domain from the multiplicative domain by taking its logarithm. The proposed framework for the FOD based HF is shown in Figure 4.10.

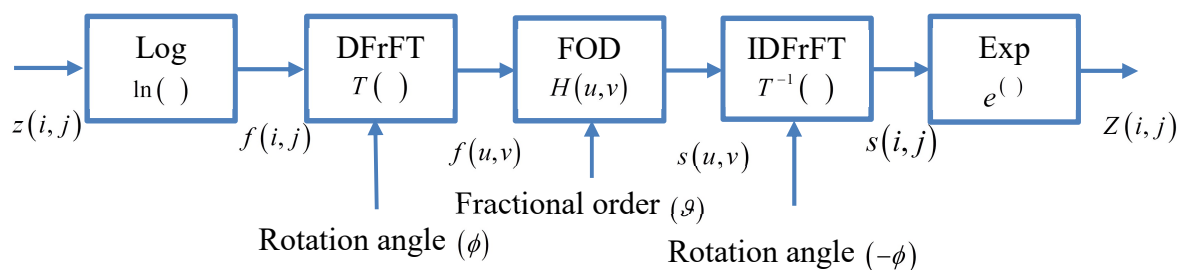


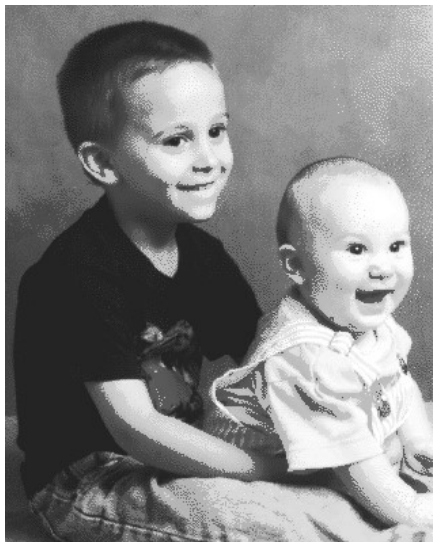
Figure 4.10: FOD based improved HF approach

The transformation of the image attained after the logarithm operation $f(i, j)$ is done into the frequency domain $f(u, v)$ by DFrFT with rotation angle (ϕ) . Afterward, the filtering is done by the FOD filter $H(u, v)$. Then, the filtered image $s(u, v)$ is transformed into the spatial

domain after taking its inverse DFrFT. Then, an enhanced image $Z(i, j)$ is finally attained by taking the exponential of the inverse transformed image $s(i, j)$.

4.6.2.1 Simulation Results for Test Images of Standard Datasets

The GL and Riesz FOD in the DFrFT domain are considered in the proposed HF technique for enhancing the images with low contrast and non-uniform illumination conditions. The test images used for the simulation include Lena, Laiton, Circuit, Kids, Pout, Tank, Barbara, and Washington Satellite from the standard datasets [175], [177], [182], and MATLAB in-built images. Moreover, the proposed approach is evaluated both qualitatively and quantitatively based on its comparison with the image enhancement methods, namely HE [21], BDPFHE [79], MHE [80], HF [187], and DCT based HF [87]. It is found that the proposed technique provided optimum results for the FrFT rotation angle varying from $\phi = 0.485\pi$ to $\phi = 0.495\pi$ and fractional order (g) ranging from 0.1-0.8 for GL and Riesz FOD. Initially, a visual comparison is performed to establish the effectiveness of the improved HF approach. Here, the scaled version of the Kids image enhanced using the proposed FOD based HF technique in the DFrFT domain and other existing techniques is illustrated in Figure 4.11 for better interpretation of results. However, the simulation results for some other test images are also presented in Figure 4.12.



HE [21]

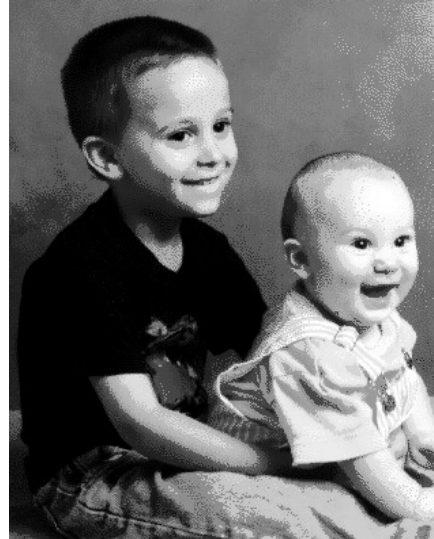


BPDFHE [79]

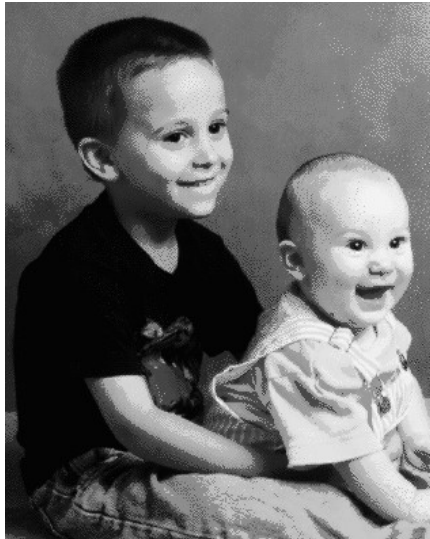
Figure 4.11: Kids image (400×318) enhanced by various image enhancement techniques (contd.)



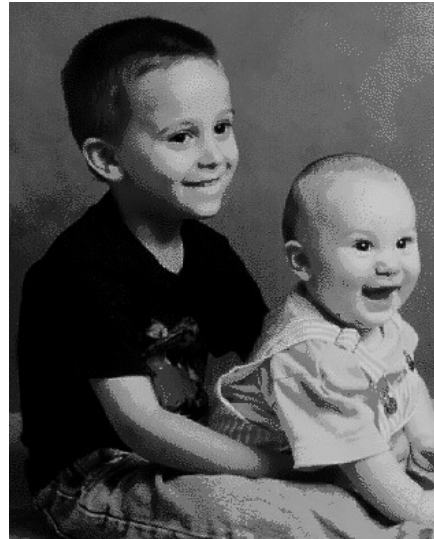
MHE [80]



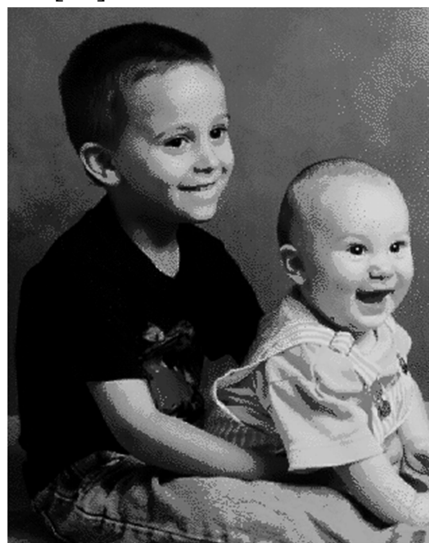
HF [187]



DCT based HF [87]



Proposed GL



Proposed Riesz

Figure 4.11: Kids image (400×318) enhanced by various image enhancement techniques

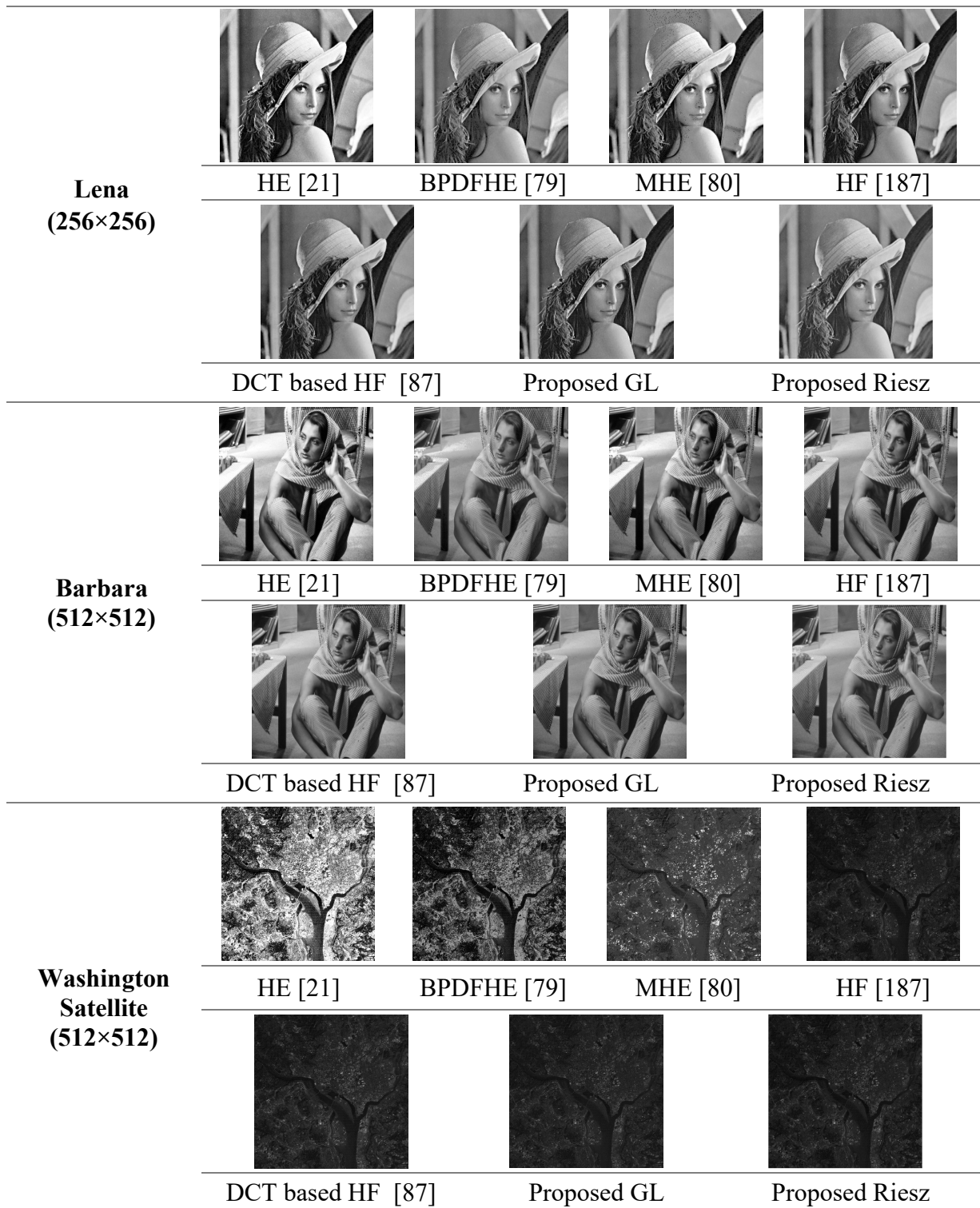


Figure 4.12: Test images enhanced by various enhancement techniques

It is clearly evident from the improved contrast in Kids image that the proposed approach possesses the ability to enhance the images with low contrast. Even in the case of other test images, there is an improvement in the contrast as well as fine details. The adequacy of the proposed HF approach is further established from the assessment parameters. PSNR (dB) and

MSE are used in Table 4.6 and Table 4.7 respectively to quantitatively evaluate the quality of enhanced images.

Table 4.6: Average PSNR (dB) for the test images

Images	HE	BPDFHE	MHE	HF	DCT	Proposed Mask	
	[21]	[79]	[80]	[187]	based HF [87]	GL	Riesz
Lena	19.1126	32.0306	24.9145	30.3044	33.1415	36.6292	37.8051
Laiton	6.4105	22.5813	13.5690	42.4720	43.1712	48.4567	48.5921
Circuit	12.6530	26.6781	20.0388	33.740	39.5597	41.6339	42.3418
Kids	6.8236	22.8815	13.4034	41.5921	44.5675	46.0547	46.1198
Pout	13.3148	25.1368	19.1888	31.8041	37.8613	47.1212	48.4159
Tank	13.7901	29.0108	22.0606	30.2198	31.9571	42.0287	44.0763
Barbara	18.0464	33.3304	24.3215	31.0498	33.2956	35.7668	39.5794
Washington Satellite	9.2130	16.5394	21.9976	36.1327	37.0283	42.5879	42.7759

Bold indicates the maximum value

Table 4.7: MSE for the test images

Images	HE	BPDFHE	MHE	HF	DCT	Proposed Mask	
	[21]	[79]	[80]	[187]	based HF [87]	GL	Riesz
Lena	797.6729	40.7400	209.7148	60.6233	31.5447	14.1304	10.7789
Laiton	14860	358.8806	2858.8	3.6803	3.1330	0.9280	0.8992
Circuit	3530	139.7250	644.4671	27.4826	7.1963	4.4637	3.7922
Kids	13512	334.9111	2969.9	4.5068	2.2716	1.6129	1.5889
Pout	3031.1	199.2492	783.7943	42.9209	10.6402	1.2617	0.9365
Tank	2716.9	81.6585	404.592	61.8157	41.4351	4.0758	2.5436
Barbara	1019.6	30.2023	240.3974	51.0623	30.4454	17.2345	7.1638
Washington Satellite	7794.4	1442.6	410.5071	15.8420	12.8900	3.5833	3.4316

Bold indicates the minimum value

It is noted that the images enhanced by RFOD based HF technique provide high PSNR and low MSE than the existing techniques. It might be because FODs enhance medium-frequency details while preserving the low-frequency and high-frequency image information. Besides, the phase and amplitude information of an image is also preserved by RFOD and DFrFT (Section 2.2). Table 4.8 shows the IE of various test images enhanced by different approaches.

Table 4.8: IE for the test images

Images	Original Image	HE [21]	BPDFHE [79]	MHE [80]	HF [187]	DCT based HF [87]	Proposed Mask	
							GL	Riesz
Lena	7.4429	5.9733	7.2328	7.4016	7.4429	7.3659	7.4673	7.4700
Laiton	4.7772	4.6416	4.1345	4.6000	4.7792	4.5850	4.7689	4.7794
Circuit	6.9439	5.9358	6.8569	6.9134	6.9426	7.0745	7.1620	7.1676
Kids	5.5169	5.2508	5.0698	5.4609	5.4847	5.4728	5.5084	5.5268
Pout	5.7599	5.4342	5.5950	5.7026	5.7551	5.9211	6.1032	6.1083
Tank	5.4957	4.9953	5.3276	5.7499	5.5017	6.2665	6.4181	6.4192
Barbara	7.4664	5.9821	7.2688	7.4245	7.4680	7.3851	7.4910	7.6170
Washington Satellite	2.8676	2.8032	2.8500	2.8676	2.8688	4.2402	4.8433	4.8515

Bold indicates the maximum value

The proposed RFOD based HF approach provides more IE than the existing techniques for all the considered images because it preserves the information content of the image (Section 2.2.4). SSIM of various test images for image enhancement approaches is shown in Table 4.9.

Table 4.9: SSIM for the test images

Images	HE [21]	BPDFHE [79]	MHE [80]	HF [187]	DCT based HF [87]	Proposed Mask	
						GL	Riesz
Lena	0.8573	0.9616	0.9014	0.9969	0.9940	0.9869	0.9957
Laiton	0.1771	0.5953	0.7712	0.9967	0.9948	0.9939	0.9937
Circuit	0.7445	0.9312	0.8825	0.9967	0.9970	0.9914	0.9911
Kids	0.2146	0.8355	0.7332	0.9750	0.9734	0.9691	0.9673
Pout	0.5644	0.8281	0.6992	0.9972	0.9977	0.9945	0.9944
Tank	0.4263	0.8643	0.6849	0.9969	0.9978	0.9879	0.9885
Barbara	0.8526	0.9649	0.9068	0.9969	0.9927	0.9871	0.9977
Washington Satellite	0.2181	0.3722	0.7106	0.9971	0.9929	0.9917	0.9926

Bold indicates the minimum value

It is perceived that the SSIM of the presented scheme is comparable to the prevailing HF techniques [87], [187]. However, SSIM is less in the case of HE [21], BPDFHE [79], and MHE [80] because images enhanced by these techniques result in a significant alteration in the image structure. Table 4.10 depicts the UIQI of various test images for image enhancement approaches.

Table 4.10: UIQI for the test images

Images	HE [21]	BPDFHE [79]	MHE [80]	HF [187]	DCT based HF [87]	Proposed Mask	
						GL	Riesz
Lena	0.8872	0.9907	0.9524	0.9967	0.9986	0.9996	0.9996
Laiton	0.2265	0.4306	0.8540	0.9945	0.9948	0.9999	0.9998
Circuit	0.7557	0.9910	0.8848	0.9944	0.9985	0.9982	0.9983
Kids	0.1154	0.6520	0.7282	0.8617	0.8567	0.8698	0.8687
Pout	0.7804	0.9776	0.9149	0.9968	0.9992	0.9999	0.9999
Tank	0.7874	0.9852	0.9539	0.9968	0.9978	0.9999	0.9999
Barbara	0.7914	0.7588	0.9309	0.9967	0.9987	0.9997	0.9998
Washington Satellite	0.6489	0.9896	0.9689	0.9965	0.9971	0.9989	0.9993

Bold indicates the maximum value

It is evident that UIQI is almost comparable to other existing techniques but it is high for both GL and Riesz FOD. It may be because DFrFT in combination with FODs preserved the information details while improving the contrast of an image (Section 2.2). The proposed method shows the minimum improvement of 6.1405 dB and 3.37% in average PSNR and IE respectively than state-of-the-art existing techniques. UIQI of the considered images is near to unity which indicates that even the enhanced images preserve their features. Therefore, it is apparent that the proposed DFrFT based FOD method provides more information details and enhancement than the existing image enhancement approaches as described in Section 2.2.

4.6.2.2 Simulation Results for Test Images with Variation in Illumination Conditions

In this section, the performance of FOD based HF approach is further analyzed by considering the c1, c2, c3, c4, statue1, statue2, statue3, statue4, and statue5 images obtained from the VIP Illumination Saliency dataset [183] in the JPEG file format. It must be noted that PSNR is constrained to 50 dB for lossy compressions such as JPEG [188]. The simulation results obtained for some of the test images with variation in illumination conditions after enhancement by the proposed FOD based HF and existing techniques are shown in Figure 4.13.

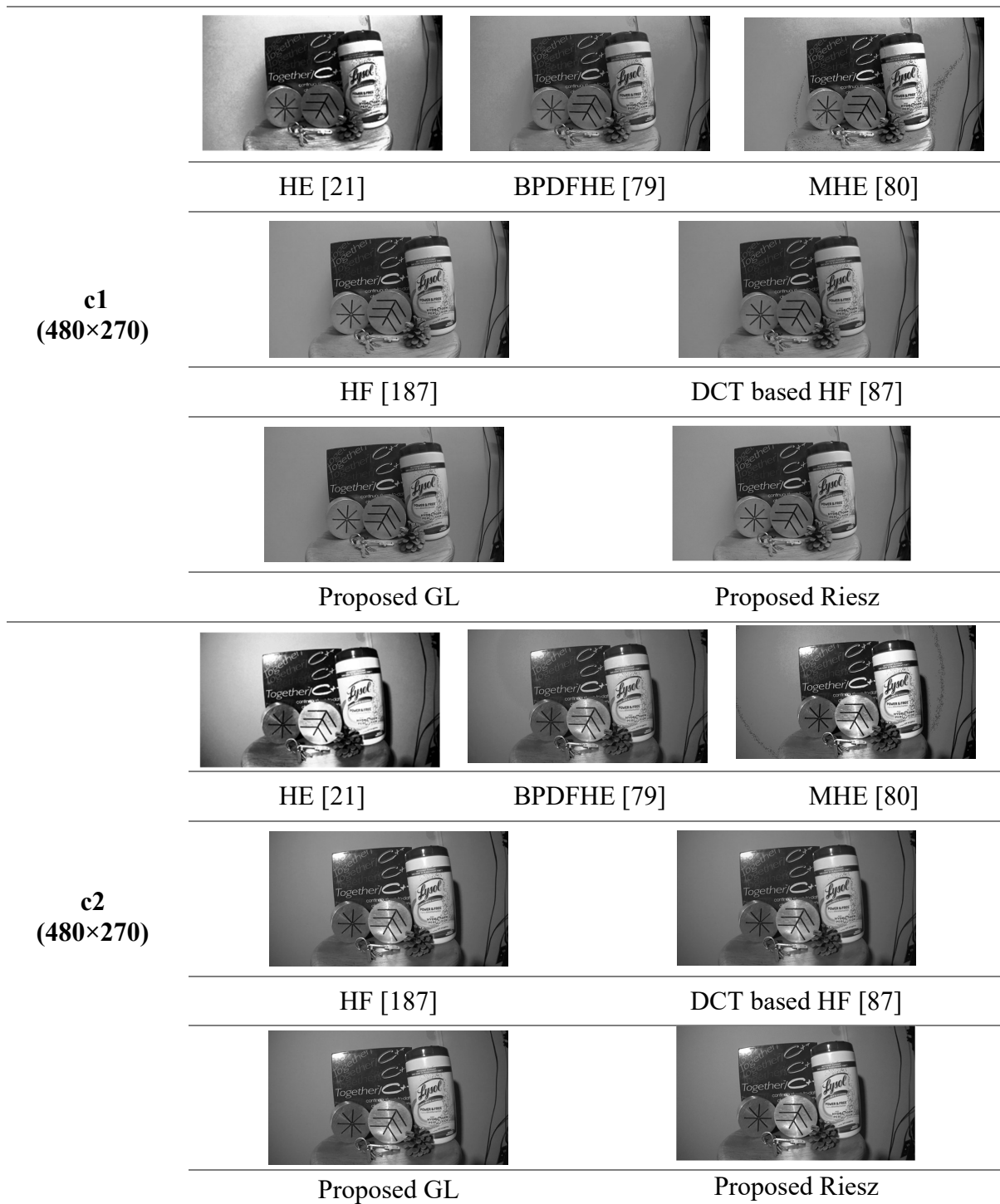


Figure 4.13: Test images with variation in illumination conditions enhanced by various image enhancement techniques (contd.)



Figure 4.13: Test images with variation in illumination conditions enhanced by various image enhancement techniques

Ostensibly, the images enhanced by the proposed FOD based HF approach provide more clarity than the existing techniques. The proposed approach enhanced the images while preserving their details. In order to further confirm its efficacy, the performance is analyzed using the image assessment parameters. Table 4.11 and Table 4.12 depicts the performance metrics, that is, PSNR and MSE of test images with variation in illumination conditions enhanced by the image enhancement techniques.

Table 4.11: PSNR (dB) of test images with variation in illumination conditions

Images	HE	BPDFHE	MHE	HF	DCT based	Proposed Mask	
	[21]	[79]	[80]	[187]	HF [87]	GL	Riesz
c1	15.3114	32.5079	24.0440	31.5845	36.2300	38.0061	39.7131
c2	14.7936	40.6294	26.2086	32.2338	36.6625	42.0412	42.2260
c3	16.1063	42.1522	29.0113	31.9091	36.5196	44.7229	44.8112
c4	17.5724	35.2970	27.5281	31.3375	36.2044	46.3373	47.4087
statue1	14.8999	18.2137	20.3881	30.7429	35.9935	38.4567	39.3985
statue2	5.2102	29.7716	31.4098	46.6751	47.1598	47.4375	47.6370
statue3	11.8799	25.5291	17.1101	31.0501	36.5901	39.1175	42.0969
statue4	16.1122	24.1622	21.5810	30.8668	36.2873	38.6202	39.4115
statue5	14.9966	29.4654	22.1456	31.3305	36.7648	37.2220	39.3918

Bold indicates the maximum value

Table 4.12: MSE of test images with variation in illumination conditions

Images	HE	BPDFHE	MHE	HF	DCT based	Proposed Mask	
	[21]	[79]	[80]	[187]	HF [87]	GL	Riesz
c1	1914	36.4994	256.2613	45.1471	15.4911	10.2913	6.9465
c2	2156.3	5.6252	155.6757	38.8780	14.0225	4.0640	3.8947
c3	1593.8	3.9615	81.6480	41.8959	14.4919	2.1918	2.1476
c4	1137.2	19.2036	114.8864	47.7897	15.5827	1.5113	1.1809
statue1	2104.2	981.0873	594.6642	54.8014	16.3580	9.2771	7.4684
statue2	19591	68.5356	47.0005	1.3982	1.2506	1.1074	1.1024
statue3	4217.8	182.0420	1264.9	51.0593	14.2584	7.9676	4.0122
statue4	1591.7	249.3818	451.8313	53.2601	15.2881	8.9342	7.4461
statue5	2057.9	73.5431	396.7531	47.8661	13.6961	12.3277	7.4800

Bold indicates the minimum value

It is evident that the proposed approach possesses high PSNR than the existing techniques. Thus, it can be inferred that the proposed technique performs efficiently even for images with variation in illumination conditions. Table 4.13 depicts the IE of test images with variation in illumination conditions enhanced by the image enhancement techniques.

Table 4.13: IE of test images with variation in illumination conditions

Images	Original Image	HE [21]	BPDFHE [79]	MHE [80]	HF [187]	DCT based HF [87]	Proposed Mask	
							GL	Riesz
c1	6.8656	5.7839	6.5291	6.7968	6.8654	6.8028	6.8770	6.8856
c2	7.2828	5.9517	6.9986	7.2077	7.2756	7.2217	7.2872	7.2995
c3	7.6681	5.9807	7.4473	7.6049	7.6498	7.6049	7.6681	7.6713
c4	7.6124	5.9874	7.3780	7.5408	7.6118	7.5472	7.6024	7.6132
statue1	5.8162	5.1384	5.5909	5.7574	5.8164	5.8071	5.8273	5.8274
statue2	3.1571	2.9151	2.4790	2.3821	3.1585	3.1501	3.1598	3.1609
statue3	3.5082	3.2699	3.3373	3.4963	3.5080	3.4960	3.5053	3.5097
statue4	6.4032	5.7295	6.2640	6.3534	6.4021	6.4020	6.4214	6.4347
statue5	6.0852	5.3904	5.7740	6.0225	6.0395	6.0725	6.0888	6.1193

Bold indicates the maximum value

It is found that the proposed approach possesses more information details as compared to existing techniques. The quantitative analysis is also subjected to the evaluation of metrics namely SSIM and UIQI for images with variation in illumination conditions. Table 4.14 and Table 4.15 show SSIM and UIQI of test images with variation in illumination conditions enhanced by the image enhancement techniques.

Table 4.14: SSIM of test images with variation in illumination conditions

Images	HE [21]	BPDFHE [79]	MHE [80]	HF [187]	DCT based HF [87]	Proposed Mask	
						GL	Riesz
c1	0.7958	0.9736	0.9055	0.9974	0.9957	0.9962	0.9992
c2	0.8323	0.9897	0.9381	0.9973	0.9959	0.9967	0.9990
c3	0.8804	0.9949	0.9599	0.9967	0.9965	0.9966	0.9991
c4	0.8955	0.9884	0.9467	0.9973	0.9966	0.9978	0.9992
statue1	0.6518	0.7622	0.7249	0.9977	0.9975	0.9984	0.9994
statue2	0.0263	0.8515	0.9217	0.9724	0.9724	0.9722	0.9725
statue3	0.6375	0.8838	0.8010	0.9980	0.9990	0.9993	0.9997
statue4	0.8080	0.8884	0.8550	0.9977	0.9980	0.9986	0.9993
statue5	0.7746	0.9255	0.8554	0.9974	0.9984	0.9986	0.9992

Bold indicates the minimum value

Table 4.15: UIQI of test images with variation in illumination conditions

Images	HE [21]	BPDFHE [79]	MHE [80]	HF [187]	DCT based HF [87]	Proposed Mask	
						GL	Riesz
c1	0.8852	0.9961	0.9745	0.9965	0.9989	0.9994	0.9993
c2	0.8567	0.9988	0.9659	0.9966	0.9989	0.9997	0.9996
c3	0.8592	0.9938	0.9407	0.9953	0.9991	0.9992	0.9992
c4	0.8964	0.9967	0.9600	0.9965	0.9989	0.9999	0.9997
statue1	0.8175	0.9364	0.9195	0.9967	0.9991	0.9995	0.9995
statue2	0.0167	0.6076	0.7818	0.9547	0.9520	0.9525	0.9538
statue3	0.7334	0.9820	0.8956	0.9968	0.9990	0.9995	0.9995
statue4	0.8440	0.9667	0.9172	0.9968	0.9992	0.9995	0.9994
statue5	0.8277	0.9774	0.9172	0.9968	0.9992	0.9993	0.9994

Bold indicates the maximum value

It is perceived from the above tables that the presented FOD based HF approach provides almost comparable SSIM and UIQI as compared to existing HF approaches. It shows that the proposed approach possesses the capability to preserve the image details while improving their contrast as mentioned in Section 2.2. However, in the case of existing techniques HE [21], BPDFHE [79], and MHE [80], the SSIM and UIQI are low. Moreover, it is also observed from Figure 4.13 that there is distortion in some of the enhanced images in the case of these existing techniques. The minimum improvement in PSNR is 4.8536 dB and IE is 0.36 % for images with variation in illumination. Therefore, the analysis performed on the basis of images with variation in illumination for the same scene validates the ability of the proposed method.

4.6.2.3 Comparative Analysis

The comparative analysis of the images enhanced by the proposed FOD based HF scheme to the original images, HE [21], BPDFHE [79], MHE [80], HF [187], and DCT based HF [87] based on the average image assessment parameters is depicted in Figure 4.14. The proposed GL and Riesz are represented by GL (P) and Riesz (P) due to space constraints. In the case of MSE, the MSE in HE [21] is not considered because its value is very large in comparison to the other techniques.

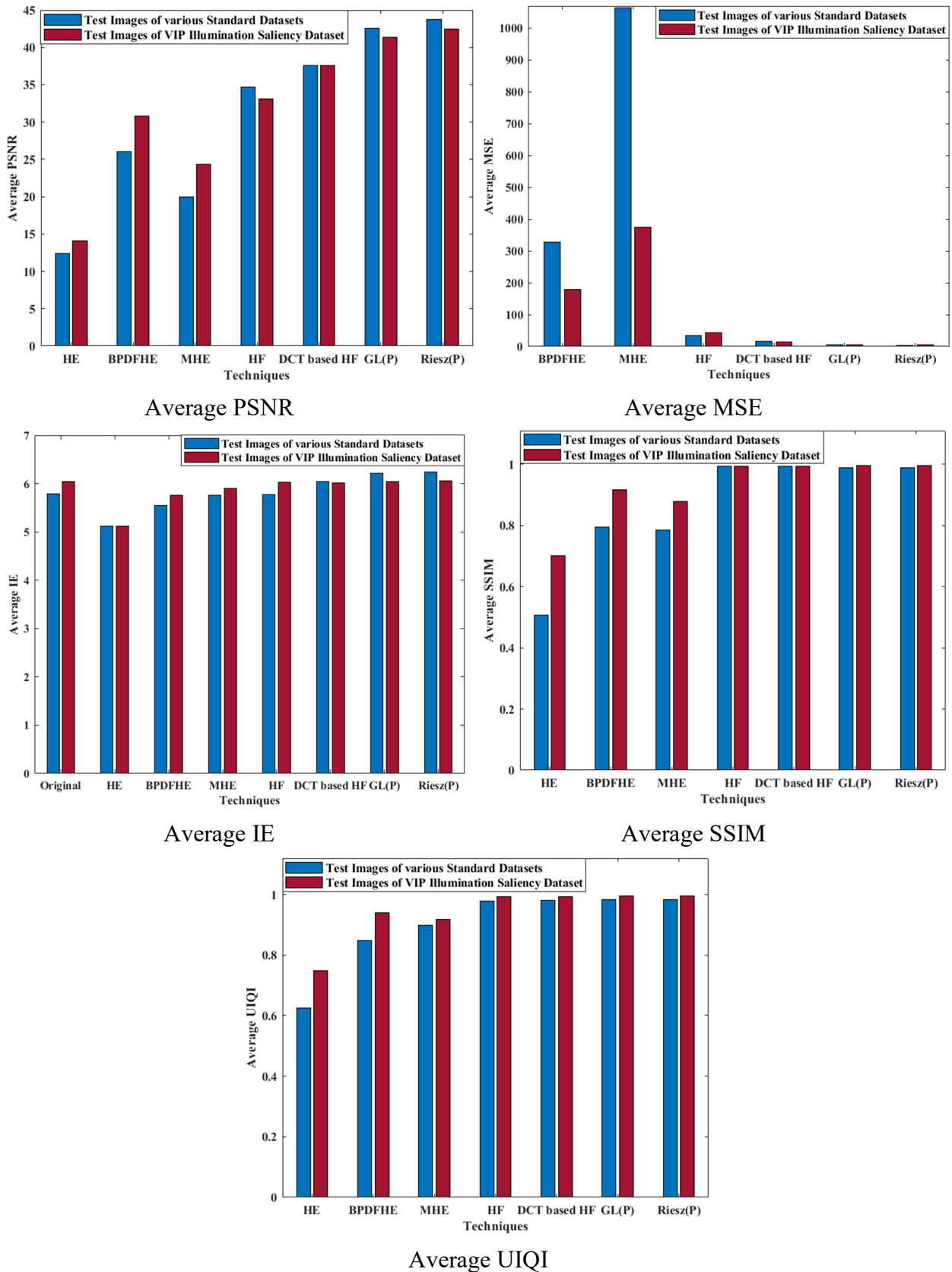


Figure 4.14: Average assessment parameters for test images enhanced by various techniques. It is exhibited that the FOD based HF approach is more effective in enhancing the images with low contrast and non-uniform illumination conditions as compared to existing

techniques. Moreover, the proposed HF approach with RFOD possesses the maximum average PSNR and IE with an improvement in the range of 4.85 dB-31.29 dB in PSNR and 0.77%-21.74% in IE. It is also observed that the average MSE is very low as compared to the existing techniques. Average SSIM is similar for HF based techniques but it is less for HE [21], BPDFHE [79], and MHE [80] due to enormous change in the image structure or distortion after its enhancement. Moreover, UIQI is close to unity for the proposed approach which indicates that image quality is preserved in accordance with the original images. Therefore, it is perceived that the proposed RFOD based improved HF approach provides more enhancement, thus, validating the theoretical concept described in Section 2.2.4.

4.7 Summary

In this chapter, a novel analytical expression in closed-form is derived for RFOD in the FrFTD. Its discrete counterpart is also obtained using the DFrFT properties. The proficiency of the presented work is established from the one-dimensional filtering and two-dimensional image enhancement applications. RFOD outperforms the existing approaches as evident from the simulation results because the former approach at the FrFT rotation angle of 0.45π for the RFOD fractional order of 0.43 achieved a minimum RMSE of 0.115136. Based on the analysis of RFOD in the FrFTD in both one-dimensional and two-dimensional applications performed in this chapter, the next chapter is devoted to its application in edge detection as well as image enhancement.

RFOD BASED APPROACH FOR EDGE DETECTION AND IMAGE ENHANCEMENT IN FRFT DOMAIN

The RFOD in the FrFTD provided significant results in the one-dimensional filtering as well as two-dimensional image enhancement applications. Therefore, RFOD based edge detection technique in the FrFTD is presented in the current chapter. The RFOD mask which is utilized in the proposed approach is developed from different interpolation methods. The performance metrics FOM and EPI are used for the selection of mask size. The proposed FrFT based RFOD technique obtained the gradient image that is further employed for enhancing the images. Furthermore, the uncontrolled features are considered for validating the robustness of the proposed approach.

5.1 RFOD based Approach in FrFTD

The spatial domain based FOD approaches are commonly used for edge detection which may increase the storage and computations of high-resolution images. Besides, the issues such as image distortion, false and discontinuous edges, etc. occur in some of the existing algorithms due to the phase shifting, noise pixels, and other difficulties in image acquisition. Hence, the proposed work is dedicated to achieve clean and continuous edges while evading the redundant edges. However, to achieve the aforementioned task, the mathematical framework is obtained for the RFOD mask.

5.1.1 RFOD Mask

By employing the second-order fractional difference model [1], [49], the RFOD in proposed approach is approximated by a step h as follows:

$$\frac{\partial^g z(t)}{\partial t^g} = \lim_{h \rightarrow 0} \frac{2}{(h)^g} \sum_{k=0}^{\infty} \frac{(-1)^k \Gamma(g+1)}{\Gamma\left(\frac{g}{2}-k+1\right)\Gamma\left(\frac{g}{2}+k+1\right)} z(t-kh) \tag{5.1.1}$$

The points $z(t-kh)$ for $k=0,1,2,\dots,n$ are considered as nodes. Assume, $\xi=t-kh+(g/2)h$ to be a node between $(t-kh-h)$ and $(t-kh+h)$. Based on the Aitken interpolation method [156], the signal $z(t)$ obtained for the three nodes $z(t-kh-h)$, $z(t-kh)$ and $z(t-kh+h)$ as:

The outcome of this chapter is published as: K. Kaur, N. Jindal, and K. Singh, "Fractional Fourier Transform based Riesz fractional derivative approach for edge detection and its application in image enhancement," *Signal Process.*, vol. 180, pp. 1-19, 2021.

$$z(\xi) = z(\xi|t-kh+h, t-kh, t-kh-h) = \frac{1}{(-t+kh-h-kh+t)} \begin{vmatrix} z(\xi|t-kh+h, t-kh) & t-kh-\xi \\ z(\xi|t-kh+h, t-kh-h) & t-kh-h-\xi \end{vmatrix} \quad (5.1.2)$$

where $z(\xi|t-kh+h, t-kh) = \frac{1}{(-t+kh-h+t-kh)} \begin{vmatrix} z(t-kh+h) & t-kh+h-\xi \\ z(t-kh) & t-kh-\xi \end{vmatrix}$, and

$$z(\xi|t-kh+h, t-kh-h) = \frac{1}{(t-kh-h-h+kh-t)} \begin{vmatrix} z(t-kh+h) & t-kh+h-\xi \\ z(t-kh-h) & t-kh-h-\xi \end{vmatrix}$$

Thus, (5.1.2) becomes,

$$z(\xi) = \frac{-1}{h} \left(\begin{aligned} &(-1/h)(t-kh-h-\xi)((t-kh-\xi)z(t-kh+h) - (t-kh+h-\xi)z(t-kh)) - \\ &(-1/(2h))(t-kh-\xi)((t-kh-h-\xi)z(t-kh+h) - (t-kh+h-\xi)z(t-kh-h)) \end{aligned} \right) \quad (5.1.3)$$

By replacing $\xi = t-kh + (\mathcal{G}/2)h$, (5.1.3) becomes,

$$z(\xi) = (-h - (\mathcal{G}/2)h)(1/h^2)((-\mathcal{G}/2)h)z(t-kh+h) - h(1 - (\mathcal{G}/2))z(t-kh) - (\mathcal{G}/2)h(1/(2h^2))((-h - (\mathcal{G}/2)h)z(t-kh+h) - h(1 - (\mathcal{G}/2))z(t-kh-h)) \quad (5.1.4)$$

$$z(\xi) = -\left(1 - \frac{\mathcal{G}}{2}\right)\left(\frac{\mathcal{G}}{4}\right)z(t-kh-h) + \left(1 - \frac{\mathcal{G}}{2}\right)\left(1 + \frac{\mathcal{G}}{2}\right)z(t-kh) + \left(1 + \frac{\mathcal{G}}{2}\right)\left(\frac{\mathcal{G}}{2} - \frac{\mathcal{G}}{4}\right)z(t-kh+h) \quad (5.1.5)$$

$$z(\xi) = z(t-kh-h)\left(\frac{\mathcal{G}^2}{8} - \frac{\mathcal{G}}{4}\right) + z(t-kh)\left(1 - \frac{\mathcal{G}^2}{4}\right) + z(t-kh+h)\left(\frac{\mathcal{G}^2}{8} + \frac{\mathcal{G}}{4}\right) \quad (5.1.6)$$

Also, the 3-point Lagrange interpolation [94], [156] can be utilized to obtain the signal $z(t)$ for the three nodes $z(t-kh-h)$, $z(t-kh)$ and $z(t-kh+h)$ as:

$$z(\xi) = \frac{(\xi-t-h+kh)(\xi-t+kh)}{(t-h-kh-t-h+kh)(t-h-kh-t+kh)}z(t-h-kh) + \frac{(\xi-t-h+kh)(\xi-t+kh+h)}{(t-kh-t-h+kh)(t-kh-t+kh+h)}z(t-kh) + \frac{(\xi-t+kh)(\xi-t+kh+h)}{(t+h-kh-t+kh)(t+h-kh-t+kh+h)}z(t-kh+h) \quad (5.1.7)$$

$$z(\xi) = \left(\frac{((\xi-t+kh)(\xi-t-h+kh))/2h^2}{z(t-h-kh)} - \left(\frac{((\xi-t+kh+h)(\xi-t-h+kh))/h^2}{z(t-kh)}\right) + \left(\frac{((\xi-t+kh+h)(\xi-t+kh))/2h^2}{z(t-kh+h)}\right)\right) \quad (5.1.8)$$

Substituting $\xi = t-kh + (\mathcal{G}/2)h$ in (5.1.8),

$$z(\xi) = \left(\frac{((t-kh+(\mathcal{G}/2)h-t+kh)(t-kh+(\mathcal{G}/2)h-t-h+kh))/2h^2}{z(t-h-kh)} - \left(\frac{((t-kh+(\mathcal{G}/2)h-t-h+kh)(t-kh+(\mathcal{G}/2)h-t+kh+h))/h^2}{z(t-kh)}\right) + \left(\frac{((t-kh+(\mathcal{G}/2)h-t+kh)(t-kh+(\mathcal{G}/2)h-t+kh+h))/2h^2}{z(t-kh+h)}\right)\right) \quad (5.1.9)$$

$$z(\xi) = z(t-kh-h)\left(\frac{\mathcal{G}^2}{8} - \frac{\mathcal{G}}{4}\right) + z(t-kh)\left(1 - \frac{\mathcal{G}^2}{4}\right) + z(t-kh+h)\left(\frac{\mathcal{G}^2}{8} + \frac{\mathcal{G}}{4}\right) \quad (5.1.10)$$

Similarly, the signal $z(t)$ is obtained utilizing the Newton Interpolation method [93], [156] by taking into consideration the three nodes $z(t-kh-h)$, $z(t-kh)$ and $z(t-kh+h)$ given by:

$$z(\xi) = z[t-kh-h] + z[t-kh-h, t-kh](\xi-t+h+kh) + z[t-kh-h, t-kh, t-kh+h](\xi-t+h+kh)(\xi-t+kh) \quad (5.1.11)$$

where $z[t-kh-h] = z(t-kh-h)$, $z[t-kh-h, t-kh] = (z(t-kh) - z(t-kh-h))/h$, and

$$z[t-kh-h, t-kh, t-kh+h] = (z[t-kh, t-kh+h] - z[t-kh-h, t-kh])/2h \\ = (z(t-kh-h) - 2z(t-kh) + z(t-kh+h))/2h^2$$

Thus, (5.1.11) becomes,

$$z(\xi) = z(t-kh-h) + (\xi-t+kh+h)(z(t-kh) - z(t-kh-h))/h + (\xi-t+kh+h)(\xi-t+kh)(z(t-kh+h) - 2z(t-kh) + z(t-kh-h))/2h^2 \quad (5.1.12)$$

Substituting $\xi = t-kh + (\mathcal{G}/2)h$, (5.1.12) becomes,

$$z(\xi) = z(t-kh-h) + (t-kh + (\mathcal{G}/2)h - t + h + kh)((z(t-kh) - z(t-kh-h))/h) + (t-kh + (\mathcal{G}/2)h - t + kh + h)(t-kh + (\mathcal{G}/2)h - t + kh) \\ ((z(t-kh+h) - 2z(t-kh) + z(t-kh-h))/2h^2) \quad (5.1.13)$$

$$z(\xi) = z(t-kh-h) + (z(t-kh) - z(t-kh-h))\left(\frac{\mathcal{G}}{2} + 1\right) + \frac{z(t-kh+h) - 2z(t-kh) + z(t-kh-h)}{2}\left(\frac{\mathcal{G}}{2} + \frac{\mathcal{G}^2}{4}\right) \quad (5.1.14)$$

$$z(\xi) = z(t-kh-h)\left(\frac{\mathcal{G}^2}{8} - \frac{\mathcal{G}}{4}\right) + z(t-kh)\left(1 - \frac{\mathcal{G}^2}{4}\right) + z(t-kh+h)\left(\frac{\mathcal{G}^2}{8} + \frac{\mathcal{G}}{4}\right) \quad (5.1.15)$$

It is observed that (5.1.6), (5.1.10), and (5.1.15) provide the same coefficients. By comparing (5.1.1) and (5.1.6), the signal $z(\xi)$ is introduced by $z(t)$ on non-node which is a linear combination of $z(t-kh-h)$, $z(t-kh)$, and $z(t-kh+h)$ nodes. Therefore, $z(\xi)$ comprises further information about its neighbors. The least change in the gray levels of an image is one pixel, so, h is considered to be one. Consequently, substituting $z(t)$ in (5.1.1) with $z(\xi)$ in (5.1.6), the following approximation is obtained:

$$\frac{\partial^{\vartheta} z(t)}{\partial t^{\vartheta}} \cong \frac{2}{(h)^{\vartheta}} \sum_{k=0}^{n-1} \frac{(-1)^k \Gamma(\vartheta+1)}{\Gamma\left(\frac{\vartheta}{2}-k+1\right)\Gamma\left(\frac{\vartheta}{2}+k+1\right)} \left[\begin{aligned} &\left(\frac{\vartheta^2}{8}-\frac{\vartheta}{4}\right)z(t-kh-h) + \left(1-\frac{\vartheta^2}{4}\right)z(t-kh) \\ &+ \left(\frac{\vartheta^2}{8}+\frac{\vartheta}{4}\right)z(t-kh+h) \end{aligned} \right] \quad (5.1.16)$$

After the expansion of (5.1.16), (5.1.17) is obtained in the following manner:

$$\begin{aligned} \frac{\partial^{\vartheta} z(t)}{\partial t^{\vartheta}} &\cong \frac{2\Gamma(\vartheta+1)}{\left(\Gamma\left(\frac{\vartheta}{2}+1\right)\right)^2} \left[\left(\frac{\vartheta^2}{8}-\frac{\vartheta}{4}\right)z(t-1) + \left(1-\frac{\vartheta^2}{4}\right)z(t) + \left(\frac{\vartheta^2}{8}+\frac{\vartheta}{4}\right)z(t+1) \right] - \\ &\frac{2\Gamma(\vartheta+1)}{\Gamma\left(\frac{\vartheta}{2}\right)\Gamma\left(\frac{\vartheta}{2}+2\right)} \left[\left(\frac{\vartheta^2}{8}-\frac{\vartheta}{4}\right)z(t-2) + \left(1-\frac{\vartheta^2}{4}\right)z(t-1) + \left(\frac{\vartheta^2}{8}+\frac{\vartheta}{4}\right)z(t) \right] + \frac{2\Gamma(\vartheta+1)}{\Gamma\left(\frac{\vartheta}{2}-1\right)\Gamma\left(\frac{\vartheta}{2}+3\right)} \\ &\left[\left(\frac{\vartheta^2}{8}-\frac{\vartheta}{4}\right)z(t-3) + \left(1-\frac{\vartheta^2}{4}\right)z(t-2) + \left(\frac{\vartheta^2}{8}+\frac{\vartheta}{4}\right)z(t-1) \right] + \dots + \frac{2(-1)^{n-1}\Gamma(\vartheta+1)}{\Gamma\left(\frac{\vartheta}{2}-n+2\right)\Gamma\left(\frac{\vartheta}{2}+n\right)} \\ &\left[\left(\frac{\vartheta^2}{8}-\frac{\vartheta}{4}\right)z(t-n) + \left(1-\frac{\vartheta^2}{4}\right)z(t-n+1) + \left(\frac{\vartheta^2}{8}+\frac{\vartheta}{4}\right)z(t-n+2) \right] \end{aligned} \quad (5.1.17)$$

By considering the top $n+2$ terms, the signal $z(t)$ is approximated as:

$$\begin{aligned} \frac{\partial^{\vartheta} z(t)}{\partial t^{\vartheta}} &\cong z(t+1) \left[\frac{2\Gamma(\vartheta+1)}{\left(\Gamma\left(\frac{\vartheta}{2}+1\right)\right)^2} \left(\frac{\vartheta^2}{8}+\frac{\vartheta}{4}\right) \right] + z(t) \left[\frac{2\Gamma(\vartheta+1)}{\left(\Gamma\left(\frac{\vartheta}{2}+1\right)\right)^2} \left(1-\frac{\vartheta^2}{4}\right) - \frac{2\Gamma(\vartheta+1)}{\Gamma\left(\frac{\vartheta}{2}\right)\Gamma\left(\frac{\vartheta}{2}+2\right)} \left(\frac{\vartheta^2}{8}+\frac{\vartheta}{4}\right) \right] + \\ &z(t-1) \left[\frac{2\Gamma(\vartheta+1)}{\left(\Gamma\left(\frac{\vartheta}{2}+1\right)\right)^2} \left(\frac{\vartheta^2}{8}-\frac{\vartheta}{4}\right) - \frac{2\Gamma(\vartheta+1)}{\Gamma\left(\frac{\vartheta}{2}\right)\Gamma\left(\frac{\vartheta}{2}+2\right)} \left(1-\frac{\vartheta^2}{4}\right) + \frac{2\Gamma(\vartheta+1)}{\Gamma\left(\frac{\vartheta}{2}-1\right)\Gamma\left(\frac{\vartheta}{2}+3\right)} \left(\frac{\vartheta^2}{8}+\frac{\vartheta}{4}\right) \right] + \\ &z(t-2) \left[-\frac{2\Gamma(\vartheta+1)}{\Gamma\left(\frac{\vartheta}{2}\right)\Gamma\left(\frac{\vartheta}{2}+2\right)} \left(\frac{\vartheta^2}{8}-\frac{\vartheta}{4}\right) + \frac{2\Gamma(\vartheta+1)}{\Gamma\left(\frac{\vartheta}{2}-1\right)\Gamma\left(\frac{\vartheta}{2}+3\right)} \left(1-\frac{\vartheta^2}{4}\right) - \frac{2\Gamma(\vartheta+1)}{\Gamma\left(\frac{\vartheta}{2}-2\right)\Gamma\left(\frac{\vartheta}{2}+4\right)} \left(\frac{\vartheta^2}{8}+\frac{\vartheta}{4}\right) \right] \\ &+ \dots + z(t-n) \left[\frac{2(-1)^{n-1}\Gamma(\vartheta+1)}{\Gamma\left(\frac{\vartheta}{2}-n+2\right)\Gamma\left(\frac{\vartheta}{2}+n\right)} \left(\frac{\vartheta^2}{8}-\frac{\vartheta}{4}\right) + \frac{2(-1)^n\Gamma(\vartheta+1)}{\Gamma\left(\frac{\vartheta}{2}-n+1\right)\Gamma\left(\frac{\vartheta}{2}+n+1\right)} \left(1-\frac{\vartheta^2}{4}\right) + \right. \\ &\left. \frac{2(-1)^{n+1}\Gamma(\vartheta+1)}{\Gamma\left(\frac{\vartheta}{2}-n\right)\Gamma\left(\frac{\vartheta}{2}+n+2\right)} \left(\frac{\vartheta^2}{8}+\frac{\vartheta}{4}\right) \right] \end{aligned} \quad (5.1.18)$$

However, while considering the images, (5.1.18) becomes:

$$\begin{aligned}
\frac{\partial^{\vartheta} z(i, j)}{\partial i^{\vartheta}} \cong & z(i+1, j) \left[\frac{2\Gamma(\vartheta+1)}{\left(\Gamma\left(\frac{\vartheta}{2}+1\right)\right)^2} \left(\frac{\vartheta^2}{8} + \frac{\vartheta}{4}\right) \right] + z(i, j) \left[\frac{2\Gamma(\vartheta+1)}{\left(\Gamma\left(\frac{\vartheta}{2}+1\right)\right)^2} \left(1 - \frac{\vartheta^2}{4}\right) - \frac{2\Gamma(\vartheta+1)}{\Gamma\left(\frac{\vartheta}{2}\right)\Gamma\left(\frac{\vartheta}{2}+2\right)} \left(\frac{\vartheta^2}{8} + \frac{\vartheta}{4}\right) \right] + \\
& z(i-1, j) \left[\frac{2\Gamma(\vartheta+1)}{\left(\Gamma\left(\frac{\vartheta}{2}+1\right)\right)^2} \left(\frac{\vartheta^2}{8} - \frac{\vartheta}{4}\right) - \frac{2\Gamma(\vartheta+1)}{\Gamma\left(\frac{\vartheta}{2}\right)\Gamma\left(\frac{\vartheta}{2}+2\right)} \left(1 - \frac{\vartheta^2}{4}\right) + \frac{2\Gamma(\vartheta+1)}{\Gamma\left(\frac{\vartheta}{2}-1\right)\Gamma\left(\frac{\vartheta}{2}+3\right)} \left(\frac{\vartheta^2}{8} + \frac{\vartheta}{4}\right) \right] + \\
& z(i-2, j) \left[-\frac{2\Gamma(\vartheta+1)}{\Gamma\left(\frac{\vartheta}{2}\right)\Gamma\left(\frac{\vartheta}{2}+2\right)} \left(\frac{\vartheta^2}{8} - \frac{\vartheta}{4}\right) + \frac{2\Gamma(\vartheta+1)}{\Gamma\left(\frac{\vartheta}{2}-1\right)\Gamma\left(\frac{\vartheta}{2}+3\right)} \left(1 - \frac{\vartheta^2}{4}\right) - \frac{2\Gamma(\vartheta+1)}{\Gamma\left(\frac{\vartheta}{2}-2\right)\Gamma\left(\frac{\vartheta}{2}+4\right)} \left(\frac{\vartheta^2}{8} + \frac{\vartheta}{4}\right) \right] \\
& + \dots + z(i-n, j) \left[\frac{2(-1)^{n-1}\Gamma(\vartheta+1)}{\Gamma\left(\frac{\vartheta}{2}-n+2\right)\Gamma\left(\frac{\vartheta}{2}+n\right)} \left(\frac{\vartheta^2}{8} - \frac{\vartheta}{4}\right) + \frac{2(-1)^n\Gamma(\vartheta+1)}{\Gamma\left(\frac{\vartheta}{2}-n+1\right)\Gamma\left(\frac{\vartheta}{2}+n+1\right)} \left(1 - \frac{\vartheta^2}{4}\right) \right] \\
& \left[+ \frac{2(-1)^{n+1}\Gamma(\vartheta+1)}{\Gamma\left(\frac{\vartheta}{2}-n\right)\Gamma\left(\frac{\vartheta}{2}+n+2\right)} \left(\frac{\vartheta^2}{8} + \frac{\vartheta}{4}\right) \right] \tag{5.1.19}
\end{aligned}$$

$$\begin{aligned}
\frac{\partial^{\vartheta} z(i, j)}{\partial j^{\vartheta}} \cong & z(i, j+1) \left[\frac{2\Gamma(\vartheta+1)}{\left(\Gamma\left(\frac{\vartheta}{2}+1\right)\right)^2} \left(\frac{\vartheta^2}{8} + \frac{\vartheta}{4}\right) \right] + z(i, j) \left[\frac{2\Gamma(\vartheta+1)}{\left(\Gamma\left(\frac{\vartheta}{2}+1\right)\right)^2} \left(1 - \frac{\vartheta^2}{4}\right) - \frac{2\Gamma(\vartheta+1)}{\Gamma\left(\frac{\vartheta}{2}\right)\Gamma\left(\frac{\vartheta}{2}+2\right)} \left(\frac{\vartheta^2}{8} + \frac{\vartheta}{4}\right) \right] + \\
& z(i, j-1) \left[\frac{2\Gamma(\vartheta+1)}{\left(\Gamma\left(\frac{\vartheta}{2}+1\right)\right)^2} \left(\frac{\vartheta^2}{8} - \frac{\vartheta}{4}\right) - \frac{2\Gamma(\vartheta+1)}{\Gamma\left(\frac{\vartheta}{2}\right)\Gamma\left(\frac{\vartheta}{2}+2\right)} \left(1 - \frac{\vartheta^2}{4}\right) + \frac{2\Gamma(\vartheta+1)}{\Gamma\left(\frac{\vartheta}{2}-1\right)\Gamma\left(\frac{\vartheta}{2}+3\right)} \left(\frac{\vartheta^2}{8} + \frac{\vartheta}{4}\right) \right] + \\
& z(i, j-2) \left[-\frac{2\Gamma(\vartheta+1)}{\Gamma\left(\frac{\vartheta}{2}\right)\Gamma\left(\frac{\vartheta}{2}+2\right)} \left(\frac{\vartheta^2}{8} - \frac{\vartheta}{4}\right) + \frac{2\Gamma(\vartheta+1)}{\Gamma\left(\frac{\vartheta}{2}-1\right)\Gamma\left(\frac{\vartheta}{2}+3\right)} \left(1 - \frac{\vartheta^2}{4}\right) - \frac{2\Gamma(\vartheta+1)}{\Gamma\left(\frac{\vartheta}{2}-2\right)\Gamma\left(\frac{\vartheta}{2}+4\right)} \left(\frac{\vartheta^2}{8} + \frac{\vartheta}{4}\right) \right] \\
& + \dots + z(i, j-n) \left[\frac{2(-1)^{n-1}\Gamma(\vartheta+1)}{\Gamma\left(\frac{\vartheta}{2}-n+2\right)\Gamma\left(\frac{\vartheta}{2}+n\right)} \left(\frac{\vartheta^2}{8} - \frac{\vartheta}{4}\right) + \frac{2(-1)^n\Gamma(\vartheta+1)}{\Gamma\left(\frac{\vartheta}{2}-n+1\right)\Gamma\left(\frac{\vartheta}{2}+n+1\right)} \left(1 - \frac{\vartheta^2}{4}\right) \right] \\
& \left[+ \frac{2(-1)^{n+1}\Gamma(\vartheta+1)}{\Gamma\left(\frac{\vartheta}{2}-n\right)\Gamma\left(\frac{\vartheta}{2}+n+2\right)} \left(\frac{\vartheta^2}{8} + \frac{\vartheta}{4}\right) \right] \tag{5.1.20}
\end{aligned}$$

The following mask coefficients are obtained from (5.1.19) and (5.1.20):

$$\left. \begin{aligned}
m_{-1} &= \frac{2\Gamma(\vartheta+1)}{\left(\Gamma\left(\frac{\vartheta}{2}+1\right)\right)^2} \left(\frac{\vartheta^2}{8} + \frac{\vartheta}{4}\right) \\
m_0 &= \frac{2\Gamma(\vartheta+1)}{\left(\Gamma\left(\frac{\vartheta}{2}+1\right)\right)^2} \left(1 - \frac{\vartheta^2}{4}\right) - \frac{2\Gamma(\vartheta+1)}{\Gamma\left(\frac{\vartheta}{2}\right)\Gamma\left(\frac{\vartheta}{2}+2\right)} \left(\frac{\vartheta^2}{8} + \frac{\vartheta}{4}\right) \\
m_1 &= \frac{2\Gamma(\vartheta+1)}{\left(\Gamma\left(\frac{\vartheta}{2}+1\right)\right)^2} \left(\frac{\vartheta^2}{8} - \frac{\vartheta}{4}\right) - \frac{2\Gamma(\vartheta+1)}{\Gamma\left(\frac{\vartheta}{2}\right)\Gamma\left(\frac{\vartheta}{2}+2\right)} \left(1 - \frac{\vartheta^2}{4}\right) + \frac{2\Gamma(\vartheta+1)}{\Gamma\left(\frac{\vartheta}{2}-1\right)\Gamma\left(\frac{\vartheta}{2}+3\right)} \left(\frac{\vartheta^2}{8} + \frac{\vartheta}{4}\right) \\
m_2 &= -\frac{2\Gamma(\vartheta+1)}{\Gamma\left(\frac{\vartheta}{2}\right)\Gamma\left(\frac{\vartheta}{2}+2\right)} \left(\frac{\vartheta^2}{8} - \frac{\vartheta}{4}\right) + \frac{2\Gamma(\vartheta+1)}{\Gamma\left(\frac{\vartheta}{2}-1\right)\Gamma\left(\frac{\vartheta}{2}+3\right)} \left(1 - \frac{\vartheta^2}{4}\right) - \frac{2\Gamma(\vartheta+1)}{\Gamma\left(\frac{\vartheta}{2}-2\right)\Gamma\left(\frac{\vartheta}{2}+4\right)} \left(\frac{\vartheta^2}{8} + \frac{\vartheta}{4}\right) \\
&\vdots \\
&\vdots \\
m_n &= \left[\frac{2(-1)^{n-1}\Gamma(\vartheta+1)}{\Gamma\left(\frac{\vartheta}{2}-n+2\right)\Gamma\left(\frac{\vartheta}{2}+n\right)} \left(\frac{\vartheta^2}{8} - \frac{\vartheta}{4}\right) + \frac{2(-1)^n\Gamma(\vartheta+1)}{\Gamma\left(\frac{\vartheta}{2}-n+1\right)\Gamma\left(\frac{\vartheta}{2}+n+1\right)} \left(1 - \frac{\vartheta^2}{4}\right) + \frac{2(-1)^{n+1}\Gamma(\vartheta+1)}{\Gamma\left(\frac{\vartheta}{2}-n\right)\Gamma\left(\frac{\vartheta}{2}+n+2\right)} \left(\frac{\vartheta^2}{8} + \frac{\vartheta}{4}\right) \right]
\end{aligned} \right\} \quad (5.1.21)$$

The mask coefficients for the RFOD are obtained from (5.1.21). The FOD masks in eight directions with $n \times n$ size are shown in Figure 5.1.

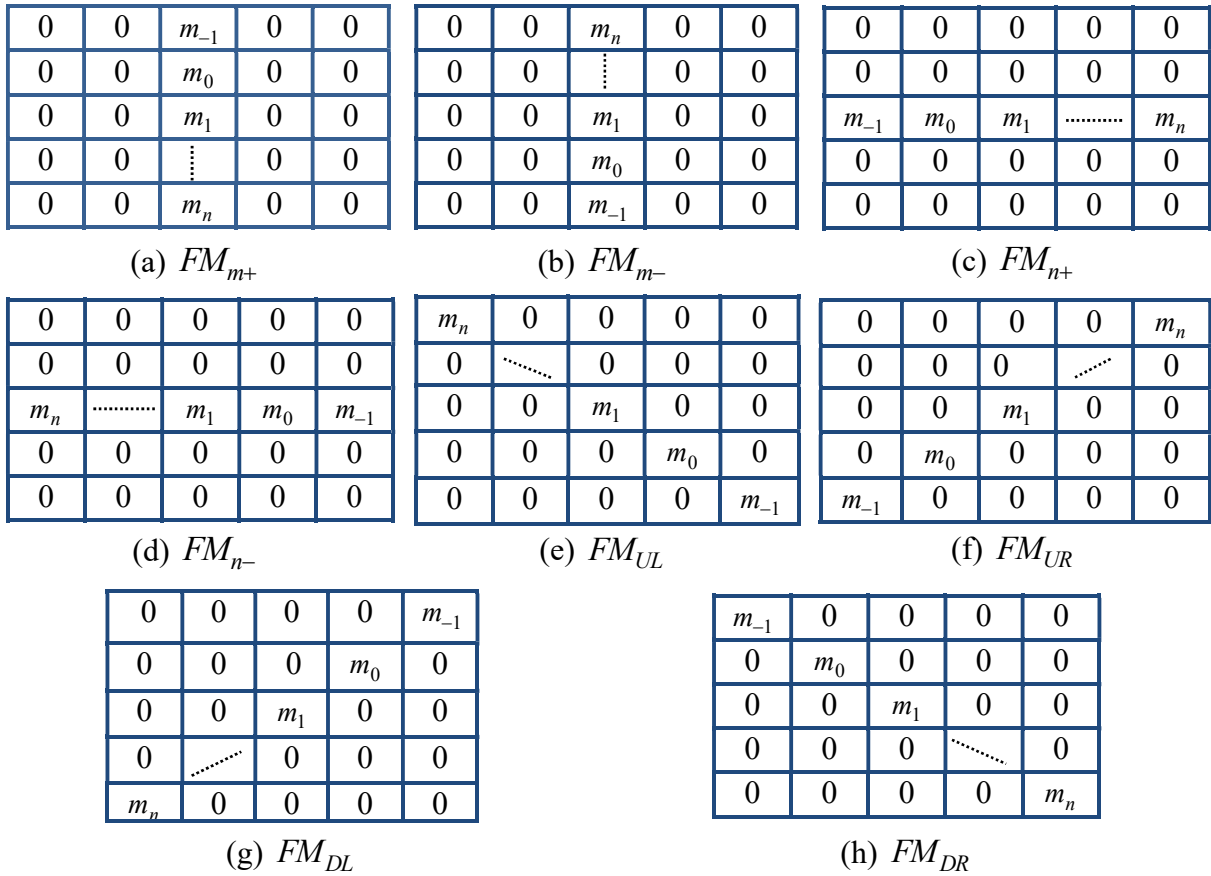


Figure 5.1: FOD masks of $n \times n$ size in eight directions

The above presented RFOD masks are applied in the eight directions, that is, positive i -axis (FM_{m+}), negative i -axis (FM_{m-}), positive j -axis (FM_{n+}), negative j -axis (FM_{n-}), upward right (FM_{UR}), upward left (FM_{UL}), downward right (FM_{DR}), and downward left (FM_{DL}) diagonals respectively.

5.1.2 Framework of Proposed Approach

The FrFT based RFOD approach for edge detection as well as image enhancement is illustrated in Figure 5.2. Initially, the bilateral filtering of an input image $z(i,j)$ is done to preserve the edges present in an image [189]. Based on the suitable fractional order (ϑ), the fractional mask $Z_{R_p}(i,j)$ is obtained from $FM_p(i,j)$ in the direction p . Then, the transformation of fractional mask coefficients and the preprocessed image is done into the FrFTD with the FrFT rotation angle (ϕ). Subsequently, their convolution is performed according to the convolution theorem in the FrFTD [37] as:

$$Z_{M_p}(u,v) = Z_F(u,v)Z_{RF_p}(u,v)e^{-(j/2)u^2 \cot \phi} \quad (5.1.22)$$

Further, the image coefficients $Z_F(u,v)$ and the fractional mask $Z_{RF_p}(u,v)$ are multiplied before passing through a chirp multiplier $e^{-(j/2)u^2 \cot \phi}$. Further, the image with edge information $Z_{M_p}(u,v)$ is inverse transformed into the spatial domain by IFrFT. In a similar manner, the images with edge information are attained in the other seven directions. Then, the obtained eight images are projected into two directions by the linear combination as [93]:

$$D_x Z_{IM}(i,j) = Z_{IM_{n-}}(i,j) - Z_{IM_{n+}}(i,j) + \frac{\sqrt{2}}{2} \left(\begin{array}{l} Z_{IM_{DR}}(i,j) - Z_{IM_{DL}}(i,j) + \\ Z_{IM_{UL}}(i,j) - Z_{IM_{UR}}(i,j) \end{array} \right) \quad (5.1.23)$$

$$D_y Z_{IM}(i,j) = Z_{IM_{m+}}(i,j) - Z_{IM_{m-}}(i,j) + \frac{\sqrt{2}}{2} \left(\begin{array}{l} Z_{IM_{DR}}(i,j) - Z_{IM_{UL}}(i,j) + \\ Z_{IM_{DL}}(i,j) - Z_{IM_{UR}}(i,j) \end{array} \right) \quad (5.1.24)$$

Then, the norm of gradient is determined from (5.1.23) and (5.1.24) as follows:

$$Z_G(i,j) = \sqrt{D_x^2 + D_y^2} \quad (5.1.25)$$

The obtained gradient image $Z_G(i,j)$ is further used for tracking and connecting the edges referred to as Edge Tracking (ET) in a manner similar to non-maxima suppression for obtaining thin and continuous edges. Eventually, the notion of high boost filtering is utilized for obtaining the edge enhanced image $Z(i,j)$. The gradient image $Z_G(i,j)$ is added to the

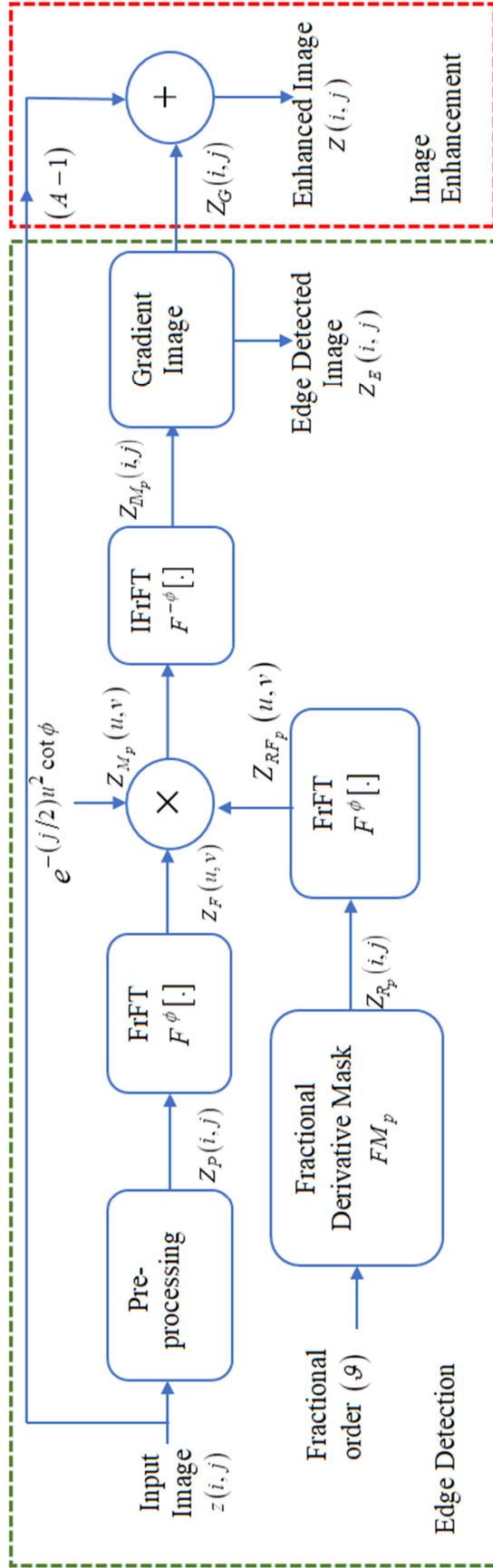


Figure 5.2: Framework of proposed FrFT based RFOD approach

image attained by multiplying the input image with the factor $(A-1)$ given by:

$$Z(i, j) = Z_G(i, j) + (A-1)z(i, j) \quad (5.1.26)$$

such that A is the factor of amplification ($A > 1$). Hence, an enhanced image is achieved that preserved the low-frequency features while emphasizing the high-frequency features. The pseudo-code of the presented FrFT based RFOD technique is described as follows:

Pseudo-code of proposed FrFT based RFOD technique

Inputs: z, \mathcal{G}, ϕ, A ; **Output:** Z

z : Test Image; \mathcal{G} : RFOD fractional order; ϕ : FrFT rotation angle

A : Factor of amplification; $FM(\)$: RFOD mask

begin

$Z_p = \text{BilateralFilter}(z)$;

$Z_F = \text{FrFT}(Z_p, \phi)$;

Computing the RFOD mask coefficients from (5.1.21);

$Z_{R_p} = FM(\mathcal{G})$;

$Z_{RF_p} = \text{FrFT}(Z_{R_p}, \phi)$;

$Z_{M_p} = Z_F Z_{RF_p} e^{-(j/2)u^2 \cot \phi}$;

$Z_{IM_p} = \text{IFrFT}(Z_{M_p}, -\phi)$;

Compute Gradient image (Z_G) using (5.1.25);

$Z_E = ET(Z_G)$;

$Z = Z_G + (A-1)z$;

end

5.2 Performance Analysis of FrFT based RFOD Approach

The robustness of the FrFT based RFOD is established from the qualitative as well as quantitative investigation by considering grayscale images of Lena, Butterfly, Palace, Fish, Vase, Cars, Barbara, Pirate, Texture, Seeds, Road, and Birds of different sizes from various datasets namely Classic 5, Set12, BSD68 [177], RESIDE [178], and Normalized Brodatz [179]. Moreover, the adequacy is confirmed based on the evaluation of the proposed approach against existing edge detection and image enhancement approaches.

5.2.1 Selection of Mask Size

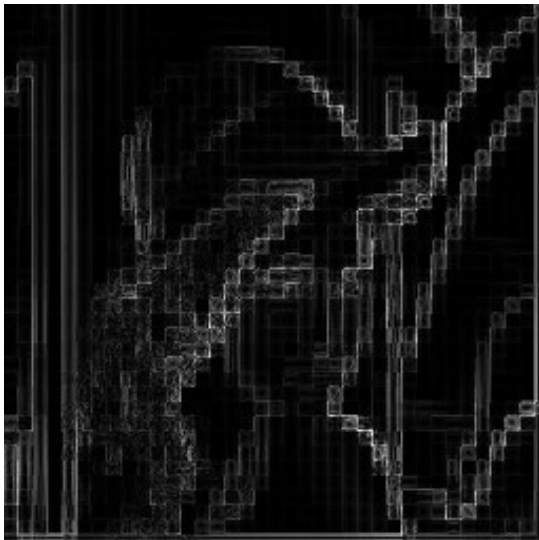
Initially, the presented FrFT based RFOD approach is executed by employing the different mask sizes, that is, 3×3 , 5×5 , 7×7 , 9×9 , and 11×11 . The scaled version of the resultant gradient images of various mask sizes obtained for the Lena image is shown in Figure 5.3.



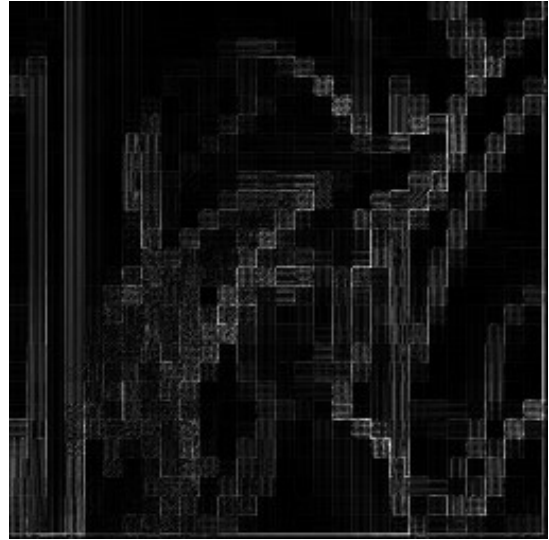
Mask size of 3×3



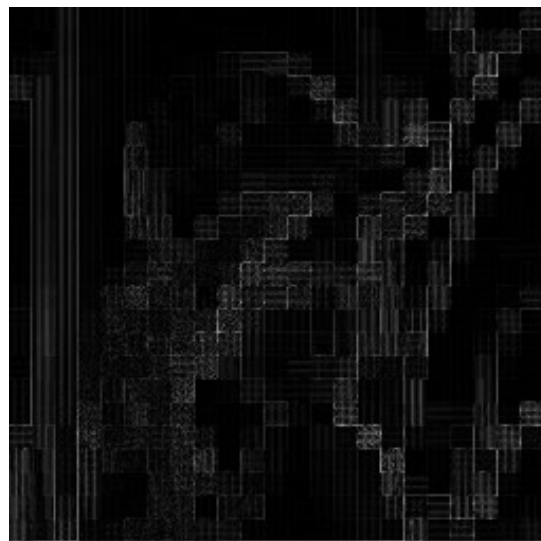
Mask size of 5×5



Mask size of 7×7



Mask size of 9×9



Mask size of 11×11

Figure 5.3: Gradient images for various mask sizes for Lena image (256×256)

As compared to the other mask sizes, the 3×3 mask provided more information about edges but for the 5×5 mask, blocking artifacts become observable causing loss of edge information. The effect of the size of the mask is also considered for the Barbara and Texture images as demonstrated in Figure 5.4.

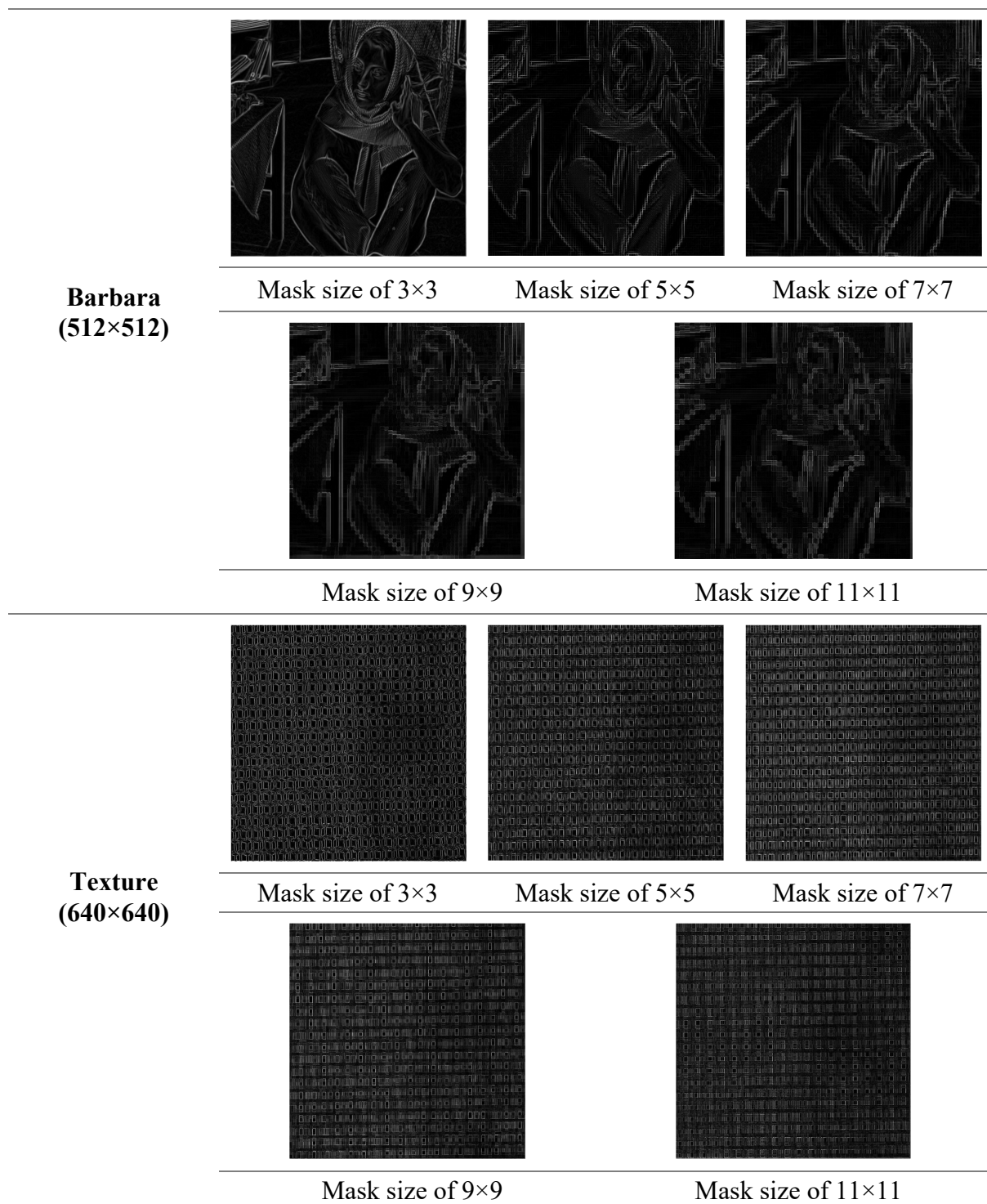


Figure 5.4: Images for different mask sizes

It is discernable from Figure 5.3 and Figure 5.4 that only a 3×3 mask can preserve the edge information because the blocking artifacts that became visible in the 5×5 mask proliferate with the further increase in the mask size. It is perhaps because of the non-periodic nature of images. Moreover, the performance metrics FOM and EPI are computed for these mask sizes in Table 5.1.

Table 5.1: Effect of variation in mask sizes on edge detection parameters

Mask Size/ Images	Parameters	3×3	5×5	7×7	9×9	11×11
Lena	FOM	0.7689	0.7194	0.3945	0.3093	0.2911
	EPI	0.7961	0.5785	0.5272	0.5136	0.3292
Barbara	FOM	0.7290	0.6004	0.5999	0.5344	0.4901
	EPI	0.8038	0.6618	0.4697	0.4730	0.4552
Texture	FOM	0.5330	0.4988	0.4583	0.4090	0.3992
	EPI	0.6887	0.6456	0.6349	0.6184	0.6038

Bold indicates the maximum value

It is worth noting that the performance metrics are also high for the mask size of 3×3 in comparison to other masks. Hence, the 3×3 mask is considered in the presented technique for edge detection as well as image enhancement.

5.2.2 Comparative Analysis with Classical Edge Detectors in FrFTD

The comparison of a proposed RFOD approach is done to prove its proficiency over the integer-order derivatives, that is, Prewitt [56], Sobel [57], and Laplacian [21] masks in the FrFTD. The qualitative and quantitative simulation results for the aforementioned comparison considering the Butterfly image are shown in Figure 5.5 and Table 5.2. The quantitative comparison is done by the edge detection parameters FOM and EPI.



Figure 5.5: Comparative analysis of proposed approach with classical edge detection operators in FrFTD for Butterfly image (256×256)

Table 5.2: Parameters of Butterfly image for various edge detection masks in FrFTD

Parameters/ Mask	Prewitt [56]	Sobel [57]	Laplacian [21]	Proposed
FOM	0.7036	0.7706	0.6614	0.7953
EPI	0.7666	0.8039	0.8727	0.8996

Bold indicates the maximum value

The results show that the integer-order masks extracted thicker edges in comparison to the proposed approach. Both quantitative and qualitative results depict the superiority of the proposed RFOD approach over the classical edge detectors in the FrFTD. As compared to Prewitt, Sobel, and Laplacian operators in the FrFTD, the proposed FrFT based RFOD

provides an improvement of 3.21-20.24% in FOM and 3.08-17.35% in EPI for the Butterfly image. Hence, the proposed approach outperformed the classical edge detectors in the FrFTD.

5.2.3 Qualitative Performance Analysis

The comparison of the proposed FrFT based RFOD to the existing approaches such as NIFD [93], extended CRONE (eCRONE) [123], RLFD [124], FrFTD [11], FOC [92], and Mod GL [141] proved its proficiency. Moreover, its comparison is also done with the techniques proposed in the previous chapter that is, HF referred to as Homomorphic filtering based on Fractional Derivative (HMFD), and image sharpening is referred to as Riesz. The fractional parameters ' ϕ ' and ' ϑ ' rely on the nature of the image or application. The FrFT rotation angle ' ϕ ' is varied from 0 to $\pi/2$ (' a ' is varied from 0 to 1) and ' ϑ ' is varied from 0 to 1. Based on the intensive simulations, it is found that better results are obtained for $\phi = 0.475\pi$ to $\phi = 0.495\pi$. Nevertheless, the selection of the optimal value of both the fractional parameters is done based on FOM and EPI. Figure 5.6 shows the surface plot obtained for the FOM of the Lena image to find the optimal values of fractional parameters.

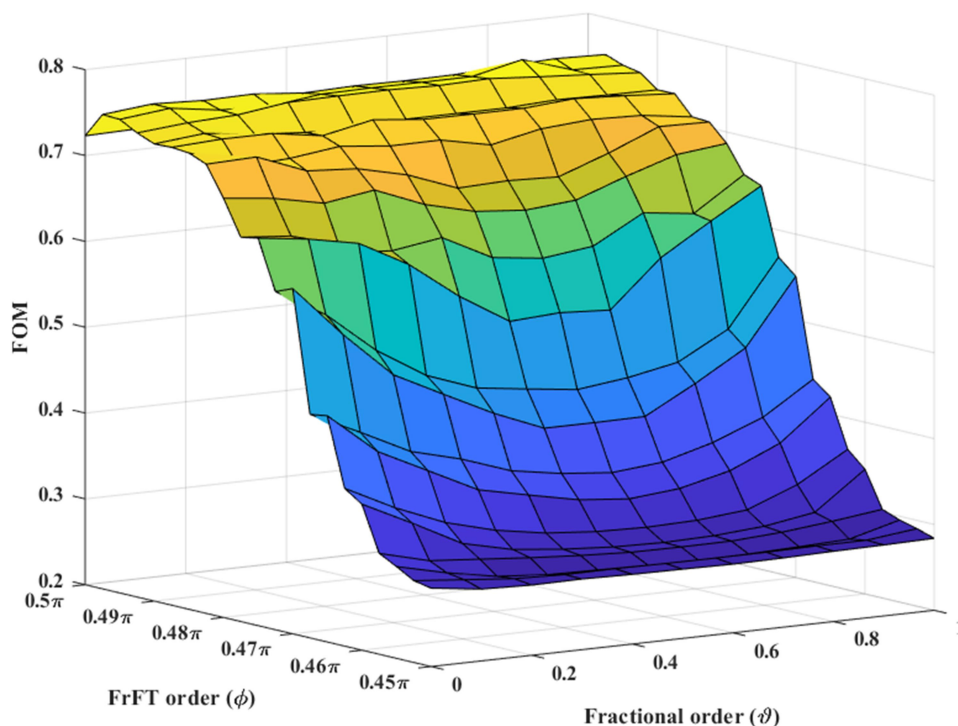


Figure 5.6: FOM based surface plot for Lena image (256×256)

5.2.3.1 Edge Detection

The presented approach is compared against the existing edge detection techniques such as NIFD [93], eCRONE [123], RLFD [124], FrFTD [11], and FOC [92] in qualitative manner. The scaled version of the edge maps obtained by various methods for the Lena image is illustrated in Figure 5.7 for better interpretation of the simulation results.



NIFD [93]



eCRONE [123]



RLFD [124]



FrFTD [11]



FOC [92]



Proposed

Figure 5.7: Edges detected by various approaches for Lena image (256×256)

The clean and continuous edges are detected as compared to the existing approaches without detecting the redundant edges. Moreover, simulation results are provided for some other test images to confirm the capability of the presented approach to detect the edges in a variety of images in Figure 5.8.

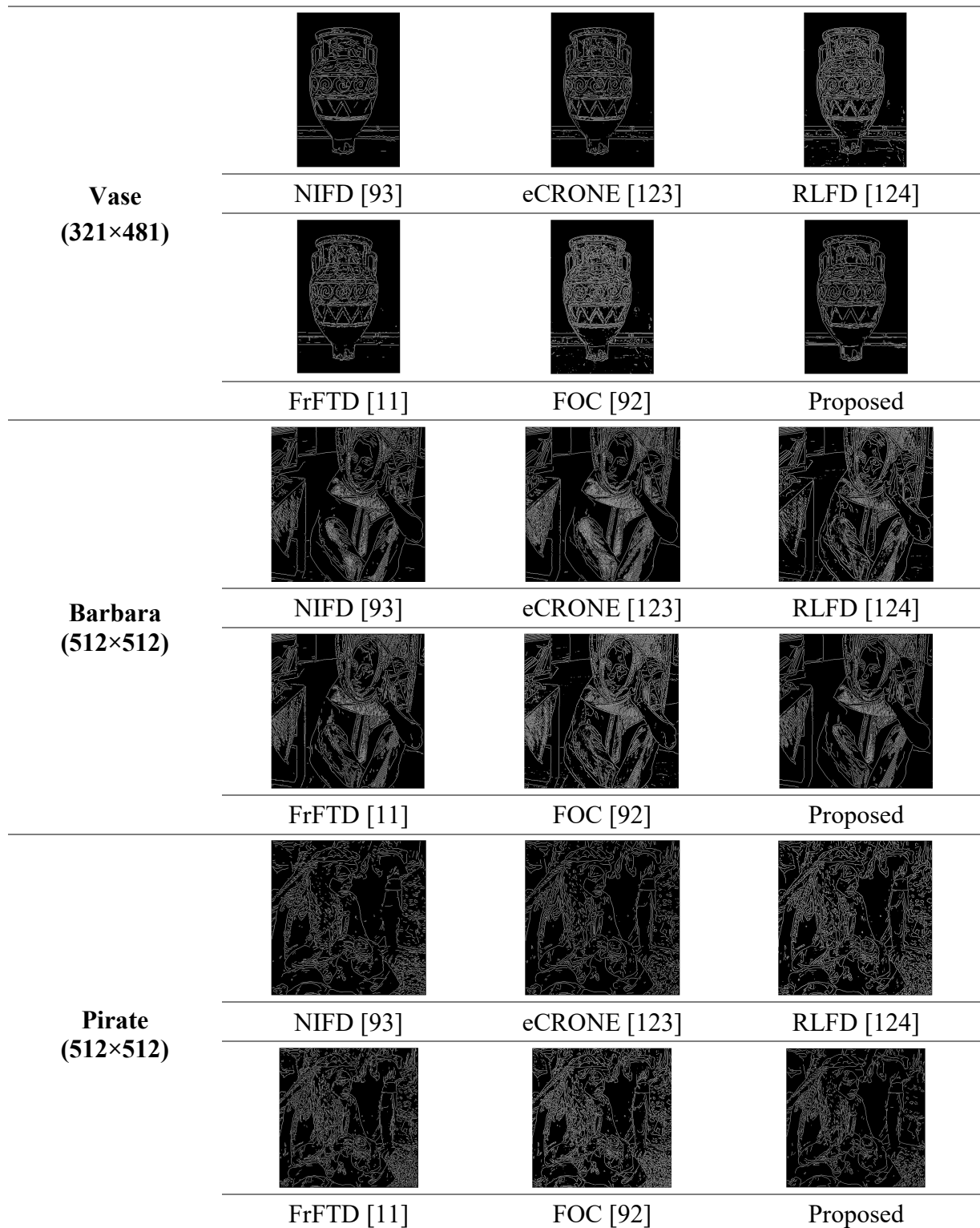


Figure 5.8: Simulation results for various edge detection techniques (contd.)

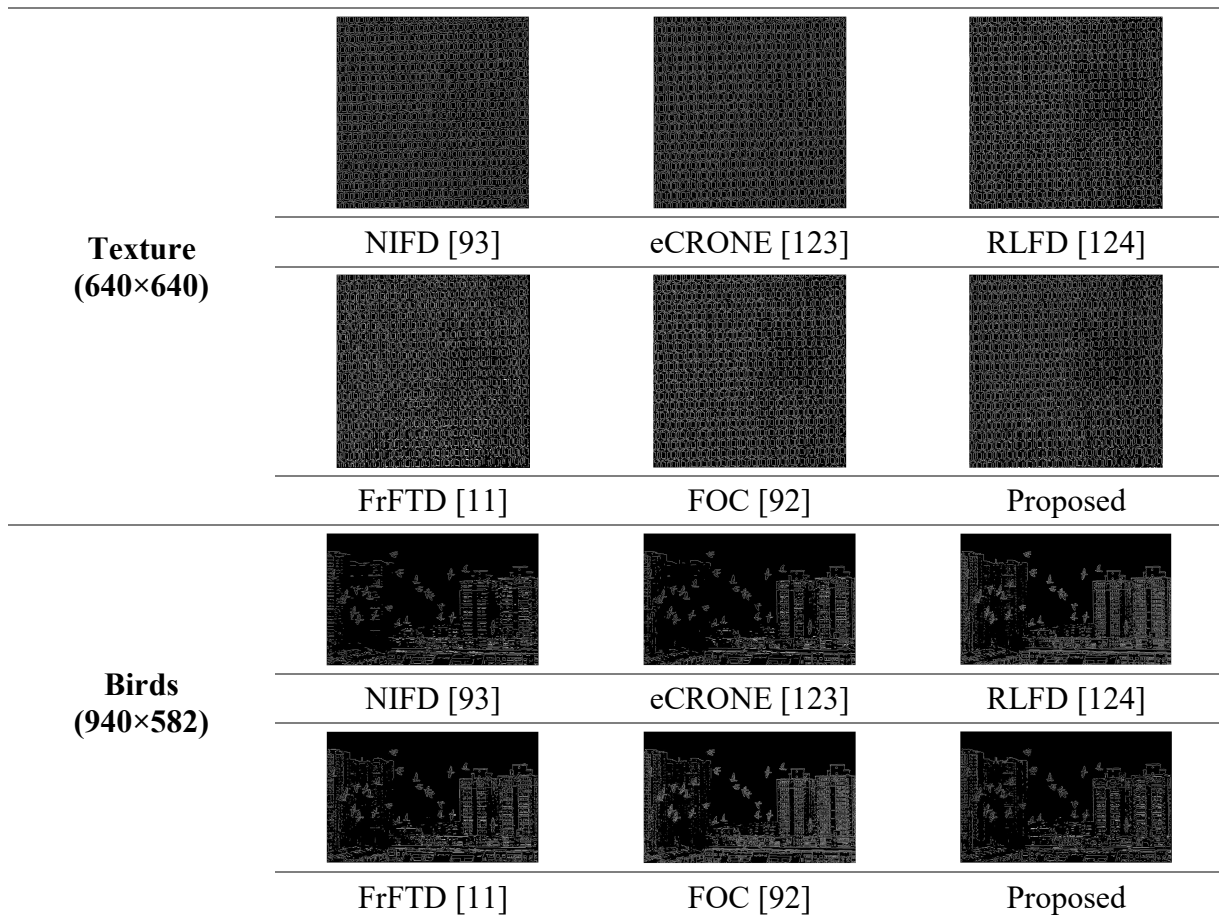


Figure 5.8: Simulation results for various edge detection techniques

It is discerned that clean and continuous edges are extracted by the proposed approach while evading the detection of false edges upon comparing with the existing edge detection techniques for different kinds of images considered for simulation. Moreover, the proposed approach provided better localization of the edges. The edge information extracted by the gradient images is further utilized for image edge enhancement.

5.2.3.2 Image Enhancement

This section is devoted to comparing the proposed approach with Mod GL [141], HMFD, and Riesz in the visual form for image enhancement. The scaled version of the Lena image enhanced by these techniques is demonstrated in Figure 5.9 to establish the capability of the proposed FrFT based RFOD approach for enhancing the images with respect to other techniques along with the zoomed portions.



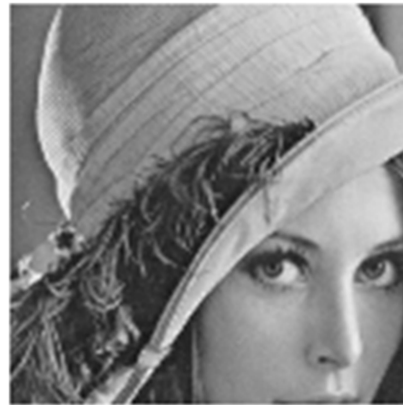
Mod GL [141]



Mod GL [141] (Zoomed)



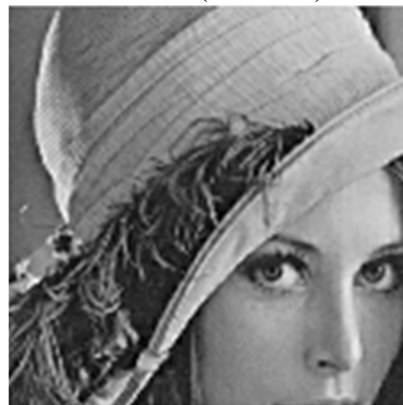
HMFD



HMFD (Zoomed)



Riesz



Riesz (Zoomed)



Proposed



Proposed (Zoomed)

Figure 5.9: Simulation results of Lena image (256×256) for image enhancement techniques

There is a substantial disparity in the images enhanced by the proposed and existing techniques, for instance, the contrast and edges of the hat in the Lena image. Moreover, the simulation results for some other images are shown in Figure 5.10 along with their zoomed portions to show the adequacy of the proposed approach.












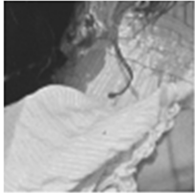
Technique/ Images	Mod GL [141]	HMFD	Riesz	Proposed
Vase (321×481)				
Vase (Zoomed)				
Barbara (512×512)				
Barbara (Zoomed)				
Pirate (512×512)				
Pirate (Zoomed)				

Figure 5.10: Images enhanced by various techniques along with the zoomed portions (contd.)

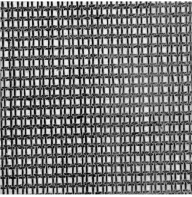
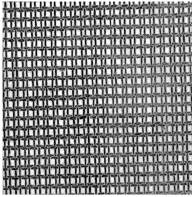
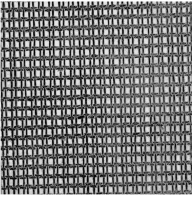
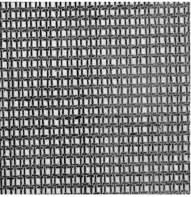
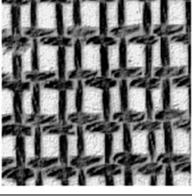
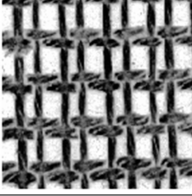
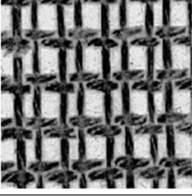
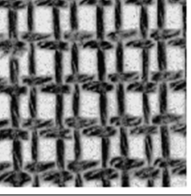








Technique/ Images	Mod GL [141]	HMFD	Riesz	Proposed
Texture (640×640)				
Texture (Zoomed)				
Birds (940×582)				
Birds (Zoomed)				

Figure 5.10: Images enhanced by various techniques along with the zoomed portions

The images enhanced by the proposed framework possess sharper edges as compared to the existing methods, for instance, the edges as well as the contrast of the animal and the crack in the vase, demonstrate a significant difference in the images enhanced by various techniques. Furthermore, the contrast enhancement and edge sharpening in other test images proved the potency of the proposed approach.

5.2.4 Quantitative Performance Analysis

The assessment parameters such as FOM, EPI, IE, AG, EI, EME, Number of Corners, Mean, and GLCM parameters are used for quantitative analysis of the FrFT based RFOD approach as compared to the existing approaches.

5.2.4.1 Edge Detection

High FOM and EPI indicate the potential of edge detection techniques. Therefore, the fractional parameters that provided maximum EPI and FOM are selected for further processing. Table 5.3 illustrates the variation of FOM according to the fractional order (ρ) for considered test images. Besides, the FOM is computed for FOD based edge detection techniques as depicted in Table 5.4.

Table 5.3: Effect of variation in fractional order (ρ) on FOM

Images	0	0.1	0.2	0.3	0.4	0.5	0.6	0.7	0.8	0.9	1
Lena	0.7516	0.7580	0.7394	0.7471	0.7548	0.7552	0.7555	0.7556	0.7689	0.7503	0.7502
Butterfly	0.7894	0.7952	0.7953	0.7936	0.7828	0.7799	0.7782	0.7799	0.7873	0.7936	0.7891
Palace	0.4808	0.4822	0.4829	0.4820	0.4829	0.4825	0.4823	0.4825	0.4823	0.4824	0.4819
Fish	0.4975	0.5000	0.5117	0.4898	0.4805	0.4737	0.4721	0.4738	0.4820	0.4961	0.4919
Vase	0.8263	0.8279	0.8267	0.8278	0.8301	0.8294	0.8291	0.8294	0.8300	0.8274	0.8253
Cars	0.8032	0.8118	0.8218	0.8213	0.7709	0.7593	0.7576	0.7592	0.7740	0.8129	0.8102
Barbara	0.7084	0.7290	0.6867	0.6634	0.6396	0.6255	0.6226	0.6281	0.6507	0.6820	0.6712
Pirate	0.7596	0.7687	0.7725	0.7745	0.7748	0.7746	0.7745	0.7758	0.7760	0.7770	0.7679
Texture	0.5212	0.5220	0.5263	0.5330	0.5310	0.5210	0.5207	0.5210	0.5209	0.5294	0.5219
Seeds	0.9391	0.9410	0.9430	0.9396	0.9276	0.9195	0.9170	0.9196	0.9298	0.9434	0.9399
Road	0.8217	0.8382	0.8472	0.8031	0.7815	0.7652	0.7591	0.7651	0.7836	0.8491	0.8377
Birds	0.4394	0.4528	0.4559	0.4577	0.4439	0.4105	0.4033	0.4056	0.4163	0.4415	0.4308

Bold indicates the maximum value

Table 5.4: FOM for the test images subjected to various edge detection techniques

Images	NIFD [93]	eCRONE[123]	RLFD [124]	FrFTD [11]	FOC [92]	Proposed
Lena	0.7674	0.7640	0.6748	0.5849	0.5703	0.7689
Butterfly	0.7238	0.7884	0.6943	0.6456	0.6156	0.7953
Palace	0.4754	0.4723	0.3053	0.4456	0.2838	0.4829
Fish	0.5099	0.4864	0.3115	0.4270	0.2833	0.5117
Vase	0.8111	0.8083	0.5656	0.7263	0.4441	0.8301
Cars	0.8202	0.8090	0.5448	0.7917	0.4860	0.8218
Barbara	0.7274	0.7023	0.6039	0.5908	0.5363	0.7290
Pirate	0.7761	0.7889	0.5485	0.5880	0.4835	0.7770
Texture	0.5309	0.5259	0.5283	0.4698	0.5039	0.5330
Seeds	0.9058	0.9026	0.5991	0.7733	0.5515	0.9434
Road	0.8468	0.8396	0.5742	0.7600	0.5305	0.8491
Birds	0.4472	0.4363	0.3814	0.4466	0.3559	0.4577

Bold indicates the maximum value

The maximum FOM is provided by the FrFT based RFOD method against the existing edge detection techniques. It is perhaps due to the fact that the FrFT based RFOD approach detected clean and coherent edges. EPI of test images subjected to edge detection techniques is illustrated in Table 5.5.

Table 5.5: EPI for the test images subjected to various edge detection techniques

Images	NIFD [93]	eCRONE[123]	RLFD [124]	FrFTD [11]	FOC [92]	Proposed
Lena	0.6728	0.6861	0.7660	0.7046	0.7881	0.7961
Butterfly	0.7505	0.7541	0.7948	0.7793	0.7899	0.8996
Palace	0.8274	0.8721	0.8839	0.8792	0.8800	0.9173
Fish	0.2943	0.3055	0.4587	0.4212	0.4594	0.4619
Vase	0.9064	0.9145	0.9151	0.8673	0.8599	0.9466
Cars	0.4390	0.4424	0.4454	0.5091	0.4706	0.5419
Barbara	0.6930	0.6972	0.7035	0.7138	0.7154	0.8038
Pirate	0.4982	0.4997	0.5095	0.5105	0.5355	0.6197
Texture	0.6127	0.6273	0.5569	0.6602	0.5750	0.6887
Seeds	0.4526	0.5252	0.5140	0.5747	0.5304	0.6568
Road	0.4183	0.4276	0.3781	0.3452	0.3808	0.4331
Birds	0.4916	0.5002	0.4985	0.5727	0.5101	0.6824

Bold indicates the maximum value

The proposed approach achieved high EPI as there is no distortion of images for RFOD (Section 2.2.4). Moreover, the bilateral filtering in preprocessing and the FrFT phase function preserved the edge information. An improvement of 1.89-50.58% for average FOM and 12.07-19.71% for average EPI is provided by the proposed approach as compared to the existing approaches. Furthermore, an average increase of 4.98 % in FOM and 4.17% in EPI is achieved by FrFT based RFOD as compared to the RFOD in the FT domain ($\phi = \pi/2$). Hence, the proposed edge detection approach outperformed the existing edge detection algorithms in both quantitative and qualitative manner.

5.2.4.2 Image Enhancement

The quantitative analysis based on the assessment parameters namely IE, AG, EI, EME, Number of Corners, Mean, and GLCM based contrast, correlation, energy, and homogeneity measures is conducted for confirming the potential of the presented approach as compared to the existing ones for image enhancement. IE determined for the test images subjected to several image enhancement techniques is shown in Table 5.6.

Table 5.6: IE of the test images enhanced by various image enhancement techniques

Images/ Techniques	Original Image	Mod GL [141]	HMFD	Riesz	Proposed
Lena	7.4429	7.5705	7.4700	7.5355	7.5847
Butterfly	7.4716	7.5062	7.5117	7.5476	7.5625
Palace	7.5641	7.5893	7.5506	7.5620	7.5912
Fish	7.0628	7.0737	7.0968	7.1604	7.2169
Vase	7.2154	7.2808	7.1137	7.2167	7.2819
Cars	6.7188	6.9139	6.7413	7.3119	7.3128
Barbara	7.4664	7.6494	7.6170	7.5533	7.6509
Pirate	7.2367	7.3303	7.2852	7.3888	7.4919
Texture	5.4556	7.6414	7.3213	7.7813	7.7893
Seeds	5.8275	7.6023	7.3644	7.7285	7.7643
Road	6.6736	6.6572	6.6624	6.5965	6.6651
Birds	6.6806	6.4958	6.5065	6.4937	6.5077

Bold indicates the maximum value obtained by enhancement techniques

The increase in IE is less for the FrFT based RFOD approach in comparison to the few of the original images but it is still superior to the existing approaches. The proposed approach achieved a slight improvement of 0.62-2.28% in IE than the existing approaches because RFOD in the FrFTD can preserve the image details. Furthermore, sharpening of image edges is done without introducing any distortion (Section 2.2.4). The clarity in the enhanced images is measured in the terms of AG as depicted in Table 5.7.

Table 5.7: AG of the test images enhanced by various image enhancement techniques

Images/ Techniques	Original Image	Mod GL [141]	HMFD	Riesz	Proposed
Lena	7.1832	8.6481	7.3336	8.4958	9.0428
Butterfly	8.8854	9.7234	9.3469	9.5598	10.0681
Palace	6.1940	7.1824	6.6537	6.9043	7.2075
Fish	4.7655	5.4713	5.0507	5.3177	6.0138
Vase	7.7347	9.1867	8.2850	8.0377	9.1984
Cars	2.9082	3.9051	3.1015	5.1468	5.7535
Barbara	8.4663	10.8475	9.0758	9.7643	10.9125
Pirate	6.1580	7.2562	6.5157	7.3840	8.4295
Texture	21.8515	20.3094	20.1978	20.2584	20.3887
Seeds	14.5310	13.7909	13.2001	13.7820	13.7919
Road	1.8975	2.4655	2.0022	2.2047	2.5245
Birds	2.2701	1.7146	2.4207	1.7161	2.4803

Bold indicates the maximum value obtained by enhancement techniques

The proposed approach provides an increased AG owing to enhancement in the visual image quality. Though AG is slightly less for the proposed FrFT based RFOD approach in comparison to the few original images nevertheless it is better than existing approaches. However, the average improvement in AG for the proposed approach is 5.28-13.55% than the existing techniques for considered images. It is perhaps due to the increased contrast and clarity. Further, Table 5.8 shows the enhancement done by various image enhancement schemes in terms of EME.

Table 5.8: EME of the test images enhanced by various image enhancement techniques

Images/ Techniques	Original Image	Mod GL [141]	HMFD	Riesz	Proposed
Lena	7.5988	8.0587	5.7868	8.1526	9.6046
Butterfly	6.9561	8.4651	7.4355	8.7995	9.0714
Palace	5.8870	8.0621	6.3100	7.925	8.1029
Fish	3.1354	4.3032	3.3835	5.4191	5.5783
Vase	5.4215	7.8808	5.8222	7.8787	8.9266
Cars	2.3419	3.6673	2.4877	4.0019	4.3371
Barbara	8.1969	11.3461	7.1496	9.7428	11.3469
Pirate	6.4943	8.9307	5.2032	7.4281	10.4053
Texture	21.7187	15.7487	17.9146	17.9509	18.4050
Seeds	14.3257	12.1111	12.1032	12.1456	12.1571
Road	1.2348	1.8474	1.3082	1.7037	2.0816
Birds	1.5641	1.4193	1.5538	1.4333	1.5551

Bold indicates the maximum value obtained by enhancement techniques

Images enhanced by the FrFT based RFOD approach achieved an average increase in EME for all the considered images due to an increase in the contrast and edge sharpness. Moreover, an average increase of 9.71-32.85% is provided by the proposed FrFT based RFOD approach as compared to the existing image enhancement approaches. Moreover, the EI parameter is also utilized for computing the intensity of edges in the enhanced images. Table 5.9 shows EI for the considered images enhanced by various image enhancement methods.

Table 5.9: EI of the test images enhanced by various image enhancement techniques

Images/ Techniques	Original Image	Mod GL [141]	HMFD	Riesz	Proposed
Lena	68.8977	77.4792	70.3022	78.6698	84.5295
Butterfly	92.1053	95.3953	96.1731	93.9389	102.3352
Palace	60.7113	68.9446	64.8191	63.7141	69.3199
Fish	49.9747	57.6371	52.6046	54.6255	61.7601
Vase	75.5512	86.8239	80.4034	84.2881	87.9681
Cars	28.1254	41.2768	29.8316	48.0591	54.5773
Barbara	74.7754	88.6186	79.6294	84.2859	88.8975
Pirate	60.9194	68.4742	64.0166	71.5837	81.8011
Texture	229.7588	210.2952	211.6164	211.6941	212.3426
Seeds	149.2857	139.0670	139.9631	139.1202	140.0902
Road	18.5860	23.1758	19.5219	20.3280	24.3379
Birds	23.4593	24.1650	24.9145	23.1088	25.2084

Bold indicates the maximum value obtained by enhancement techniques

It is perceived that the presented FrFT based RFOD framework enhanced the images as it provides an average increase in EI owing to improvement in the contrast of edges. It shows an improvement of 5.28-10.64% in average EI than the existing techniques. Moreover, the mean and number of corners are also used as performance parameters as illustrated in Table 5.10 and Table 5.11 for various image enhancement techniques.

Table 5.10: Mean of the test images enhanced by various image enhancement techniques

Images/ Techniques	Original Image	Mod GL [141]	HMFD	Riesz	Proposed
Lena	124.0085	116.0335	126.6459	116.9666	116.9781
Butterfly	112.8625	106.4021	114.9554	106.3826	107.0078
Palace	113.5003	103.6329	106.6367	101.0578	104.4865
Fish	105.6770	83.4360	104.4477	81.4688	83.4634
Vase	123.6291	103.1273	116.5762	105.2461	105.0324
Cars	111.9326	116.2730	113.9575	124.0670	125.0259
Barbara	112.4468	105.6778	114.6891	112.1036	112.4485
Pirate	111.6399	105.8717	110.6069	103.3756	102.5697
Texture	127.5017	124.2162	129.7311	123.5744	127.1238
Seeds	127.5017	121.9738	130.0542	121.9872	125.4037
Road	130.9659	109.5360	113.6522	109.8260	110.0780
Birds	198.4646	178.3121	179.1014	176.4413	179.7867

Bold indicates the maximum value obtained by enhancement techniques

Table 5.11: Number of Corners for the test images enhanced by various image enhancement techniques

Images/ Techniques	Original Image	Mod GL [141]	HMFD	Riesz	Proposed
Lena	221	242	227	243	257
Butterfly	275	325	266	280	326
Palace	441	453	440	442	554
Fish	107	139	112	132	147
Vase	340	457	344	448	667
Cars	414	554	405	436	677
Barbara	1071	1232	1040	1070	1248
Pirate	866	1077	862	855	1296
Texture	6699	7426	6765	7024	7758
Seeds	2895	3581	2997	3410	4513
Road	158	179	157	148	236
Birds	303	352	306	336	354

Bold indicates the maximum value

It is perceived that the mean for the FrFT based RFOD method is slightly higher or almost comparable to the other enhancement schemes except for RFOD based HMFD approach. The mean is dependent on the overall image intensity that is enhanced by all the techniques, but RFOD based HMFD is dedicated to improve the contrast of an image. Hence, the mean is maximum for most images enhanced by RFOD based HMFD. However, Table 5.11 demonstrates that more corners are detected from the images enhanced by the FrFT based RFOD approach than the existing techniques. Table 5.12 shows the maximum contrast for various techniques.

Table 5.12: GLCM based contrast measure for various images with rotation offsets

Images/ Techniques	Rotation offset	Original Image	Mod GL [141]	HMFD	Riesz	Proposed
Lena	135°	0.5413	0.8588	0.5617	0.8190	0.8786
Butterfly	45°	0.8734	0.9506	0.9663	0.9789	0.9947
Palace	135°	0.6381	0.9340	0.7114	0.7991	0.9349
Fish	135°	0.3148	0.4073	0.3432	0.3938	0.4088
Vase	45°	0.6517	0.7918	0.7234	0.7406	0.8041
Cars	45°	0.1781	0.3135	0.1934	0.3937	0.4332
Barbara	135°	0.8133	1.4815	0.9341	1.0692	1.4879
Pirate	135°	0.3644	0.5906	0.4001	0.5403	0.5476
Texture	135°	2.1225	2.0096	2.1657	1.9966	1.9984
Seeds	45°	1.1083	1.2449	1.2090	1.1108	1.1492
Road	135°	0.1264	0.1752	0.1354	0.1421	0.1644
Birds	135°	0.1911	0.1967	0.2078	0.1914	0.1919

Bold indicates the maximum value

The proposed method provided high contrast for all the images except pirate, foggy, and texture based images at different rotation offsets. This is because Mod GL [141] and HMFD methods are utilized for enhancing both contrast and texture. Table 5.13, Table 5.14, and Table 5.15 illustrate the correlation, energy, and homogeneity respectively for various techniques.

Table 5.13: GLCM based correlation measure for various images with rotation offsets

Images/ Techniques	Rotation offset	Original Image	Mod GL [141]	HMFD	Riesz	Proposed
Lena	135°	0.8823	0.8191	0.8819	0.8463	0.8346
Butterfly	45°	0.8505	0.8315	0.8412	0.8264	0.8237
Palace	135°	0.8955	0.8604	0.8857	0.8561	0.8553
Fish	135°	0.9102	0.8868	0.9059	0.8808	0.8806
Vase	45°	0.8799	0.8418	0.8670	0.8413	0.8492
Cars	45°	0.9192	0.8934	0.9127	0.9114	0.8929
Barbara	135°	0.8155	0.7507	0.7956	0.7811	0.7493
Pirate	135°	0.9177	0.8587	0.9130	0.8993	0.9044
Texture	135°	0.8024	0.7599	0.7974	0.7803	0.7992
Seeds	45°	0.8927	0.8702	0.8919	0.8692	0.8674
Road	135°	0.9438	0.8890	0.9308	0.9245	0.9152
Birds	135°	0.9126	0.8630	0.9053	0.8898	0.8866

Bold indicates the minimum value

Table 5.14: GLCM based energy measure for various images with rotation offsets

Images/ Techniques	Rotation offset	Original Image	Mod GL [141]	HMFD	Riesz	Proposed
Lena	135°	0.1089	0.0918	0.1049	0.0910	0.0818
Butterfly	45°	0.1030	0.0993	0.1000	0.0946	0.0892
Palace	135°	0.1048	0.1064	0.1071	0.1154	0.1056
Fish	135°	0.2103	0.1931	0.1991	0.1850	0.1732
Vase	45°	0.1198	0.1046	0.1143	0.1251	0.1024
Cars	45°	0.2171	0.1684	0.2135	0.1416	0.1412
Barbara	135°	0.0885	0.0639	0.0853	0.0776	0.0635
Pirate	135°	0.1199	0.1053	0.1149	0.0857	0.0849
Texture	135°	0.0368	0.0331	0.0383	0.0348	0.0324
Seeds	45°	0.0507	0.0432	0.0510	0.0474	0.0425
Road	45°	0.2308	0.2412	0.2319	0.2332	0.2311
Birds	135°	0.2597	0.2713	0.2639	0.2720	0.2697

Bold indicates the minimum value obtained by enhancement techniques

Table 5.15: GLCM based homogeneity measure for various images with rotation offsets

Images/ Techniques	Rotation offset	Original Image	Mod GL [141]	HMFD	Riesz	Proposed
Lena	135°	0.8520	0.8647	0.8487	0.8263	0.8061
Butterfly	45°	0.8481	0.8464	0.8442	0.8503	0.8158
Palace	90°	0.8981	0.8731	0.8913	0.8914	0.8695
Fish	0°	0.9311	0.9086	0.9278	0.9097	0.9044
Vase	0°	0.8879	0.8145	0.8266	0.8436	0.8142
Cars	45°	0.9218	0.8996	0.9176	0.8787	0.8619
Barbara	135°	0.8115	0.7644	0.8031	0.7909	0.7643
Pirate	135°	0.8716	0.8230	0.8655	0.8313	0.8226
Texture	135°	0.6389	0.6030	0.6296	0.6224	0.6028
Seeds	45°	0.7460	0.7169	0.7424	0.7248	0.7164
Road	45°	0.9502	0.9369	0.9376	0.9401	0.9360
Birds	135°	0.9575	0.9347	0.9457	0.9514	0.9334

Bold indicates the minimum value

The proposed approach provides less correlation for either GLCM of Mod GL or the proposed approach, thus indicating the enhancement by various techniques. Moreover, less energy and homogeneity are achieved by the presented technique at different rotation offsets for all the images, consequently providing superior enhancement than the existing approaches. Thus, the assessment parameters show increased sharpness and clarity of an image. Therefore, it is ascertained that the presented FrFT based RFOD approach provided superior performance which confirms the theoretical notion described in Section 2.2.4.

5.3 Performance Analysis on the basis of Uncontrolled Features

The images usually get corrupted with uncontrolled features while capturing the images. Therefore, the effect of uncontrolled features particularly the noise, varying illumination effects, and JPEG compression artifacts are taken into consideration for validating the robustness of the proposed technique.

5.3.1 Noise immunity

Noise is the most commonly occurring challenge in signal and image processing applications. Therefore, in this section, the standard image of Lena is corrupted with Poisson as well as Gaussian noises to analyze their effect on the proposed approach.

5.3.1.1 Gaussian Noise

The experimentation is done by the Gaussian noise corrupted Lena image having zero mean and variance from 0.005 to 0.03 with a step size of 0.005. Figure 5.11 exhibits the edges detected by Gaussian noise corrupted Lena image.

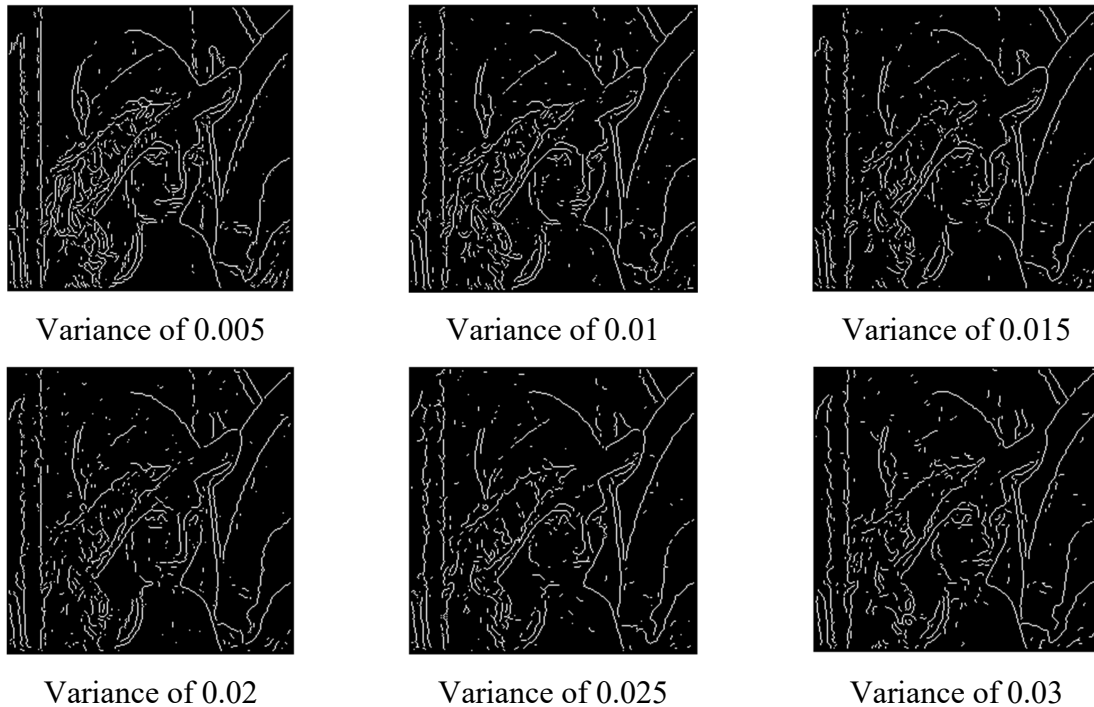


Figure 5.11: Edge maps of Lena image (256×256) corrupted with Gaussian noise

It is exhibited that the proposed FrFT based RFOD technique is immune to the Gaussian noise. It is observed that with an increase in variance, the noise immunity is reduced because the noise pixels tend to appear in the obtained image. Although being capable of detecting edges in the presence of Gaussian noise yet its performance needs to be improved for a high concentration of noise.

5.3.1.2 Poisson Noise

The confirmation of the adequacy of the proposed approach is done by corrupting the Lena image with Poisson noise. Figure 5.12 and Table 5.16 show the edge maps and performance metrics for the Poisson noise corrupted Lena image for various edge detection techniques respectively.

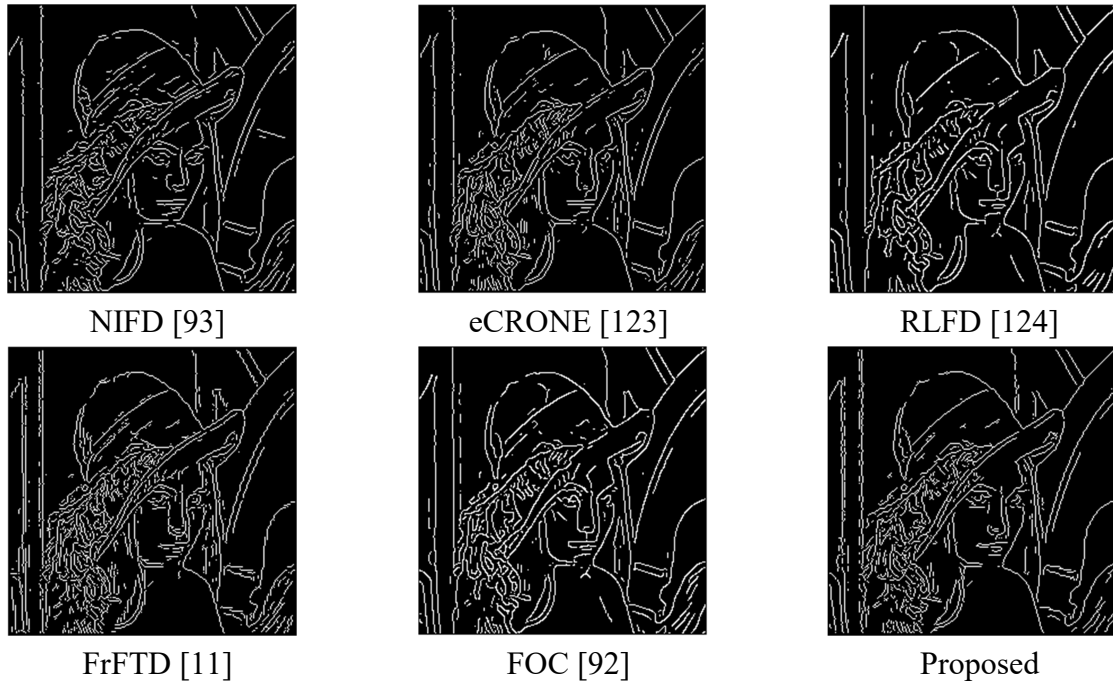


Figure 5.12: Edge maps of Lena image (256×256) corrupted with Poisson noise for various techniques

Table 5.16: Performance metrics for the Lena image corrupted with Poisson noise

Metrics	NIFD [93]	eCRONE [123]	RLFD [124]	FrFTD [11]	FOC [92]	Proposed
FOM	0.7974	0.7807	0.7673	0.6576	0.6741	0.8107
EPI	0.6622	0.6781	0.7004	0.6422	0.7081	0.6930

Bold indicates the maximum value

It is found that the edges are capably detected by the proposed technique while eliminating the Poisson noise. However, EPI is slightly less for the presented FrFT based RFOD technique as perhaps few edges are not preserved, but FOM is maximum thus indicating efficient edge detection by eradicating the noise. However, the images enhanced by the proposed and existing methods are almost comparable.

5.3.2 Illumination Conditions

The robustness of the presented technique is established from the uncontrolled feature of variation in illumination conditions. Here, c1, c2, c3, and c4 images from the VIP Illumination Saliency Dataset [183] are considered for testing the adequacy of the proposed approach.

5.3.2.1 Edge Detection

The presented technique is visually compared against the existing edge detection approaches for images with variation in illumination conditions as shown in Figure 5.13.

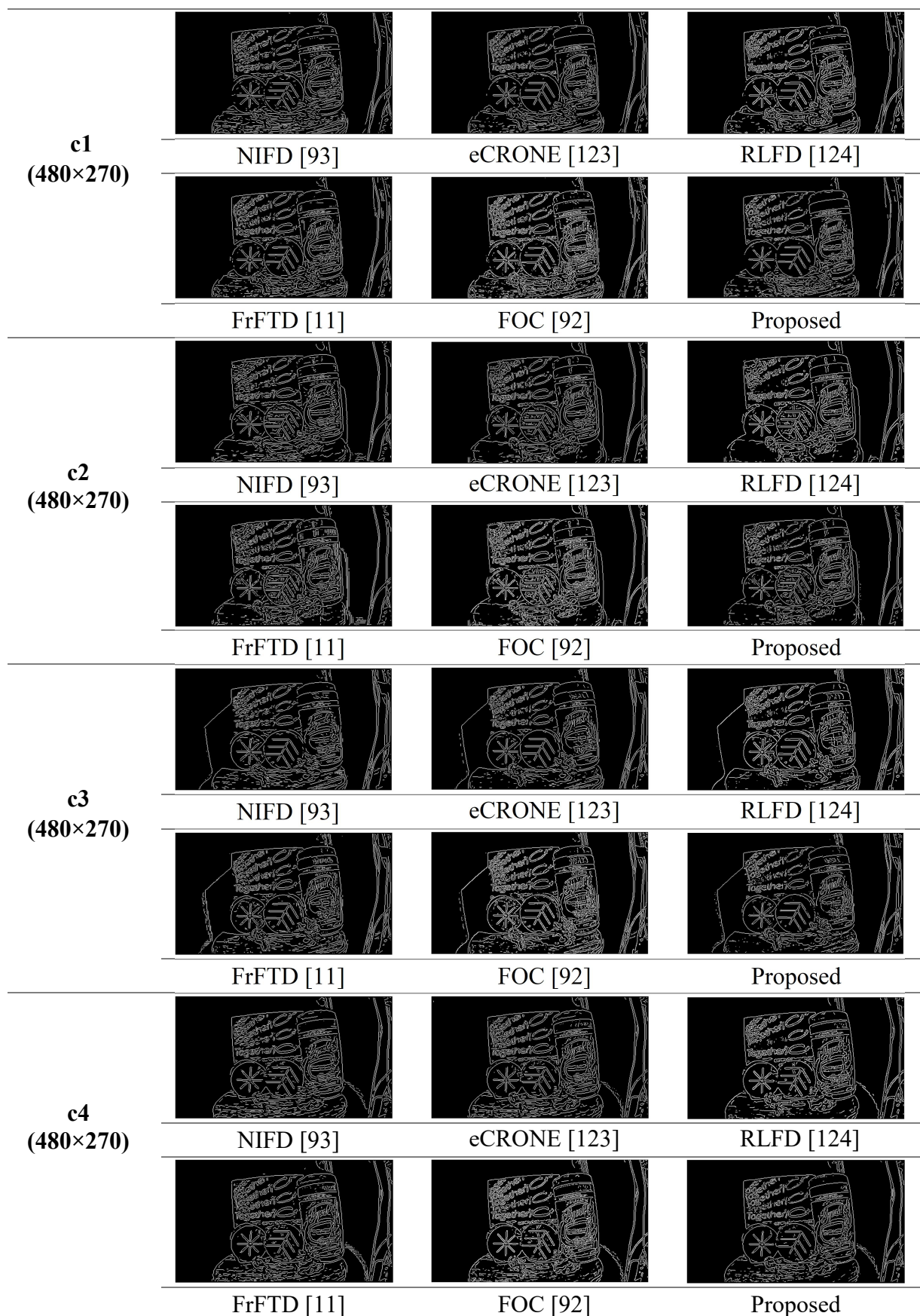


Figure 5.13: Edge maps obtained by various techniques for test images with variation in illumination conditions

The words in images with variation in illumination conditions are accurately detected by the proposed approach. Moreover, it detected fewer redundant edges than the existing edge detection techniques. Furthermore, a quantitative analysis is conducted to confirm its efficacy. Table 5.17 illustrated performance metrics for the edges detected for images with variation in illumination conditions by various approaches.

Table 5.17: FOM and EPI obtained from various edge detection approaches for test images with variation in illumination conditions

Parameters	Images	NIFD [93]	eCRONE [123]	RLFD [124]	FrFTD [11]	FOC [92]	Proposed
FOM	c1	0.8277	0.8326	0.7508	0.8231	0.6432	0.8359
	c2	0.7913	0.7899	0.7120	0.7089	0.6031	0.7939
	c3	0.8018	0.8106	0.7069	0.7460	0.5943	0.8185
	c4	0.8041	0.7614	0.7347	0.6993	0.6253	0.8092
EPI	c1	0.7836	0.8689	0.9329	0.8596	0.9765	0.9891
	c2	0.8141	0.8990	0.9787	0.8639	0.9843	0.9866
	c3	0.5633	0.5874	0.6501	0.6174	0.6504	0.7141
	c4	0.6590	0.6706	0.7544	0.6457	0.7581	0.7592

Bold indicates the maximum value

Apparently, maximum FOM and EPI are provided by the proposed technique than the existing ones for all the test images taken into consideration. Based on both qualitative and quantitative analysis, it is discerned that the edges are capably detected by the presented technique for images with variation in illumination conditions.

5.3.2.2 Image Enhancement

The efficacy of the presented framework for the enhancement of images with variation in illumination conditions is also confirmed by performing both qualitative and quantitative analysis. The comparative analysis of the proposed FrFT based RFOD technique as compared to the image enhancement algorithms for images obtained from the VIP Illumination Saliency Dataset [183] is illustrated in Figure 5.14 and Table 5.18.

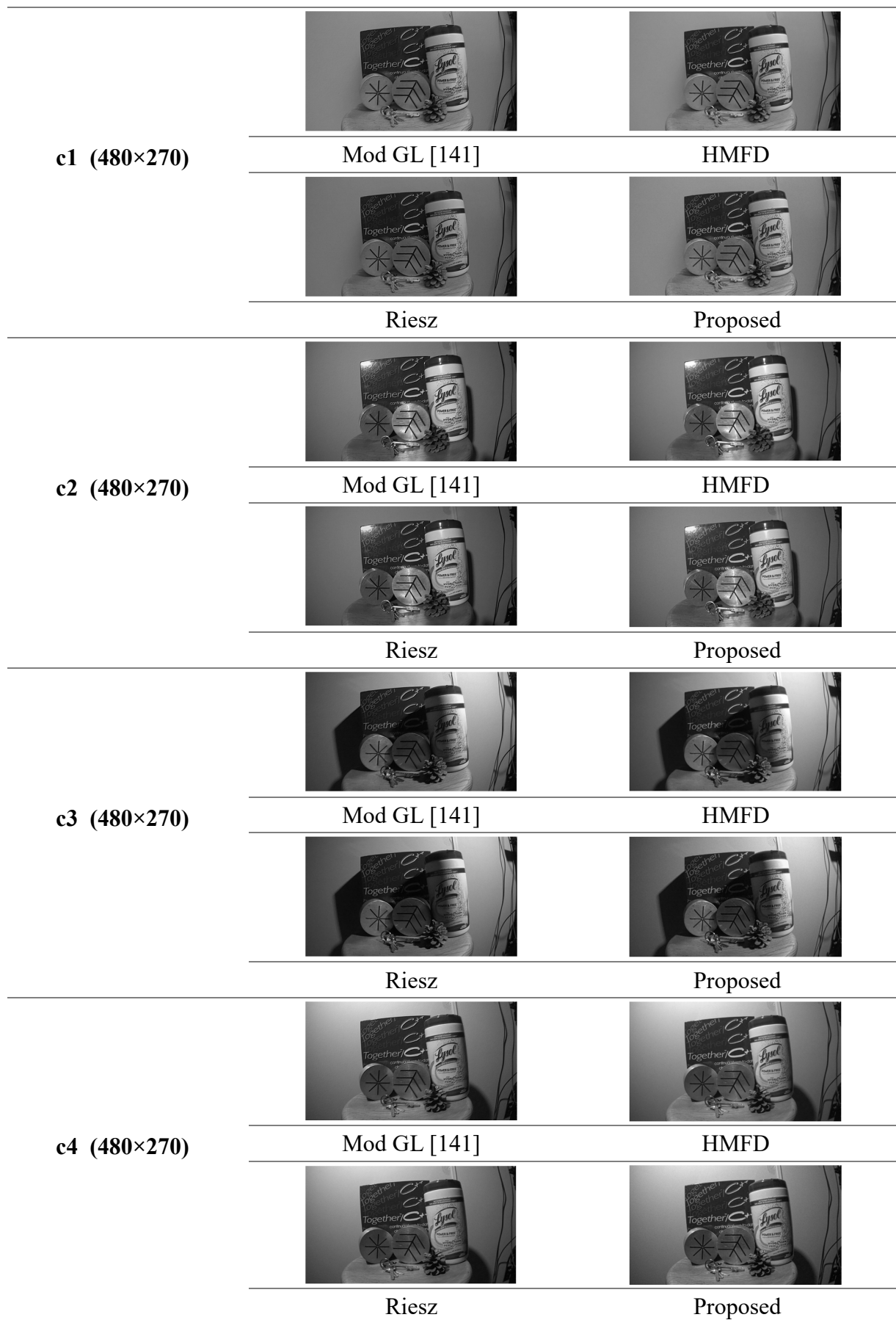


Figure 5.14: Enhancement results for test images with variation in illumination conditions

Table 5.18: Performance metrics for image enhancement techniques for test images with variation in illumination conditions

Images	c1	c2	c3	c4	c1	c2	c3	c4	c1	c2	c3	c4
Metrics	IE				EME				Mean			
Original Image	6.8656	7.2828	7.6681	7.6124	5.2500	5.3946	6.7071	5.5139	107.6015	98.9080	93.2514	105.5563
Mod GL [141]	6.8585	7.2630	7.6374	7.5969	5.1858	5.2425	6.6055	5.4043	101.7298	93.3557	88.2254	99.9059
HMFD	6.8856	7.2995	7.6713	7.6132	5.0213	4.7402	5.2205	4.2612	108.0898	97.6998	92.5635	103.6069
Riesz	6.7590	7.2473	7.5736	7.5298	5.4150	5.1733	6.6436	5.3457	98.8385	89.0275	82.6857	99.5875
Proposed	6.8699	7.1899	7.6374	7.5963	5.4161	5.2459	6.7410	5.4069	108.3031	97.9739	92.6164	101.2426
Metrics	AG				EI				Number of Corners			
Original Image	4.8922	5.3054	4.3333	4.5952	49.0434	53.3913	44.7881	47.3381	350	309	133	319
Mod GL [141]	5.5198	5.6407	5.0197	5.3194	54.5707	54.4286	49.6240	53.2267	385	335	153	317
HMFD	5.0376	5.4784	4.4355	4.6993	50.4146	54.9332	45.7236	48.2410	344	303	125	316
Riesz	5.0625	5.5672	4.9625	5.0633	49.6987	54.6069	46.3998	49.4257	364	318	148	321
Proposed	5.5227	5.6466	5.1872	5.3934	54.5935	55.9696	49.7651	53.4269	393	373	198	376

Bold indicates maximum value obtained by enhancement techniques

It is observed that better enhancement is obtained by the proposed technique for images with variation in illumination conditions. Nevertheless, better results are provided for IE by the HMFD approach as it is devised specifically for enhancing the images with non-uniform illumination while preserving their information details. Table 5.19 shows GLCM parameters computed for various image enhancement schemes.

Table 5.19: GLCM parameters obtained by various image enhancement techniques for test images with variation in illumination conditions

Parameters	Images	Rotation Offset	Original Image	Mod GL [141]	HMFD	Riesz	Proposed
Contrast	c1	135°	0.4514	0.5038	0.4672	0.4532	0.4944
	c2	135°	0.4850	0.5479	0.5152	0.4839	0.4977
	c3	135°	0.3140	0.4309	0.3298	0.3407	0.3454
	c4	135°	0.3519	0.4978	0.3711	0.3845	0.4113
Correlation	c1	135°	0.8701	0.7507	0.8649	0.8272	0.8558
	c2	135°	0.8632	0.7369	0.8586	0.7993	0.8444
	c3	135°	0.9558	0.9131	0.9541	0.9402	0.9478
	c4	135°	0.9344	0.8609	0.9307	0.9182	0.9237
Energy	c1	135°	0.2108	0.1548	0.2232	0.1986	0.1534
	c2	135°	0.1639	0.1698	0.1583	0.1945	0.1696
	c3	135°	0.1097	0.1095	0.1079	0.1117	0.1092
	c4	135°	0.1207	0.1127	0.1196	0.1278	0.1097
Homogeneity	c1	135°	0.8982	0.8669	0.8998	0.8923	0.8583
	c2	135°	0.9017	0.8794	0.8869	0.8939	0.8782
	c3	135°	0.9104	0.8858	0.9088	0.9041	0.8807
	c4	135°	0.9064	0.8804	0.9041	0.9040	0.8792

Bold indicates the optimum value obtained by enhancement techniques

It is found that contrast and correlation are more in the case of Mod GL [141] as it enhanced the image texture, thus, showing improvement in its contrast. However, the remaining performance metrics still demonstrate the efficacy of the presented technique for images with variation in illumination conditions.

5.3.3 JPEG Compression Artifacts

Here, the efficiency of the proposed approach is established against compression artifacts by varying the quality factor of JPEG images of Lena from 50 to 95 against the existing techniques.

5.3.3.1. Edge Detection

The qualitative and quantitative analysis of the presented FrFT based RFOD approach compared to the existing techniques for the JPEG compressed Lena image is conducted.

Figure 5.15 illustrates the edge maps obtained by various edge detection techniques for JPEG Lena images with the quality factors of 50, 75, and 95.

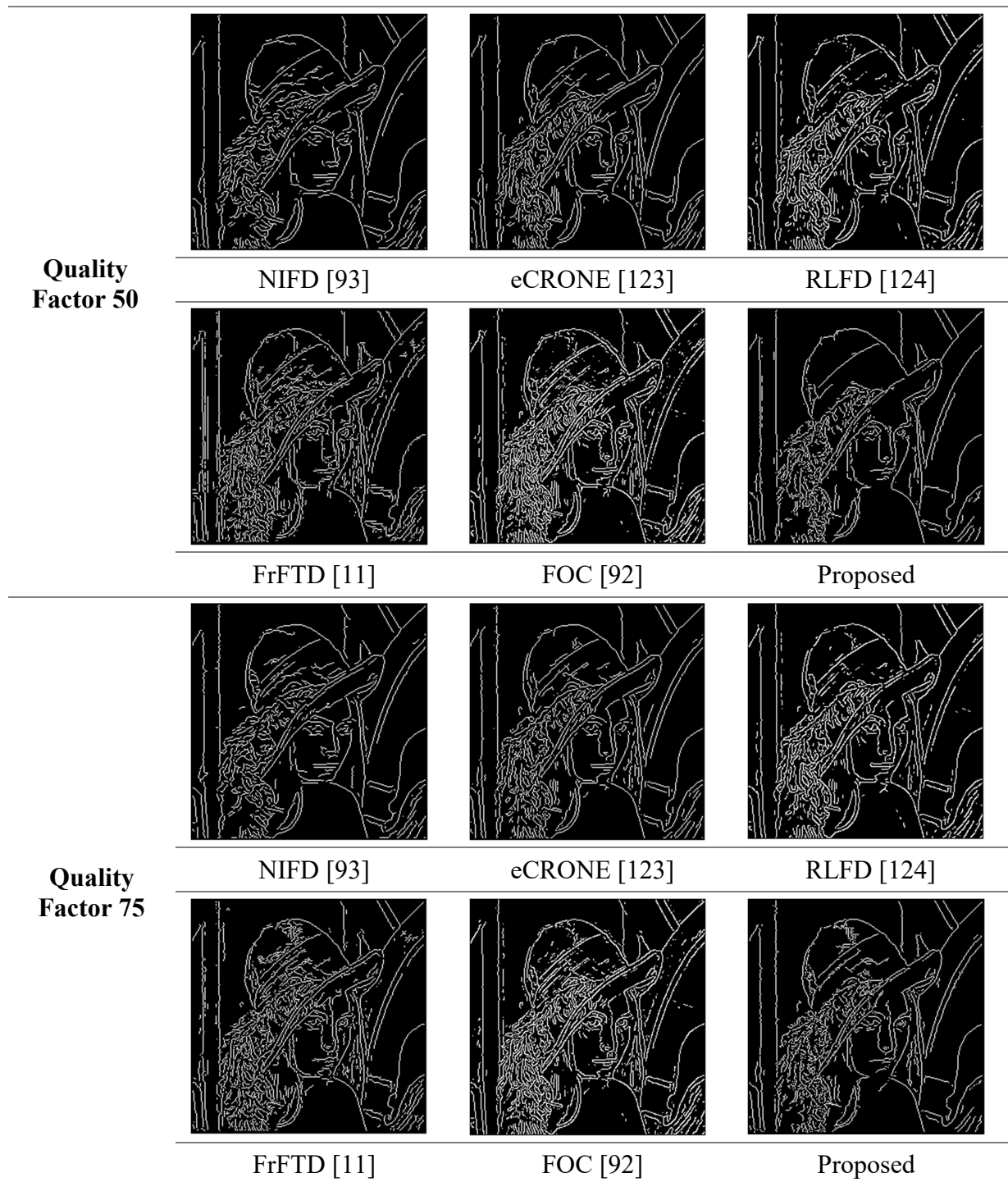


Figure 5.15: Edges detected by various techniques for JPEG compressed images of Lena (256×256) with different quality factors (contd.)

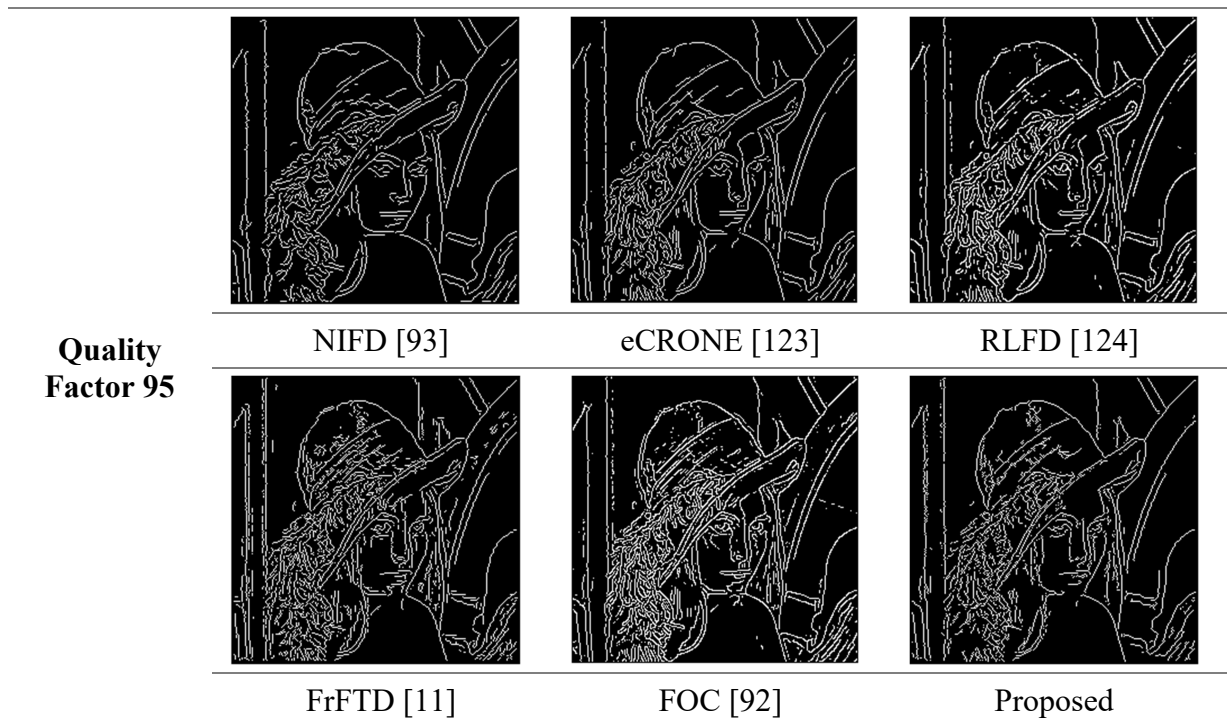


Figure 5.15: Edges detected by various techniques for JPEG compressed images of Lena (256×256) with different quality factors

It is perceived that the presented technique can efficiently detect the edges for JPEG images of Lena with varying quality factors. Figure 5.16 provides the comparative analysis of the proposed scheme with NIFD [93], eCRONE [123], RLFD [124], FrFTD [11], and FOC [92] in terms of FOM and EPI with variation in quality factors.

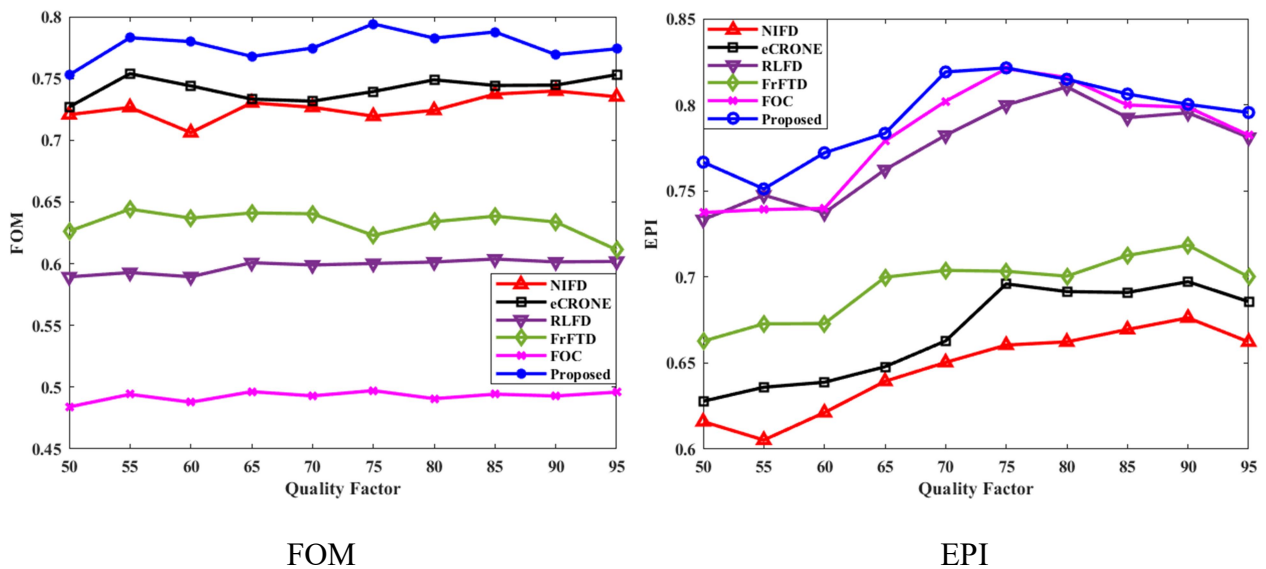


Figure 5.16: Comparative analysis for edge detection methods with respect to quality factors

It is discerned that the FOM and EPI for the presented method are maximum for the considered quality factors that show an improvement of 4.66-57.64 % and 2.44-22.71 % for

average FOM and average EPI respectively.

5.3.3.2 Image Enhancement

The comparative analysis of the proposed FrFT based RFOD technique with respect to Mod GL [141], HMFD, and Riesz techniques is illustrated in Figure 5.17 for the JPEG Lena image compressed with the quality factors of 50, 75, and 95.

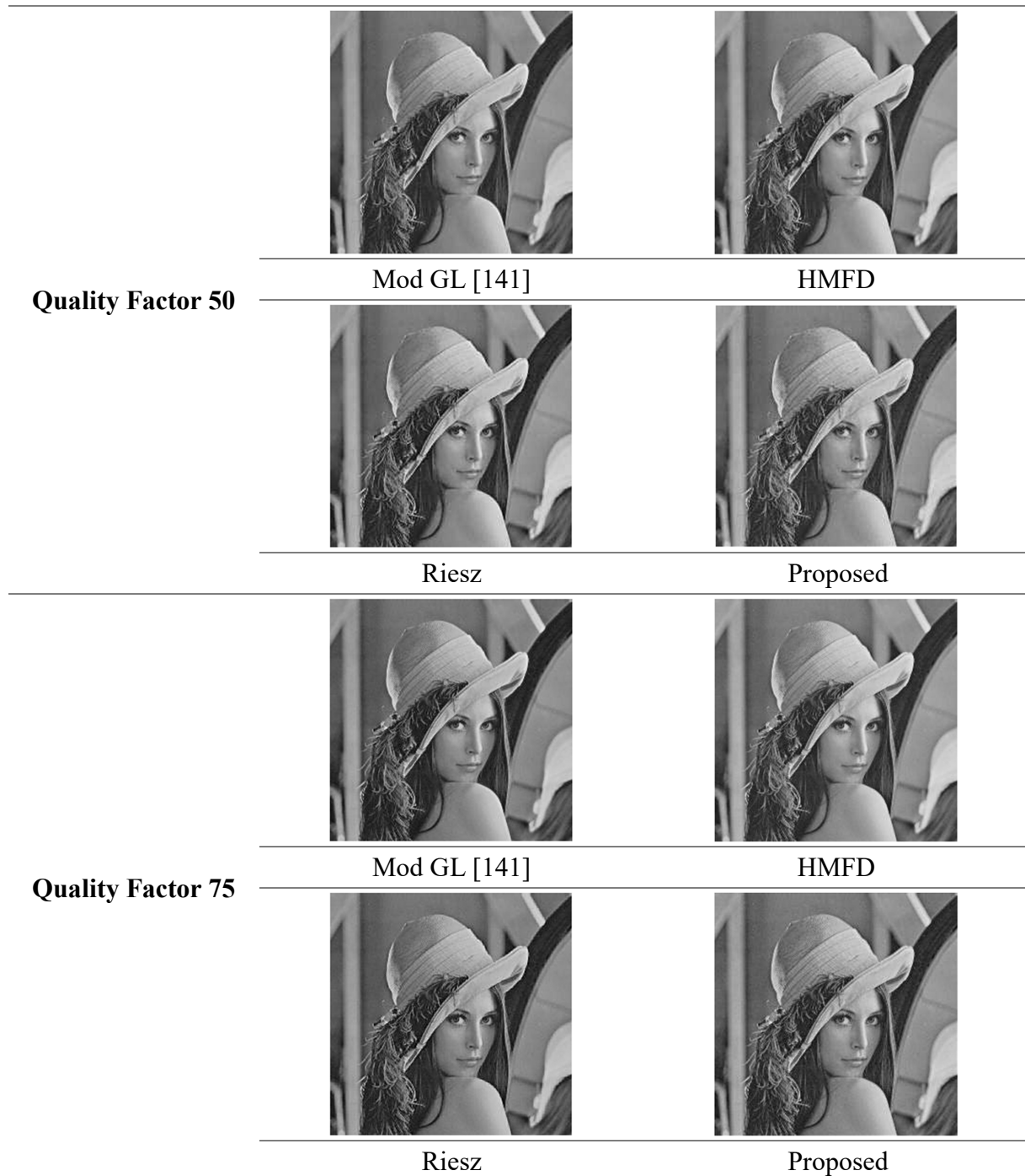


Figure 5.17: Simulation results for JPEG compressed images of Lena (256×256) with different quality factors (contd.)

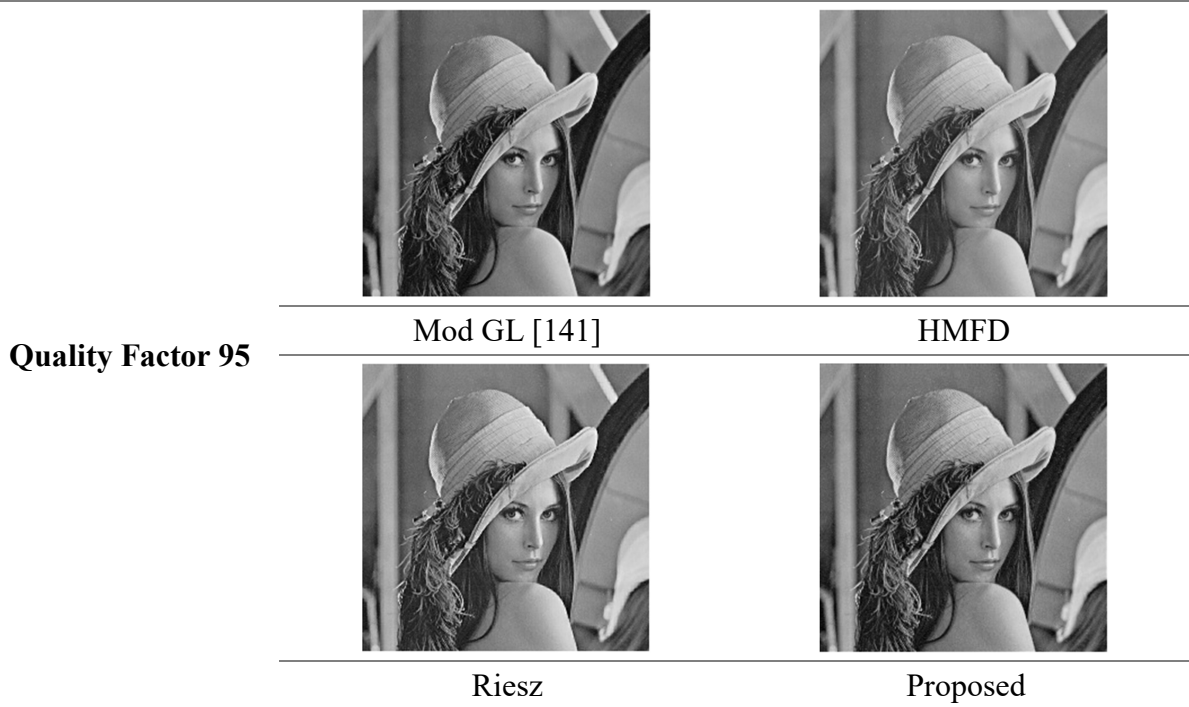


Figure 5.17: Simulation results for JPEG compressed images of Lena (256×256) with different quality factors

It is found that sharper edges are provided by the presented FrFT based RFOD approach as compared to the existing techniques. Figure 5.18 further established the efficacy in the form of assessment parameters attained with the variation of quality factors.

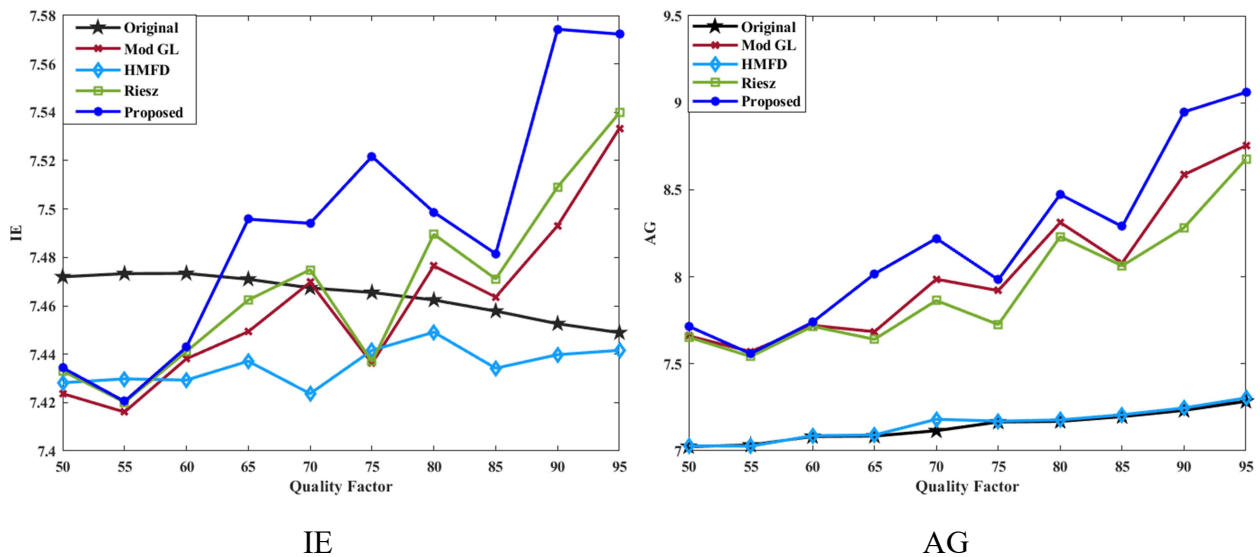


Figure 5.18: Comparative analysis of image enhancement techniques based on various performance metrics with variation in quality factors (contd.)

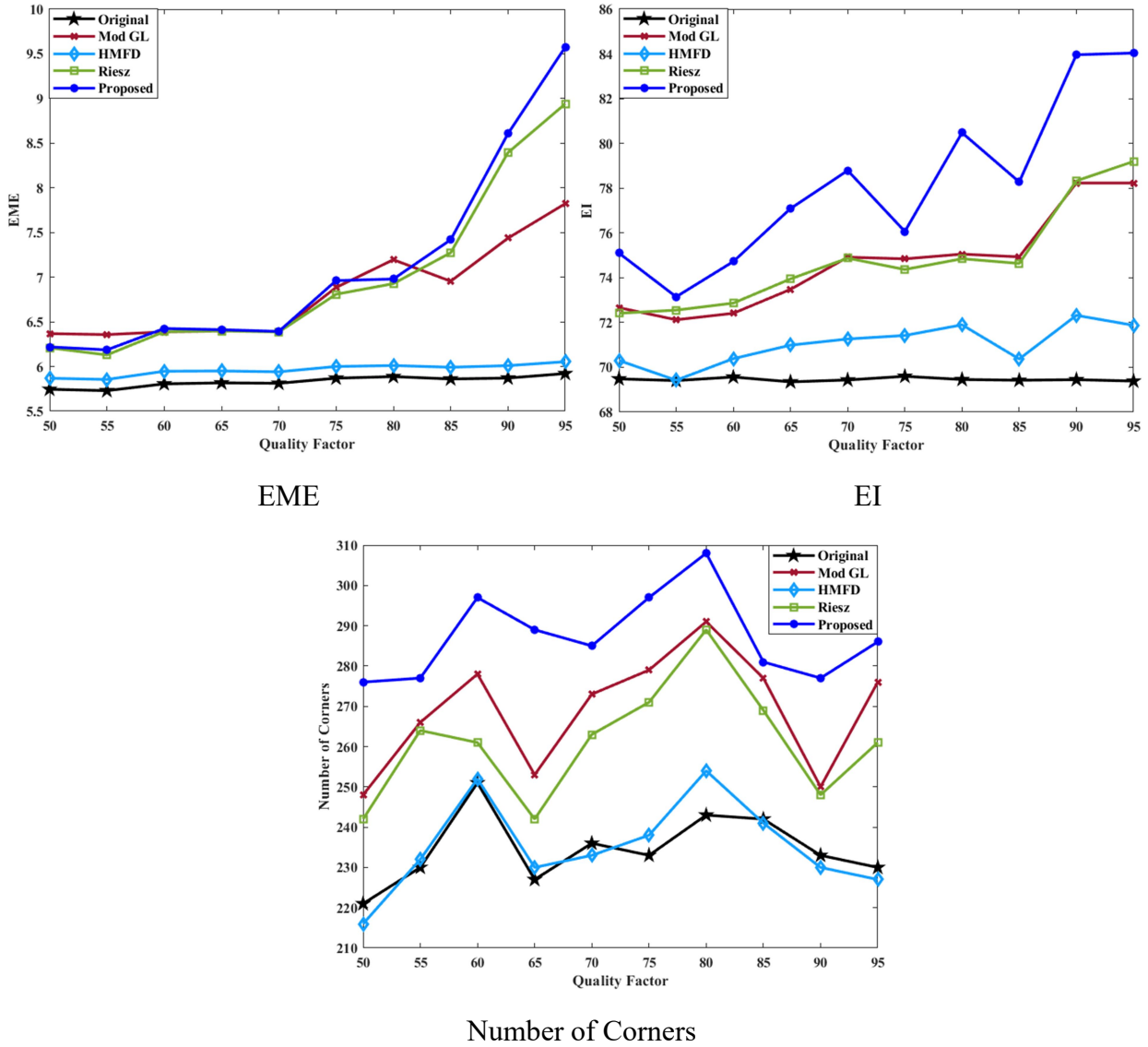


Figure 5.18: Comparative analysis of image enhancement techniques based on various performance metrics with variation in quality factors

It is ascertained that high IE and AG are achieved by the proposed technique with an improvement of 0.34-0.78% and 2.15-14.66% respectively than the existing techniques. Further, maximum EME is achieved by the proposed technique for the quality factors ranging from 85 to 95 elsewhere; it is slightly lower or comparable to the other enhancement methods. Conversely, the maximum EI and number of corners are provided by the presented approach for all the considered quality factors. Therefore, the intensity of edges is efficiently improved by the proposed FrFT based RFOD approach. An average improvement of 4.5-10.05% is provided by the proposed approach for average EI than the existing techniques. However, there is only negligible variation in the mean and GLCM parameters in reference to

the variation in quality factors. Hence, the proposed RFOD technique in the FrFTD can be efficiently employed to detect and enhance edges.

5.4 Computational Cost

The computational complexity and processing time are computed to determine the computational cost of various approaches. The computational complexity is determined in the terms of image size $M \times N$ whereas the time elapsed for executing the approaches is calculated in seconds. The computational cost of various approaches is shown in Table 5.20.

Table 5.20: Computational cost of various approaches

Approaches	Computational Complexity	Average Processing Time (sec)
NIFD [93]	$8\left(O(MN)+O\left(MN(\log MN)^2\right)+O\left(MN(\log MN)\right)\right)$	6.9354
eCRONE [123]	$O(MN)+O(MN \log MN)+O\left(MN(\log MN)^2\right)$	8.4287
RLFD [124]	$4O(MN \log MN)+O(MN)$	5.6476
FrFTD [11]	$O(MN)+2MN+\frac{MN}{2}\log MN+O\left(MN(\log MN)^2\right)$	17.1653
FOC [92]	$O(MN \log MN)+2MN+\frac{MN}{2}\log MN+3\left(O\left(MN(\log MN)^2\right)+O(MN)\right)$	11.8792
Mod GL [141]	$2\left(O(MN)+O\left(MN(\log MN)^2\right)+O\left(MN(\log MN)\right)\right)$	7.1245
HMFD	$O(MN)+2MN+\frac{MN}{2}\log MN+O\left(MN(\log MN)^2\right)$	18.1247
Riesz	$5MN+\frac{MN}{2}\log_2 MN+O(MN \log MN)+3O\left(MN(\log MN)^2\right)$	20.1654
Proposed	$8\left(O\left(MN(\log MN)^2\right)+O(MN)\right)+2MN+\frac{MN}{2}\log MN$	21.9815

The computational cost of the presented approach is slightly higher than the existing algorithms. Nevertheless, the existing approaches either detected edges or enhanced images whereas the proposed FrFT based RFOD approach efficiently performed both tasks.

5.5 Summary

In this chapter, the FrFT based RFOD technique is implemented for edge detection. The edge information thus extracted is further used for enhancing the images. The qualitative analysis demonstrated that the edge maps obtained by the proposed technique are clean and coherent thus evading the redundant edges. Moreover, the performance metrics FOM and EPI are utilized for analyzing the edge detection achieved by the presented technique. The potential of the presented approach in image enhancement is established from the IE, AG, EI, EME, GLCM parameters, etc. It is ascertained from several performance parameters that the presented FrFT based RFOD technique outperformed the existing approaches in the form of better enhancement. Moreover, the uncontrolled features further confirmed the proficiency of the proposed approach. An overall increase of 1.01-57.64%, 2.37-22.71%, 0.34-2.28%, 1.16-14.66%, 1.02-32.85%, and 0.9-10.64% is achieved by the presented technique for FOM, EPI, IE, AG, EME, and EI respectively. Thus, it is noteworthy that superior results are achieved by the proposed FrFT based RFOD approach than the existing approaches for grayscale images. Hence, it motivated to analyze the effect of RFOD in these image processing applications for color images.

QUATERNION BASED RFOD FOR COLOR IMAGE EDGE DETECTION AND IMAGE ENHANCEMENT

This chapter is primarily dedicated to edge detection in color images and their application in image enhancement using RFOD owing to the favorable results provided for the grayscale images. Most of the edge detection techniques in the prevailing literature either transform the color image into grayscale images before processing or process the individual color channels, but it leads to the loss of correlation and information details. Therefore, this chapter is focused on a quaternion based RFOD edge detection approach that processes all the channels of a color image simultaneously. In the presented work, an edge map is obtained by applying the quaternion based RFOD mask to the color image expressed in a quaternion form. The extensive experiments conducted on the standard datasets exhibit the effectiveness of the technique as compared to classical edge detection methods. Moreover, the robustness of the proposed approach is established against various uncontrolled features that arise while procuring the images. Besides, its potential is also confirmed from the Fundus images. Moreover, the edge information extracted by the proposed technique is further utilized in the application of image enhancement.

6.1 Quaternion Riesz Fractional Order Directional Derivative (QRFODD) Mask

Quaternion Fractional Differential (QFD) approach based on GLFOD is applied for color image edge detection. It provided better edge detection results that are more compatible with the human visual characteristics [68], [75]. However, the phase shifting in GLFOD may result in the loss of image details. Hence, the quaternion based RFOD is proposed to deal with the issues of information loss and phase shifting in color images. Initially, the mask coefficients are obtained using the (5.1.21) which are further transformed into the quaternion domain. These coefficients are used to obtain the quaternion based RFOD masks in eight directions w_p , such that, $p=1,2,3,\dots,8$ denotes the direction of the quaternion based RFOD mask, that is, positive i -axis (FM_{m+}), positive j -axis (FM_{n+}), negative i -axis (FM_{m-}), negative j -axis (FM_{n-}), upward left (FM_{UL}), upward right (FM_{UR}), downward left (FM_{DL}), and downward right (FM_{DR}) diagonals respectively as shown in Figure 6.1.

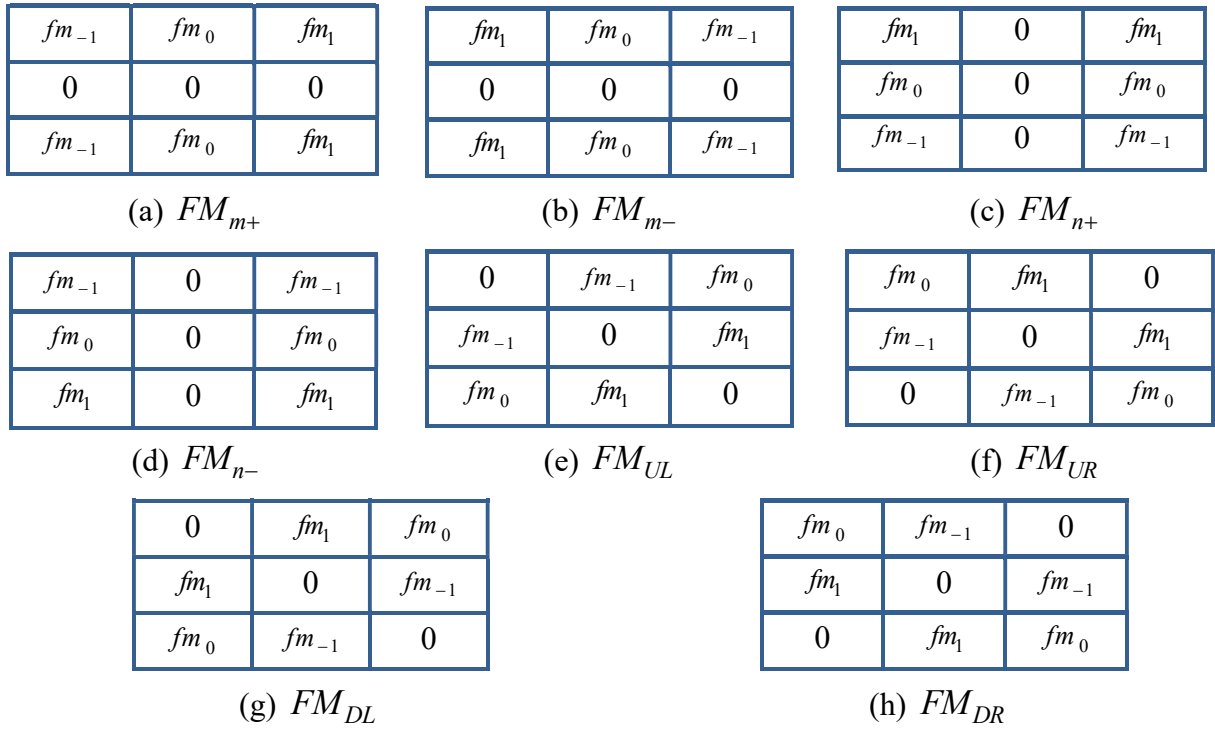


Figure 6.1: Quaternion based RFOD masks in eight directions

Thus, quaternion domain based RFOD masks obtained by the variation in the arrangement of fractional coefficients among different directions are utilized in the presented technique.

6.2 Proposed Approach for Edge Detection in Color Images

The existing color image edge detection methods result in the loss of correlation as well as information that exists among color channels leading to the color artifacts. Besides, classical edge detectors cause the problems of missing edges or the detection of redundant edges. Thus, to deal with these problems, the QRFODD approach is proposed for detecting edges in color images as shown in Figure 6.2.

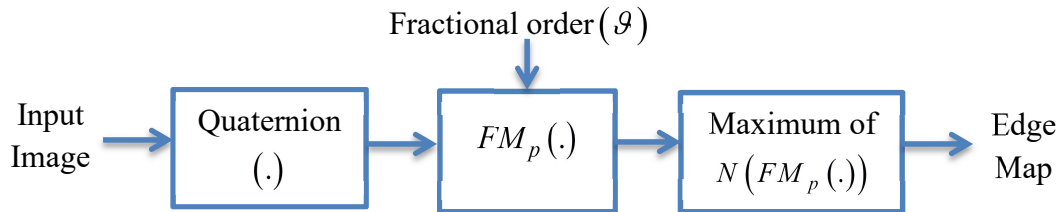


Figure 6.2: Proposed framework based on QRFODD

Initially, the input image $z(m,n)$ is converted into the quaternion form $z_i(m,n)$ defined as:

$$z_i(m,n) = z_{re}(m,n) + z_R(m,n) + z_G(m,n) + z_B(m,n) \quad (6.2.1)$$

Here, the real component, $z_{re}(m,n)=0$ while the imaginary components $z_R(m,n)$, $z_G(m,n)$, and $z_B(m,n)$ represent the red, green, and blue channels of RGB image respectively. Then,

QRFODD masks in the eight directions are obtained. The mask size of 3×3 is selected based on extensive simulations which is further used for the implementation of the proposed approach. Finally, the image is filtered by moving the masks pixel by pixel [68] on the input image by the following generalized expression:

$$\frac{\partial^{\mathcal{G}} z(m, n)}{\partial w_p^{\mathcal{G}}} = \sum_{s=-a}^a \sum_{t=-b}^b Z_{R_p}(s, t) z(m+s, n+t) \quad (6.2.2)$$

where m and n are varied such that every pixel in Z_{R_p} obtained from FM_p based on fractional order (\mathcal{G}) visits each pixel in $z(m, n)$ and p denotes the direction of fractional mask. The QRFODD for an image $z(m, n)$ is given as [75]:

$$d_{\mathcal{G}} z = \sum_{p=1}^8 \frac{\partial_{\mathcal{G}} z}{\partial w_p^{\mathcal{G}}} dw_p^{\mathcal{G}} \quad (6.2.3)$$

It exhibits a change of quaternion image $z(m, n)$ in the direction of w . The norm of $d_{\mathcal{G}} z$ is computed as [75]:

$$N(d_{\mathcal{G}} z) = d_{\mathcal{G}} z \cdot \overline{d_{\mathcal{G}} z} = \sum_{p=1}^8 \sum_{q=1}^8 b_{pq} dw_p^{\mathcal{G}} dw_q^{\mathcal{G}} \quad (6.2.4)$$

where b_{pq} denotes the coefficients of $d_{\mathcal{G}} z \cdot \overline{d_{\mathcal{G}} z}$ such that $p = 1, 2, 3, \dots, 8$, $q = 1, 2, 3, \dots, 8$. Here, $N(d_{\mathcal{G}} z)$ is the variation of $z(m, n)$ in the direction w . The maximum of $N(d_{\mathcal{G}} z)$ is computed to find the edges, that is, the local maximum of $z(m, n)$ in direction w in accordance with Definition 1 in [68]. Eventually, the edge map is yielded by tracking and connecting the edges of an image based on the norm of gradient image in a procedure similar to the non-maximum suppression in Canny edge detection [58]. The pseudo-code of the proposed QRFODD based edge detection approach for color images is described as:

Pseudo-code of the proposed approach

Inputs: z, \mathcal{G} ; **Output:** Z

z : Test Image; \mathcal{G} : Order of derivative; p : Direction

begin

$z_i = \text{Quaternion}(z)$;

for $i = p$ **do**

$Z_R = FM(\mathcal{G})$;

$Z_M = \text{Filter}(Z_R, z_i)$;

end for

$Z_N = \text{Maximum of norm}(Z_M)$;

$Z = \text{Edge map}(Z_N)$;

end

6.3 Performance Analysis of Proposed Approach for Edge Detection in Color Images

The efficacy of the proposed QRFODD approach is established from the natural test images of BSDS300 and BSDS500 [180], [181] datasets that comprise 100 and 200 test images respectively. The proposed method is implemented on all the test images, but the detailed analysis is carried out by considering some of the test images shown in Figure 6.3.



Car (481×321)



Zebra (481×321)



Building (481×321)



Vase_Color (321×481)

Figure 6.3: Test images used for simulation

6.3.1 Selection of Mask Size

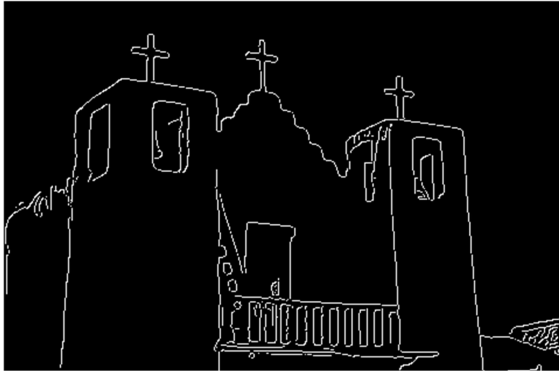
Initially, the implementation of the presented technique is carried out by utilizing QRFODD masks of sizes varying from 3×3 , 5×5 , 7×7 , 9×9 , and 11×11 . Here, the House image is considered for evaluating the performance of the masks of various sizes in both quantitative and qualitative manner. Figure 6.4 illustrates the effect of varying the mask size on the performance of the proposed approach.



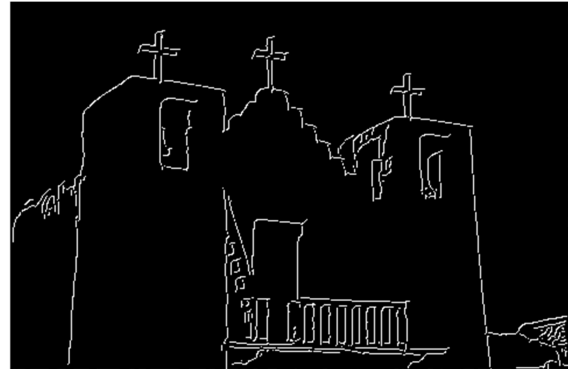
Original Image



Ground truth



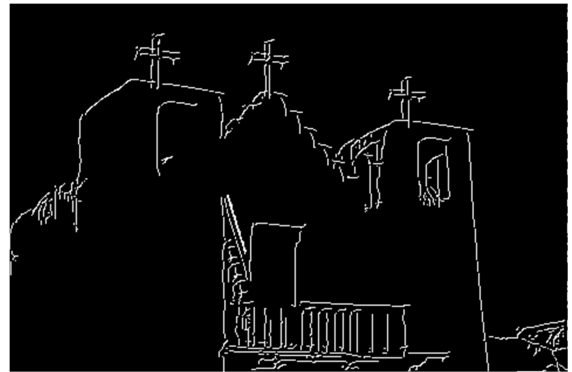
Mask size 3×3



Mask size 5×5



Mask size 7×7



Mask size 9×9



Mask size 11×11

Figure 6.4: Effect of variation in mask size on edge detection for House image (481×321)

It is perceived that edge information is lost with an increase in the mask size. It is clearly visible that there are missing edges for the windows present in the House image. However, it is seen that edge information obtained with mask size 3×3 is more similar to the GT of an image. After the visual analysis, it is also confirmed from the performance metrics, that is, FOM and F-Score as shown in Table 6.1.

Table 6.1: Variation of performance metrics based on mask size

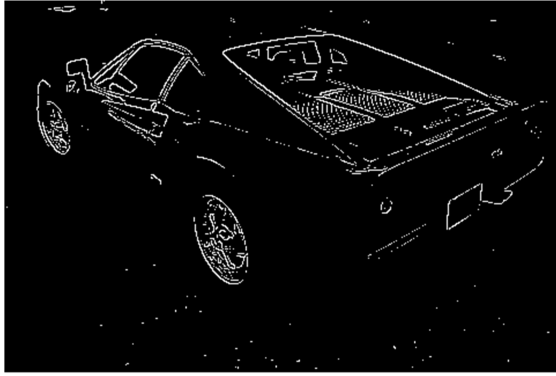
Image	Mask size / Parameter	3×3	5×5	7×7	9×9	11×11
House	FOM	0.4472	0.4157	0.4194	0.3736	0.2735
	F-Score	0.8436	0.7842	0.7963	0.7714	0.5781

Bold indicates the maximum value

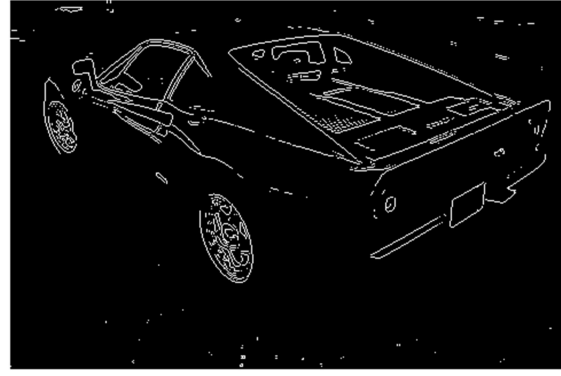
It is evident that the mask size of 3×3 provided better results in terms of FOM and F-Score. Hence, it is ascertained that the mask size of 3×3 outperformed the masks of other sizes both quantitatively and qualitatively. Thus, the mask size of 3×3 is used for the implementation of the proposed approach.

6.3.2 Qualitative Performance Analysis

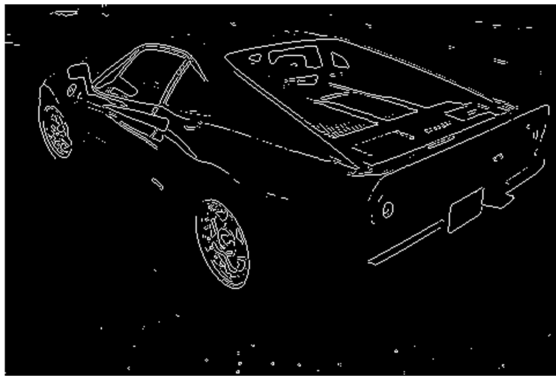
The proficiency of the presented QRFODD technique is validated by evaluating it against the classical edge detectors namely Roberts [55], Prewitt [56], Sobel [57], LoG [21], and Canny [58] edge detectors. The experimentation of the proposed approach is done by varying the fractional order ' ρ ' from 0 to 2. The optimal fractional order ' ρ ' for an image is obtained from the quantitative measures. Moreover, it is notable from the intensive simulations that the value of fractional order ' ρ ' depends on the nature of the image and application. The scaled version of the edge maps yielded by the proposed QRFODD approach as compared to the classical edge detectors for the Car image is demonstrated in Figure 6.5.



Edges detected by Roberts [55]



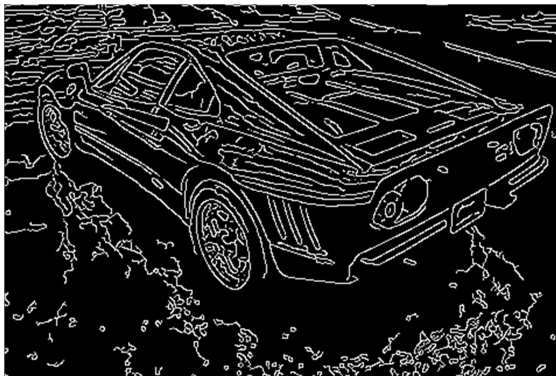
Edges detected by Prewitt [56]



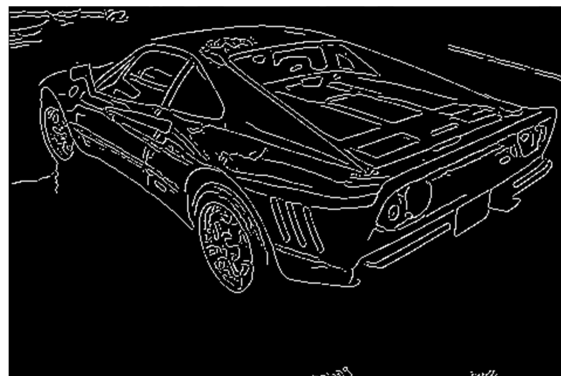
Edges detected by Sobel [57]



Edges detected by LoG [21]



Edges detected by Canny [58]



Edges detected by Proposed approach

Figure 6.5: Edge maps yielded by various approaches for the Car image (481×321)

The clean and coherent edges are detected by the proposed technique as compared to the classical edge detectors. However, some other simulation results are illustrated in Figure 6.6 that further confirmed the effectiveness of the proposed QRFODD edge detection approach.

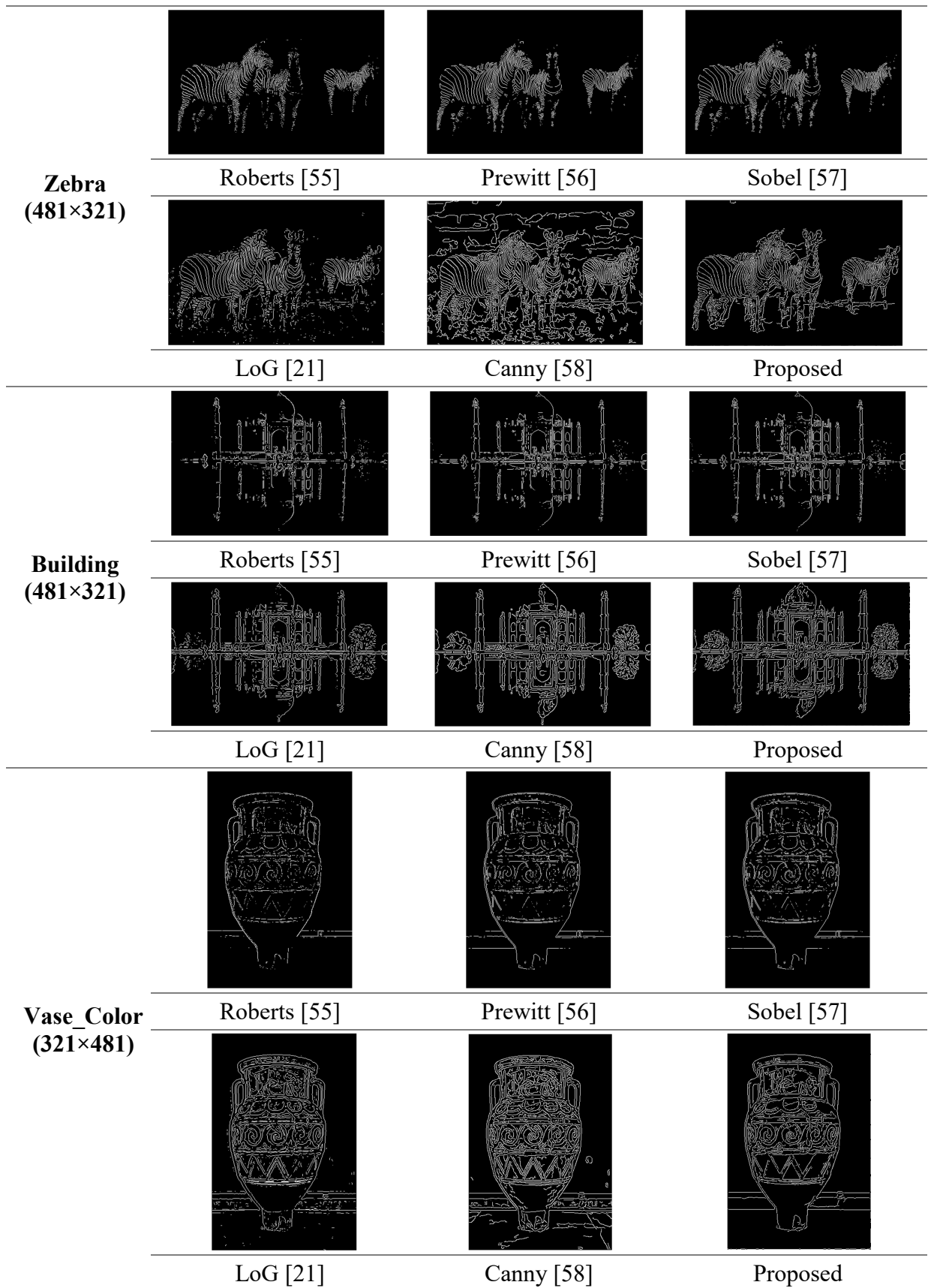


Figure 6.6: Edge maps yielded for various approaches

It is perceived that the clean and continuous edges are extracted by the proposed approach but occasionally it also detected redundant edges. However, the redundant edges extracted by the proposed approach are almost negligible in comparison to Canny and LoG operators. Moreover, it extracted the edges even for the shadow areas in an image, for instance, the dome in the Building image. Besides, the quantitative analysis of the proposed scheme is carried out in the subsequent section to validate its potency in comparison to existing edge detection techniques.

6.3.3 Quantitative Performance Analysis

The performance metrics namely FOM and F-Score are used to quantitatively evaluate the proposed approach. These parameters are evaluated on the basis of a comparison between the edge map obtained by the presented technique and all human-annotated ground truths. The variation of FOM with respect to changes in the fractional order ' ρ ' is shown in Table 6.2.

Table 6.2: Variation of FOM with respect to the fractional order (ρ)

Fractional order (ρ)	0	0.2	0.4	0.6	0.8	1
Car	0.8019	0.8034	0.8051	0.8061	0.8058	0.8056
Fractional order (ρ)	1.2	1.4	1.6	1.8	2	
Car	0.8029	0.8018	0.8029	0.8026	0.7962	
Fractional order (ρ)	0	0.2	0.4	0.6	0.8	1
Zebra	0.8544	0.8582	0.8600	0.8645	0.8629	0.8568
Fractional order (ρ)	1.2	1.4	1.6	1.8	2	
Zebra	0.8286	0.7889	0.825	0.8155	0.8149	
Fractional order (ρ)	0	0.2	0.4	0.6	0.8	1
Building	0.8566	0.8569	0.8571	0.8577	0.8583	0.8601
Fractional order (ρ)	1.2	1.4	1.6	1.8	2	
Building	0.8602	0.8655	0.8539	0.8508	0.8503	
Fractional order (ρ)	0	0.2	0.4	0.6	0.8	1
Vase_Color	0.8118	0.8126	0.8247	0.8170	0.7955	0.8043
Fractional order (ρ)	1.2	1.4	1.6	1.8	2	
Vase_Color	0.8096	0.7918	0.7828	0.7799	0.7707	

Bold indicates the maximum value

It is found that different images provide optimal performance at different fractional orders. Similarly, the optimal fractional order is selected for the remaining test images. Moreover, the comparative analysis on the basis of FOM and F-Score with the classical edge detection techniques is shown in Table 6.3.

Table 6.3: Performance metrics of the proposed approach as compared to classical edge detection approaches

Images/ Techniques	Metrics	Roberts [55]	Prewitt [56]	Sobel [57]	LoG [21]	Canny [58]	Proposed
Car	FOM	0.4817	0.5270	0.5292	0.7191	0.5033	0.8056
	F-Score	0.5399	0.5768	0.5749	0.6202	0.5417	0.6717
Zebra	FOM	0.5924	0.6053	0.6168	0.8316	0.5457	0.8723
	F-Score	0.7396	0.7536	0.7601	0.8428	0.7007	0.8646
Building	FOM	0.5948	0.6309	0.6422	0.8240	0.8612	0.8655
	F-Score	0.7302	0.7463	0.7541	0.8249	0.8200	0.8013
Vase_Color	FOM	0.7443	0.7660	0.7736	0.7383	0.5391	0.8312
	F-Score	0.8399	0.8498	0.8543	0.8141	0.8542	0.8924

Bold indicates the maximum value

It is observed that the F-Score is less for Building image because it extracted more edges. However, it is capable of detecting the dome of the building which is not detected by the LoG [21] and Canny [58] edge detector. The comparative analysis of proposed and existing approaches based on average FOM and F-Score for both datasets are shown in Table 6.4 and Table 6.5. However, due to the unavailability of source codes, the comparative analysis of GLIS [72] and Learning-based Edge Detection (LED) [67] is done solely on the basis of quantitative measures.

Table 6.4: Performance metrics of various edge detection approaches for BSDS500

Technique/ Metrics	Roberts [55]	Prewitt [56]	Sobel [57]	LoG [21]	Canny [58]	LED [67]	Proposed
FOM	0.5269	0.5735	0.5763	0.5927	0.4553	NC	0.6618
F-Score	0.5392	0.5656	0.5716	0.5600	0.5467	0.614	0.6643

NC: Not Calculated in [67] and Bold indicates the maximum value

Table 6.5: Performance metrics of various edge detection approaches for BSDS300

Technique/ Metrics	Roberts [55]	Prewitt [56]	Sobel [57]	LoG [21]	Canny [58]	GLIS [72]	Proposed
FOM	0.5432	0.5921	0.5954	0.5711	0.4234	0.71	0.7152
F-Score	0.5403	0.5669	0.5631	0.5432	0.5262	NC	0.6809

NC: Not Calculated in [72] and Bold indicates the maximum value

Thus, the proposed RFOD based approach provided promising results because it obtained more edge information as compared to the existing edge detection algorithms. It may be due to the unique combination in the proposed approach that aids in preserving the correlation and phase information while providing an additional degree of freedom in terms of the order

of fractional derivatives (Section 2.2.4). Furthermore, to confirm its superiority over the existing quaternion approach [68], Detect Correct Similarity (DCS) is computed for two images namely 3096 and 147091. DCS obtained for these images by the proposed approach is 0.3136 and 0.2991 in comparison to 0.2756 and 0.2540 in [68] (extracted from Table 1 and Table 4 of [68]). Thus, it is apparent from the above performance measures that the proposed approach effectively yields the edge details as compared to the existing ones.

6.4 Performance Analysis on the basis of Uncontrolled Features

Despite taking precautionary measures, images get corrupted with uncontrolled features namely noise, JPEG compression artifacts, and variation in illumination while acquiring the images. Some of these features can be neglected depending on the nature of the application but they generally play a crucial role in the further processing of images. Hence, these uncontrolled features are taken into account for evaluating the proposed approach.

6.4.1 Noise Immunity

Noise is one of the commonly occurring issues during image capturing or transmission. Hence, the Salt and Pepper and Gaussian noises are considered for assessing the performance of the presented technique in a noisy environment. Here, the Car image is corrupted by Salt and Pepper as well as Gaussian noise to confirm the capability of the proposed technique in case of noisy images.

6.4.1.1 Salt and Pepper Noise

Here, the Salt and Pepper noise corrupted images with variation in density from 0.01 to 0.06 are used to evaluate the proposed approach. Figure 6.7 demonstrates the edge maps obtained by various techniques for Salt and Pepper noise corrupted Car image having noise density of 0.02 and 0.04 respectively.

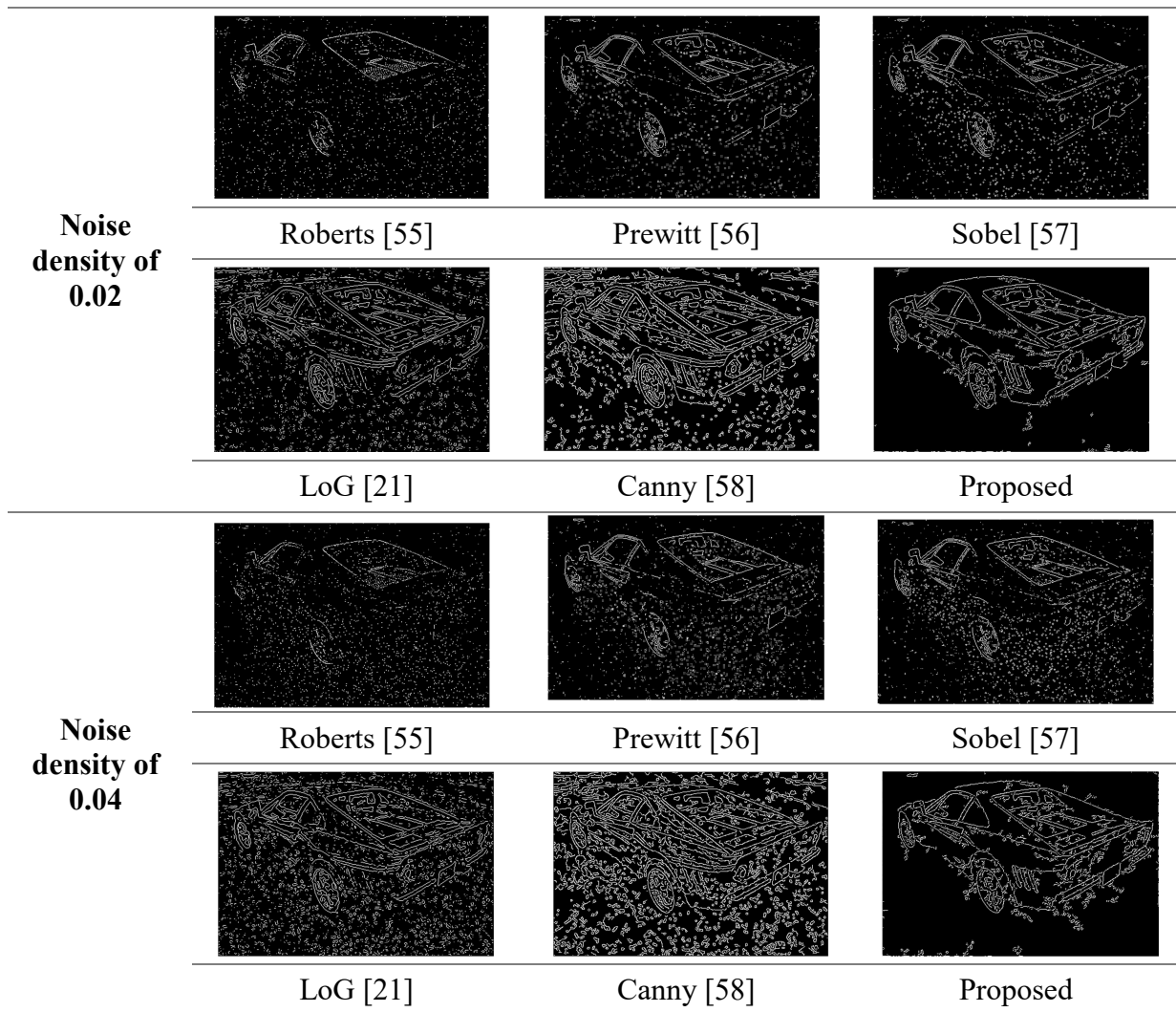


Figure 6.7: Edge maps obtained by various techniques for Car images (481×321) corrupted by Salt and Pepper noise having noise density of 0.02 and 0.04

It can be perceived from the edge maps that the proposed technique yielded more edges than the classical edge detection approaches for the noise density of 0.02 and 0.04. Moreover, it is also deduced from the edge maps obtained for various noise densities that the performance of detection of edges degrades with the increase in noise density. Moreover, the effect of variations in noise density in salt and pepper noise on the performance metrics, that is, FOM and F-Score for the proposed approach and classical edge detection operators are illustrated in Figure 6.8.

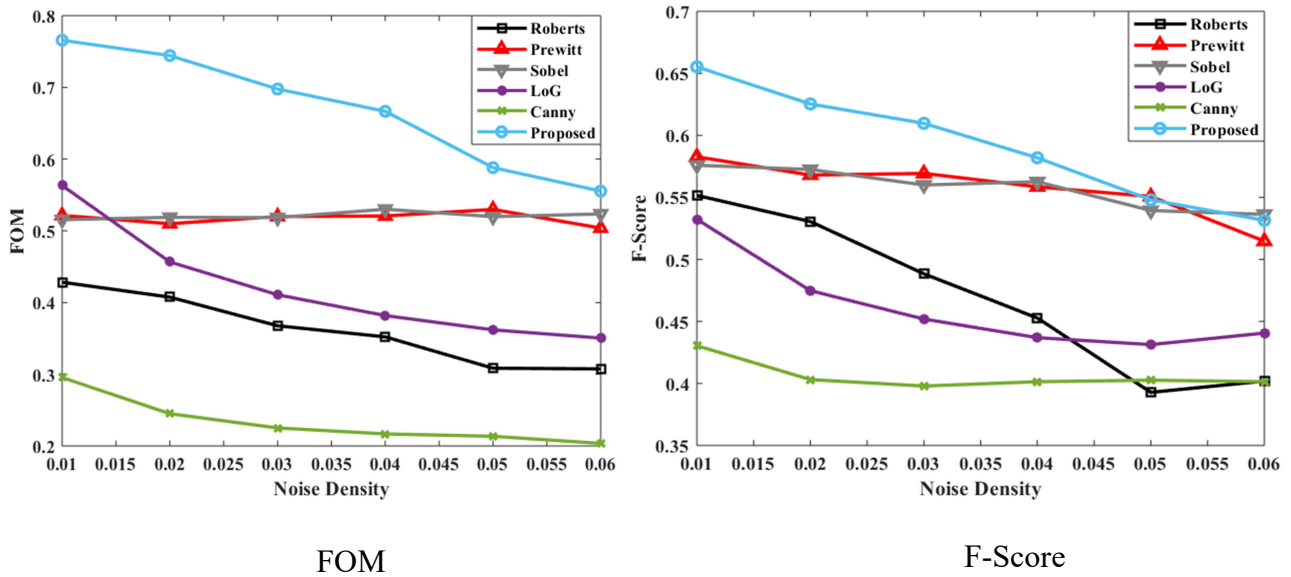


Figure 6.8: Effect on performance metrics with respect to variation in noise density

It is perceived that the value of performance metrics decreases with the increase in noise density. The proposed approach performs better in comparison to the classical edge detectors in the case of Salt and Pepper noise. Nevertheless, the value of F-Score for Prewitt [56] and Sobel [57] is almost comparable to the proposed approach because the noise pixels are considered edge pixels. It is also evident from Figure 6.7 that the noise pixels are present in most of the edge detection operators. Moreover, Gaussian noise is considered for evaluating the performance of the presented QRFODD approach in the subsequent sub-section.

6.4.1.2 Gaussian Noise

Images corrupted by Gaussian noise with variation in variance from 0.01 to 0.06 and zero mean are considered for evaluating the adequacy of the proposed QRFODD technique as compared to other edge detection techniques. Figure 6.9 illustrates the edge maps yielded by the proposed QRFODD approach and various classical edge detection techniques for Gaussian noise corrupted Car image having zero mean and variance of 0.02 and 0.04 respectively.

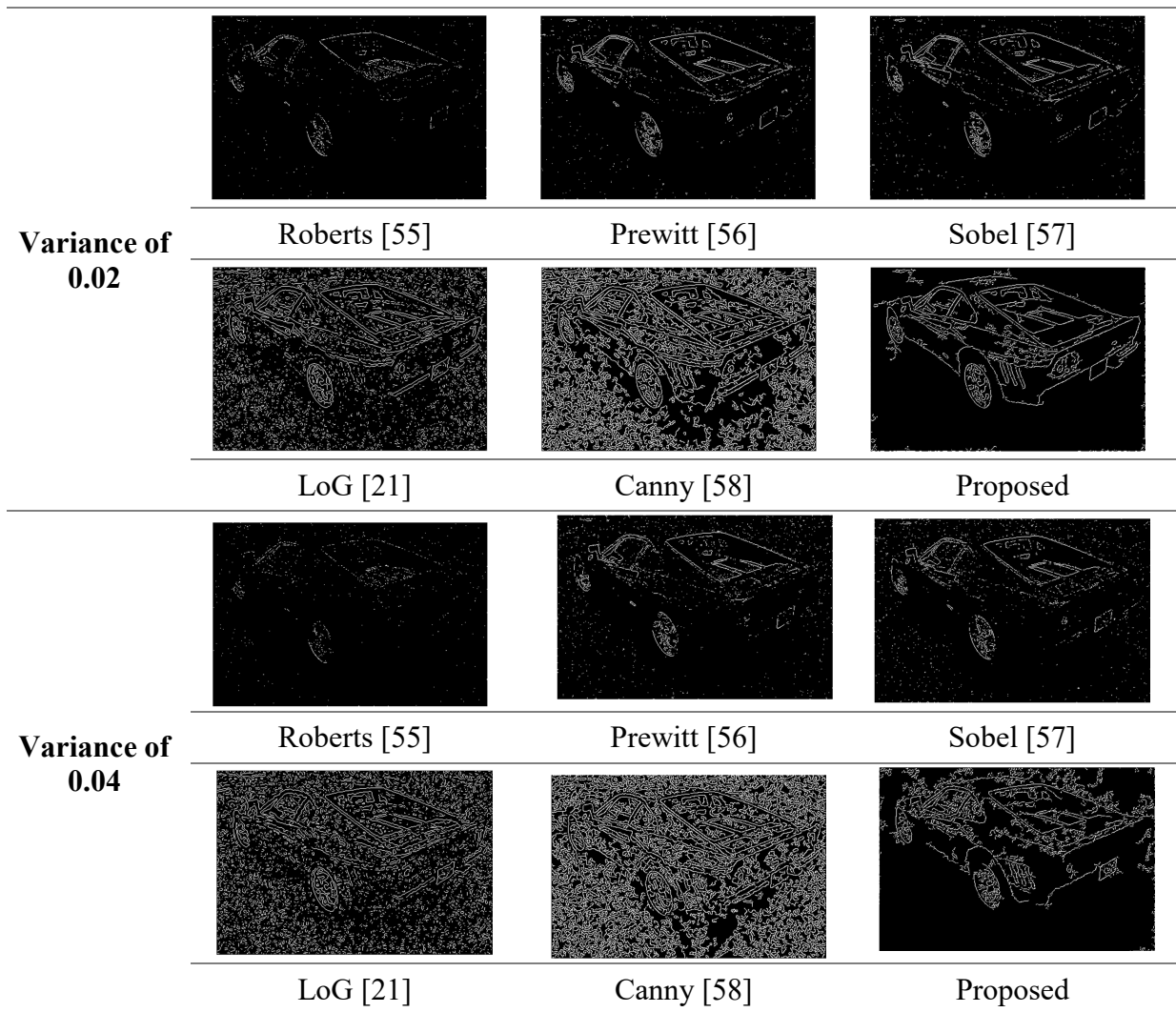


Figure 6.9: Edge maps obtained by various techniques for Car images (481×321) corrupted by the Gaussian noise having zero mean and variance of 0.02 and 0.04

It can be observed from the edge maps that the presented QRFODD approach obtained superior results to the existing classical edge detectors. The coherent edges are detected for the variance of 0.02 as observed from Figure 6.9. It is visually clear that the performance of all the techniques decreases with the increase in variance. Moreover, the effect of variations in the variance of Gaussian noise is considered quantitatively on the basis of performance metrics, that is, FOM and F-Score as shown in Figure 6.10.

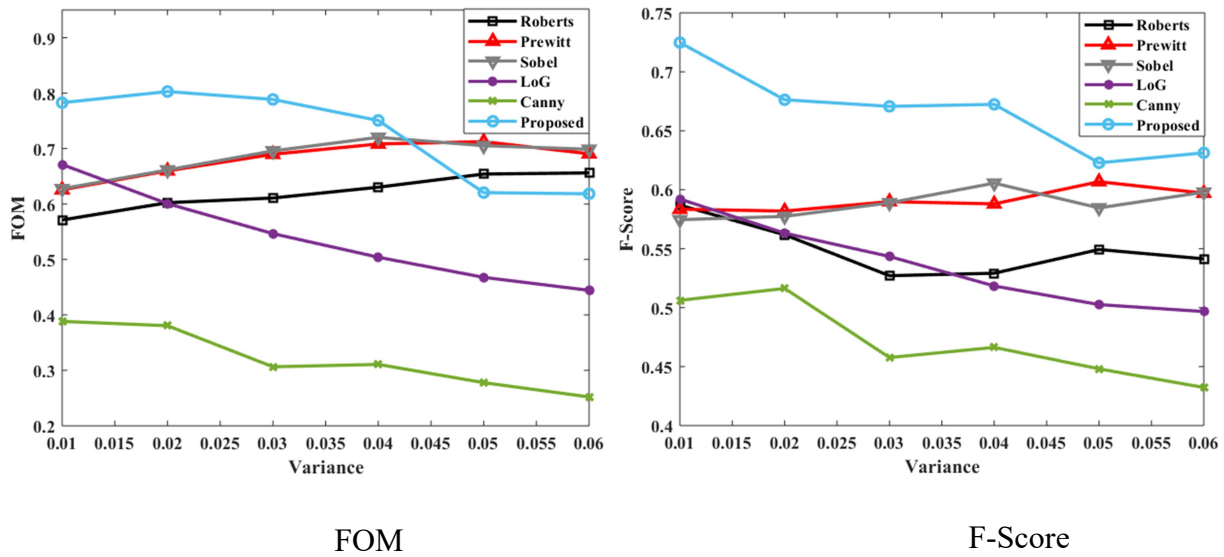


Figure 6.10: Effect on performance metrics with respect to variation in variance of Gaussian noise

It is observed that the value of performance metrics decreases with the variation in a variance of Gaussian noise. The FOM of the proposed approach is less than Roberts [55], Prewitt [56], and Sobel [57] operator because in FOM, the fluctuations in noise are classified as edge points while balancing other errors [53]. However, it is apparent from the visual comparison in Figure 6.9 that the coherent edges are not detected by the Roberts [55], Prewitt [56], and Sobel [57] edge detection techniques. Thus, the proposed approach performs better than the classical edge detection techniques in a noisy environment.

6.4.2 Illumination Conditions

This section is devoted to explore the performance of the edge detection approaches in the illumination conditions that usually occur while acquiring the images. The proposed approach is evaluated with the color images of c1_color, c2_color, c3_color, and c4_color from VIP Illumination Saliency Dataset [183] with varying illumination conditions of the same scene both qualitatively and quantitatively. Figure 6.11 shows the edge maps obtained by the proposed and existing edge detection approaches for color images with variation in illumination conditions for the same scene.

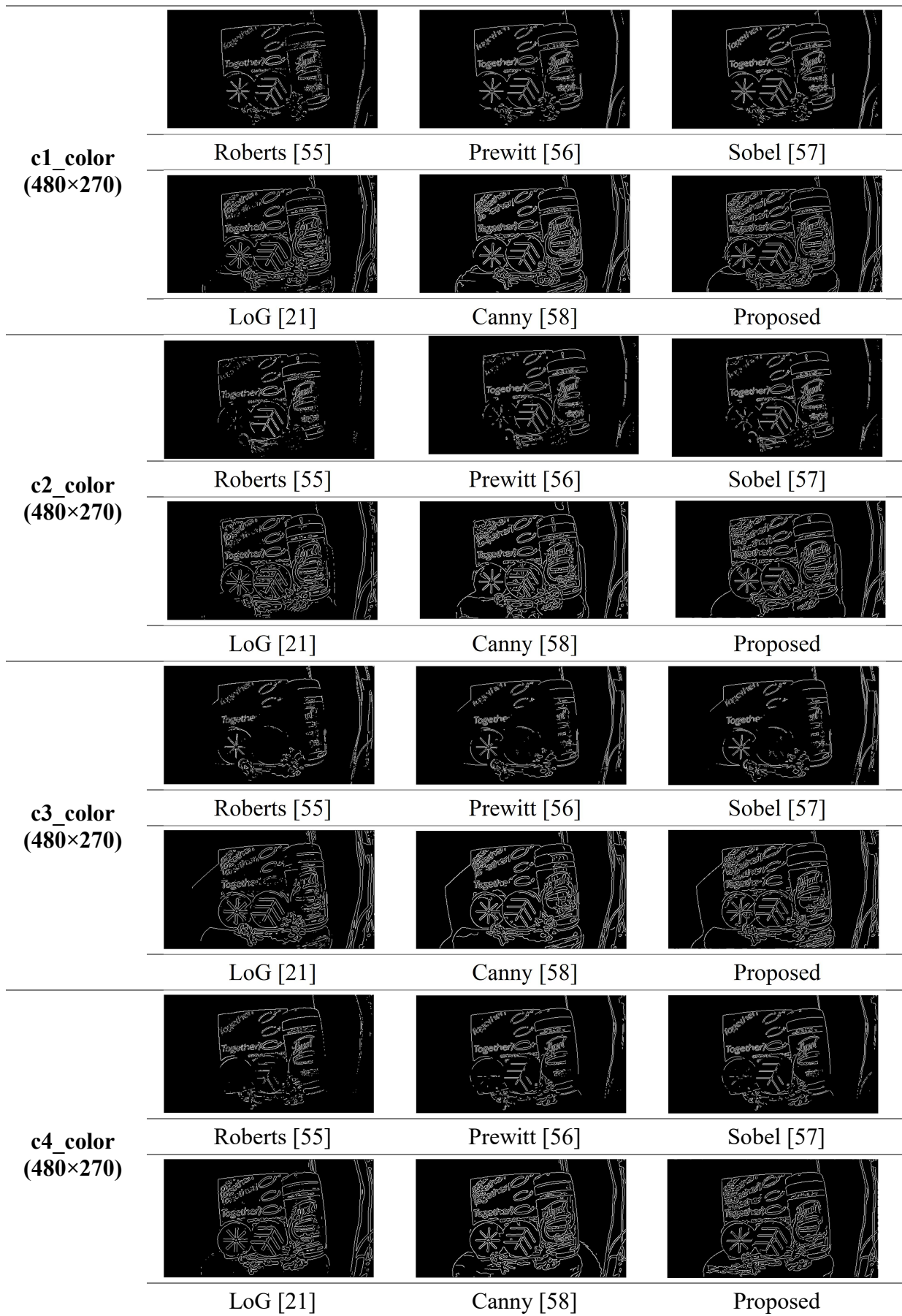


Figure 6.11: Simulation results obtained by various edge detection approaches

The presented QRFODD approach capably extracted the coherent edges even for images with variation in illumination conditions. Moreover, it is noticeably perceived that the edge map obtained using the QRFODD approach efficiently detected the words in images that are not detected by any other classical edge detection technique. To further confirm its efficacy, the quantitative analysis is done considering only FOM using the method described in [74] as shown in Table 6.6. However, F-Score is not computed as the GT is not available for the VIP Illumination Saliency Dataset [183].

Table 6.6: FOM of the proposed approach as compared to classical edge detection techniques

Image	Roberts [55]	Prewitt [56]	Sobel [57]	LoG [21]	Canny [58]	Proposed
c1_color	0.5151	0.6507	0.6566	0.8181	0.8883	0.8857
c2_color	0.4320	0.5413	0.5453	0.7397	0.8179	0.8004
c3_color	0.4239	0.4979	0.5083	0.7383	0.8221	0.8197
c4_color	0.7937	0.8845	0.8910	0.9426	0.7920	0.8273

Bold indicates the maximum value

FOM is less for the proposed approach as the GT is computed based on edge points that are present in a minimum of two classical edge detection techniques. It is clearly visible from Figure 6.11 that the words are not efficiently detected by any classical edge detection techniques. Hence, it can be concluded that FOM doesn't provide accurate results for the considered images without ground truths. However, the visual comparative analysis confirmed the proficiency of the proposed QRFODD technique as compared to the classical edge detection techniques.

6.4.3 JPEG Compression Artifacts

The effect of JPEG compression artifacts is considered in this section for evaluating the capability of the presented QRFODD method. The Car image is taken into account for analyzing the effect of variation in the quality factors from 50 to 95. Figure 6.12 shows the edge map yielded for JPEG images of Car with quality factors 50, 80, and 95 respectively for various edge detection approaches.

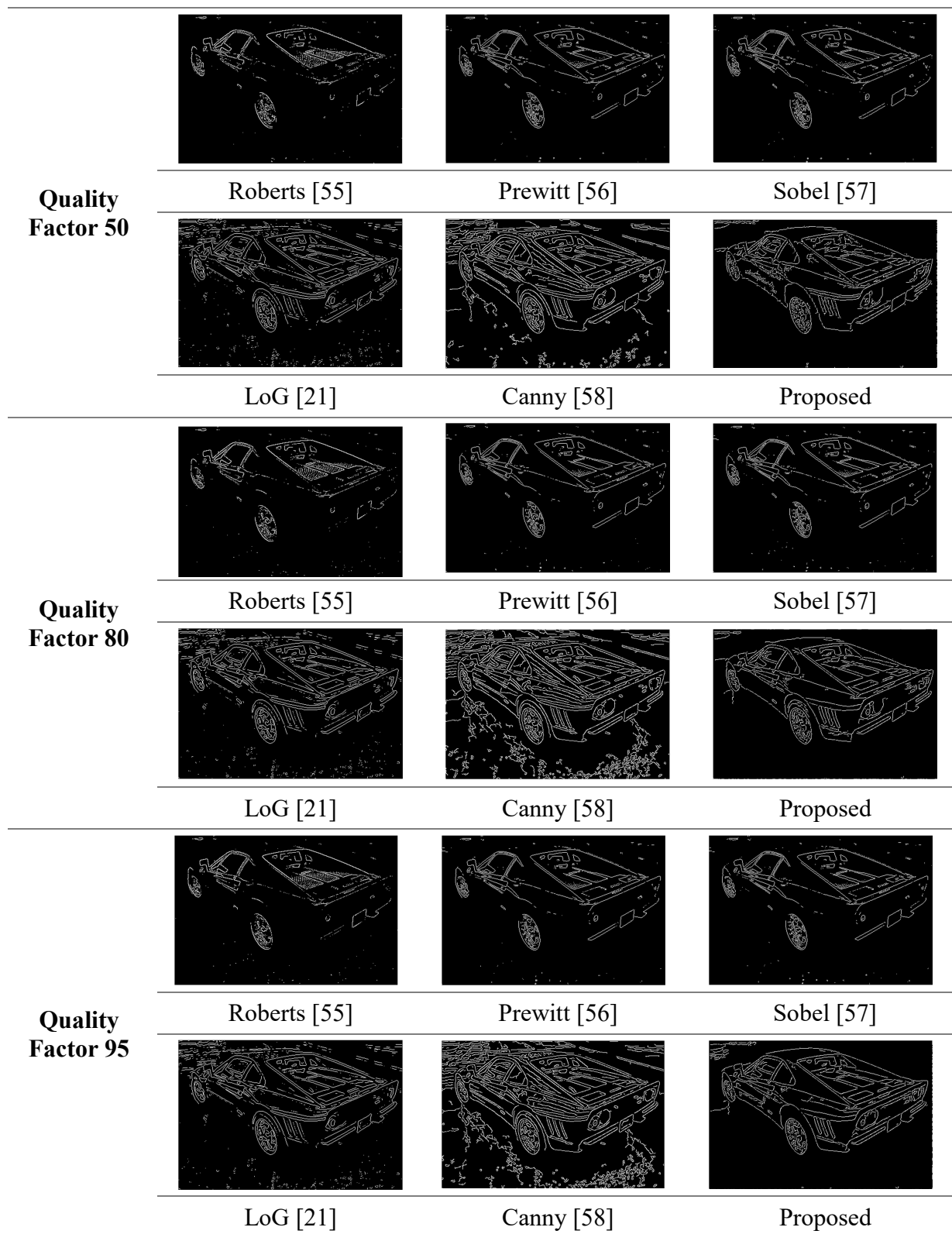


Figure 6.12: Edge maps yielded by various approaches for JPEG compressed Car images (481×321) with quality factor of 50, 80, and 95

It is perceived that the QRFODD approach efficiently yielded the edge maps for images compressed with the quality factors of 50, 80, and 95 without detecting the redundant edges

as detected by LoG and Canny edge detectors. Thus, the adequacy of the presented QRFODD approach in the form of visual comparison is proved by comparing it with traditional edge detection techniques. In order to further explore the effect of various edge detection approaches on quantitative measures, the variation of FOM and F-Score with respect to the quality factors is demonstrated in Figure 6.13.

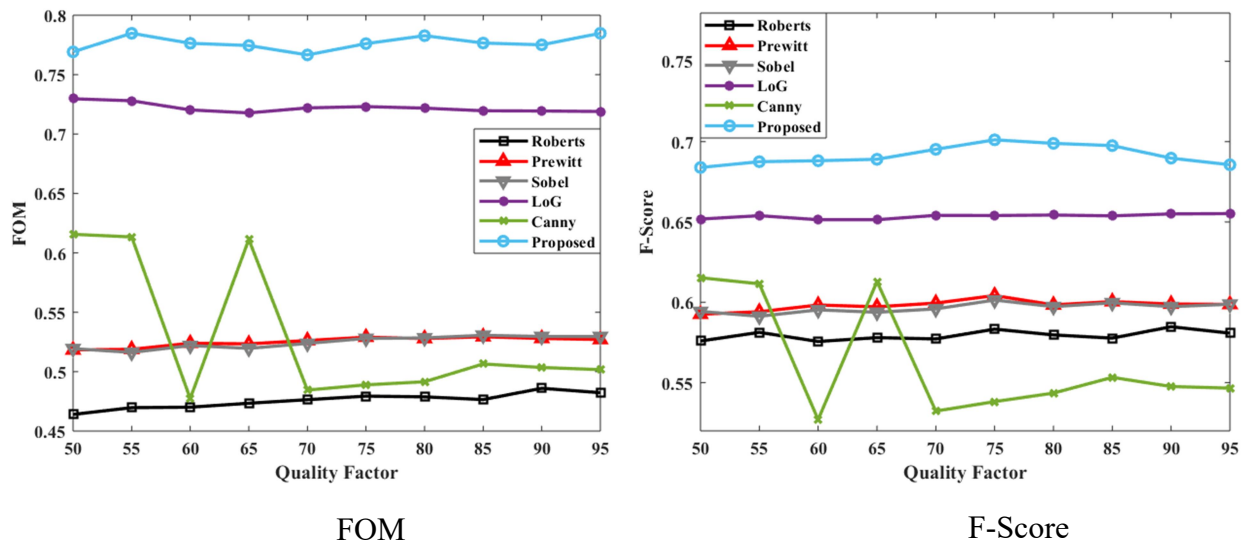


Figure 6.13: Comparison of performance metrics with respect to quality factors

The FOM is approximately same for the quality factor of 80 and 95 whereas there is a dip at a quality factor of 70. However, F-Score gradually increases, becomes highest at a quality factor of 75 and then, starts decreasing with an increase in quality factor. It is noticed that FOM is high while F-Score is less for the quality factor of 95. This may be due to fact that FOM is a measure of well-located edge while balancing errors that is, missing ideal edges, failure in localizing the edges, and classifying fluctuations in noise as edge points whereas F-Score is used to compute only the accuracy of edges [53], [66].

6.5 Computational Cost

The proposed and classical edge detection methods are simulated on the test images of both datasets. The average time (seconds) elapsed to implement them is shown in Table 6.7.

Table 6.7: Computational time of various techniques (in seconds)

Dataset/ Techniques	Roberts [55]	Prewitt [56]	Sobel [57]	LoG [21]	Canny [58]	GLIS [72]	LED [67]	Proposed
BSDS500	0.2309	0.2538	0.2701	0.3641	0.3543	NC	0.0082	6.0492
BSDS300	0.2101	0.2370	0.2646	0.3751	0.3444	0.8124	NC	5.9616

NC: Not Calculated in [67] and [72]

The computational cost incurred to implement the proposed technique is more than the existing edge detection techniques due to the computational time of computing the gamma function for the RFODD mask.

6.6 Real Application of Edge Detection in Fundus Images

Edge detection approaches found their applications in realistic scenarios such as license plate detection, medical images, etc. Therefore, the potential of the proposed approach is established by detecting edge maps for the Fundus images obtained from the HRF database [184]. The simulation results obtained for the Fundus images are illustrated in Figure 6.14.

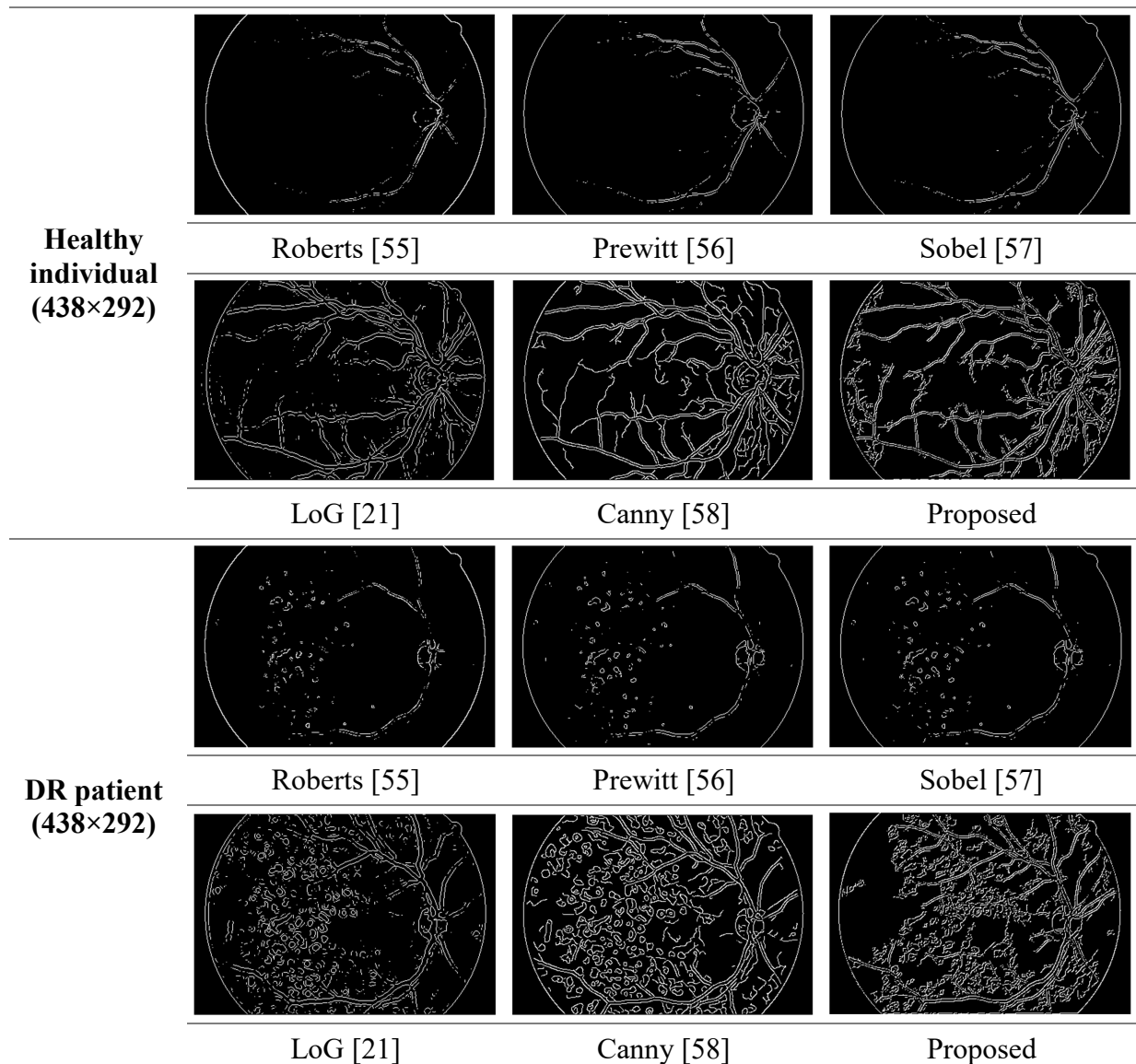


Figure 6.14: Edge map obtained for Fundus images

The simulation results demonstrate that the proposed technique accurately detects the tiny blood vessels as well as the soft and hard exudates in the Fundus images of healthy person

and DR patients. Therefore, it can aid in the early detection of the changes in fundus that occur due to Diabetes. To further confirm its effectiveness in Fundus images, it is also assessed quantitatively in the form of performance metrics as shown in Table 6.8.

Table 6.8: Performance metrics of the proposed approach as compared to classical edge detection approaches

Image	Metrics	Roberts [55]	Prewitt [56]	Sobel [57]	LoG [21]	Canny [58]	Proposed
Healthy	FOM	0.0639	0.0743	0.0776	0.2531	0.3985	0.4051
Individual	F-Score	0.2822	0.3231	0.3358	0.7570	0.7779	0.7791
DR	FOM	0.0705	0.0832	0.0846	0.2626	0.4864	0.4873
patient	F-Score	0.2754	0.3140	0.3202	0.6297	0.6599	0.7101

Bold indicates the maximum value

Therefore, it is evident that the proposed technique performs better even in the case of performance metrics. Therefore, it is inferred from the quantitative and qualitative analysis that the proposed technique can also be successfully implemented for edge detection in Fundus images.

6.7 Application of Proposed Approach for Image Enhancement

This section is intended to provide the merits of the proposed approach in image enhancement. Several spatial and transform-based techniques exist for the enhancement of images, but the issue of extra smoothing persists in some cases that leads to the reduction in image quality [148]. Moreover, the existing techniques usually enhanced the contrast or texture of an image. Therefore, it is required to sharpen the image edges besides improving its contrast and texture. Hence, the image gradient obtained with the proposed approach is added to the original image for image enhancement. The proposed approach mainly performs the task of sharpening the edge details of an image whose potential is established on the basis of its comparison with the RFOD approach in the FrFTD proposed in Chapter-4 referred to as Riesz for the test images shown in Figure 6.3. In Chapter-4, the color channels are processed separately to enhance the images while the proposed approach processed the channels simultaneously, thus, preserving the correlation that exists in the color channels. The scaled version of the images enhanced by these approaches is shown in Figure 6.15 in addition to their zoomed portions.



Original Image



Original Image (zoomed)



Image enhanced by Riesz approach



Image enhanced by Riesz approach (zoomed)



Image enhanced by proposed approach



Image enhanced by proposed approach (zoomed)

Figure 6.15: Simulation results obtained for image enhancement of Building image (481×321)

It is observed that the sharp edges and better texture are obtained with the proposed QRFODD approach than the Riesz approach. The zoomed portion of the images exhibits the improvement in the details of an image by the presented QRFODD approach. The ability of the proposed QRFODD technique in image enhancement is illustrated for the Car, Zebra and Vase_Color images along with their zoomed versions in Figure 6.16.

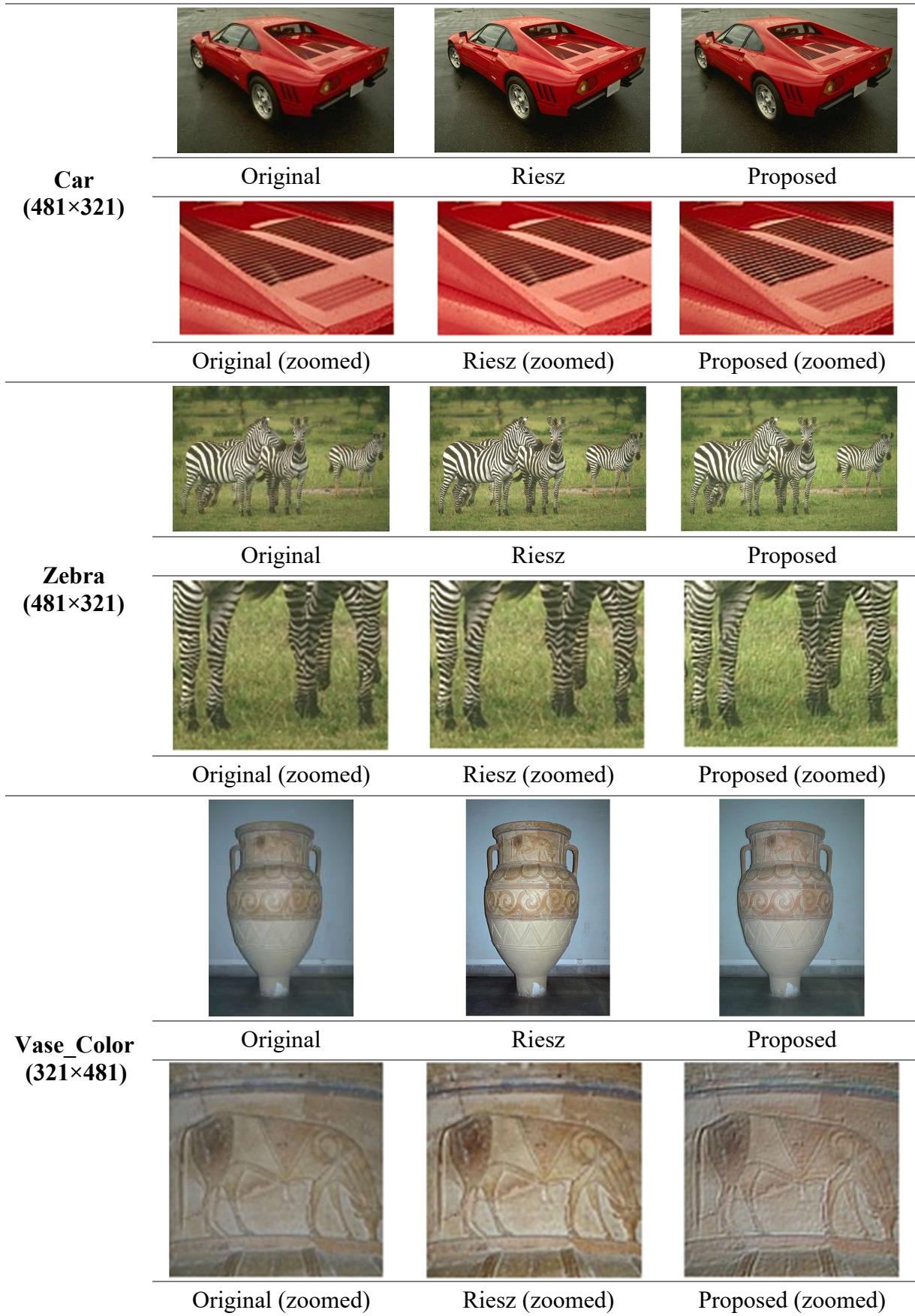


Figure 6.16: Simulation results for image enhancement of various color images

The proposed approach enhanced the edges while preserving the correlation and color of the images as evident from Figure 6.16. Besides, its performance in image enhancement applications is confirmed from the quantitative measures, IE, AG, EME, and EI in Table 6.9.

Table 6.9: Image assessment parameters for test images

Image	Metrics	IE	AG	EME	EI
Car	Original	7.4238	6.0858	7.4923	54.5584
	RFOD	7.5301	6.7197	7.5810	57.4886
	Proposed	7.5933	7.0892	7.7372	61.6162
Zebra	Original	7.2679	10.8931	7.7354	105.0766
	RFOD	7.2899	11.7921	7.8556	111.4608
	Proposed	7.3829	11.8669	8.3578	111.8122
Building	Original	7.4636	7.4780	5.3761	75.1682
	RFOD	7.4378	7.9498	5.3860	77.4224
	Proposed	7.4992	8.4389	7.0346	81.6289
Vase_Color	Original	6.9043	2.9807	2.3797	28.9296
	RFOD	7.4100	4.8984	3.5153	46.9742
	Proposed	7.4137	5.1241	4.0909	47.5965

Bold indicates the maximum value

It becomes evident from the image assessment metrics that the proposed QRFODD approach enhanced the images while efficiently preserving their information and correlation (Section 2.2.4). Moreover, the improvement in AG and EME illustrates the clarity in an enhanced image. In addition to this, improvement in EI justified the enhancement in the edges of an image.

6.8 Summary

In this chapter, a QRFODD mask is utilized for the detection of edges. A mask of suitable size is selected that efficiently detected the clean and continuous edges by preserving the correlation among color channels. Moreover, the results obtained from the extensive experimentation confirmed that the proposed approach is less prone to produce spurious edges. The QRFODD approach provided the minimum improvement of 0.73% in FOM and 8.19% in F-Score as compared to existing edge detection approaches. Additionally, the adequacy of the proposed approach is established from the uncontrolled features that occur while acquiring the images. Furthermore, the benefit of the proposed approach in real applications such as edge detection in Fundus images and image enhancement is also analyzed.

CONCLUSIONS AND FUTURE SCOPE

This chapter is devoted to providing conclusions of the findings of the research work carried out in the field of FODs in image processing in this thesis. Besides, it also provides main highlights and future prospective of the research work.

7.1 Conclusions

The work reported in this study deals with the performance analysis of FOD in various domains for the applications of edge detection and image enhancement. As articulated by various researchers and mathematicians, the fractional parameter possesses the inherent benefit of an extra degree of freedom that aids to model the real systems which are more adequate as compared to the integer-order systems.

After a comprehensive investigation of the available literature, it is found that RL and GL based techniques are extensively used for the applications of image processing. Despite being able to provide better results in comparison to integer-order based techniques, they possess certain demerits that can be resolved by RFOD. However, the selection of RFOD for carrying out the presented work in image processing is done only after the thorough analysis of theoretical concepts as well as simulation work in various domains. In the spatial domain, FOD based UM technique utilized the RL, GL, and Riesz based masks in combination with the Laplacian mask for image enhancement. The experimental results exhibit that the presented RFOD mask provides an increase of at least 1.43%, 24.20%, and 6.25% in IE, AG, and EME respectively for the test images obtained from various standard datasets in comparison to the existing techniques. Moreover, the enhanced Fundus images confirmed their effectiveness in practical applications. Owing to the beneficial results provided by RFOD in the spatial domain, its mathematical analysis is conducted in the FrFTD, thus, deriving a closed-form analytical expression for RFOD in the FrFTD. The robustness of derivation is established by designing a low pass FIR differentiator algorithm which is tested on the one-dimensional design example that outperforms the existing algorithms. In order to further confirm its effectiveness, the proposed notion of RFOD in FrFTD is extended to the two-dimensional applications of image sharpening and HF. The comparative analysis of the proposed RFOD based HF provides an improvement in the range of 4.85 dB-31.29 dB in PSNR and 0.77%-21.74% in IE with respect to the existing approaches. Further, the

mathematical framework is developed for RFOD using various interpolation methods for the applications of image processing. The developed RFOD mask is utilized for proposing an integrated approach for the task of edge detection and image enhancement of grayscale images in FrFTD as well as for color images in the quaternion domain. The gradient images obtained from the proposed approaches are subsequently used for enhancement. The mask size of 3×3 is selected for executing the proposed techniques because it provides more details as compared to masks of other sizes. The extensive simulations demonstrated that the work carried out in this thesis extracted clean and coherent edges while evading the redundant edges. Moreover, the QRFODD approach is capable of preserving the information and correlation details by processing all the color channels simultaneously as it showed the minimum improvement of 0.73% in FOM and 8.19% in F-Score as compared to the existing edge detection techniques. It is also evident from the edges extracted in the case of Fundus images. The robustness of these proposed approaches is further confirmed qualitatively as well as quantitatively by taking into consideration the uncontrolled features. RFOD approach in FrFTD efficiently obtained the edge map for the Poisson noise corrupted images, but there is a scope of improvement in its performance for the high concentration of the Gaussian noise. Based on performance metrics, the overall improvement of 1.01-57.64%, 2.37-22.71%, 0.34-2.28%, 1.16-14.66%, 0.9-10.64%, and 1.02-32.85% for FOM, EPI, IE, AG, EI, and EME respectively is achieved by the proposed RFOD approach in FrFTD.

Some of the observations that are worth noting in this research work for the research fraternity is that the blocking artifacts become significant with the increase in mask size for RFOD in the FrFTD. The proposed HF approach efficiently enhanced the images with low contrast and non-uniform lighting that was an issue in FOD based UM in the spatial domain. Moreover, the proposed RFOD based approaches efficiently detected the edges in both grayscale and color images even in the case of most of the uncontrolled features. The gradient images are utilized to enhance the image features mainly the edges. Hence, a new algorithm is successfully developed for performing the task of both edge detection and image enhancement even when subjected to uncontrolled features.

“RFOD based approaches in FrFT and quaternion domains exhibited better performance with improved qualitative and quantitative measures even when subjected to uncontrolled features in the image processing applications.”

7.2 Main Highlights of the Research Work

The major highlights of the presented work in the field of FODs are as follows:

- FOD based UM approach is proposed for the image enhancement. The evaluation of proposed approach on various images from standard datasets provided promising results for RFOD based UM.
- A closed-form analytical expression is derived for RFOD in the FrFTD. Its discrete counterpart established its applicability by considering a design example that outperformed the existing ones with a minimum RMSE of 0.115136.
- RFOD approach in the FrFTD is extended for the two-dimensional application of image enhancement. Moreover, it is utilized in the HF approach for enhancing the images with low contrast and non-uniform illumination.
- The mathematical framework is obtained for the image processing applications based on RFOD by using the interpolation methods.
- FrFT based RFOD algorithm is developed for detecting edges in grayscale images. The gradient images thus obtained are further used for the purpose of image enhancement.
- Quaternion based RFOD technique is proposed for color image edge detection. The adequacy of the presented approach is validated in realistic scenarios by considering the Fundus images. Furthermore, the proposed approach is explored to find its application in image enhancement.

The novelty of the presented work is that RFOD approach provides better results for both edge detection and image enhancement even when subjected to uncontrolled features specifically noise, illumination conditions, and JPEG compression artifacts. Furthermore, the presented work on FODs in the field of image processing will be beneficial for the research fraternity working in the field of watermarking, computer vision, etc.

7.3 Future Scope

The research work in this thesis can be extended in the following directions for further explorations in this field:

- An analytical expression is derived in the closed-form only for the RFOD in the FrFTD. In a similar manner, the mathematical analysis of other definitions of FODs such as Caputo-Fabrizio, Atangana-Baleanu can be explored in the fractional transforms.

- The proposed RFOD based algorithms can also be extended to biomedical, infrared images, etc. for the extraction of edges as well as enhancement of images. To exemplify, the RFOD mask can be applied to the MRI images for extracting the edges as well as abnormality present in the images. The extracted edges can be further added to the original MRI images for enhancing the image features that assist in better diagnosis.
- It is expected that the presented work can be employed in the case of image forensics for the detection of tampered location. As the tampered locations generally have blurred edges, therefore, FrFT based RFOD approach can be applied to the tampered images for extracting edges which can assist in distinguishing the tampered images from the original images.
- The presented RFOD approaches for edge detection and image enhancement can be further utilized for extracting and enhancing more features that can be fed to the learning model for applications of pattern recognition and computer vision.
- The concept of the presented work can also be examined for the videos. The presented RFOD based edge detection and image enhancement approaches can be applied to the frames extracted from the videos for the purpose of edge detection or video enhancement.

REFERENCES

- [1] M. D. Ortigueira, *Fractional Calculus for Scientists and Engineers*, vol. 84, Netherlands: Springer, 2011.
- [2] Q. Yang, D. Chen, T. Zhao, and Y. Q. Chen, "Fractional calculus in image processing: A review," *Fract. Calc. Appl. Anal.*, vol. 19, no. 5, pp.1222-1249, Nov. 2016, doi: 10.1515/fca-2016-0063.
- [3] S. Das and I. Pan, *Fractional order signal processing: Introductory Concepts and Applications*, New York, NY, USA: Springer-Verlag, 2012.
- [4] S. Das, *Functional Fractional Calculus*, 2nd ed., Heidelberg, Berlin, Germany: Springer-Verlag, 2011.
- [5] H. M. Ozaktas, Z. Zalevsky, M. A. Kutay, *The Fractional Fourier Transform with Applications in Optics and Signal Processing*, New York, NY, USA: John Wiley & Sons, 2001.
- [6] N. Jindal and K. Singh, "Image and video processing using discrete fractional transforms," *SIViP*, vol. 8, pp. 1543-1553, Nov. 2014, doi: 10.1007/s11760-012-0391-4.
- [7] Y. Zhang *et al.*, "A Comprehensive Survey on Fractional Fourier Transform," *Fundam. Inform.*, vol. 151, no. 1-4, pp. 1-48, Mar. 2017, doi: 10.3233/FI-2017-1477.
- [8] A. A. Kilbas, Y. F. Luchko, H. Martínez, and J. J. Trujillo, "Fractional Fourier transform in the framework of fractional calculus operators," *Integr. Transform. Spec. Funct.*, vol. 21, no. 10, pp. 779-795, Oct. 2010, doi: 10.1080/10652461003676099.
- [9] K. Singh, R. Saxena, and S. Kumar, "Caputo-Based Fractional Derivative in Fractional Fourier Transform Domain," *IEEE J. Emerg. Sel. Top. Circuits Syst.*, vol. 3, no. 3, pp. 330-337, Sep. 2013, doi: 10.1109/JETCAS.2013.2272837.
- [10] S. Kumar, K. Singh, and R. Saxena, "Closed-Form Analytical Expression of Fractional Order Differentiation in Fractional Fourier Transform Domain," *Circuits, Syst. Signal Process.*, vol. 32, pp. 1875-1889, Aug. 2013, doi: 10.1007/s00034-012-9548-1.
- [11] S. Kumar, R. Saxena, and K. Singh, "Fractional Fourier Transform and Fractional-Order Calculus-Based Image Edge Detection," *Circuits, Syst. Signal Process.*, vol. 36, pp. 1493- 1513, Apr. 2017, doi: 10.1007/s00034-016-0364-x.
- [12] A. K. Jain, *Fundamentals of Digital Image Processing*, Englewood Cliffs, NJ, USA: Prentice Hall, 1989.

- [13] M. Javed, P. Nagabhushan, B. B. Chaudhuri, and S. K. Singh, "Edge based enhancement of retinal images using an efficient JPEG-compressed domain technique," *J. Intell. Fuzzy Syst.*, vol. 36, no. 1, pp. 541-556, Feb. 2019, doi: 10.3233/JIFS-18859.
- [14] G. Li, Y. Yang, X. Qu, D. Cao, and K. Li, "A deep learning based image enhancement approach for autonomous driving at night," *Knowledge-Based Syst.*, vol. 213, Feb. 2021, Art. no. 106617, doi: 10.1016/j.knosys.2020.106617.
- [15] Y. He and L. M. Ni, "A Novel Scheme Based on the Diffusion to Edge Detection," *IEEE Trans. Image Process.*, vol. 28, no. 4, pp. 1613-1624, Apr. 2019, doi: 10.1109/TIP.2018.2880568.
- [16] S. Borse and P. K. Bora, "A novel approach to image edge detection using Kalman filtering," in *Proc. IEEE 7th Annu. Inf. Technol. Electron. Mobile Commun. Conf.*, Vancouver, BC, Canada, 2016, pp. 1-5, doi: 10.1109/IEMCON.2016.7746258.
- [17] O. Karakuş, E. E. Kuruoğlu, and M. A. Altinkaya, "Generalized Bayesian model selection for speckle on remote sensing images," *IEEE Trans. Image Process.*, vol. 28, no. 4, pp. 1748-1758, Apr. 2019, doi: 10.1109/TIP.2018.2878322.
- [18] B. Deka and P. K. Bora, "Despeckling of medical ultrasound images using sparse representation," in *Proc. 2010 Int. Conf. Signal Process. Commun.*, Bangalore, India, 2010, pp. 1-5, doi: 10.1109/SPCOM.2010.5560519.
- [19] M. S. Umar and M. Q. Rafiq, "Select-to-Spawn: A novel recognition-based graphical user authentication scheme," in *Proc. 2012 IEEE Int. Conf. Signal Process. Comput. Control*, Wanknaghat Solan, India, 2012, pp. 1-5, doi: 10.1109/ISPCC.2012.6224382.
- [20] G. Sethi, B. S. Saini, and D. Singh, "Segmentation of cancerous regions in liver using an edge-based and phase congruent region enhancement method," *Comput. Electr. Eng.*, vol. 53, pp. 244-262, Jul. 2016, doi: 10.1016/j.compeleceng.2015.06.025.
- [21] R. C. Gonzalez, R. E. Woods, and S. L. Eddins, *Digital Image Processing using MATLAB*, 2nd ed., Chennai, India: McGraw Hill, 2004.
- [22] S. G. Samko, A. A. Kilbas, and O. I. Marichev, *Fractional Integrals and Derivatives Theory and Applications*, New York, NY, USA: Gordon & Breach, 1993.
- [23] B. T. Krishna, "Studies on fractional order differentiators and integrators: A survey," *Signal Process.*, vol. 91, no. 3, pp. 386-426, Mar. 2011, doi: 10.1016/j.sigpro.2010.06.022.
- [24] A. Atangana and D. Baleanu, "New fractional derivatives with non-local and non-singular kernel: Theory and application to heat transfer model," *Therm. Sci.*, vol.20,

- no. 2, pp. 763-769, 2016, doi: 10.2298/TSCII60111018A.
- [25] M. Caputo and M. Fabrizio, "A new definition of fractional derivative without singular Kernel," *Prog. Fract. Differ. Appl.*, vol. 1, no. 2, pp. 73-85, Apr. 2015, doi: 10.12785/pfda/010201.
- [26] K. S. Miller and B. Ross, *An Introduction To The Fractional Calculus And Fractional Differential Equations*, New York, NY, USA: John Wiley & Sons, 1993.
- [27] K. B. Oldham and J. Spanier, *The Fractional Calculus Theory and Applications of Differentiation and Integration to Arbitrary Order*, San Diego, California, USA: Academic Press, 1974.
- [28] L. Yaroslavsky, *Fast Transform Methods in Digital Signal Processing: Theory, Applications, Efficient Algorithms*, vol. 2, Bentham Science, 2011.
- [29] N. Jindal and K. Singh, "Applicability of fractional transforms in image processing - review, technical challenges and future trends," *Multimed. Tools Appl.*, vol. 78, pp. 10673-10700, Apr. 2019, doi: 10.1007/s11042-018-6594-0.
- [30] S. Kumar, "Analysis and design of non recursive digital differentiators in fractional domain for signal processing applications," Ph.D. dissertation, Dept. Electron. Commun. Eng., Thapar Inst. Engg. Tech., Patiala, Punjab, India, 2013. [Online]. Available: <http://hdl.handle.net/10603/230330>.
- [31] V. Namias, "The Fractional Order Fourier Transform and its Application to Quantum Mechanics," *IMA J. Appl. Math.*, vol. 25, no. 3, pp. 241-265, Mar. 1980, doi: 10.1093/imamat/25.3.241.
- [32] R. Saxena and K. Singh, "Fractional Fourier transform: A novel tool for signal processing," *J. Indian Inst. Sci.*, vol. 85, no. 1, pp. 11-26, Jan.-Feb. 2005.
- [33] A. C. McBride and F. H. Kerr, "On namias's fractional fourier transforms," *IMA J. Appl. Math.*, vol. 39, no. 2, pp. 159-175, May 1987, doi: 10.1093/imamat/39.2.159.
- [34] A. K. Singh and R. Saxena, "On Convolution and Product Theorems for FRFT," *Wireless Pers. Commun.*, vol. 65, pp. 189-201, Jul. 2012, doi: 10.1007/s11277-011-0235-5.
- [35] O. Akay and G. F. Boudreaux-Bartels, "Fractional convolution and correlation via operator methods and an application to detection of linear FM signals," *IEEE Trans. Signal Process.*, vol. 49, no. 5, pp. 979-993, May 2001, doi: 10.1109/78.917802.
- [36] K. K. Sharma and S. D. Joshi, "On scaling properties of fractional Fourier transform and its relation with other transforms," *Opt. Commun.*, vol. 257, no. 1, pp. 27-38, Jan. 2006, doi: 10.1016/j.optcom.2005.07.013.

- [37] A. I. Zayed, "A convolution and product theorem for the fractional Fourier transform," *IEEE Signal Process. Lett.*, vol. 5, no. 4, pp. 101-103, Apr. 1998, doi: 10.1109/97.664179.
- [38] L. B. Almeida, "Product and Convolution Theorems for the Fractional Fourier Transform," *IEEE Signal Process. Lett.*, vol. 4, no. 1, pp. 15-17, Jan. 1997, doi: 10.1109/97.551689.
- [39] D. Wei, "Novel convolution and correlation theorems for the fractional Fourier transform," *Optik*, vol. 127, no. 7, pp. 3669-3675, Apr. 2016, doi: 10.1016/j.ijleo.2015.12.069.
- [40] A. I. Zayed, "Two-dimensional fractional Fourier transform and some of its properties," *Integr. Transform. Spec. Funct.*, vol. 29, no. 7, pp. 553-570, Jul. 2018, doi: 10.1080/10652469.2018.1471689.
- [41] H. M. Ozaktas, O. Arikan, M. A. Kutay, and G. Bozdagt, "Digital computation of the fractional Fourier transform," *IEEE Trans. Signal Process.*, vol. 44, no. 9, pp. 2141-2150, Sep. 1996, doi: 10.1109/78.536672.
- [42] S. C. Pei and J. J. Ding, "Closed-form discrete fractional and affine fourier transforms," *IEEE Trans. Signal Process.*, vol. 48, no. 5, pp. 1338-1353, May 2000, doi: 10.1109/78.839981.
- [43] Ç. Candan, M. A. Kutay, and H. M. Ozaktas, "The discrete fractional fourier transform," *IEEE Trans. Signal Process.*, vol. 48, no. 5, pp. 1329-1337, May 2000, doi: 10.1109/78.839980.
- [44] Ç. Candan, M. A. Kutay, and H. M. Ozaktas, "The discrete fractional Fourier transform," in *Proc. 1999 IEEE Int. Conf. Acoust. Speech Signal Process.*, Phoenix, AZ, USA, 1999, pp. 1713-1716, doi: 10.1109/icassp.1999.756324.
- [45] A. K. Singh and R. Saxena, "DFRFT: A Classified Review of Recent Methods with Its Application," *J. Eng.*, vol. 2013, Apr. 2013, Art. no. 214650, doi: 10.1155/2013/214650.
- [46] S. Kumar, K. Singh, and R. Saxena, "Analysis of Dirichlet and Generalized "Hamming" window functions in the fractional Fourier transform domains," *Signal Process.*, vol. 91, no. 3, pp. 600-606, Mar. 2011, doi: 10.1016/j.sigpro.2010.04.01.
- [47] K. Dubey, M. Y. Shams, S. C. Sharma, A. Alarifi, M. Amoon, and A. A. Nasr, "A Management System for Servicing Multi-Organizations on Community Cloud Model in Secure Cloud Environment," *IEEE Access*, vol. 7, pp. 159535-159546, Oct. 2019, doi: 10.1109/ACCESS.2019.2950110.

- [48] A. Singh and P. K. Jain, "A comparative study of SVD and ICA for target detection in through-the-wall radar images," in *Proc. 2016 11th Int. Conf. Ind. Inf. Syst.*, Roorkee, India, 2016, pp. 608-613, doi: 10.1109/ICIINFS.2016.8263011.
- [49] K. S. Raghunandan *et al.*, "Riesz Fractional Based Model for Enhancing License Plate Detection and Recognition," *IEEE Trans. Circuits Syst. Video Technol.*, vol. 28, no. 9, pp. 2276-2288, Sep. 2018, doi: 10.1109/TCSVT.2017.2713806.
- [50] G. Torkhani, A. Ladgham, A. Sakly, and M. N. Mansouri, "A 3D–2D face recognition method based on extended Gabor wavelet combining curvature and edge detection," *SIViP*, vol. 11, pp. 969-976, Jul. 2017, doi: 10.1007/s11760-016-1046-7.
- [51] D. An, J. Hao, Y. Wei, Y. Wang, and X. Yu, "Application of computer vision in fish intelligent feeding system—A review," *Aquac. Res.*, vol. 52, no. 2, pp. 423-427, Feb. 2021, doi: 10.1111/are.14907.
- [52] A. C. Bovik, *The Essential Guide to Image Processing*, San Diego, California, USA: Academic Press, 2009.
- [53] W. K. Pratt, *Introduction to Digital Image Processing*, Boca Raton, FL, USA: CRC Press, 2014.
- [54] D. K. Yadav, G. Kuldeep, and S. D. Joshi, "Ramanujan Sums as Derivatives and Applications," *IEEE Signal Process. Lett.*, vol. 25, no. 3, pp. 413-416, Mar. 2018, doi: 10.1109/LSP.2017.2721966.
- [55] L. G. Roberts, "Machine perception of three-dimensional solids," Ph.D. dissertation, Dept. Elect. Eng., Massachusetts Inst. Tech., Cambridge, Massachusetts, US, 1963. [Online]. Available: <http://hdl.handle.net/1721.1/11589>.
- [56] J. Prewitt, "Object enhancement and extraction," in *Picture processing and Psychopictorics*, vol. 10, no. 1, B. S. Lipkin and A. Rosenfeld, Eds., San Diego, NY, USA: Academic Press, 1970, pp. 75-150.
- [57] I. Sobel, "Camera Models and Machine Perception," Comp. Sci. Dept., Technion-Israel Inst. Tech., Haifa, Israel, Rep. No. CS Technion report CS0016, 1972.
- [58] J. Canny, "A Computational Approach to Edge Detection," *IEEE Trans. Pattern Anal. Mach. Intell.*, vol. PAMI-8, no. 6, pp. 679-698, Nov. 1986, doi: 10.1109/TPAMI.1986.4767851.
- [59] P. Dollár and C. L. Zitnick, "Fast Edge Detection Using Structured Forests," *IEEE Trans. Pattern Anal. Mach. Intell.*, vol. 37, no. 8, pp. 1558-1570, Aug. 2015, doi: 10.1109/TPAMI.2014.2377715.
- [60] S. Li, S. Dasmahapatra, and K. Maharatna, "Dynamical System Approach for Edge

- Detection Using Coupled FitzHugh-Nagumo Neurons,” *IEEE Trans. Image Process.*, vol. 24, no. 12, pp. 5206-5219, Dec. 2015, doi: 10.1109/TIP.2015.2467206.
- [61] J. J. Liu, Q. Hou, and M. M. Cheng, “Dynamic Feature Integration for Simultaneous Detection of Salient Object, Edge, and Skeleton,” *IEEE Trans. Image Process.*, vol. 29, pp. 8652-8667, Aug. 2020, doi: 10.1109/TIP.2020.3017352.
- [62] S. Konishi, A. L. Yuille, J. M. Coughlan, and S. C. Zhu, “Statistical edge detection: learning and evaluating edge cues,” *IEEE Trans. Pattern Anal. Mach. Intell.*, vol. 25, no. 1, pp. 57-74, Jan. 2003, doi: 10.1109/TPAMI.2003.1159946.
- [63] Y. Li, Y. Bi, W. Zhang, and C. Sun, “Multi-Scale Anisotropic Gaussian Kernels for Image Edge Detection,” *IEEE Access*, vol. 8, pp. 1803-1812, Dec. 2019, doi: 10.1109/ACCESS.2019.2962520.
- [64] D. D. Y. Po and M. N. Do, “Directional multiscale modeling of images using the contourlet transform,” *IEEE Trans. Image Process.*, vol. 15, no. 6, pp. 1610-1620, Jun. 2006, doi: 10.1109/TIP.2006.873450.
- [65] G. Zhang *et al.*, “FoGDbED: Fractional-order Gaussian derivatives-based edge-relevant structure detection using Caputo-Fabrizio definition,” *Digit. Signal Process. A Rev. J.*, vol. 98, Mar. 2020, Art. no. 102639, doi: 10.1016/j.dsp.2019.102639.
- [66] C. Akinlar and C. Topal, “ColorED: Color edge and segment detection by Edge Drawing (ED),” *J. Vis. Commun. Image Represent.*, vol. 44, pp. 82-94, Apr. 2017, doi: 10.1016/j.jvcir.2017.01.024.
- [67] Y. Liu, Z. Xie, and H. Liu, “An Adaptive and Robust Edge Detection Method Based on Edge Proportion Statistics,” *IEEE Trans. Image Process.*, vol. 29, pp. 5206-5215, Mar. 2020, doi: 10.1109/TIP.2020.2980170.
- [68] C. B. Gao, J. L. Zhou, J. R. Hu, and F. N. Lang, “Edge detection of colour image based on quaternion fractional differential,” *IET Image Process.*, vol. 5, no. 3, pp. 261-272, Apr. 2011, doi: 10.1049/iet-ipr.2009.0409.
- [69] A. M. Grigoryan and S. S. Agaian, *Quaternion and Octonion Color Image Processing with MATLAB*, Bellingham, WA, USA: SPIE, 2018.
- [70] J. Fan, W. G. Aref, M. S. Hacid, and A. K. Elmagarmid, “An improved automatic isotropic color edge detection technique,” *Pattern Recognit. Lett.*, vol. 22, no. 13, pp. 1419-1429, Nov. 2001, doi: 10.1016/S0167-8655(01)00082-4.
- [71] S. K. Naik and C. A. Murthy, “Standardization of edge magnitude in color images,” *IEEE Trans. Image Process.*, vol. 15, no. 9, pp. 2588-2595, Sep. 2006, doi: 10.1109/TIP.2006.877408.

- [72] V. Kothapalli, S. Arora, and M. Hanmandlu, "Edge detection using fractional derivatives and information sets," *J. Electron. Imaging*, vol. 27, no. 5, Jun. 2018, Art. no. 051226, doi: 10.1117/1.jei.27.5.051226.
- [73] J. E. Lavín-Delgado, J. E. Solís-Pérez, J. F. Gómez-Aguilar, and R. F. Escobar-Jiménez, "A New Fractional-Order Mask for Image Edge Detection Based on Caputo–Fabrizio Fractional-Order Derivative Without Singular Kernel," *Circuits, Syst. Signal Process.*, vol. 39, pp. 1419-1448, Mar. 2020, doi: 10.1007/s00034-019-01200-3.
- [74] O. P. Verma and A. S. Parihar, "An Optimal Fuzzy System for Edge Detection in Color Images Using Bacterial Foraging Algorithm," *IEEE Trans. Fuzzy Syst.*, vol. 25, no. 1, pp. 114-127, Feb. 2017, doi: 10.1109/TFUZZ.2016.2551289.
- [75] C. Gao, J. Zhou, F. Lang, Q. Pu, and C. Liu, "A Novel Approach to Edge Detection of Color Image Based on Quaternion Fractional Directional Differentiation," in *Advances in Automation and Robotics*, vol. 122, G. Lee, Ed., Berlin, Heidelberg, Germany: Springer, 2011, pp. 163-170, doi: 10.1007/978-3-642-25553-3_22.
- [76] W. Bi and K. I. Kou, "A novel color edge detection algorithm based on quaternion hardy filter," 2018. [Online]. Available: arXiv:1807.10586v2.
- [77] R. Wang, S. Li, and E. E. Kuruoglu, "A novel algorithm for image denoising based on unscented Kalman filtering," *Int. J. Inf. Commun. Technol.*, vol. 5, no. 3/4, pp. 343-353, Jun. 2013, doi: 10.1504/IJICT.2013.054944.
- [78] C. Solomon and T. Breckon, *Fundamentals of Digital Image Processing: A Practical Approach with Examples in Matlab*, Hoboken, NJ: USA, Wiley-Blackwell, 2010.
- [79] D. Sheet, H. Garud, A. Suveer, M. Mahadevappa, and J. Chatterjee, "Brightness preserving dynamic fuzzy histogram equalization," *IEEE Trans. Consum. Electron.*, vol. 56, no. 4, pp. 2475-2480, Nov. 2010, doi: 10.1109/TCE.2010.5681130.
- [80] K. Singh and R. Kapoor, "Image enhancement via Median-Mean Based Sub-Image-Clipped Histogram Equalization," *Optik*, vol. 125, no. 17, pp. 4646-4651, Sep. 2014, doi: 10.1016/j.ijleo.2014.04.093.
- [81] A. Polesel, G. Ramponi, and V. J. Mathews, "Image enhancement via adaptive unsharp masking," *IEEE Trans. Image Process.*, vol. 9, no. 3, pp. 505-510, Mar. 2000, doi: 10.1109/83.826787.
- [82] T. C. Aysal and K. E. Barner, "Quadratic Weighted Median Filters for Edge Enhancement of Noisy Images," *IEEE Trans. Image Process.*, vol. 15, no. 11, pp. 3294-3310, Nov. 2006, doi: 10.1109/TIP.2006.882010.
- [83] N. Kwok and H. Shi, "Design of unsharp masking filter kernel and gain using particle

- swarm optimization,” in *Proc.2014 7th Int. Congr. Image Signal Process.*, Dalian, China, 2014, pp. 217-222, doi: 10.1109/CISP.2014.7003780.
- [84] S. Kansal, S. Purwar, and R. K. Tripathi, “Image contrast enhancement using unsharp masking and histogram equalization,” *Multimed. Tools Appl.*, vol. 77, pp. 26919-26938, Mar. 2018, doi: 10.1007/s11042-018-5894-8.
- [85] J. Joseph, B. N. Anoop, and J. Williams, “A modified unsharp masking with adaptive threshold and objectively defined amount based on saturation constraints,” *Multimed. Tools Appl.*, vol. 78, pp. 11073-11089, Apr. 2019, doi: 10.1007/s11042-018-6682-1.
- [86] W. Ye and K. K. Ma, “Blurriness-Guided Unsharp Masking,” in *IEEE Trans. Image Process.*, vol. 27, no. 9, pp. 4465-4477, Sep. 2018, doi: 10.1109/TIP.2018.2838660.
- [87] C. C. Tseng and S. L. Lee, “A weak-illumination image enhancement method using homomorphic filter and image fusion,” in *Proc. 2017 IEEE 6th Global Conf. Consum. Electron.*, Nagoya, Japan, 2017, pp.1-2, doi: 10.1109/GCCE.2017.8229192.
- [88] S. L. Lee and C. C. Tseng, “Image enhancement using DCT-based matrix homomorphic filtering method,” in *Proc. 2016 IEEE Asia Pacific Conf. Circuits Syst.*, Jeju, South Korea, 2016, pp. 1-4, doi: 10.1109/APCCAS.2016.7803880.
- [89] Y. Chu, S. Kosunalp, P. D. Mitchell, D. Grace, and T. Clarke, “Application of reinforcement learning to medium access control for wireless sensor networks,” *Eng. Appl. Artif. Intell.*, vol. 46, part A, pp. 23-32, Nov. 2015, doi: 10.1016/j.engappai.2015.08.004.
- [90] R. Thangaraj, T. R. Chelliah, M. Pant, A. Abraham, and P. Bouvry, “Applications of Nature Inspired Algorithms for Electrical Engineering Optimization Problems,” in *Handbook of Optimization*, I. Zelinka, V. Snášel, and, A. Abraham, Eds., vol. 38, Heidelberg, Berlin, Germany: Springer, 2013, pp. 991-1024, doi: 10.1007/978-3-642-30504-7_39.
- [91] M. Kumar, “Fractional order FIR differentiator design using particle swarm optimization algorithm,” *Int. J. Numer. Model. Electron. Netw. Devices Fields*, vol. 32, no. 2, Mar./Apr. 2019, Art. no. e2514, doi: 10.1002/jnm.2514.
- [92] A. Nandal *et al.*, “Image Edge Detection Using Fractional Calculus with Feature and Contrast Enhancement,” *Circuits, Syst. Signal Process.*, vol. 37, pp. 3946-3972, Sep. 2018, doi: 10.1007/s00034-018-0751-6.
- [93] C. B. Gao, J. Zhou, and W. Zhang, “Edge detection based on the newton interpolation’s fractional differentiation,” *Int. Arab J. Inf. Technol.*, vol. 11, no. 3, pp. 223-228, May 2014.

- [94] Y. F. Pu, J. L. Zhou, and X. Yuan, "Fractional differential mask: A fractional differential-based approach for multiscale texture enhancement," *IEEE Trans. Image Process.*, vol. 19, no. 2, pp. 491-511, Feb. 2010, doi: 10.1109/TIP.2009.2035980.
- [95] C. C. Tseng and S. L. Lee, "Design of digital Riesz fractional order differentiator," *Signal Process.*, vol. 102, pp. 32-45, Sep. 2014, doi: 10.1016/j.sigpro.2014.02.017.
- [96] V. Garg and K. Singh, "An Improved Grunwald-Letnikov Fractional Differential Mask for Image Texture Enhancement," *Int. J. Adv. Comput. Sci. Appl.*, vol. 3, no. 3, pp. 130-135, 2012, doi: 10.14569/ijacsa.2012.030322.
- [97] M. D. Ortigueira and J. A. T. Machado, "What is a fractional derivative?," *J. Comput. Phys.*, vol. 293, pp. 4-13, Jul. 2015, doi: 10.1016/j.jcp.2014.07.019.
- [98] I. Podlubny, *Fractional Differential Equations: An Introduction to Fractional Derivatives, Fractional Differential Equations, to Methods of their solution and some of their Applications*, vol. 198, San Diego, California, USA: Academic Press, 1999.
- [99] M. D. Ortigueira, "Riesz potential operators and inverses via fractional centred derivatives," *Int. J. Math. Math. Sci.*, vol. 2006, Aug. 2006, Art. no. 048391, doi: 10.1155/IJMMS/2006/48391.
- [100] M. D. Ortigueira, "Fractional central differences and derivatives," *J. Vib. Control*, vol. 14, no. 9-10, pp. 1255-1266, Sept. 2008, doi: 10.1177/1077546307087453.
- [101] J. L. Lovoie, T. J. Osler, and R. Tremblay, "Fractional Derivatives and Special Functions," *SIAM Rev.*, vol. 18, no. 2, pp. 240-268, Apr. 1976, doi: 10.1137/1018042.
- [102] C. A. Monje, Y. Q. Chen, B. M. Vinagre, D. Xue, and V. Feliu, *Fractional-order Systems and Control Fundamentals and Applications*, New York, NY, USA: Springer-Verlag, 2010.
- [103] C. C. Tseng, S. C. Pei, and S. C. Hsia, "Computation of fractional derivatives using Fourier transform and digital FIR differentiator," *Signal Process.*, vol. 80, no. 1, pp. 151-159, Jan. 2000, doi: 10.1016/S0165-1684(99)00118-8.
- [104] C. C. Tseng, "Design of fractional order digital FIR differentiators," *IEEE Signal Process. Lett.*, vol. 8, no. 3, pp. 7-9, Mar. 2001, doi: 10.1109/97.905945.
- [105] S. Samadi, M. O. Ahmad, and M. N. S. Swamy, "Exact fractional-order differentiators for polynomial signals," *IEEE Signal Process. Lett.* vol. 11, no. 6, pp. 529-532, Jun. 2004, doi: 10.1109/LSP.2004.827917.
- [106] H. Zhao, G. Qiu, L. Yao, and J. Yu, "Design of fractional order digital FIR differentiators using frequency response approximation," in *Proc. 2005 Int. Conf. Commun. Circuits Syst.*, Hong Kong, China, 2005, pp. 1318-1321, doi:

- 10.1109/icccas.2005.1495349.
- [107] C. C. Tseng and S. L. Lee, "Design of Fractional Order Digital Differentiator Using Radial Basis Function," *IEEE Trans. Circuits Syst. I Regul. Pap.*, vol. 57, no. 7, pp. 1708-1718, Jul. 2010, doi: 10.1109/TCSI.2009.2034808.
- [108] D. Chen, Y. Q. Chen, and D. Xue, "Digital Fractional Order Savitzky-Golay Differentiator," *IEEE Trans. Circuits Syst. II Express Briefs*, vol. 58, no. 11, pp. 758-762, Nov. 2011, doi: 10.1109/TCSII.2011.2168022.
- [109] C. C. Tseng and S. L. Lee, "Closed-form design of fractional order differentiator using discrete cosine transform," in *Proc. IEEE Int. Symp. Circuits Syst.*, Beijing, China, 2013, pp. 2609-2612, doi: 10.1109/ISCAS.2013.6572413.
- [110] S. Khare, M. Kumar, and T. K. Rawat, "Window based design of fractional order FIR digital differentiator using type-III discrete cosine transform," in *Proc. 2014 Int. Conf. Signal Propag. Comput. Tech.*, Ajmer, India, 2014, pp. 39-43, doi: 10.1109/ICSPCT.2014.6884909.
- [111] M. Kumar, T. K. Rawat, and A. A. Singh, "Transform methods based designing of matrix fractional order differentiators," in *Proc. 2015 Annu. IEEE India Conf. (INDICON)*, Ne Delhi, India, 2015, pp. 1-6, doi: 10.1109/INDICON.2015.7443708.
- [112] C. C. Tseng and S. L. Lee, "Designs of matrix fractional order differentiators," *Signal Process.*, vol. 111, pp. 73-88, Jun. 2015, doi: 10.1016/j.sigpro.2014.12.010.
- [113] M. Kumar, T. K. Rawat, R. Anand, R. Karwayun, and A. Jain, "Design of Riesz Fractional Order Differentiator Using Discrete Sine Transform," in *Proc. 2016 3rd Int. Conf. Signal Process. Integr. Netw.*, Noida, India, 2016, pp. 702-706, doi: 10.1109/SPIN.2016.7566788.
- [114] M. Kumar and T. K. Rawat, "Fractional Order Digital Differentiator Design Based on Power Function and Least squares," *Int. J. Electron.*, vol. 103, no. 10, pp. 1639-1653, Feb. 2016, doi: 10.1080/00207217.2016.1138520.
- [115] M. Kumar and T. K. Rawat, "Design of fractional order differentiator using type-III and type-IV discrete cosine transform," *Eng. Sci. Technol. an Int. J.*, vol. 20, no. 1, pp. 51-58, Feb. 2017, doi: 10.1016/j.jestch.2016.07.002.
- [116] J. M. Cruz-Duarte, J. Rosales-Garcia, C. R. Correa-Cely, A. Garcia-Perez, and J. G. Avina-Cervantes, "A closed form expression for the Gaussian-based Caputo-Fabrizio fractional derivative for signal processing applications," *Commun. Nonlinear Sci. Numer. Simul.*, vol. 61, pp. 138-148, Aug. 2018, doi: 10.1016/j.cnsns.2018.01.020.
- [117] M. Salinas, R. Salas, D. Mellado, A. Glaría, and C. Saavedra, "A Computational

- Fractional Signal Derivative Method,” *Model. Simul. Eng.*, vol. 2018, Aug. 2018, Art. no. 7280306, doi: 10.1155/2018/7280306.
- [118] A. Kaur, S. Kumar, A. Agarwal, and R. Agarwal, “An Efficient R-Peak Detection Using Riesz Fractional-Order Digital Differentiator,” *Circuits, Syst. Signal Process.*, vol. 39, pp. 1965-1987, Apr. 2020, doi: 10.1007/s00034-019-01238-3.
- [119] C. Nayak, S. K. Saha, R. Kar, and D. Mandal, “Efficient Design of Zero-Phase Riesz Fractional Order Digital Differentiator Using Manta-Ray Foraging Optimisation for Precise Electrocardiogram QRS Detection,” *IEEE Open J. Circuits Syst.*, vol. 1, pp. 280-292, Dec. 2020, doi: 10.1109/ojcas.2020.3035771.
- [120] C. Nayak, S. K. Saha, R. Kar, and D. Mandal, “Optimal design of zero-phase digital Riesz FIR fractional-order differentiator,” *Soft Comput.*, pp. 1-22, Nov. 2020, doi: 10.1007/s00500-020-05440-3.
- [121] B. Mathieu, P. Melchior, A. Oustaloup, and C. Ceyral, “Fractional differentiation for edge detection,” *Signal Process.*, vol. 83, no. 11, pp. 2421-2432, Nov. 2003, doi: 10.1016/S0165-1684(03)00194-4.
- [122] H. Yang, Y. Ye, D. Wang, and B. Jiang, “A novel fractional-order signal processing based edge detection method,” in *Proc. 11th Int. Conf. Control Automat. Robot. Vision*, Singapore, 2010, pp. 1122-1127, doi: 10.1109/ICARCV.2010.5707865.
- [123] C. Telke and M. Beitelschmidt, “Edge detection based on fractional order differentiation and its application to railway track images,” in *Proc. Appl. Math. Mechanics*, Lecce, Italy, 2015, pp. 671-672, doi: 10.1002/pamm.201510325.
- [124] P. Amoako-Yirenkyi, J. K. Appati, and I. K. Dontwi, “A new construction of a fractional derivative mask for image edge analysis based on Riemann-Liouville fractional derivative,” *Adv. Differ. Equ.*, vol. 2016, Sep. 2016, Art. no. 238, doi: 10.1186/s13662-016-0946-8.
- [125] P. Amoako-Yirenkyi, J. K. Appati, and I. K. Dontwi, “Performance Analysis of Image Smoothing Techniques on a New Fractional Convolution Mask for Image Edge Detection,” *Open J. Appl. Sci.*, vol. 6, no. 7, pp. 478-488, Jul. 2016, doi: 10.4236/ojapps.2016.67048.
- [126] M. Mekideche and Y. Ferdi, “Edge Detection Optimization Using Fractional Order Calculus,” *Int. Arab J. Inf. Technol.*, vol. 16, no. 5, pp. 827-832, Sep. 2019.
- [127] C. Georgescu, “Improved Edge Detection Algorithms Based on a Riesz Fractional Derivative,” in *Proc. Int. Conf. Image Anal. Recognit.*, Póvoa de Varzim, Portugal, 2018, pp. 201-209, doi: 10.1007/978-3-319-93000-8_23.

- [128] N. Aboutabit, "A new construction of an image edge detection mask based on Caputo–Fabrizio fractional derivative," *The Vis. Comput.*, pp. 1-13, Jul. 2020, doi: 10.1007/s00371-020-01896-4.
- [129] B. Ghanbari and A. Atangana, "Some new edge detecting techniques based on fractional derivatives with non-local and non-singular kernels," *Adv. Differ. Equ.*, vol. 2020, Aug. 2020, Art. no. 435, doi: 10.1186/s13662-020-02890-9.
- [130] Y. Pu, "Fractional Calculus Approach to Texture of Digital Image," in *Proc. Int. Conf. Signal Process.*, Guilin, China, 2006, pp. 1-5, doi: 10.1109/ICOSP.2006.345713.
- [131] Y. Pu, W. Wang, J. Zhou, Y. Wang, and H. Jia, "Fractional differential approach to detecting textural features of digital image and its fractional differential filter implementation," *Sci. China Ser. F Inf. Sci.*, vol. 51, pp. 1319-1339, Sep. 2008, doi: 10.1007/s11432-008-0098-x.
- [132] Z. Gan and H. Yang, "Texture enhancement through multiscale mask based on RL fractional differential," in *Proc. Int. Conf. Inf. Netw. Automat.*, Kunming, China, 2010, pp. V1-333-V1337, doi: 10.1109/ICINA.2010.5636376.
- [133] Q. Chen, G. Huang, and X. Zhang, "A Fractional Differential Approach to Low Contrast Image Enhancement," *Int. J. Knowl. Lang. Process.*, vol. 3, no. 2, pp. 20-29, Aug. 2012.
- [134] C. C. Tseng and S. C. Cheng, "Digital color image sharpening using fractional differentiation and discrete cosine transform," in *Proc. 2012 Int. Symp. Commun. Inf. Technol.*, Gold Coast, QLD, Australia, 2012, pp. 181-186, doi: 10.1109/ISCIT.2012.6380886.
- [135] H. A. Jalab and R. W. Ibrahim, "Texture Enhancement Based on the Savitzky-Golay Fractional Differential Operator," *Math. Probl. Eng.*, vol. 2013, Feb. 2013, Art. no. 149289, doi: 10.1155/2013/149289.
- [136] Q. Yu, F. Liu, I. Turner, K. Burrage, and V. Vegh, "The use of a Riesz fractional differential-based approach for texture enhancement in image processing," *ANZIAM Journal*, vol. 54, pp. C590-C607, Aug. 2013, doi: 10.21914/anziamj.v54i0.6325.
- [137] C. C. Tseng and S. L. Lee, "Digital image sharpening using Riesz fractional order derivative and discrete hartley transform," in *Proc. IEEE Asia-Pacific Conf. Circuits Syst.*, Ishigaki, Japan, 2014, pp. 483-486, doi: 10.1109/APCCAS.2014.7032824.
- [138] C. Gao, J. Zhou, C. Liu, and Q. Pu, "Image enhancement based on fractional directional derivative," *Int. J. Mach. Learn. & Cybern.*, vol. 6, pp. 35-41, Feb. 2015, doi: 10.1007/s13042-014-0247-z.

- [139] Q. Yu, V. Vegh, F. Liu, and I. Turner, "A Variable Order Fractional Differential-Based Texture Enhancement Algorithm with Application in Medical Imaging," *PLoS ONE*, vol. 10, no. 7, Jul. 2015, Art. no. e0132952, doi: 10.1371/journal.pone.0132952.
- [140] S. L. Lee and C. C. Tseng, "Image sharpening using matrix Riesz fractional order differentiator and discrete sine transform," in *Proc. 2016 IEEE Int. Conf. Consum. Electron.-Taiwan*, Nantou, Taiwan, 2016, pp. 1-2, doi: 10.1109/ICCE-TW.2016.7520915.
- [141] S. Hemalatha and S. M. Anuncia, "G-L fractional differential operator modified using auto-correlation function: Texture enhancement in images," *Ain Shams Eng. J.*, vol. 9, no. 4, pp. 1689-1704, Dec. 2018, doi: 10.1016/j.asej.2016.12.003.
- [142] J. Guan, J. Ou, Z. Lai, and Y. Lai, "Medical Image Enhancement Method Based on the Fractional Order Derivative and the Directional Derivative," *Int. J. Pattern Recognit. Artif. Intell.*, vol. 32, no. 03, Mar. 2018, Art. no. 1857001, doi: 10.1142/S021800141857001X.
- [143] X. Luo, T. Zeng, W. Zeng, and J. Huang, "Comparative analysis on landsat image enhancement using fractional and integral differential operators," *Computing*, vol. 102, pp. 247-261, Jan. 2020, doi: 10.1007/s00607-019-00737-0.
- [144] H. Singh, A. Kumar, L. K. Balyan, and H. N. Lee, "Fractional-Order Integration Based Fusion Model for Piecewise Gamma Correction Along with Textural Improvement for Satellite Images," *IEEE Access*, vol. 7, pp. 37192-37210, Mar. 2019, doi: 10.1109/ACCESS.2019.2901292.
- [145] G. P. Kumar and R. R. Sahay, "Low Rank Poisson Denoising (LRPD): A Low Rank Approach Using Split Bregman Algorithm for Poisson Noise Removal From Images," in *Proc. IEEE/CVF Conf. Comput. Vision Pattern Recognit. Workshops*, Long Beach, CA, USA, 2019, pp. 1907-1916, doi: 10.1109/CVPRW.2019.00242.
- [146] U. Seger, "HDR Imaging in Automotive Applications," in *High Dynamic Range Video: From Acquisition to Display and Applications*, F. Dufaux, P. L. Callet, R. K. Mantiuk, and M. Mrak, Eds., Academic Press, 1st ed., San Diego, California, USA: Academic Press, 2016, pp. 477-498.
- [147] J. Singh, S. Singh, D. Singh, and M. Uddin, "Detection method and filters for blocking effect reduction of highly compressed images," *Signal Process. Image Commun.*, vol. 26, no. 8-9, pp. 493-506, Oct. 2011, doi: 10.1016/j.image.2011.04.002.
- [148] G. Singh and K. Singh, "Counter JPEG Anti-Forensic Approach Based on the Second-Order Statistical Analysis," *IEEE Trans. Inf. Forensics Secur.*, vol. 14, no. 5, pp. 1194-

- 1209, May 2019, doi: 10.1109/TIFS.2018.2871751.
- [149] N. Wiener, "Hermitian Polynomials and Fourier Analysis," *J. Math. Phys.*, vol. 8, no. 1-4, pp. 70-73, Apr. 1929, doi: 10.1002/sapm19298170.
- [150] L. B. Almeida, "The fractional Fourier Transform and time-frequency representations," *IEEE Trans. Signal Process.*, vol. 42, no. 11, pp. 3084-3091, Nov. 1994, doi: 10.1109/78.330368.
- [151] K. Singh, "Performance of Discrete Fractional Fourier TransformClasses in Signal Processing Applications," Ph.D. dissertation, Dept. Electron. Commun. Eng., Thapar Inst. Engg. Tech., Patiala, Punjab, India, 2006. [Online]. Available: <http://tudr.thapar.edu:8080/jspui/bitstream/123456789/94/1/P92233.pdf>
- [152] N. Jindal, "Performance of Fractional Transforms in Image and Video Processing," Ph.D. dissertation, Dept. Electron. Commun. Eng., Thapar Inst. Engg. Tech., Patiala, Punjab, India, 2013. [Online]. Available: <http://hdl.handle.net/10603/230325>.
- [153] M. A. Kutay, H. M. Ozaktas, O. Arikan, and L. Onural "Optimal filtering in fractional fourier domains," *IEEE Trans. Signal Process.*, vol. 45, no. 5, pp. 1129-1143, May 1997, doi: 10.1109/78.575688.
- [154] S. C. Pei, M. H. Yeh, and C. C. Tseng, "Discrete fractional Fourier transform based on orthogonal projections," *IEEE Trans. Signal Process.*, vol. 47, no. 5, pp. 1335-1348, May 1999, doi: 10.1109/78.757221.
- [155] P. K. Anh, L. P. Castro, P. T. Thao, and N. M. Tuan, "Two New Convolutions for the Fractional Fourier Transform," *Wireless Pers. Commun.*, vol. 92, pp. 623-637, Jan. 2017, doi: 10.1007/s11277-016-3567-3.
- [156] M. Abramowitz and I. A. Stegun, Eds., *Handbook of Mathematical Functions With Formulas, Graphs, and Mathematical Tables (Applied Mathematics Series 55)*. Washington, DC, USA: NBS, 1972.
- [157] L. C. Andrews, *Special Functions for Engineers and Applied Mathematicians*, New York, NY, USA: Macmillan, 1985.
- [158] I. S. Gradshteyn and I. M. Ryzhik, *Tables of Integrals, Series, and Products*, A. Jeffery, D. Zwillinger, Eds., 7th ed., San Diego, California, USA: Academic Press, 2007.
- [159] E. W. Weisstein, "Parabolic Cylinder Function." *Wolfram MathWorld*. <https://mathworld.wolfram.com/ParabolicCylinderFunction.html> (Accessed Jun.19, 2019).
- [160] J. W. Brown and R. V. Churchill, *Complex Variables and Applications*, 8th ed., New

- York, NY, USA: McGraw Hill, 2009.
- [161] R. Kress, *Graduate Texts in Mathematics: Numerical Analysis*, New York, NY, USA: Springer-Verlag, 1998.
- [162] H. Jeffreys and B. S. Jeffreys, "Lagrange's Interpolation Formula," in *Methods of Mathematical Physics*, 3rd ed., Cambridge, England: Cambridge University Press, 1988, Ch. 9, pp. 261-314.
- [163] S. R. K. Iyengar and R. K. Jain, *Numerical Methods*, New Delhi, India: New Age International, 2009.
- [164] T. Chai and R. R. Draxler, "Root mean square error (RMSE) or mean absolute error (MAE)? -Arguments against avoiding RMSE in the literature," *Geosci. Model Dev.*, vol. 7, pp. 1247-1250, Jun. 2014, doi: 10.5194/gmd-7-1247-2014.
- [165] F. Sattar, L. Floreby, G. Salomonsson, and B. Lövsström, "Image enhancement based on a nonlinear multiscale method," *IEEE Trans. Image Process.*, vol. 6, no. 6, pp. 888-895, Jun. 1997, doi: 10.1109/83.585239.
- [166] M. Gaur, S. Makonin, I. V. Bajić, and A. Majumdar, "Performance Evaluation of Techniques for Identifying Abnormal Energy Consumption in Buildings," *IEEE Access*, vol. 7, pp. 62721-62733, May 2019, doi: 10.1109/ACCESS.2019.2915641.
- [167] K. Panetta, A. Samani, and S. Agaian, "Choosing the Optimal Spatial Domain Measure of Enhancement for Mammogram Images," *Int. J. Biomed. Imaging*, vol. 2014, Aug. 2014, Art. no. 937849, doi: 10.1155/2014/937849.
- [168] T. Yuan, X. Zheng, X. Hu, W. Zhou, and W. Wang, "A Method for the Evaluation of Image Quality According to the Recognition Effectiveness of Objects in the Optical Remote Sensing Image Using Machine Learning Algorithm," *PLoS ONE*, vol. 9, no. 1, Jan. 2014, Art. no. e86528, doi: 10.1371/journal.pone.0086528.
- [169] I. E. G. Richardson, *H.264 and MPEG-4 video compression: Video Coding for Next-generation Multimedia*, Hoboken, NJ, USA: Wiley, 2003.
- [170] Z. Wang, A. C. Bovik, H. R. Sheikh, and E. P. Simoncelli, "Image quality assessment: from error visibility to structural similarity," *IEEE Trans. Image Process.*, vol. 13, no. 4, pp. 600-612, Apr. 2004, doi: 10.1109/TIP.2003.819861.
- [171] Z. Wang and A. C. Bovik, "A universal image quality index," *IEEE Signal Process. Lett.*, vol. 9, no. 3, pp. 81-84, Mar. 2002, doi: 10.1109/97.995823.
- [172] N. Tsafack, J. Kengne, B. Abd-El-Atty, A. M. Iliyasu, K. Hirota, and A. A. Abd EL-Latif, "Design and implementation of a simple dynamical 4-D chaotic circuit with applications in image encryption," *Inf. Sci.*, vol. 515, pp. 191-217, Apr. 2020, doi:

- 10.1016/j.ins.2019.10.070.
- [173] M. Singh, S. Singh, and S. Gupta, "An information fusion based method for liver classification using texture analysis of ultrasound images," *Inf. Fusion*, vol. 19, pp. 91-96, Sep. 2014, doi: 10.1016/j.inffus.2013.05.007.
- [174] R. M. Haralick, K. Shanmugam, and I. Dinstein, "Textural Features for Image Classification," *IEEE Trans. Syst. Man Cybern.*, vol. SMC-3, no. 6, pp. 610-621, Nov. 1973, doi: 10.1109/TSMC.1973.4309314.
- [175] "The USC-SIPI Image Database." USC Viterbi School of Engineering. <http://sipi.usc.edu/database/database.php>. (Accessed: Jul. 20, 2020)
- [176] H. R. Sheikh, Z. Wang, L. Cormack, and A. C. Bovik, "LIVE image quality assessment database release 2." Laboratory for Image & Video Engineering. <http://live.ece.utexas.edu/research/quality>. (Accessed: Sep 10, 2019).
- [177] K. Zhang, W. Zuo, Y. Chen, D. Meng, and L. Zhang, "Beyond a Gaussian Denoiser: Residual Learning of Deep CNN for Image Denoising," *IEEE Trans. Image Process.*, vol. 26, no. 7, pp. 3142-3155, Jul. 2017, doi: 10.1109/TIP.2017.2662206.
- [178] B. Li *et al.*, "Benchmarking Single-Image Dehazing and Beyond," *IEEE Trans. Image Process.*, vol. 28, no. 1, pp. 492-505, Jan. 2019, doi: 10.1109/TIP.2018.2867951.
- [179] S. Abdelmounaime and H. D. Chen, "New Brodatz-Based Image Databases for Grayscale Color and Multiband Texture Analysis," *Int. Scholarly Res. Notices*, vol. 2013, Feb. 2013, Art. no. 876386, doi: 10.1155/2013/876386.
- [180] D. Martin, C. Fowlkes, D. Tal, and J. Malik, "A database of human segmented natural images and its application to evaluating segmentation algorithms and measuring ecological statistics," *Proc. IEEE Int. Conf. Comput. Vis.*, Vancouver, BC, Canada, 2001, pp. 416-423, doi: 10.1109/ICCV.2001.937655.
- [181] P. Arbeláez, M. Maire, C. Fowlkes, and J. Malik, "Contour Detection and Hierarchical Image Segmentation," *IEEE Trans. Pattern Anal. Mach. Intell.*, vol. 33, no. 5, pp. 898-916, May 2011, doi: 10.1109/TPAMI.2010.161.
- [182] I. Bloch, "TP-RDMM." LTCI. <https://perso.telecom-paristech.fr/bloch/P6Image/TP-RDMM/Images/>. (Accessed: Jul. 26, 2017).
- [183] "VIP Illumination Saliency Dataset." Vision and Image Processing Lab. <https://uwaterloo.ca/vision-image-processing-lab>. (Accessed: Jul 27, 2020).
- [184] A. Budai, R. Bock, A. Maier, J. Hornegger, and G. Michelson, "Robust vessel segmentation in fundus images," *Int. J. Biomed. Imaging*, vol. 2013, Dec. 2013, Art. no. 154860, doi: 10.1155/2013/154860.

- [185] Z. Ying, G. Li, Y. Ren, R. Wang, and W. Wang, "A new image contrast enhancement algorithm using exposure fusion framework," in *Proc. Int. Conf. Comput. Anal. Images Patterns*, Ystad, Sweden, 2017, pp. 36-46, doi: 10.1007/978-3-319-64698-5_4.
- [186] W. Zeng and H. Gao, "Image processing research based on fractional Fourier transform," *J. Softw. Eng.*, vol. 9, no. 2, pp. 318–327, 2015, doi: 10.3923/jse.2015.318.327.
- [187] H. G. Adelman, "Butterworth equations for homomorphic filtering of images," *Comput. Biol. Med.*, vol. 28, no. 2, pp. 169-181, Jun. 1998, doi: 10.1016/S0010-4825(98)00004-3.
- [188] L. H. Lin and T. J. Chen, "Mutual Information Correlation with Human Vision in Medical Image Compression," *Curr. Med. Imaging Rev.*, vol. 14, no. 1, pp. 64-70, Feb. 2018, doi: 10.2174/1573405613666171003151036.
- [189] A. Azeroual and K. Afdel, "Fast Image Edge Detection based on Faber Schauder Wavelet and Otsu Threshold," *Heliyon*, vol. 3, no. 12, Dec. 2017, Art. no. e00485, doi: 10.1016/j.heliyon.2017.e00485.

IMAGES USED FOR SIMULATION

A.1 Grayscale Images

The following grayscale images from USC-SIPI [175], LIVE [176], MATLAB in-built images, Classic 5, BSD68, Set12 [177], RESIDE [178], Normalized Brodatz [179], and TP-RDMM [182] datasets are used for the simulation work in Chapter-3, Chapter-4, and Chapter-5.



Butterfly (256×256)



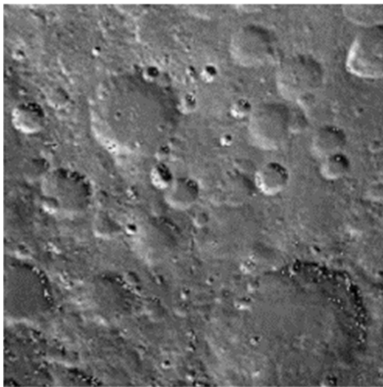
Laiton (256×256)



Lena (256×256)



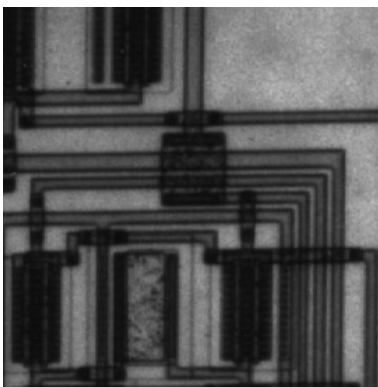
Moon (256×256)



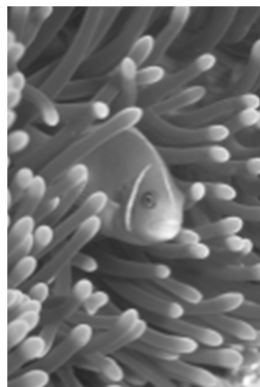
Surface (256×256)



Pout (240×291)



Circuit (272×280)



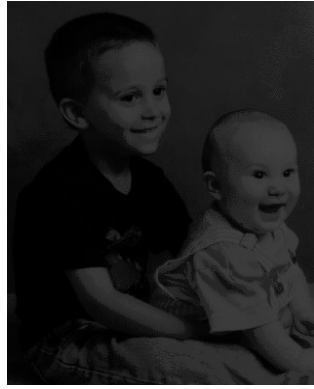
Fish (321×481)



Palace (321×481)



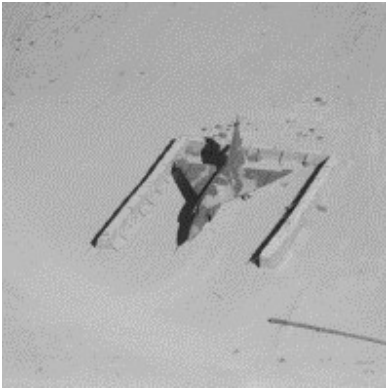
Vase (321×481)



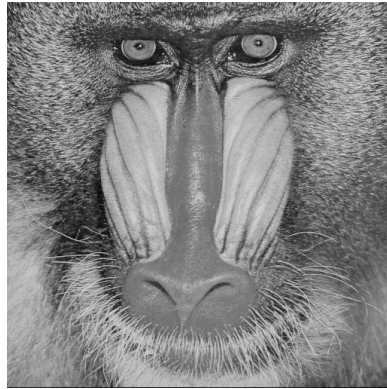
Kids (400×318)



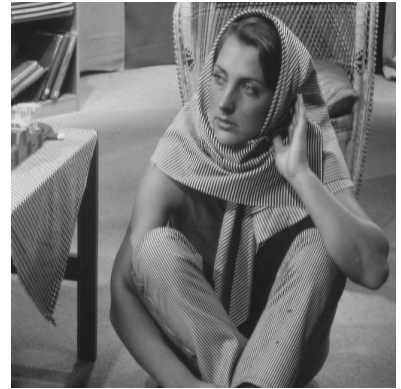
Cars (481×321)



Airplane (512×512)



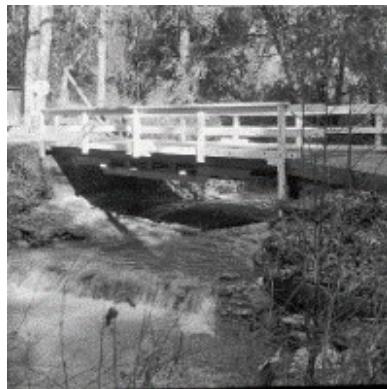
Baboon (512×512)



Barbara (512×512)



Bark (512×512)



Bridge (512×512)



Lighthouse (512×512)



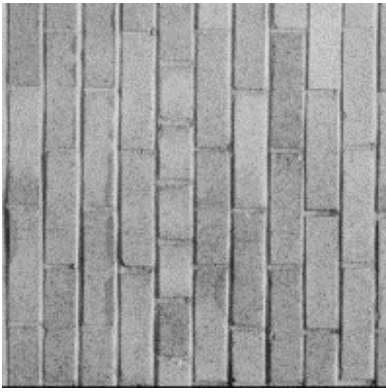
Pirate (512×512)



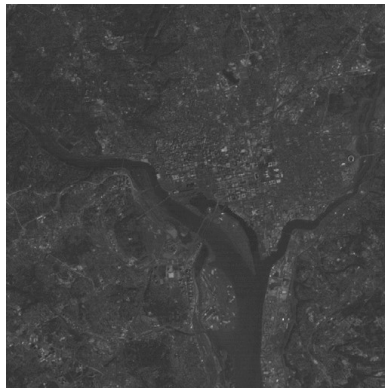
Tank (512×512)



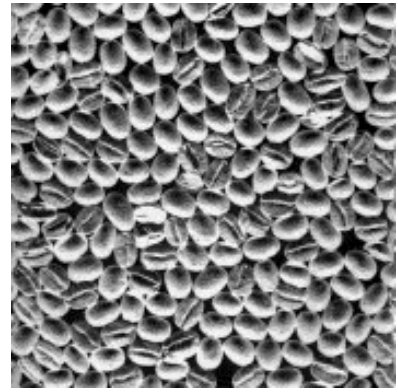
Truck (512×512)



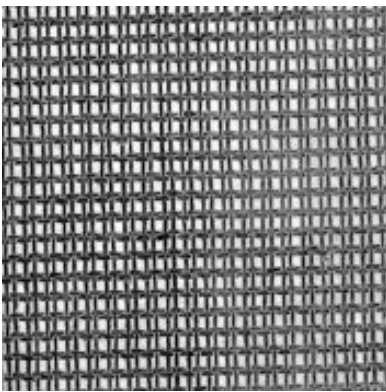
Wall (512×512)



Washington Satellite
(512×512)



Seeds (640×640)



Texture (640×640)



Road (800×445)



Birds (940×582)

A.2 Color Images

The following color images from Test images, BSDS300, and BSDS500 datasets [95], [180], [181] are used for the simulation work in Chapter-4. However, all the test images from the BSDS300 and BSDS500 datasets [180], [181] are used for the simulation work in Chapter-6.



Vase_Color (321×481)



Rabbit (341×455)



Building (481×321)



Car (481×321)

A.3 Images with varying Illumination conditions

The following grayscale images from VIP Illumination Saliency Dataset [183] are used for the simulation work in Chapter-3, Chapter-4, and Chapter-5.



c1 (480×270)



c2 (480×270)



c3 (480×270)



c4 (480×270)



Statue1 (352×240)



Statue2 (352×240)



Statue3 (352×240)



Statue4 (352×240)



Statue5 (352×240)

The following color images from VIP Illumination Saliency Dataset [183] are used for the simulation work in Chapter-4 and Chapter-6.



c1_color (480×270)



c2_color (480×270)



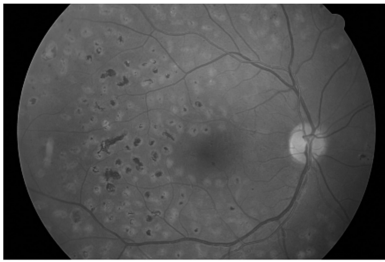
c3_color (480×270)



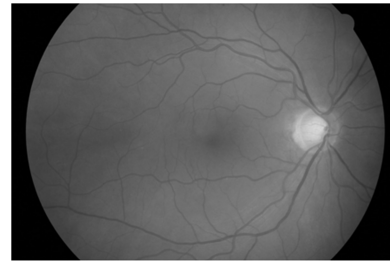
c4_color (480×270)

A.4 Fundus Images

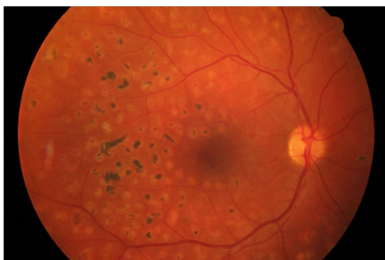
The following grayscale and color images from the HRF database [184] are used for the simulation work in Chapter-3 and Chapter-6.



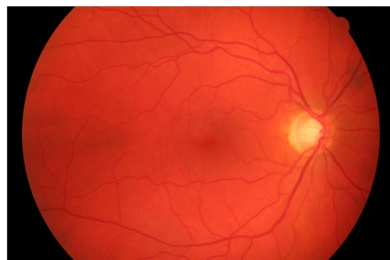
DR (438×292)



Healthy (438×292)



DR patient (438×292)



Healthy Individual (438×292)

VITA

Kanwarpreet Kaur was born in Ludhiana, Punjab, India in 1992. She received the B. Tech and M. Tech degree in Electronics and Communication Engineering from Guru Nanak Dev Engineering College, Ludhiana, Punjab, India in 2014 and 2016 respectively. She is presently working towards the Ph.D. degree in the Electronics and Communication Engineering Department, Thapar Institute of Engineering and Technology, Patiala, Punjab, India. Her research interests include fractional calculus and signal processing. Her email id is kpreet2392@gmail.com.

ORIGINALITY REPORT

9%

SIMILARITY INDEX

3%

INTERNET SOURCES

8%

PUBLICATIONS

1%

STUDENT PAPERS

PRIMARY SOURCES

- 1 Kanwarpreet Kaur, Neeru Jindal, Kulbir Singh. "Fractional Fourier Transform based Riesz fractional derivative approach for edge detection and its application in image enhancement", *Signal Processing*, 2021
Publication 2%
 - 2 Kanwarpreet Kaur, Neeru Jindal, Kulbir Singh. "Fractional derivative based Unsharp masking approach for enhancement of digital images", *Multimedia Tools and Applications*, 2020
Publication 2%
 - 3 Kanwarpreet Kaur, Neeru Jindal, Kulbir Singh. "Riesz fractional order derivative in Fractional Fourier Transform domain: An insight", *Digital Signal Processing*, 2019
Publication 1%
 - 4 rutcor.rutgers.edu
Internet Source <1%
 - 5 link.springer.com
Internet Source <1%
-